



Universiteit
Leiden
The Netherlands

Modeling vascular diseases using human induced pluripotent stem cells

Cao, X.

Citation

Cao, X. (2020, September 9). *Modeling vascular diseases using human induced pluripotent stem cells*. Retrieved from <https://hdl.handle.net/1887/136521>

Version: Publisher's Version

License: [Licence agreement concerning inclusion of doctoral thesis in the Institutional Repository of the University of Leiden](#)

Downloaded from: <https://hdl.handle.net/1887/136521>

Note: To cite this publication please use the final published version (if applicable).

Cover Page



Universiteit Leiden



The handle <http://hdl.handle.net/1887/136521> holds various files of this Leiden University dissertation.

Author: Cao, X.

Title: Modeling vascular diseases using human induced pluripotent stem cells

Issue Date: 2020-09-09

Modeling Vascular Diseases Using Human Induced Pluripotent Stem Cells

Xu Cao

曹旭

Colophon

Modeling Vascular Diseases Using Human Induced Pluripotent Stem Cells

PhD thesis

This thesis was prepared at the department of Anatomy and Embryology of the Leiden University Medical Center, Leiden, the Netherlands

Copyright © Xu Cao, Leiden, The Netherlands, 2020.

All rights reserved. No part of this book may be reproduced or transmitted, in any form or by any means, without permission in writing of the author. The copyright of the articles that have been published has been transferred to the respective journals.

The research in described in this thesis was supported by the European Research Council and a grant from Moller Foundation.

ISBN: 978-94-92597-43-4

Printed by Boekenddeal, The Netherlands.

Cover: Oil-red O staining of M1 macrophages derived from human induced pluripotent stem cells. The background image was granted by Pixabay (from Paul McManus)
<https://pixabay.com/zh/illustrations/fibres-fibers-fibre-fiber-organic-4113337/>.

Modeling Vascular Diseases Using Human Induced Pluripotent Stem Cells

Proefschrift

Ter verkrijging van
de graad van Doctor aan de Universiteit Leiden,
op gezag van Rector Magnificus prof.mr. C.J.J.M. Stolker
volgens besluit van het College voor Promoties
te verdedigen op

woensdag 09 september 2020

klokke 10.00 uur

door

Xu Cao

geboren te Linyi, China in 1990

Promotor: Prof. dr. C. L. Mummery

Co-promoter: Dr. V. V. Orlova

Promotiecommissie:

Prof.dr. M.J.T.H. Goumans

Prof.dr. P.C.J.J. Passier

Dr. S. Semrau

Prof.dr. F.J.T. Staal

Prof. dr. D. Salvatori (Universiteit Utrecht)

Table of Contents

Chapter 1

General Introduction..... - 7 -

Chapter 2

Differentiation and Functional Comparison of Monocytes and Macrophages from hiPSCs with Peripheral Blood Derivatives..... - 45 -

Chapter 3

Generation and Functional Characterization of Monocytes and Macrophages Derived from Human Induced Pluripotent Stem Cells - 81 -

Chapter 4

Transcriptional Dynamics During Segregation of Endothelial and Myocardial Lineages from Cardiac Mesoderm..... - 123 -

Chapter 5

Vascular defects associated with Hereditary Hemorrhagic Telangiectasia revealed in patient-derived isogenic iPSCs..... - 155 -

Chapter 6

Pseudomyogenic hemangioendothelioma recapitulated in endothelial cells from human induced pluripotent stem cells engineered to express the SERPINE1-FOSB translocation - 191 -

Appendix Chapter 6:

Follow up bioinformatics analysis of hiPSC-endothelial cells expressing the SERPINE1-FOSB translocation - 224 -

Chapter 7

Discussion and Future Perspectives - 233 -

APPENDIX..... - 250 -

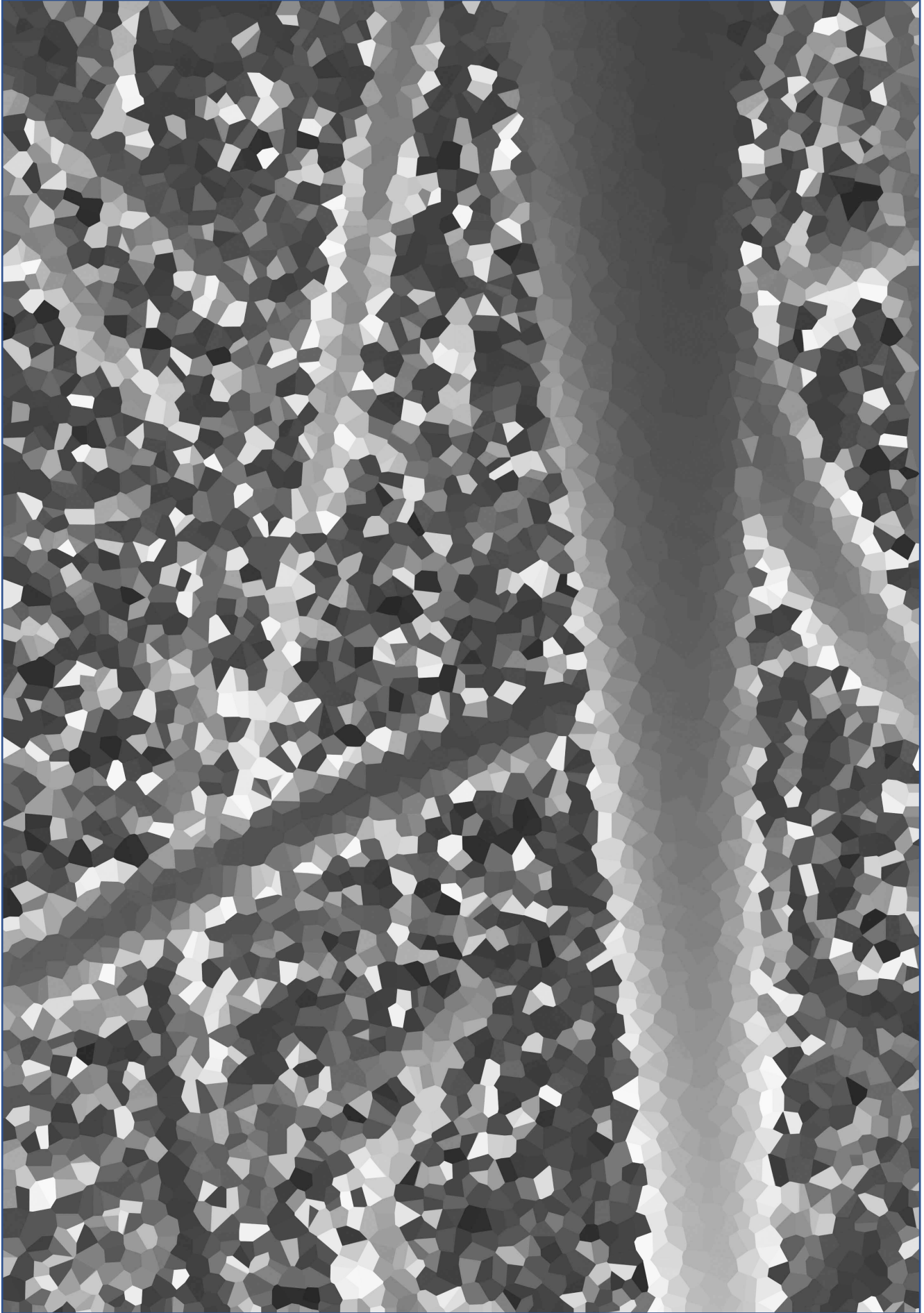
SUMMARY..... - 252 -

SAMENVATTING..... - 254 -

CURRICULUM VITAE..... - 255 -

LIST OF PUBLICATIONS - 249 -

ACKNOWLEDGMENTS - 259 -



Chapter 1

General Introduction

Abnormal vascular physiology and precipitating inflammatory pathways underlie many different diseases, including hemorrhage, stroke, vascular dementia and even cancer. Pluripotent stem cells (PSCs) can now be derived by reprogramming from any individual so that it is possible in principle to derive all somatic cells of the human body that would normally be difficult to access. In this thesis, I studied the derivation of myeloid cells from human induced pluripotent stem cells (hiPSCs) to model the inflammatory component of vascular disease and characterized the development path of hiPSC-derived endothelial cells (hiPSC-ECs) which form the vascular walls. Functional defects in either of these cell types can cause or exacerbate vascular disease. I then used these cell types to gain insight into the mechanisms underlying two genetic diseases: Hereditary Hemorrhagic Telangiectasia (HHT) which is caused by mutations in a gene called Endoglin expressed on cells of the vascular wall and inflammatory macrophages, and a vascular tumor called Pseudomyogenic hemangioendothelioma (PHE) in which endothelial cells are thought to be the tumor cell of origin but this remained to be proven. I developed new differentiation protocols to generate inflammatory cells from hiPSC, characterized these cells functionally and used Next-Generation Sequencing and bioinformatic analysis to gain insight into the molecular pathways controlling development of one particular type of endothelial cells from hiPSC and the underlying tumorigenic mechanisms of PHE.

1.1 Myeloid cells derived from hiPSCs

1.1.1 Derivation of myeloid cells from hiPSCs

Myeloid cells mainly refer to the monocytes and granulocytes in the blood but also include the derivatives of monocytes in tissue, including macrophages and dendritic cells. In this thesis, I mainly considered monocytes and macrophages within the myeloid lineage, as these cells express high levels of endoglin and thus may be most relevant to HHT type 1 (HHT1).

Macrophages in tissue have two different development origins: primitive hematopoiesis that occurs in the yolk sac of early embryo and which can give rise to primitive erythrocytes and primitive macrophages; monocytes that differentiate from hematopoietic stem cells in the bone marrow, which can differentiate into macrophages after transmigration through blood vessels during inflammation. Macrophages not only provide protection from pathogens, but also play a key role in the regulation of angiogenesis and tissue regeneration by secreting a wide range of cytokines, chemokines and growth factors. When polarized by different stimuli, macrophages can be divided functionally into several subtypes, termed M1 (LPS and IFN- γ sensitive), M2a (IL4), M2b (Fc receptors and immune-complex expression) and M2c (IL10 and glucocorticoid expression) (Mantovani et al., 2004).

Currently, tumor derived macrophage cell lines and peripheral blood monocyte-derived macrophages are commonly used as a source of macrophages for research. Both sources have limitations: tumor cell lines differ considerably from physiologically normal macrophages and primary macrophages from blood are different from those in organ tissues, have limited availability and have ethical challenges associated with informed consent and invasive methods of collection. Furthermore, studying macrophage biology in rare genetic diseases is even more difficult since there are only few patients to donate tissue. Thus, by comparison, hiPSCs differentiated to macrophages could represent an unlimited supply of human macrophages, that are either healthy or carry specific patient genotypes (Zhang and Reilly, 2017); they can thus be used for in vitro disease modelling to understand underlying disease mechanisms and consequently improve therapeutic strategies.

In 2008, Karlsson et al. reported an “embryoid body” (EB)-based protocol to differentiate hESCs into monocyte-like cells. M-CSF and IL-3 were added to induce the monocytes from EBs and floating single cells were collected continuously and then further differentiated into macrophages (Karlsson et al., 2008). Choi et al. used OP9 coculture to induce the hematopoietic differentiation from hPSCs. From the coculture system, lin-CD34+CD43+CD45+ multipotent progenitors were expanded with GM-CSF and then further differentiated into macrophages using M-CSF and IL-1 β (Choi et al., 2009; 2011). In 2013, Yanagimachi and colleagues developed a monocyte differentiation protocol using monolayer culture and defined conditions. With their protocol, a large number of monocytes could be harvested continuously from day 16 to day 28, and macrophages could be derived from these monocytes after one more week (Yanagimachi et al., 2013). Meanwhile, Cowley’s group also developed a serum-free protocol which was based on EB formation. They found monocytes could be continuously harvested from 14 days of differentiation onwards for a period of almost one year, although the differentiation efficiency decreased dramatically after about 6 months (van Wilgenburg et al., 2013). Lachmann and colleagues also established a EB-based differentiation protocol for continuous production of monocytes and neutrophils over a 2 month timespan using M-CSF and G-CSF respectively (Lachmann et al., 2015). Zhang et al. reported a stepwise differentiation method, in which highly pure populations of CD14+ monocytes could be derived from hiPSCs after 15 days of induction (Zhang et al., 2015). Most protocols reported so far for the differentiation of monocytes and macrophages from hiPSCs are EB-based or do not use fully defined conditions (Brault et al., 2014; Choi et al., 2011; Karlsson et al., 2008; Lachmann et al., 2015; Yanagimachi et al., 2013; Zhang et al., 2015). Recently, Takata et al. established a serum-free monolayer differentiation protocol to induce primitive macrophages from hiPSCs by Wnt inhibition from day 6 to day 10. They also showed that coculture of these macrophages with hiPSC-derived neurons could promote differentiation of microglia-

like cells (Takata et al., 2017).

One of the main aims of this thesis was to establish a more robust method for differentiation of myeloid cells from hiPSCs and show this was applicable to multiple hiPSC lines. Specifically, we aimed to use a monolayer protocol based on serum- and feeder cell-free culture conditions for the differentiation and hoped to see that the protocol was faster and more robust from line to line.

1.1.2 Characterization of hiPSC-derived macrophages

Although several differentiation methods have been established so far for monocyte and/or macrophage differentiation from hiPSCs, the question remains whether hiPSC-derived macrophages (IPSDMs) behave similarly to primary human macrophages *in vitro* and *in vivo*. A thorough characterization of IPSDMs may provide the field with a critical reference to what extent primary macrophages can be replaced by IPSDMs for disease modeling, drug screening and cell replacement therapies in the future.

Characterization of IPSDMs is usually based on their morphology, gene expression, surface marker expression, cytokine secretion, lipid uptake, cholesterol efflux, and phagocytotic activities. Cowley's group compared macrophages derived from hiPSCs using their EB-based protocol with peripheral blood-derived macrophages (PBDMs) by Scanning Electron Microscopy and Transmission Electron Microscopy, which showed similar morphologies of these two sources of cells. Their IPSDMs expressed normal levels of CD14, CD16, CD163 and CD86 compared with primary cells, whereas MHCII levels were much lower on IPSDMs than PBDMs. They also showed that IPSDMs secreted high levels of pro-inflammatory cytokines after stimulation by LPS and IFN- γ , including IL-6, TNF- α , RNATES and IL-23 (van Wilgenburg et al., 2013). With Lachmann's protocol, it was reported that IPSDMs expressed most of the macrophage specific markers, although CD11b was lower on IPSDMs compared with PBDMs. These IPSDMs could also phagocytose bacteria and secrete some of inflammatory cytokines including TNF- α , IL-6, IL-8, MCP-1 and IL-10 (Lachmann et al., 2015). Zhang et al. compared gene expression in IPSDMs and PBDMs derived from the same subject by transcriptomic analysis. They found that around 12% genes were differentially expressed between IPSDMs and PBDMs, which mainly related to the immune and defense responses (Zhang et al., 2015). They also compared the morphology, surface marker expression, LDL-uptake, bacterial phagocytosis, and cytokine secretion of M0, M1 and M2a subtypes of IPSDMs and PBDMs. Their results indicated high similarities between IPSDMs and PBDMs (Zhang et al., 2015).

However, so far only some aspects of functional activities of IPSDMs have been examined and only some subtypes of macrophages compared. Efferocytosis, a characteristic mainly of tissue resident macrophages, can remove and clear apoptotic

cells after tissue damage which is critical to maintaining tissue hemostasis. Defective efferocytosis can lead to disease including cystic fibrosis, Chronic Obstructive Pulmonary Disease and asthma. Efferocytosis activity of IPSDMs would thus greatly facilitate their application in disease modelling and studies of the pathology of these conditions.

Increasing evidence showed macrophages as one of the main effector cells of monoclonal antibody (mAb) based cancer therapy (Gul and van Egmond, 2015). Human primary macrophages phagocytose tumor cells efficiently *in vitro* through antibody-dependent cell phagocytosis and antibody-independent phagocytosis. CD47 serve as “don’t eat me” signals on tumor cells by binding to SIRP α expressed on macrophages and inhibiting their phagocytotic activity. Thus CD47-SIRP α pathway can serve as a target to enhance phagocytosis of tumor cells by macrophages *in vitro* and *in vivo* (Majeti et al., 2009; Theocharides et al., 2012; Tseng et al., 2013; Willingham et al., 2012). CD47 and SIRP α blocking antibodies synergize with tumor specific mAb to promote the efficiency of cancer therapy (Chao et al., 2010; Tseng et al., 2013). Human primary macrophages have commonly been used as a tool to test CD47-SIRP α blocking antibodies and tumor specific mAb *in vitro* (Chao et al., 2010; Majeti et al., 2009; Willingham et al., 2012). However, the variations among different individuals and limited availability make primary macrophages less than ideal for pre-clinical drug screening. Instead, IPSDMs can be a better option due to their patient-specific genetic background and unlimited source. However, at the outset of the research in this thesis, tumor phagocytotic activity of IPSDMs still needed to be carefully checked.

To date, IPSDMs have already been used to model several genetic diseases, including Tangier disease, chronic granulomatous disease, Blau syndrome neuronal ceroid lipofuscinoses, Gaucher disease and chronic infantile neurological cutaneous, articular syndrome, mycobacterial disease (Aflaki et al., 2014; Jiang et al., 2012; Neehus et al., 2018; Panicker et al., 2012; Tanaka et al., 2012; Uusi-Rauva et al., 2017). There are no reports so far for modeling of vascular diseases using IPSDMs to the best of our knowledge.

1.2 Endothelial cells derived from hiPSCs

1.2.1 Tight-regulation of endothelial cell (EC) specification *in vivo*

During vertebrate embryo development, a functional circulatory system is a prerequisite for organ formation to meet their increasing demand for nutrients and oxygen. Together with the increasing organ size during cell specification and morphogenesis of different organs, the vasculature is also expanding, remodeling and specializing to fulfill the requirement of each organ they “serve”. Blood vessels are formed through two mechanisms, termed vasculogenesis and angiogenesis. Vasculogenesis mainly refers to *de novo* EC differentiation and specification from

mesoderm precursors and occurs before the onset of blood flow. Vascular progenitors first appear in yolk sac, which come from mesodermal progenitors and form the blood islands. The outer cells of blood island differentiate into ECs and the inner cells become hematopoietic cells. Within the embryo, vascular progenitors form angioblasts which aggregate to form the ventral and dorsal aortas and the vitelline arteries and veins. Then, primary vasculature thus formed starts to expand and remodel through angiogenesis; this includes ECs sprouting, vessel branching, and intussusception from existing blood vessels (Patan, 2004). Also, further specialization of the endothelium to arterial, venous, hemogenic, and lymphatic subtypes is necessary to fulfill diverse functions of the vasculature (Marcelo et al., 2013).

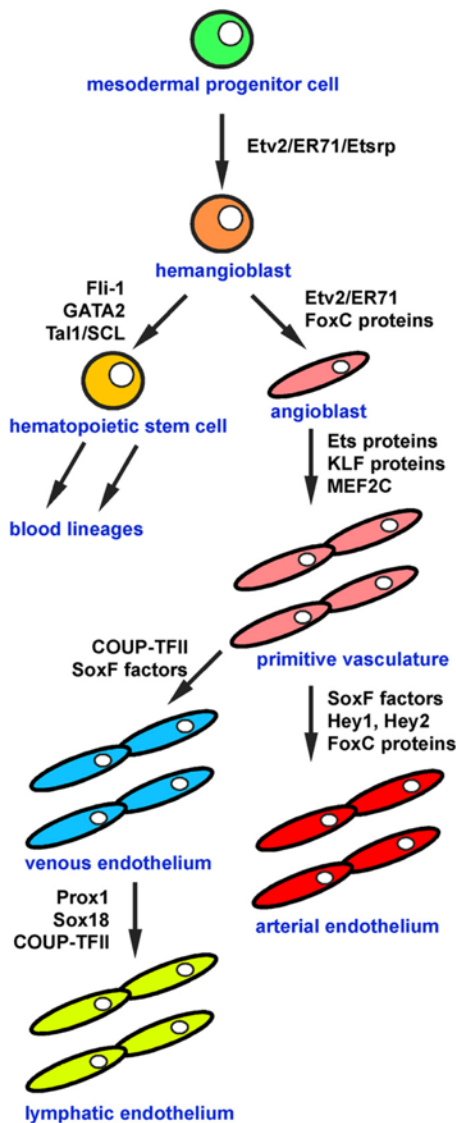
The signaling pathways that are involved in vasculogenesis and angiogenesis have been intensively studied (Figure 1). Although the hierarchy of these signals has not been clearly defined *in vivo*, numerous data have been obtained from studies using embryonic stem (ES) cell systems. Studies using mouse ES cells indicated bone morphogenic protein 4 (BMP4) as the earliest key factor that drives mesoderm differentiation and initiates fibroblast growth factor 2 (FGF2)-dependent specification of EC progenitors (Park, 2004; Pearson et al., 2008). However, with human ES cells, FGF2 is required for maintaining the undifferentiated state thus its role in the commitment of mesoderm cells to ECs is not essential. Instead, Indian Hedgehog was found as a critical factor downstream of BMP4, which promotes EC differentiation from mesoderm cells (Kelly and Hirschi, 2009). Like IHH, VEGF is another visceral endoderm-derived factor that is a key regulator of vasculogenesis. Heterozygous knockout of VEGF-A was embryonic lethal due to the failure of vascular development (Carmeliet et al., 1996; Ferrara et al., 1996). On the other hand, overexpression of VEGF-A also lead to embryonic lethality in mice due to the impaired cardiac development (Miquerol et al., 2000). These data indicate that a precise dosage of VEGF-A is required for cardiovascular development.

E-twenty six (ETS) transcription factors are also well-known as key regulators of EC development. Several members of the ETS family, including Ets1, Erg, Fli-1 and Etv2 have been shown to play essential roles in endothelial and hematopoietic differentiation (Dejana et al., 2007). Notably, all characterized enhancers and promoters of endothelial related genes so far contain multiple essential ETS binding sites, and ETS motifs are strongly associated with endothelial genes throughout the human genome (Bernat et al., 2006; Val et al., 2008). Many ETS share redundant functions, except for ETV2, which plays a specific and critical role for the differentiation of mesoderm toward an EC-fate and will be discussed specifically later.

Although it is known that ETS play a central role in the transcriptional control of EC specification, the wide spread binding sites of Ets proteins make it difficult to fully understand the regulatory network of ETS factors. Except for the canonical binding sites, ETS can also bind to noncanonical sites in conjunction of other factors (Hollenhorst et

al., 2007). Studies identified evolutionarily conserved FOX:ETS motifs which can be bound by FoxC2 and ETV2 simultaneously, and these motifs are located in the promoters and enhancers of endothelial genes including Tal1, Tie2, flk1, and VE-cadherin (Cdh5) (Val et al., 2008) .

Forkhead (Fox) Proteins also play a key role in EC specification; they include members of FoxC, FoxF, FoxH and FoxO subfamilies. FoxO1 is required for vascular development and functions as both a positive and negative regulator of transcription, suggesting that it may act as a transcriptional switch in EC specification (Paik et al., 2007).



FoxF1 is also necessary for vascular development and it may regulate the BMP signaling in splanchnic mesoderm prior to EC specification (Astorga and Carlsson, 2007). By contrast, FoxH1 overexpression impaired the vascular development and may act as an inhibitor by negatively regulating flk1 expression (Choi et al., 2007). FoxC subfamily also play an important role in vascular development. FoxC1 and FoxC2 knockout mice showed severe vascular defects and indicated that these transcription factors were required for early endothelial development (Swift and Weinstein, 2009; Val et al., 2008). Besides, FoxC1 and FoxC2 also play an important role in arterial and lymphatic endothelial cell specification and act as key downstream effectors of Notch signaling (Chu et al., 2016; Hayashi and Kume, 2008).

Figure 1. Different Stages in Endothelial Development Are Regulated by Distinct Sets of Transcription Factors. This figure is adapted from (Sarah et al., 2009).

1.2.2 Roles of *ETV2* in ECs development

The specification of ECs from mesoderm progenitors is highly depend on the activity of the *Etv2* transcription factors (van Bueren and Black, 2012; Koyano-

Nakagawa and Garry, 2017; Val, 2011). Studies in zebrafish embryos showed that *ETV2* alone is necessary for vasculogenesis, while *Etv2* and another ETS factor *Fli1b* function redundantly during early embryo angiogenesis (Craig et al., 2015). Genetic ablation of *Etv2* leads to complete loss of blood and vessels, and overexpression of this factor has been shown to convert non-ECs to the endothelial lineage (Ferdous et al., 2009; Morita et al., 2015). Expression of *ETV2* starts to appear in (mouse) development in the *KDR*+ and *PDGFRα*- mesoderm cells in yolk sack and embryo. At embryonic day 7.5 (E7.5), angioblasts that migrate back to the embryo express high levels of *ETV2*. From E8.5 to E9.5, *ETV2* was observed in perivascular cells rather than differentiated ECs (Kobayashi et al., 2013). Then from E10.5, *ETV2* expression dramatically decreased except in the region of dorsal aorta (Koyano-Nakagawa et al., 2012). Postnatally, only testis still expresses *ETV2* constitutively (Haro and Janknecht, 2002). Some tissues may express *ETV2* transiently, such as hematopoietic stem cells (HSCs) (Lee et al., 2011). However, *ETV2* expression is significantly upregulated after injury which indicated its essential role in neovascularization (Park et al., 2016).

One of the key target genes that regulated by *Etv2* in ECs is *Flk1/VEGFR2* (Becker et al., 2016). Upregulation of *VEGFR2* and neovascularization after ischemic injury in mice require the de novo expression of *Etv2* in adult ECs (Park et al., 2016). Overexpression of *Etv2* in vascular progenitor cells in the postnatal arterial adventitia can directed them to endothelial cell fate. Endothelial-specific genes could be upregulated in *Etv2*-transduced *Sca1*+ progenitor cells which inhibit intimal hyperplasia in wire-injured femoral arteries when grafted onto the adventitial side of the femoral artery wall (Bras et al., 2018). Many other genes were also identified as target genes that are regulated by *ETV2* either using overexpression studies or identification of direct binding to promoter sequences, including *Pecam1*, *Tie2*, *VE-Cadherin*, *Gata1*, *Gata2*, *Lmo2*, *Elk3*, *Cebpd*, *Scl*, *Mef2c*, *Notch4* *Spi1*, *Fli1*, *Sox7*, *Ece1*, *Nrp1*, *Nrp2*, *Flt1and Erg* (Abedin et al., 2014; Ferdous et al., 2009; Kataoka et al., 2011; Koyano-Nakagawa et al., 2012; 2015; Lee et al., 2008; Liu et al., 2012; 2015; Robinson et al., 2014). *miR-130a* is also a downstream target of *Etv2*, which promote EC differentiation from mesoderm cells prior to their patterning (Singh et al., 2015). In chapter 4 of this thesis, we generated an *ETV2^{mCherry}* reporter hiPSC line and used it to track and label the *ETV2* expression during the derivation of ECs from hiPSCs. Roles of *ETV2* played during the segregation of endothelial and myocardial lineages were also revealed using this reporter line in combination with bulk and scRNAseq approaches.

1.2.3 Derivation of ECs from hiPSCs

Since ECs are the major cell type affected in multiple vascular diseases, derivation of functional ECs from hiPSCs similar to patient primary ECs is the first and most essential step in modeling vascular diseases using hiPSCs. Most hiPSC-EC

differentiation protocols are based on our understanding of vascular development in the embryo. So far, most protocols for hiPSC-ECs have relied on three different approaches: coculture with stromal cells, EB formation and monolayer differentiation.

In 2009, two groups independently reported two similar methods for the differentiation of ECs from hiPSCs. Both groups found that coculture of hiPSCs with OP9 feeder cells resulted in the formation of endothelial progenitors which could be isolated and further induced into functional ECs (Choi et al., 2009; Taura et al., 2009). Later, several aggregation or EB-based differentiation methods were reported for the induction of ECs from hiPSCs (Adams et al., 2013; James et al., 2010; Kane et al., 2011; Nourse et al., 2010; Park et al., 2014; White et al., 2012). With EB-based methods, EBs are first cultured in pro-endothelial growth media (EGM) supplemented with VEGFA and BMP4 to induce mesodermal lineages. These mesoderm progenitors eventually give rise to ECs. The study also found that a Transforming Growth Factor beta (TGF β) signaling inhibitor improved differentiation efficiency and maintained of endothelial phenotype over several passages (James et al., 2010). With these culture conditions, CD144 and CD31 positive cells were derived and purified for further expansion and differentiation. However, the majority of EB based protocols had low differentiation efficiencies, high heterogeneity of differentiated cells and were also time-consuming.

An alternative strategy now widely used is to culture hiPSC on a matrix-coated culture plate in monolayer and induce the stepwise differentiation from hiPSCs to mesoderm and finally ECs by timed addition of specific molecules and growth factors. Monolayer differentiation methods for EC differentiation from hPSCs were first described in 2010 although details were missing (Kane et al., 2010). Orlova et al. developed highly efficient monolayer differentiation methods for simultaneously producing CD31+ ECs and CD31- pericytes from hiPSCs using defined medium conditions (Orlova et al., 2014). With this protocol, a large number of ECs could be derived from hiPSCs in ~2 weeks. Notably, this protocol was tested using multiple hiPSC lines that were derived from different somatic cell types using different reprogramming methods. The functionalities of these hiPSC-ECs were evidenced by their ability to form primary vascular plexus in vitro and be incorporated into the vasculature of zebrafish (Orlova et al., 2014a). Meanwhile, others found that addition of retinoic acid could promote the expression of the mature endothelial cell marker VE-Cadherin and enhance the barrier function of differentiated ECs using monolayer protocols (Katt et al., 2016; Lippmann et al., 2014). Later, Patsch et al. developed a protocol in which Wnt activation and BMP4 were used to induce mesoderm for 3 days, followed by VEGF and Forskolin treatment for another 2 days, and then VEGF for 4 days. With this differentiation method, the authors reported up to 90% differentiation efficiency of ECs from hiPSCs (Patsch et al., 2015). Recently, an even shorter differentiation protocol was established which could induce ECs from hiPSCs in just 8 days with an efficiency of more than 80% (Harding et

al., 2017). It was reported recently that cyclic AMP synergistically enhanced the VEGF effects for the differentiation of ECs from the mesoderm stage in a serum-free 2D monolayer culture. Almost pure populations of ECs could be derived using stage-specific addition VEGF and cyclic AMP combined with the elimination of non-responder cells at early stages (Rajasingh et al., 2017). In this thesis, I used the method described by Orlova et al (2014b) to produce hiPSC-ECs from patients with inherited vascular disease and used an ETV2 reporter hiPSC line to examine molecular characteristics of the early and intermediate stages of differentiation. This allowed detailed examination of any heterogeneity in the cell populations.

1.2.4 Characterization of hiPSC-ECs

ECs derived from hiPSCs have been isolated mainly based on their KDR, CD31 and VEG expression but their heterogeneity has been less studied. Rufaihah et al. found that high concentrations of VEGF-A (50 ng/ml) together with 8Br-cAMP could induce arterial ECs and low VEGF-A concentrations (10 ng/ml) led to a venous like EC identity. A combination of high concentration of VEGF-A and VEGF-C, together with angiopoietin 1 could induce lymphatic ECs (Rufaihah et al., 2013). Another group also confirmed that arterial and venous identities could be obtained by using different VEGF concentrations (Ram et al., 2015).

Although hiPSC-ECs have numerous features common with human primary ECs, including surface marker expression and 2D tube formation *in vitro*, comparing their functionality requires different kinds of assays. *In vivo* vessel formation is commonly used to examine functionality of hiPSC-ECs. In this assay, ECs are first mixed with 3D matrix (collagen, Matrigel, fibrinogen etc.) and transplanted subcutaneously into mice. Transplanted EC functionality is then assessed based on the vessel formation in the 3D matrix. We used this method to examine the functionality of diseased hiPSC-EC *in vivo* in chapter 6. Other *in vivo* models that have also been developed to test the therapeutic potential of hiPSC-ECs, included experimental hindlimb ischemia, myocardial infarction and retinopathy (Park et al., 2014; Prasain et al., 2014; Rufaihah et al., 2011; Sahara et al., 2014; Yoo et al., 2013). However, 3D matrix transplantation is the most reproducible and straightforward functional assay for hiPSC-ECs. In addition to mouse models, zebrafish embryos have also been used to test functionality of hiPSC-ECs *in vivo* (Kane et al., 2010; Orlova et al., 2014a). More recently, new methods to examine functionality through 3D vessel formation *in vitro* have been developed. hiPSC-ECs are first mixed in matrix and then cultured under static or flow conditions, where ECs can self-organize into vessel-like lumenised structures (Chan et al., 2015; Kusuma et al., 2013; Palpant et al., 2016; Park et al., 2014; Zanutelli et al., 2016; Zhang et al., 2017). It had been shown that ECs cultured in this way are more similar to those isolated from the 3D matrix transplant *in vivo* than ECs cultured in 2D culture dishes (Zanutelli et al., 2016; Zhang et

al., 2017).

Patient-specific hiPSC-ECs can be used as a model to study disease mechanisms and screen of candidate drugs. hiPSC-ECs had been used to model a number of genetic (cardio)vascular diseases to date, including Moyamoya disease, Pulmonary arterial hypertension and Calcified aortic valve disease. (Lin et al., 2017).

1.2.5 Whole transcriptome analysis of hiPSC-ECs in development and disease

Along with the development of Next-generation sequencing (NGS) technologies, the emergence of RNA sequencing (RNAseq) brings new opportunities for diagnosis and treatment of human disease and to gain insights into how different cell types form in differentiation and development. RNAseq provides an in-depth view of the whole transcriptome within a cell sample and has a number of advantages compared to most conventional RNA measurement platforms, including qPCR and microarray. This includes higher throughput. In comparison to more conventional methods, RNAseq can detect a greater range of transcripts expression than microarray, thus thousands of differentially expressed genes (DEGs) can be identified from comparison of two or more different samples.

Droplet-based single cell RNA sequencing (scRNAseq) is a commonly used method which I also used in my thesis. It proved an excellent tool for the study of global transcriptional dynamics during EC differentiation from hiPSCs. Several scRNAseq studies had been performed prior to my study for hiPSC-ECs differentiated with different methods. In one study, scRNAseq was performed on day 8 and day 12 of EC differentiation, although ECs accounted for only less than 10% of the total population while most cells were cardiac lineage. However, the transcriptional control and dynamics during the developmental process of EC were not further investigated in this study (Paik et al., 2018). In another study, scRNAseq was done at multiple time points during hESC-derived EC differentiation using a different protocol (McCracken et al., 2019). The transcriptional dynamics during EC specification and maturation were characterized using “pseudotime analysis” (McCracken et al., 2019). They observed a mesodermal population at day 4, followed by an emergence of endothelial and mesenchymal populations. Transcriptional signatures of endothelial commitment and maturation during the differentiation process were identified based on the transcriptional changes along pseudotime trajectory. Recently, our group developed a co-differentiation method for both ECs and cardiomyocytes from hiPSCs through a cardiac mesoderm stage (Giacomelli et al., 2017). The developmental process and transcriptional dynamics during the specification, as well as the segregation of these two lineages from mesoderm progenitors in this protocol had not so far been studied. Thus, in this thesis, we have carried out both bulk and scRNAseq to study the transcriptional control and dynamics of this differentiation system. We first generated

an ETV2^{mCherry} hiPSC reporter line in order to study the ETV2 expression pattern and its role during endothelial and myocardial lineages segregation and development. Bulk RNAseq could give a more in-depth view of the transcriptome profile, while scRNAseq could generate an overview of the whole cell population in the differentiation system as well as the dynamics of each individual genes along the differentiation time.

In addition, transcriptomic analyses were also performed for ECs in HHT1 and PHE hiPSC models established in this thesis. Majorly, differentially expressed gene (DEG) and gene ontology (GO) enrichment analyses were utilized to reveal the underlying disease mechanisms of HHT1 and PHE.

1.3 Modeling HHT1 with hiPSCs

1.3.1 HHT

HHT is an autosomal dominant genetic vascular disease with a prevalence of 1 in 5000-10000 (Dakeishi et al., 2002; Marchuk et al., 1998; Westermann et al., 2003). HHT is characterized by recurrent nosebleeds and telangiectasias, especially on patients' lips, finger tips and nasal mucosa. There is a high chance for HHT patients to develop large arteriovenous malformations (AVM) in several organs, including lung (PAVM, 13-35%), brain (CAVM, 5-13%) and liver (HAVM, ~32%) (Letteboer, 2005). CAVM can lead to stroke and brain abscess. Most HHT patients show normal life spans. However, disease symptoms usually get worse during aging and new symptoms, for example gastrointestinal bleeding, may arise in old age. The "Curacao criteria" have been used for the diagnosis of HHT based on patient symptoms since 2000 (Shovlin et al., 2000). In practice, family history and the presence of AVM are often sufficient for diagnosis, due to the rare occurrence of AVM in the general population. There are few drugs that have proven consistently effective for the treatment of HHT patients yet. Treatment and care for the HHT nowadays mainly focused on prophylaxis of different symptoms, such as stroke and liver AVMs. Thalidomide and Bevacizumab are the two main drugs that are considered for HHT treatment and under clinical test (www.clinicaltrials.gov). Thalidomide and bevacizumab are known anti-angiogenic drugs that are used to treat nosebleeds in HHT patients. Thalidomide has shown ability to promote vascular maturation via PDGF-B activation (Lebrin et al., 2010). Bevacizumab is a monoclonal antibody against vascular endothelial growth factor (VEGF) and has been used to treat fragile vessels and excessive angiogenesis that could cause nosebleeds in patients with HHT (Dupuis-Girod et al., 2012; Fleagle et al., 2012). However, their functional mechanisms and possible side-effects need to be further studied and alternative drugs are still being sought. More recently, an immune modulator, tacrolimus, is also being tested clinically.

Around 85% of HHT patients in the world have mutations in either *ENG* gene (HHT

type 1) or *ACVRL1* gene (HHT type 2). At least 525 different ENG mutations and 430 *ACVRL1* mutations have been reported so far in the HHT database (see <http://www.hhtmut.org>). These mutations are distributed across all exons of these two genes, even though several exons seem to have higher chance to carry the mutation (Figure 2 A-B). In addition, mutations in *MADH4* gene were found to contribute the development of both HHT and juvenile polypsis. Notably, all genes found so far that could lead to HHT are involved in TGF β superfamily signaling pathway. In this thesis I focused on HHT1 caused by an ENDOGLIN mutation.

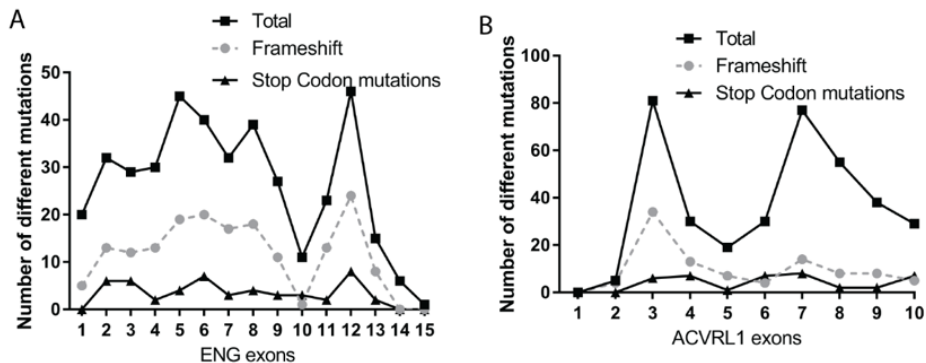


Figure 2 Distribution of all known ENG (A) and ACVRL1 (B) mutation on all exons of these two genes (all information about HHT mutations are coming from the HHT database: <http://www.hhtmut.org>)

1.3.2 TGF β superfamily signaling pathway and endoglin

Endoglin is a receptor that is part of the TGF β signaling pathway. The TGF β superfamily includes a large number of secreted cytokines including TGF β s, activins, Bone Morphogenetic Protein (BMPs) and Growth Differentiation Factors (GDFs), which play crucial roles in different process during development and in the maintenance of hemostasis. The TGF β family of ligands act on cells through their specific binding to transmembrane type I and type II receptors, which then can phosphorylate different R-SMADs mediators and regulate specific genes expression.

Different combinations of type I and type II receptors bind to different TGF β family ligands. For example, TGF β signals mainly by binding firstly to TGF β Receptor II (TGFB β R2) which recruits TGF β Receptor I (TGFB β R1, ALK5) to the receptor complex. BMP type II Receptor (BMP β R2) and ALK1 type I receptor respond to different BMP ligands. Type III receptors such as betaglycan and endoglin, are essential for the regulation of TGF β signaling specificity and affinity of ligand binding.

Human endoglin is 180 kDa disulfide-linked homodimeric transmembrane glycoprotein. It contains a large 561 amino acid extracellular domain and a serine/threonine-rich cytoplasmic region which contain 47 amino acid in the long isoform (L-endoglin) and 14 amino acid in the short isoform (S-endoglin). The extracellular domain contain an orphan domain which can mediate its interaction with TGF β superfamily ligands, especially BMP9 and BMP10 (Castonguay et al., 2011; Saito et al., 2017). An arginine-glycine-aspartic (RGD) tripeptide is also present in the extracellular domain at Arg399-Asp401, suggesting that endoglin may also mediate cell adhesion process. Endoglin is highly expressed on vascular ECs and on activated monocytes, macrophages and smooth muscle cells. Mutations in Endoglin may thus affect the vascular cells directly or indirectly via inflammatory cells.

1.3.3 Role of endoglin in angiogenesis

Endoglin plays an important role in angiogenesis. This is evidenced by the fact that endoglin knockout mice die on gestational day 10.5 due to vascular development defects in the embryo (Arthur et al., 2000; Bourdeau et al., 1999; Li et al., 1999). Even though EC differentiation takes place, mature vascular networks do not form in the knock out mice, indicating that endoglin plays an essential role in angiogenesis rather than vasculogenesis (the differentiation of EC) (Arthur et al., 2000; Li et al., 1999). ES cells derived from endoglin knockout mice failed to undergo hematopoietic differentiation while endothelial differentiation was not affected. Proliferating Human Umbilical Vein Endothelial Cells (HUVECs) in culture showed clearly higher endoglin expression than quiescent HUVECs (Fonsatti et al., 2001). Evidence has shown that endoglin may be important for keeping the balance of TGF β signaling through ALK1 and ALK5. Endoglin promotes ALK1 activation and indirectly inhibits ALK5 activity (Lebrin et al., 2004). Activation of TGF β -ALK1 could induce EC proliferation and migration through Smad1/5/8 signaling pathway (in most cells only activated downstream of BMP signaling but exceptionally in ECs through TGF β signaling), while TGF β -ALK5 downstream activation of Smad 2 and 3 inhibits their proliferation and migration (Goumans et al., 2003). Knockout or blocking of endoglin in ECs could inhibit their proliferation and migration and enhance the effect of TGF β 1 on the inhibition of EC growth (Lebrin et al., 2004; Li et al., 2000). However, controversy still exists on the exact role of endoglin in angiogenesis. For example, both enhanced and reduced growth inhibition by TGF β 1 were observed with ECs derived from endoglin knockout mice (Lebrin et al., 2004; Pece-Barbara et al., 2005).

BMPs is another group of multifunctional growth factors in the TGF β superfamily. Recent studies show emerging roles of BMPs played in angiogenesis. Like TGF β s, BMPs elicit their effects by binding to type I and type II receptors on the cell surface. But unlike TGF β s, BMPs showed high affinity of binding to both type I and type II receptors alone

independently. The receptor complex for BMPs also include a type III co-receptor, including betaglycan and endoglin. Endoglin can be shed from the cell surface by matrix metalloproteinase, suggesting that they can modulate the activity of BMP signaling pathway through the changing their surface expression levels (Hawinkels et al., 2010). BMP9 can bind to both ALK1 and ALK6, but with a much higher affinity to ALK1 compared to ALK6 (David et al., 2006). BMP9 triggers Smad1/5/8 phosphorylation in ECs with an EC₅₀ of around 50 pg/ml. Different BMP type I receptors showed different specificities to Smad 1/5/8. ALK3 and ALK6 can activate all three Smads, whereas ALK2 can only activate Smad 1 and 5 (Miyazono et al., 2005; Reddi, 2001). Freshly-isolated mouse aorta and pulmonary endothelium showed high phosphorylation of Smad 1/5/8, indicating that ECs were physiologically activated by BMPs (Valdimarsdottir et al., 2002). Studies showed that BMP signaling through ALK1 is mainly implicated in the maturation phase of angiogenesis. BMP9 could inhibit the proliferation and migration of dermal Human Mammary Epithelial Cells (HMECs) and Bovine Aorta Endothelial Cells (BAECs) (David et al., 2006; Scharpfenecker et al., 2007). The inhibitory effect of BMP9 on ECs was confirmed in an ex vivo metatarsal culture model (Scharpfenecker et al., 2007). Besides, BMP9 also showed inhibition of neo-angiogenesis *in vivo* (David et al., 2008). All these *in vivo* and *in vitro* studies demonstrated that endoglin/ALK1/BMPRII signaling pathway play important roles in angiogenesis.

Heterozygous *ENG*^{+/-} mice showed mild phenotypes but using a different strain of mice, they showed different disease phenotypes, providing evidence that genetic background also plays a role in the development of the disease (Bourdeau et al., 1999). Aside from a mild disease phenotype, it also appeared at very low frequency in heterozygous mice (Bourdeau et al., 1999; Torsney et al., 2003). Reduced angiogenesis in adult *ENG*^{+/-} mice has been reported in pathological conditions, like femoral artery ligation (Jerkic et al., 2006), myocardial infarction (van Laake et al., 2006), and stroke (Shen et al., 2014). Treatment of *ENG*^{+/-} mice with pro-angiogenic factors could induce abnormal angiogenesis but not AVMs, indicating other stimulations were necessary for the development of AVMs in mice models (Xu et al., 2016). Lebrin and colleagues found that treatment of *ENG*^{+/-} mice with Thalidomide could promote vascular maturation through increased PDGF-B expression in ECs (Lebrin et al., 2010). Cell type specific loss of *ENG* showed that the endoglin deficiency in ECs was a prerequisite for AVM formation, whereas specific knockout in pericytes, vSMCs and macrophages had no effect on the AVM formation (Choi et al., 2014; Garrido-Martin et al., 2014). However, both complete knockout and conditional knockout mice model are distinct from the situation of HHT1 patients. So far, based on the studies that had been done with heterozygous mouse models, it is still not clear how these severe symptoms developed in HHT1 patients.

1.3.4 Role of myeloid cells in HHT1

1.3.4.1 Inflammation and HHT1

Inflammation is an adaptive immune response that is triggered by various conditions including infection, tissue injury, tissue stress and malfunction. A controlled inflammation response is beneficial as it could provide protection from infection and promote tissue repair and adaption to stress. However, dysregulated inflammation may have pathological consequences. For example, uncontrolled inflammation can lead to autoimmunity, fibrosis and tumor growth.

Inflammation is an important trigger for the development of HHT1 disease phenotypes in endoglin knockout mouse models. The failure to recapitulate (heterozygous) HHT1 patient phenotypes in mice suggested that additional triggers may be needed for the development of disease symptoms, including aging, wounding and inflammation. Pro-angiogenic factors or inflammatory stimuli could successfully induce AVMs in these conditional knockout *ENG* deficient mice (Choi et al., 2014; Garrido-Martin et al., 2014). Some researchers have proposed that at least three events were needed for the development of AVMs: endoglin haploinsufficiency in ECs; loss of heterozygosity (becoming homozygous) in some tissues due to accumulated endoglin mutation or shedding during inflammation by MMPs; pro-angiogenic or inflammatory stimuli (Tual-Chalot et al., 2015).

Evidence has shown that the inflammation responses were also affected due to the endoglin deficiency in both HHT1 patients and mouse models. The prevalence of severe infection in HHT1 patients is around 22.8%, which is much higher than chance in the general healthy population. It also had been shown that HHT1 patients had much higher chance of developing cerebral infection than HHT2 and HHT3 patients (Girod et al., 2007). *ENG*^{+/-} mice also developed more severe colon inflammation induced by DSS compared with control mice (Jerkic et al., 2010). Another study found that after injection of LPS, *ENG*^{+/-} mice exhibit reduced myeloid cell recruitment in lung tissue compared to the control mice in a systemic inflammation model (Rossi et al., 2013). In addition, functions of myeloid cells also seemed to be impaired because of the endoglin mutation. Conditional knockout of *ENG* specifically in macrophages in mice impaired the phagocytotic activity of macrophages (Ojeda-Fernandez et al., 2016). Interestingly, compared with mononuclear cells isolated from healthy individuals, mononuclear cells from HHT1 patients showed defective repair and migratory activity to the injured heart following myocardial infarction in mice (van Laake et al., 2006). Post and colleagues found that HHT1 patient blood monocytes showed impaired response to SDF-1 α (Post et al., 2010). All of these studies indicated a correlation between inflammation and HHT1. On the one hand, inflammation serves as a trigger for the development of HHT1 disease symptoms. On the other hand, endoglin mutation impairs functions of myeloid cells and leads to an abnormal inflammation response in

both patients and mouse models.

1.3.4.2 Monocytes and ECs interaction in inflammation

Monocytes play a pivotal role in both the initiation and resolution of inflammation. Recruitment of blood monocytes to the site of injury or infection by extravasation through endothelium are essential for the inflammation response. The extravasation of blood monocytes is a tightly regulated process that consists of a series of interactions between monocytes and ECs and the final transmigration step. The adhesion between monocytes and ECs is mainly via the interaction between integrins (extracellular matrix protein receptors) expressed on monocytes and the immunoglobulin superfamily that is expressed on ECs (Meerschaert and Furie, 1995) (Figure 3).

Upon stimulation, for example after infection, tissue resident macrophages can be activated and secrete proinflammatory cytokines including tumor necrosis factor- α (TNF- α) and IL-1 β . These inflammatory cytokines can transiently activate ECs of blood vessels nearby and upregulate their expression of chemokines and adhesion molecules, mainly P- and E-selectin, ICAM-1 and VCAM1. First, the interaction between selectins on endothelium can bind to O-glycosylated carbohydrate ligands displayed on P-selectin glycoprotein ligand-1 (PSGL-1) that expressed on monocytes. This interaction could capture monocytes and slow them down in the blood flow and then enable them to roll on the endothelium wall. The slow rolling process was strongly depend on the expression VLA-4 ($\alpha 4\beta 1$ integrin) and CD44 that expressed on monocytes (Mestas and Ley, 2008). Then interaction between VCAM1 on activated endothelium and VLA-4 on monocytes mediates the transition from slow rolling to firm adhesion. Next is the directional chemotactic and mechanotactic step, in which monocytes spread, polarize, and subsequently locomote laterally to find preferred sites of extravasation. The intraluminal crawling depends on the interaction of leucocyte integrins lymphocyte function-associated antigen-1 (LFA-1) and macrophage-1-antigen (Mac-1) on monocytes and their ligands ICAM-1 and ICAM-2 on ECs. Blocking of these adhesion molecules was shown to disable crawling and the subsequent transmigration (Wong et al., 2010). Notably, ICAM-1 and VCAM-1 are expressed diffusely on endothelial cell surface in rest condition, but will be concentrated to the interface with monocytes during the adhesion and rolling (Shaw et al., 2004), which is depend on the actin cytoskeleton and remodeling events that include the Src-mediated phosphorylation of cortactin, an actin binding protein (Schnoor et al., 2011; Yang et al., 2006). Finally, to migrate out of blood vessels, monocytes must negotiate the endothelium, the lamina basalis and the embedded pericytes (Figure 3). As all adhesion and rolling processes discussed above are reversible, the majority of monocytes that initially bind to endothelium cannot finish the transmigration step. Transmigration seems to be the crucial event in the monocyte adhesion cascade, as it is the only step that is hardly ever

reversed although with some notable exceptions (Woodfin et al., 2011).

Monocytes transmigrate through vascular endothelium by two different modes: the paracellular route by which monocytes migrate through the junctions between ECs and requires junctional remodeling; the transcellular route that directly through fusing vesicles in the endothelial cell. The paracellular mode is predominant although it's still difficult to accurately quantify the ratio of these two modes (Carman et al., 2007). The transmigration process is tightly regulated by the junctional molecules on ECs, including VE-Cadherin, the junctional adhesion molecule (JAM) family, PECAM-1 PVR/DNAM-1, and CD99 and their interaction with integrin on monocytes (Gerhardt and Ley, 2015; Muller, 2015; Schnoor et al., 2015).

It is known already that the adhesion to endothelium and transmigration could change the gene expression profile of monocytes dramatically. Genes that related to chemokines, immune response and inhibition of apoptosis were upregulated after transmigration of monocytes (Thomas-Ecker et al., 2007; Williams et al., 2009). After transmigrating into the tissue, monocytes will terminally differentiate into macrophages and dendritic cells, which can phagocytose pathogens and regulate the inflammation process by secretion of pro-inflammatory and anti-inflammatory cytokines. During the resolution phase of inflammation, macrophages are responsible for the cleaning up dead cells through efferocytosis, and also promote tissue regeneration and angiogenesis through the secretion of various growth factors.

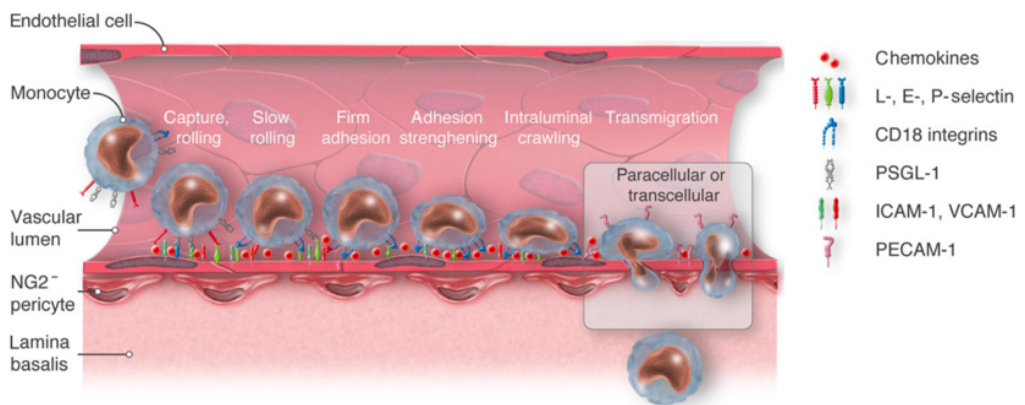


Figure 3 Schematic overview of monocyte adhesion and transmigration through vessel wall.

A multistep cascade of capture, rolling, slow rolling, firm adhesion, adhesion strengthening, and intraluminal crawling precedes the transendothelial migration of monocytes. Two modes of transmigration are indicated: a paracellular and a transcellular. Activated ECs express adhesion molecules and chemokines that interact with monocytic ligands. Such interactions essentially mediate the various steps of the adhesion cascade. This figure is adapted from (Gerhardt and Ley, 2015).

1.3.4.3 Regulation of angiogenesis by macrophages

Macrophages are specialized cells that play diverse roles in human body, including immune response, tissue repair and homeostasis (Wynn et al., 2013). Macrophages derived from precursor monocytes are continuously produced from hematopoietic stem cells (HSCs), which develop through definitive hematopoiesis (Medvinsky et al., 2011). Direct association with macrophages has been well documented in wide range of diseases (Wynn et al., 2013). Macrophages are highly heterogeneous and can change their phenotype and function depending on the stimuli or immune response induced by local tissue environment. Depending on the distinct immune function they possess, macrophages have been classified into different subsets, known as M1, M2a, M2b and M2c (Mantovani et al., 2013; Röszer, 2015). M1 macrophages secrete various proinflammatory cytokines and chemokines to enhance the inflammation response and recruit more immune cells to the inflamed tissue, mainly neutrophils and monocytes. Dead neutrophils and tissues can then stimulate and change M1 macrophages into an M2 state (alternative activated macrophages), which can inhibit the inflammation process and promote tissue repair and angiogenesis after the injury or infection.

Macrophages can regulate angiogenesis through the secretion of variety of proangiogenic and antiangiogenic growth factors or cytokines (Corliss et al., 2016). Studies showed that VEGFA secreted by macrophages was essential for angiogenesis during wound healing (Lucas et al., 2010; Stockmann et al., 2011; Urbich et al., 2003; Willenborg et al., 2012). Also, evidence indicates that different subtypes of macrophages may exert regulatory roles in different stages of angiogenesis, according to their different secretion profiles. For example, M1 macrophages may be involved in the initiation of angiogenesis as they produce high level of VEGF-A and FGF2. M2a macrophages secrete high amounts of PDGF-BB and M2c produce high level of MMP9. M1 macrophages stimulate capillary sprouting, while M2 macrophages may aid in vessel stabilization through pericyte recruitment (Spiller et al., 2014).

Macrophages have been shown to make direct contact with ECs to regulate angiogenesis. During the development of hindbrain of mouse and zebrafish, macrophages can bridge two EC sprouts and promote tip cell fusion (Fantin et al., 2010). Studies have also shown that microglia are associated with tip cells during retina development. Knockout of microglia resulted in sparser retinal vascular network with less branching (Kubota et al., 2009). A better understanding of macrophages and their role in angiogenesis may inspire new therapeutic strategies for regenerating tissues and curing diseases that are caused by deregulated angiogenesis, such as HHT1.

1.3.5 Modeling HHT1 using hiPSCs

Until now, most of our knowledge about the disease pathology of HHT1 comes from

the study of either patient material or mutant mouse models. Using patient material is unavoidably restricted by its availability. Peripheral blood or small tissue biopsies of HHT1 patients can be obtained under certain conditions from HHT hospital centres. However, given the condition is rare, it would be difficult to draw statistically significant conclusions based on studies using cells collected from a single or low number of patients, as the disease phenotype largely depends on genetic background, patient age and general health condition. Nevertheless, some researchers have managed to obtain sufficient numbers of patient cells for gene profiling analysis, where they found nasal telangiectasia of HHT1 patients express abnormal levels of genes that involved in angiogenesis, TGF β and Wnt signaling pathways (Tørring et al., 2015).

Although mouse models of HHT1 are most commonly used for the study of disease pathology, they do have several drawbacks. First of all, the genetic background of mice and human are quite different. Second, phenotypes showed in mouse models are different from disease phenotypes found in human patients. For example, it is still a question on how to induce AVMs in ENG^{+/-} mice. Third, it may take a long time for the generation of endoglin knockout mice and the appearance of disease phenotypes, especially those related to ageing. Last but not least, mouse experiments raise ethical issues and animal protection concerns.

In 2006, iPSCs were first generated from mouse fibroblasts by overexpressing four transcription factors (known as Yamanaka factors) normally expressed in ES cells. These mouse iPSC were similar to ES cells (Takahashi and Yamanaka, 2006). Shortly thereafter, human somatic cells were also successfully reprogrammed to hiPSCs (Takahashi et al., 2007). hiPSCs can also self-renew indefinitely in culture and differentiate into many different kinds of cell types, which make them potentially an excellent tool for disease modeling since they capture the genome of the patient from who they are derived. hiPSC derived cells can be used for the study of disease pathologies and drug screening (Robinton and Daley, 2012). Recent advances in genome editing, including TALENs and CRISPR/Cas systems, now allow rapid and efficient introduction of genetic modifications in hiPSCs. Both techniques apply nuclease to cut genome DNA to get a double strand break in the specific location with the help of guiding RNA sequence. Then specific modification of the sequence could be achieved through DNA repair by non-homologous end joining (NHEJ) or homology directed recombination (HDR) when a template DNA molecule is available (Kim, 2016). These techniques further facilitate the application of hiPSCs for the modeling of different genetic diseases. For example, in order to study the effect of genetic background on the development of a genetic disease, a same mutation could be introduced into a control hiPSC line and compare it with the patient-derived hiPSC line. The mutation carried by the patient hiPSC line could also be corrected using genome editing to create an isogenic control, by which the effect of genetic variation except the mutation on the pathogenic gene could be excluded.

There are several potential advantages of using hiPSC-derived cells for modeling of HHT1. First, patient-specific hiPSCs and their derivatives carry the same genetic background as HHT1 patients. Second, unlimited numbers and different types of vascular and other cells likely similar to primary cells from patients can be derived from patient specific hiPSCs. Third, the differentiation processes of different cells types from hiPSCs are relatively short compared to the generation of mouse models, as described in section 1.1.1 and 1.2.3. Fourth, CRISPR/Cas 9 genetic modification technologies make it much easier to correct the *ENG* mutation in patient specific hiPSC lines to generate isogenic control lines, which are necessary for the study of disease related phenotypes. The potential disadvantage is that the hiPSC derivatives may not be mature enough to mimic the disease in adults.

One of the major aims of this thesis is establishing a multicellular vascular model of HHT1 using patient-derived hiPSCs. To better recapitulate the microenvironment of blood vessels *in vivo*, 3D culture combining different cellular components associated with blood vessel development and functions are required. Previous work in our group showed that in hiPSC-ECs with endoglin haploinsufficiency the TGF β signaling pathway was unaffected and functionalities normal in 2D culture conditions (unpublished data). Here, we decided to investigate whether patient -like phenotypes would be evident in a 3D culture model combining ECs and mural cells-vascular smooth muscle cells (vSMCs) derived from isogenic HHT1 hiPSC lines. We found dysregulated interactions between EC and mural cells which had been shown to be a major underlying pathology of HHT1 in mutant mice, evidenced by impaired vSMC development and mural cell recruitment and coverage of blood vessels (Lebrin et al., 2010).

As the next step (not included in this chapter), we modeled the inflammation process with patient derivativs by thesting adhesion of monocyets on ECs. We are also working on including of inflammatory cell component – IPSDMs in our 3D vascular model. As above in **section 1.3.5** of this thesis, inflammation and myeloid cells (especially macrophages) are closely related to the onset and development of HHT1 phenotypes. Thus, by including IPSDMs in our model, we expected to observe new disease phenotypes related to inflammation condition and to identify new disease pathologies which would provide essential clues for the drug development and screening in the future.

1.4 Modeling PHE with hiPSCs

1.4.1 PHE

PHE is tumor associated with blood vessels with intermediate malignant potential which mainly affects young adults and has a male predominance. PHE has similar clinical presentation as epithelioid sarcoma. The tumor is known to express several EC markers

although with morphology distinct from vasculature and involving different anatomic planes, including dermis, subcutis, and skeletal muscle (Al-Qaderi and Mansour, 2019).

In 2014, Walther and colleagues revealed a balanced t(7;19)(q22;q13) chromosome translocation in several PHE patients which lead to a fusion of the *SERPINE1* and *FOSB* genes (Walther et al., 2014). *FOSB* dimerizes with Jun proteins to form AP-1 transcriptional complex which was found to drive various tumors. The overexpression of *FOSB* under the *SERPINE1* promoter after translocation is considered as the mechanism underlying the pathology of PHE.

Local recurrence was commonly observed in PHE, while few patients develop distant metastasis (Inyang et al., 2016). Currently there is still no effective treatment for this tumor, although drugs targeted rapamycin inhibitors are under clinical test, including everolimus (Ozeki et al., 2017) and sirolimus (Gabor et al., 2018).

1.4.2 Disease Modeling of PHE

Establishing an in vitro model of PHE would greatly facilitate the study of underlying disease mechanisms and development of screening platforms for candidate drugs. However, no tumor cell line has so far been established for this disease in part because PHE is so rare. hiPSC would an alternative approach to model PHE and they could be produced by introducing the chromosomal translocation into WT hiPSCs by genome editing. Previously, chromosomal translocations have been successfully introduced into human umbilical cord-derived mesenchymal stromal cells (hMSCs), umbilical cord blood-derived CD34+ cells, and more recently human induced pluripotent stem cells (hiPSCs) using CRISPR/Cas9 (Schneidawind et al., 2018; Torres et al., 2014; Torres-Ruiz et al., 2017; Vanoli et al., 2017). Thus, we hypothesized that by introducing *SERPINE1-FOSB* translocation into hiPSCs and differentiating them into EC using established protocol (Halaidych et al., 2018; Orlova et al., 2014b; 2014a) we may establish an hiPSC disease model for PHE which could be further used for further study. This was indeed carried out in the study presented in chapter 6 where my focus was primarily on the transcriptional analysis of the mutant hiPSC-derived ECs in relationship to the isogenic wild-type cells.

1.4.3 Transcriptomic analysis of the hiPSCs model of PHE

Whole transcriptome sequencing and analysis provides a powerful tool for the revealing of dysregulated transcription networks and indicating potential underlying disease mechanisms of PHE using the PHE-hiPSC model. The study demonstrated that ECs are indeed the likely cell of origin of PHE as postulated before this study. Comparison of ECs derived from PHE and isogenic WT hiPSCs could then provide new insights into the nature of the disease. Although *FOSB* overexpression had been identified as the major driver of tumor development, it is still not fully clear what the downstream

transcriptional changes are and their correlation with observed disease phenotypes of PHE. Whole transcriptome sequencing allowed us to identify the majority of dysregulated genes in PHE-hiPSC-EC model. Gene Ontology (GO) enrichment analysis enabled us to link these identified DEGs with different cell signaling pathways and activities. Moreover, gene regulation networks could be generated using available gene-gene interaction prediction tools like Ingenuity Pathway Analysis (IPA). Novel therapeutic targets and candidate drugs could this be identified based on these RNAseq analyses.

1.5 Aims of this thesis

The overall aim of the work in this thesis was to establish vascular models in culture using hiPSC-ECs and myeloid cells for a genetic vascular diseases HHT1 and a vascular tumor PHE. To achieve this goal, several questions needed to be addressed first and each is presented in the chapters of this thesis.

Much of the research in this thesis is intended to address the underlying mechanisms of HHT1, a major focus of our research group. To model the crucial inflammatory component of HHT1 using hiPSCs, **first** we needed to establish a robust differentiation protocol for monocytes and macrophages from hiPSCs, which could be included in the vascular part of the HT-hiPSC model. The protocol for this was established (chapters 2 and 3) and the monocytes/macrophages (IPSDMs) functionally characterized. A detailed comparison of IPSDMs with PBDMs was performed in terms of gene expression and functional behavior. **Second**, the derivation and characterization of hiPSC-derived ECs, as EC is the major cell type affected in HHT1 and the major component of HHT1 hiPSC model. A reporter hiPSC line for *ETV2* was generated using CRISPR/Cas9 technology and used to initiate a study the developmental origin and maturation process of hiPSC-derived ECs (chapter 4). **Third**, derivation of an hiPSC line from HHT1 patient somatic cells and generation of its isogenic control line without endoglin mutation. Fortunately, this did not require genetic engineering since we have identified a mosaic patient who carried the endoglin mutation only in some but not all tissues. We thus managed to establish a pair of isogenic hiPSC lines from both wild type and mutated cells from this mosaic patient. **Fourth**, differentiation and characterization of ECs from isogenic HHT-hiPSC lines based on their transcriptome profile and functional analysis. **Finally**, an *in vitro* disease model for HHT1 by combining ECs and mural cells in 2D and 3D culture systems was established (chapter 5). With the disease model established the aim was to ultimately provide new insight into the HHT1 disease mechanisms and an experimental platform for screening potential drugs for disease treatment.

Finally, another disease we modeled in this thesis was PHE. This was part of a

collaborative study; my contribution was whole transcriptomic sequencing and bioinformatic analysis of PHE and WT hiPSC-ECs to identify the dysregulated transcriptional network which could contribute to revealing of the underlying pathology of PHE and identify new therapeutic targets (chapter 6). At the end, a general Discussion of the outcome of this thesis is provided in Chapter 7. A number of important issues have been addressed that would be needed to create representative human models for HHT1 and PHE in culture. The outcome has provided important cellular tools that can help move the field forward and proved the basis for better understanding of the mechanisms underlying the genetic forms of vascular disease.

References

- Abedin, M., Nguyen, A., Jiang, N., Perry, C., Shelton, J., Watson, D., and Ferdous, A. (2014). Fli1 acts downstream of Etv2 to govern cell survival and vascular homeostasis via positive autoregulation. *Circ Res* 114, 1690–1699.
- Adams, W.J., Zhang, Y., Cloutier, J., Kuchimanchi, P., Newton, G., Sehrawat, S., Aird, W.C., Mayadas, T.N., Luscinskas, F.W., and García-Cardeña, G. (2013). Functional Vascular Endothelium Derived from Human Induced Pluripotent Stem Cells. *Stem Cell Rep* 1, 105–113.
- Aflaki, E., Stubblefield, B., Maniawang, E., Lopez, G., Moaven, N., Goldin, E., Marugan, J., Patnaik, S., Dutra, A., Southall, N., et al. (2014). Macrophage models of Gaucher disease for evaluating disease pathogenesis and candidate drugs. *Sci Transl Med* 6, 240ra73.
- Al-Qaderi, A., and Mansour, A. (2019). Pseudomyogenic Hemangioendothelioma. *Arch Pathol Lab Med* 143, 763–767.
- Arthur, H.M., Ure, J., Smith, A.J., Renforth, G., Wilson, D.I., Torsney, E., Charlton, R., Parums, D.V., Jowett, T., Marchuk, D.A., et al. (2000). Endoglin, an Ancillary TGF β Receptor, Is Required for Extraembryonic Angiogenesis and Plays a Key Role in Heart Development. *Dev Biol* 217, 42–53.
- Astorga, J., and Carlsson, P. (2007). Hedgehog induction of murine vasculogenesis is mediated by Foxf1 and Bmp4. *Development* 134, 3753–3761.
- Becker, P., Sacilotto, N., Nornes, S., Neal, A., Thomas, M., Liu, K., Preece, C., Ratnayaka, I., Davies, B., Bou-Gharios, G., et al. (2016). An Intronic Flk1 Enhancer Directs Arterial-Specific Expression via RBPJ-Mediated Venous Repression. *Arteriosclerosis Thrombosis Vasc Biology* 36, 1209–1219.
- Bernat, J., Crawford, G., Ogurtsov, A., Collins, F., Ginsburg, D., and Kondrashov, A. (2006). Distant conserved sequences flanking endothelial-specific promoters contain tissue-specific DNase-hypersensitive sites and over-represented motifs. *Hum Mol Genet* 15, 2098–2105.
- Bourdeau, A., Dumont, D., and Letarte, M. (1999). A murine model of hereditary hemorrhagic telangiectasia. *J Clin Invest* 104, 1343–1351.
- Bras, A., Yu, B., Bhaloo, S., Hong, X., Zhang, Z., Hu, Y., and Xu, Q. (2018). Adventitial Sca1+ Cells

- Transduced With ETV2 Are Committed to the Endothelial Fate and Improve Vascular Remodeling After Injury. *Arteriosclerosis Thrombosis Vasc Biology* 38, 232–244.
- Brault, J., Goutagny, E., Telugu, N., Shao, K., Baquié, M., Satre, V., Coutton, C., Grunwald, D., Brion, J.-P., Barlogis, V., et al. (2014). Optimized Generation of Functional Neutrophils and Macrophages from Patient-Specific Induced Pluripotent Stem Cells: Ex Vivo Models of X O-Linked, AR22 O- and AR47 O- Chronic Granulomatous Diseases. *BioResearch Open Access* 3, 311–326.
- van Bueren, K., and Black, B.L. (2012). Regulation of endothelial and hematopoietic development by the ETS transcription factor Etv2. *Curr Opin Hematol* 19, 199–205.
- Carman, C., Sage, P., Sciuto, T., de la Fuente, M., Geha, R., Ochs, H., Dvorak, H., Dvorak, A., and Springer, T. (2007). Transcellular diapedesis is initiated by invasive podosomes. *Immunity* 26, 784–797.
- Carmeliet, P., Ferreira, V., Breier, G., Pollefeyt, S., Kieckens, L., Gertsenstein, M., Fahrig, M., Vandenhoek, A., Harpal, K., Eberhardt, C., et al. (1996). Abnormal blood vessel development and lethality in embryos lacking a single VEGF allele. *Nature* 380, 435–439.
- Castonguay, R., Werner, E., Matthews, R., Presman, E., Mulivor, A., Solban, N., Sako, D., Pearsall, R., Underwood, K., Seehra, J., et al. (2011). Soluble endoglin specifically binds bone morphogenetic proteins 9 and 10 via its orphan domain, inhibits blood vessel formation, and suppresses tumor growth. *J Biol Chem* 286, 30034–30046.
- Chan, X., Black, R., Dickerman, K., Federico, J., Lévesque, M., Mumm, J., and Gerecht, S. (2015). Three-Dimensional Vascular Network Assembly From Diabetic Patient-Derived Induced Pluripotent Stem Cells. *Arteriosclerosis Thrombosis Vasc Biology* 35, 2677–2685.
- Chao, M., Alizadeh, A., Tang, C., Myklebust, J., Varghese, B., Gill, S., Jan, M., Cha, A., Chan, C., Tan, B., et al. (2010). Anti-CD47 antibody synergizes with rituximab to promote phagocytosis and eradicate non-Hodgkin lymphoma. *Cell* 142, 699–713.
- Choi, E.-J., Chen, W., Jun, K., Arthur, H.M., Young, W.L., and Su, H. (2014). Novel brain arteriovenous malformation mouse models for type 1 hereditary hemorrhagic telangiectasia. *Plos One* 9, e88511.
- Choi, J., Dong, L., Ahn, J., Dao, D., Hammerschmidt, M., and Chen, J. (2007). FoxH1 negatively modulates flk1 gene expression and vascular formation in zebrafish. *Dev Biol* 304, 735–744.
- Choi, K.-D., Yu, J., Smuga-Otto, K., Salvagiotto, G., Rehrauer, W., Vodyanik, M., Thomson, J., and Slukvin, I. (2009). Hematopoietic and Endothelial Differentiation of Human Induced Pluripotent Stem Cells. *Stem Cells* 27, 559–567.
- Choi, K.-D., Vodyanik, M., and Slukvin, I.I. (2011). Hematopoietic differentiation and production of mature myeloid cells from human pluripotent stem cells. *Nat Protoc* 6, 296–313.
- Chu, M., Li, T., Shen, B., Cao, X., Zhong, H., Zhang, L., Zhou, F., Ma, W., Jiang, H., Xie, P., et al. (2016). Angiopoietin receptor Tie2 is required for vein specification and maintenance via regulating COUP-TFII. *Elife* 5, 4552.
- Corliss, B., Azimi, M., Munson, J., Peirce, S., and Murfee, W. (2016). Macrophages: An

Inflammatory Link Between Angiogenesis and Lymphangiogenesis. *Microcirculation* 23, 95–121.

Craig, M.P., Grajevskaja, V., Liao, H.-K., Balciuniene, J., Ekker, S.C., Park, J.-S., Essner, J.J., Balciunas, D., and Sumanas, S. (2015). Etv2 and Fli1b Function Together as Key Regulators of Vasculogenesis and Angiogenesis. *Arteriosclerosis Thrombosis Vasc Biology* 35, 865–876.

Dakeishi, M., Shioya, T., Wada, Y., Shindo, T., Otaka, K., Manabe, M., Nozaki, J.-I., Inoue, S., and Koizumi, A. (2002). Genetic epidemiology of hereditary hemorrhagic telangiectasia in a local community in the northern part of Japan. *Hum Mutat* 19, 140–148.

David, L., Mallet, C., Mazerbourg, S., Feige, J.-J., and Bailly, S. (2006). Identification of BMP9 and BMP10 as functional activators of the orphan activin receptor-like kinase 1 (ALK1) in endothelial cells. *Blood* 109, 1953–1961.

David, L., Mallet, C., Keramidas, M., Lamande, N., Gasc, J., Dupuis-Girod, S., Plauchu, H., Feige, J., and Bailly, S. (2008). Bone Morphogenetic Protein-9 Is a Circulating Vascular Quiescence Factor. *Circ Res* 102, 914–922.

Dejana, E., Taddei, A., and Randi, A. (2007). Foxs and Ets in the transcriptional regulation of endothelial cell differentiation and angiogenesis. *Biochimica Et Biophysica Acta Bba - Rev Cancer* 1775, 298–312.

Dupuis-Girod, S., Ginon, I., Saurin, J.-C., Marion, D., Guillot, E., Decullier, E., Roux, A., Carette, M.-F., Gilbert-Dussardier, B., Hatron, P.-Y., et al. (2012). Bevacizumab in Patients With Hereditary Hemorrhagic Telangiectasia and Severe Hepatic Vascular Malformations and High Cardiac Output. *Jama* 307, 948–955.

Fantin, A., Vieira, J., Gestri, G., Denti, L., Schwarz, Q., Prykhodzhiy, S., Peri, F., Wilson, S., and Ruhrberg, C. (2010). Tissue macrophages act as cellular chaperones for vascular anastomosis downstream of VEGF-mediated endothelial tip cell induction. *Blood* 116, 829–840.

Ferdous, A., Caprioli, A., Iacovino, M., Martin, C.M., Morris, J., Richardson, J.A., Latif, S., Hammer, R.E., Harvey, R.P., Olson, E.N., et al. (2009). Nkx2–5 transactivates the Ets-related protein 71 gene and specifies an endothelial/endocardial fate in the developing embryo. *Proc National Acad Sci* 106, 814–819.

Ferrara, N., Carver-Moore, K., Chen, H., Dowd, M., Lu, L., O’Shea, K., Powell-Braxton, L., Hillan, K., and Moore, M. (1996). Heterozygous embryonic lethality induced by targeted inactivation of the VEGF gene. *Nature* 380, 439–442.

Fleagle, J., Bobba, R., Kardinal, C., and Freter, C. (2012). Iron deficiency anemia related to hereditary hemorrhagic telangiectasia: response to treatment with bevacizumab. *Am J Medical Sci* 343, 249–251.

Fonsatti, E., Vecchio, L., Altomonte, M., Sigalotti, L., Nicotra, M., Coral, S., Natali, P., and Maio, M. (2001). Endoglin: An accessory component of the TGF- β -binding receptor-complex with diagnostic, prognostic, and bioimmunotherapeutic potential in human malignancies. *J Cell Physiol* 188, 1–7.

- Gabor, K., Sapi, Z., Tiszlavicz, L., Fige, A., Bereczki, C., and Bartyik, K. (2018). Sirolimus therapy in the treatment of pseudomyogenic hemangioendothelioma. *Pediatr Blood Cancer* 65, e26781.
- Garrido-Martin, E.M., Nguyen, H.-L., Cunningham, T.A., Choe, S., Jiang, Z., Arthur, H.M., Lee, Y.-J., and Oh, P.S. (2014). Common and Distinctive Pathogenetic Features of Arteriovenous Malformations in Hereditary Hemorrhagic Telangiectasia 1 and Hereditary Hemorrhagic Telangiectasia 2 Animal Models—Brief Report. *Arteriosclerosis Thrombosis Vasc Biology* 34, 2232–2236.
- Gerhardt, T., and Ley, K. (2015). Monocyte trafficking across the vessel wall. *Cardiovasc Res* 107, 321–330.
- Giacomelli, E., Bellin, M., Sala, L., van Meer, B.J., Tertoolen, L.G., Orlova, V.V., and Mummery, C.L. (2017). Three-dimensional cardiac microtissues composed of cardiomyocytes and endothelial cells co-differentiated from human pluripotent stem cells. *Development* 144, 1008–1017.
- Girod, S., Giraud, S., Decullier, E., Lesca, G., Cottin, V., Faure, F., Merrot, O., Saurin, J., Cordier, J., and Plauchu, H. (2007). Hemorrhagic Hereditary Telangiectasia (Rendu-Osler Disease) and Infectious Diseases: An Underestimated Association. *Clin Infect Dis* 44, 841–845.
- Goumans, M., Valdimarsdottir, G., Itoh, S., Lebrin, F., Larsson, J., Mummery, C., Karlsson, S., and ten Dijke, P. (2003). Activin receptor-like kinase (ALK)1 is an antagonistic mediator of lateral TGFbeta/ALK5 signaling. *Mol Cell* 12, 817–828.
- Gul, N., and van Egmond, M. (2015). Antibody-Dependent Phagocytosis of Tumor Cells by Macrophages: A Potent Effector Mechanism of Monoclonal Antibody Therapy of Cancer. *Cancer Res* 75, 5008–5013.
- Halaidych, O., Freund, C., van den Hil, F., Salvatori, D., Riminucci, M., Mummery, C., and Orlova, V. (2018). Inflammatory Responses and Barrier Function of Endothelial Cells Derived from Human Induced Pluripotent Stem Cells. *Stem Cell Rep* 10, 1642–1656.
- Harding, A., Cortez-Toledo, E., Magner, N., Beegle, J., Coleal-Bergum, D., Hao, D., Wang, A., Nolte, J., and Zhou, P. (2017). Highly Efficient Differentiation of Endothelial Cells from Pluripotent Stem Cells Requires the MAPK and the PI3K Pathways. *Stem Cells* 35, 909–919.
- Haro, D.L., and Janknecht, R. (2002). Functional analysis of the transcription factor ER71 and its activation of the matrix metalloproteinase-1 promoter. *Nucleic Acids Res* 30, 2972–2979.
- Hawinkels, L., Kuiper, P., Wiercinska, E., Verspaget, H., Liu, Z., Pardali, E., Sier, C., and ten Dijke, P. (2010). Matrix Metalloproteinase-14 (MT1-MMP)-Mediated Endoglin Shedding Inhibits Tumor Angiogenesis. *Cancer Res* 70, 4141–4150.
- Hayashi, H., and Kume, T. (2008). Foxc transcription factors directly regulate Dll4 and Hey2 expression by interacting with the VEGF-Notch signaling pathways in endothelial cells. *Plos One* 3, e2401.
- Hollenhorst, P., Shah, A., Hopkins, C., and Graves, B. (2007). Genome-wide analyses reveal properties of redundant and specific promoter occupancy within the ETS gene family.

Genes Amp Dev 21, 1882–1894.

Inyang, A., Mertens, F., Puls, F., Sumathi, V., Inwards, C., Folpe, A., Lee, C., Zhang, Y., Symmans, P., Rubin, B., et al. (2016). Primary Pseudomyogenic Hemangioendothelioma of Bone. *40*, 587–598.

James, D., Nam, H., Seandel, M., Nolan, D., Janovitz, T., Tomishima, M., Studer, L., Lee, G., Lyden, D., Benezra, R., et al. (2010). Expansion and maintenance of human embryonic stem cell–derived endothelial cells by TGF β inhibition is Id1 dependent. *Nat Biotechnol* 28, 161–166.

Jerkic, M., RODRIGUEZBERO, A., PRIETO, M., Toporsian, M., Pericacho, M., RIVASELENA, J., OBREO, J., WANG, A., PEREZRIOCANAL, F., and AREVALO, M. (2006). Reduced angiogenic responses in adult endoglin heterozygous mice. *Cardiovasc Res* 69, 845–854.

Jerkic, M., Peter, M., Ardelean, D., Fine, M., Konerding, M., and Letarte, M. (2010). Dextran sulfate sodium leads to chronic colitis and pathological angiogenesis in Endoglin heterozygous mice. *Inflamm Bowel Dis* 16, 1859–1870.

Jiang, Y., Cowley, S.A., Siler, U., Melguizo, D., Tilgner, K., Browne, C., Dewilton, A., Przyborski, S., Saretzki, G., James, W.S., et al. (2012). Derivation and Functional Analysis of Patient-Specific Induced Pluripotent Stem Cells as an In Vitro Model of Chronic Granulomatous Disease. *Stem Cells* 30, 599–611.

Kane, N.M., Meloni, M., Spencer, H.L., Craig, M.A., Strehl, R., Milligan, G., Houslay, M.D., Mountford, J.C., Emanuelli, C., and Baker, A.H. (2010). Derivation of Endothelial Cells From Human Embryonic Stem Cells by Directed Differentiation. *Arteriosclerosis Thrombosis Vasc Biology* 30, 1389–1397.

Kane, N.M., Xiao, Q., Baker, A.H., Luo, Z., Xu, Q., and Emanuelli, C. (2011). Pluripotent stem cell differentiation into vascular cells: A novel technology with promises for vascular re(generation). *Pharmacol Therapeut* 129, 29–49.

Karlsson, K., Cowley, S., Martinez, F., Shaw, M., Minger, S., and James, W. (2008). Homogeneous monocytes and macrophages from human embryonic stem cells following coculture-free differentiation in M-CSF and IL-3. *Exp Hematol* 36, 1167–1175.

Kataoka, H., Hayashi, M., Nakagawa, R., Tanaka, Y., Izumi, N., Nishikawa, S., Jakt, M., Tarui, H., and Nishikawa, S.-I. (2011). Etv2/ER71 induces vascular mesoderm from Flk1+PDGFR α + primitive mesoderm. *Blood* 118, 6975–6986.

Katt, M.E., Xu, Z.S., Gerecht, S., and Searson, P.C. (2016). Human Brain Microvascular Endothelial Cells Derived from the BC1 iPS Cell Line Exhibit a Blood-Brain Barrier Phenotype. *Plos One* 11, e0152105.

Kelly, M.A., and Hirschi, K.K. (2009). Signaling Hierarchy Regulating Human Endothelial Cell Development. *Arteriosclerosis Thrombosis Vasc Biology* 29, 718–724.

Kim, J.-S. (2016). Genome editing comes of age. *Nat Protoc* 11, 1573–1578.

Kobayashi, K., Ding, G., Nishikawa, S.-I., and Kataoka, H. (2013). Role of Etv2-positive cells in the remodeling morphogenesis during vascular development. *Genes Cells* 18, 704–721.

- Koyano-Nakagawa, N., and Garry, D.J. (2017). Etv2 as an essential regulator of mesodermal lineage development. *Cardiovasc Res* 113, 1294–1306.
- Koyano-Nakagawa, N., Kweon, J., Iacovino, M., Shi, X., Rasmussen, T.L., Borges, L., Zirbes, K.M., Li, T., Perlingeiro, R.C., Kyba, M., et al. (2012). Etv2 Is Expressed in the Yolk Sac Hematopoietic and Endothelial Progenitors and Regulates Lmo2 Gene Expression. *Stem Cells* 30, 1611–1623.
- Koyano-Nakagawa, N., Shi, X., Rasmussen, T.L., Das, S., Walter, C.A., and Garry, D.J. (2015). Feedback Mechanisms Regulate Ets Variant 2(Etv2) Gene Expression and Hematoendothelial Lineages. *J Biol Chem* 290, 28107–28119.
- Kubota, Y., Takubo, K., Shimizu, T., Ohno, H., Kishi, K., Shibuya, M., Saya, H., and Suda, T. (2009). M-CSF inhibition selectively targets pathological angiogenesis and lymphangiogenesis. *J Exp Medicine* 206, 1089–1102.
- Kusuma, S., Shen, Y., Hanjaya-Putra, D., Mali, P., Cheng, L., and Gerecht, S. (2013). Self-organized vascular networks from human pluripotent stem cells in a synthetic matrix. *Proc National Acad Sci* 110, 12601–12606.
- van Laake, L.W., van den Driesche, S., Post, S., Feijen, A., Jansen, M.A., Driessens, M.H., Mager, J.J., Snijder, R.J., Westermann, C.J., Doevendans, P.A., et al. (2006). Endoglin Has a Crucial Role in Blood Cell-Mediated Vascular Repair. *Circulation* 114, 2288–2297.
- Lachmann, N., Ackermann, M., Frenzel, E., Liebhaber, S., Brenning, S., Happle, C., Hoffmann, D., Klimenkova, O., Lüttge, D., Buchegger, T., et al. (2015). Large-Scale Hematopoietic Differentiation of Human Induced Pluripotent Stem Cells Provides Granulocytes or Macrophages for Cell Replacement Therapies. *Stem Cell Rep* 4, 282–296.
- Lebrin, F., Goumans, M.-J., Jonker, L., Carvalho, R.L., Valdimarsdottir, G., Thorikay, M., Mummery, C., Arthur, H.M., and ten Dijke, P. (2004). Endoglin promotes endothelial cell proliferation and TGF- β /ALK1 signal transduction. *Embo J* 23, 4018–4028.
- Lebrin, F., n, S., Raymond, K., Martin, S., van den Brink, S., Freitas, C., Bréant, C., Mathivet, T., Larrivée, B., Thomas, J.-L., et al. (2010). Thalidomide stimulates vessel maturation and reduces epistaxis in individuals with hereditary hemorrhagic telangiectasia. *Nat Med* 16, 420–428.
- Lee, D., Park, C., Lee, H., Lugus, J.J., Kim, S., Arentson, E., Chung, Y., Gomez, G., Kyba, M., Lin, S., et al. (2008). ER71 Acts Downstream of BMP, Notch, and Wnt Signaling in Blood and Vessel Progenitor Specification. *Cell Stem Cell* 2, 497–507.
- Lee, D., Kim, T., and Lim, D.-S. (2011). The Er71 Is an Important Regulator of Hematopoietic Stem Cells in Adult Mice. *Stem Cells* 29, 539–548.
- Letteboer, T. (2005). Genotype-phenotype relationship in hereditary haemorrhagic telangiectasia. *J Med Genet* 43, 371–377.
- Li, C., Hampson, I., Hampson, L., Kumar, P., Bernabeu, C., and Kumar, S. (2000). CD105 antagonizes the inhibitory signaling of transforming growth factor beta1 on human vascular endothelial cells. *The FASEB Journal* 14, 55–64.

- Li, D., Sorensen, L., Brooke, B., Urness, L., Davis, E., Taylor, D., Boak, B., and Wendel, D. (1999). Defective angiogenesis in mice lacking endoglin. *Science* 284, 1534–1537.
- Lin, Y., Gil, C.-H., and Yoder, M.C. (2017). Differentiation, Evaluation, and Application of Human Induced Pluripotent Stem Cell–Derived Endothelial Cells. *Arteriosclerosis Thrombosis Vasc Biology* 37, 2014–2025.
- Lippmann, E.S., Al-Ahmad, A., Azarin, S.M., Palecek, S.P., and Shusta, E.V. (2014). A retinoic acid-enhanced, multicellular human blood-brain barrier model derived from stem cell sources. *Sci Rep-Uk* 4, 178.
- Liu, F., Kang, I., Park, C., Chang, L.-W., Wang, W., Lee, D., Lim, D.-S., Vittet, D., Nerbonne, J.M., and Choi, K. (2012). ER71 specifies Flk-1+ hemangiogenic mesoderm by inhibiting cardiac mesoderm and Wnt signaling. *Blood* 119, 3295–3305.
- Liu, F., Li, D., Yu, Y., Kang, I., Cha, M.-J., Kim, J., Park, C., Watson, D.K., Wang, T., and Choi, K. (2015). Induction of hematopoietic and endothelial cell program orchestrated by ETStanscription factor ER71/ ETV2. *Embo Rep* 16, 654–669.
- Lucas, T., Waisman, A., Ranjan, R., Roes, J., Krieg, T., Müller, W., Roers, A., and Eming, S.A. (2010). Differential Roles of Macrophages in Diverse Phases of Skin Repair. *J Immunol* 184, 3964–3977.
- Majeti, R., Chao, M., Alizadeh, A., Pang, W., Jaiswal, S., Gibbs, J.K., van Rooijen, N., and Weissman, I. (2009). CD47 is an adverse prognostic factor and therapeutic antibody target on human acute myeloid leukemia stem cells. *Cell* 138, 286–299.
- Mantovani, A., Sica, A., Sozzani, S., Allavena, P., Vecchi, A., and Locati, M. (2004). The chemokine system in diverse forms of macrophage activation and polarization. *Trends Immunol* 25, 677–686.
- Mantovani, A., Biswas, S., Galdiero, M., Sica, A., and Locati, M. (2013). Macrophage plasticity and polarization in tissue repair and remodelling. *J Pathology* 229, 176–185.
- Marcelo, K.L., Goldie, L.C., and Hirschi, K.K. (2013). Regulation of Endothelial Cell Differentiation and Specification. *Circ Res* 112, 1272–1287.
- Marchuk, D., Guttmacher, A., Penner, J., and Ganguly, P. (1998). Report on the workshop on Hereditary Hemorrhagic Telangiectasia, July 10-11, 1997. *American Journal of Medical Genetics* 76, 269–273.
- McCracken, I.R., Taylor, R.S., Kok, F.O., de la Cuesta, F., Dobie, R., Henderson, B.E., Mountford, J.C., Caudrillier, A., Henderson, N.C., Ponting, C.P., et al. (2019). Transcriptional dynamics of pluripotent stem cell-derived endothelial cell differentiation revealed by single-cell RNA sequencing. *Eur Heart J* 385, 9963117.
- Medvinsky, A., Rybtsov, S., and Taoudi, S. (2011). Embryonic origin of the adult hematopoietic system: advances and questions. *Development* 138, 1017–1031.
- Meerschaert, J., and Furie, M. (1995). The adhesion molecules used by monocytes for migration across endothelium include CD11a/CD18, CD11b/CD18, and VLA-4 on monocytes and ICAM-1, VCAM-1, and other ligands on endothelium. *The Journal of Immunology* 154,

4099–4112.

- Mestas, J., and Ley, K. (2008). Monocyte-Endothelial Cell Interactions in the Development of Atherosclerosis. *Trends Cardiovas Med* 18, 228–232.
- Miquerol, L., Langille, B., and Nagy, A. (2000). Embryonic development is disrupted by modest increases in vascular endothelial growth factor gene expression. *Development* 127, 3941–3946.
- Miyazono, K., Maeda, S., and Imamura, T. (2005). BMP receptor signaling: Transcriptional targets, regulation of signals, and signaling cross-talk. *Cytokine Growth F R* 16, 251–263.
- Morita, R., Suzuki, M., Kasahara, H., Shimizu, N., Shichita, T., Sekiya, T., Kimura, A., Sasaki, K., Yasukawa, H., and Yoshimura, A. (2015). ETS transcription factor ETV2 directly converts human fibroblasts into functional endothelial cells. *Proc National Acad Sci* 112, 160–165.
- Muller, W.A. (2015). The regulation of transendothelial migration: new knowledge and new questions. *Cardiovasc Res* 107, 310–320.
- Neehus, A.-L., Lam, J., Haake, K., Merkert, S., Schmidt, N., Mucci, A., Ackermann, M., Schubert, M., Happle, C., Kühnel, M., et al. (2018). Impaired IFN γ -Signaling and Mycobacterial Clearance in IFN γ R1-Deficient Human iPSC-Derived Macrophages. *Stem Cell Rep* 10, 7–16.
- Nourse, M.B., Halpin, D.E., Scatena, M., Mortisen, D.J., Tulloch, N.L., Hauch, K.D., Torok-Storb, B., Ratner, B.D., Pabon, L., and Murry, C.E. (2010). VEGF Induces Differentiation of Functional Endothelium From Human Embryonic Stem Cells. *Arteriosclerosis Thrombosis Vasc Biology* 30, 80–89.
- Ojeda-Fernandez, L., Recio-Poveda, L., Aristorena, M., Lastres, P., Blanco, F.J., Sanz-Rodríguez, F., Gallardo-Vara, E., de Casas-Engel, M., Corbi, A., Arthur, H.M., et al. (2016). Mice Lacking Endoglin in Macrophages Show an Impaired Immune Response. *Plos Genet* 12, e1005935.
- Orlova, V., van den Hil, F., Petrus-Reurer, S., Drabsch, Y., Dijke, T.P., and Mummery, C. (2014a). Generation, expansion and functional analysis of endothelial cells and pericytes derived from human pluripotent stem cells. *Nat Protoc* 9, 1514–1531.
- Orlova, V., Drabsch, Y., Freund, C., Petrus-Reurer, S., van den Hil, F., Muenthaisong, S., Dijke, P., and Mummery, C. (2014b). Functionality of endothelial cells and pericytes from human pluripotent stem cells demonstrated in cultured vascular plexus and zebrafish xenografts. *Arteriosclerosis Thrombosis Vasc Biology* 34, 177–186.
- Ozeki, M., Nozawa, A., Kanda, K., Hori, T., Nagano, A., Shimada, A., Miyazaki, T., and Fukao, T. (2017). Everolimus for Treatment of Pseudomyogenic Hemangioendothelioma. *J Pediatric Hematology Oncol* 39, e328–e331.
- Paik, D.T., Tian, L., Lee, J., Sayed, N., Chen, I.Y., Rhee, S., Rhee, J.-W., Kim, Y., Wirka, R.C., Buikema, J.W., et al. (2018). Large-Scale Single-Cell RNA-Seq Reveals Molecular Signatures of Heterogeneous Populations of Human Induced Pluripotent Stem Cell-Derived Endothelial Cells. *Circ Res* 123, 443–450.
- Paik, J.-H., Kollipara, R., Chu, G., Ji, H., Xiao, Y., Ding, Z., Miao, L., Tothova, Z., Horner, J.W., Carrasco, D.R., et al. (2007). FoxOs Are Lineage-Restricted Redundant Tumor Suppressors

and Regulate Endothelial Cell Homeostasis. *Cell* 128, 309–323.

- Palpant, N.J., Pabon, L., Friedman, C.E., Roberts, M., Hadland, B., Zaunbrecher, R.J., Bernstein, I., Zheng, Y., and Murry, C.E. (2016). Generating high-purity cardiac and endothelial derivatives from patterned mesoderm using human pluripotent stem cells. *Nat Protoc* 12, 15–31.
- Panicker, L., Miller, D., Park, T., Patel, B., Azevedo, J., Awad, O., Masood, M., Veenstra, T., Goldin, E., Stubblefield, B., et al. (2012). Induced pluripotent stem cell model recapitulates pathologic hallmarks of Gaucher disease. *Proc National Acad Sci* 109, 18054–18059.
- Park, C. (2004). A hierarchical order of factors in the generation of FLK1- and SCL-expressing hematopoietic and endothelial progenitors from embryonic stem cells. *Development* 131, 2749–2762.
- Park, C., Lee, T.-J., Bhang, S., Liu, F., Nakamura, R., Oladipupo, S.S., Pitha-Rowe, I., Capoccia, B., Choi, H., Kim, T., et al. (2016). Injury-Mediated Vascular Regeneration Requires Endothelial ER71/ETV2. *Arteriosclerosis Thrombosis Vasc Biology* 36, 86–96.
- Park, T., Bhutto, I., Zimmerlin, L., Huo, J.S., Nagaria, P., Miller, D., Rufaihah, A., Talbot, C., Aguilar, J., Grebe, R., et al. (2014). Vascular Progenitors From Cord Blood–Derived Induced Pluripotent Stem Cells Possess Augmented Capacity for Regenerating Ischemic Retinal Vasculature. *Circulation* 129, 359–372.
- Patan, S. (2004). Vasculogenesis and angiogenesis. *Cancer Treatment and Research* 117, 3–32.
- Patsch, C., Challet-Meylan, L., Thoma, E.C., Urich, E., Heckel, T., O’Sullivan, J.F., Grainger, S.J., Kapp, F.G., Sun, L., Christensen, K., et al. (2015). Generation of vascular endothelial and smooth muscle cells from human pluripotent stem cells. *Nat Cell Biol* 17, 994–1003.
- Pearson, S., czynska, P., Lacaud, G., and Kouskoff, V. (2008). The stepwise specification of embryonic stem cells to hematopoietic fate is driven by sequential exposure to Bmp4, activin A, bFGF and VEGF. *Development* 135, 1525–1535.
- Pece-Barbara, N., Vera, S., Kathirkamathamby, K., Liebner, S., Guglielmo, D.G., Dejana, E., Wrana, J., and Letarte, M. (2005). Endoglin Null Endothelial Cells Proliferate Faster and Are More Responsive to Transforming Growth Factor β 1 with Higher Affinity Receptors and an Activated Alk1 Pathway. *J Biol Chem* 280, 27800–27808.
- Post, S., Smits, A., van den Broek, A., Sluijter, J., Hoefer, I., Janssen, B., Snijder, R., Mager, J., Pasterkamp, G., Mummery, C., et al. (2010). Impaired recruitment of HHT-1 mononuclear cells to the ischaemic heart is due to an altered CXCR4/CD26 balance. *Cardiovasc Res* 85, 494–502.
- Prasain, N., Lee, M., Vemula, S., Meador, J., Yoshimoto, M., Ferkowicz, M.J., Fett, A., Gupta, M., Rapp, B.M., Saadatzaheh, M., et al. (2014). Differentiation of human pluripotent stem cells to cells similar to cord-blood endothelial colony-forming cells. *Nat Biotechnol* 32, 1151–1157.
- Rajasingh, J., Ikuno, T., Masumoto, H., Yamamizu, K., Yoshioka, M., Minakata, K., Ikeda, T., Sakata, R., and Yamashita, J.K. (2017). Efficient and robust differentiation of endothelial cells

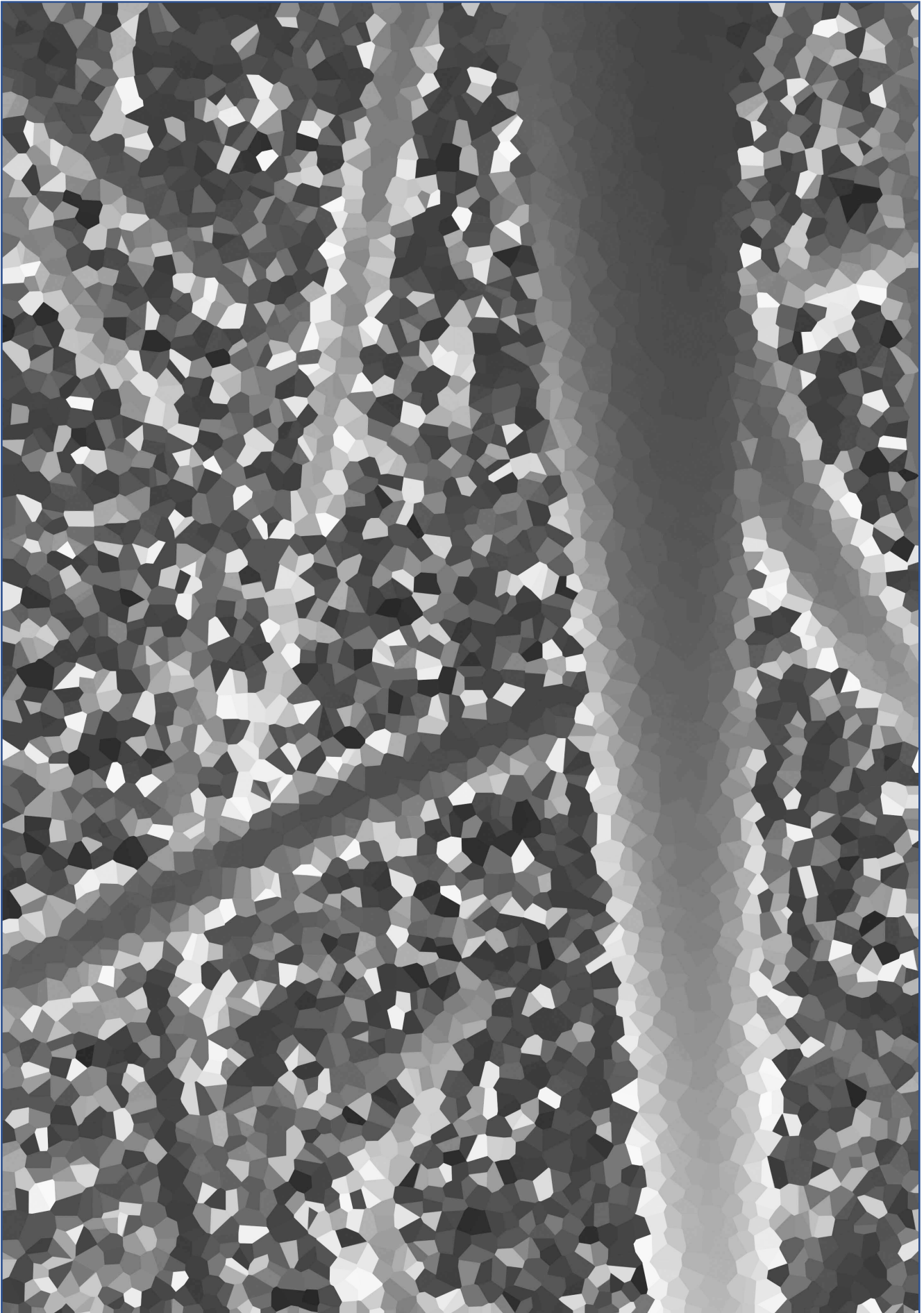
- from human induced pluripotent stem cells via lineage control with VEGF and cyclic AMP. *Plos One* 12, e0173271.
- ram, G., Tan, J., Islam, I., Rufaihah, A., and Cao, T. (2015). Efficient differentiation of human embryonic stem cells to arterial and venous endothelial cells under feeder- and serum-free conditions. *Stem Cell Res Ther* 6, 43.
- Reddi, A. (2001). Interplay between bone morphogenetic proteins and cognate binding proteins in bone and cartilage development: noggin, chordin and DAN. *Arthritis Res* 3, 1–5.
- Robinson, A.S., Materna, S.C., Barnes, R.M., Val, S., Xu, S.-M., and Black, B.L. (2014). An arterial-specific enhancer of the human endothelin converting enzyme 1 (ECE1) gene is synergistically activated by Sox17, FoxC2, and Etv2. *Dev Biol* 395, 379–389.
- Robinton, D.A., and Daley, G.Q. (2012). The promise of induced pluripotent stem cells in research and therapy. *Nature* 481, 295–305.
- Rossi, E., Sanz-Rodríguez, F., Eleno, N., Düwell, A., Blanco, F.J., Langa, C., Botella, L.M., Cabañas, C., Lopez-Novoa, J.M., and Bernabeu, C. (2013). Endothelial endoglin is involved in inflammation: role in leukocyte adhesion and transmigration. *Blood* 121, 403–415.
- Rószter, T. (2015). Understanding the Mysterious M2 Macrophage through Activation Markers and Effector Mechanisms. *Mediat Inflamm* 2015, 1–16.
- Rufaihah, A., Huang, N.F., Jamé, S., Lee, J.C., Nguyen, H.N., Byers, B., De, A., Okogbaa, J., Rollins, M., Reijo-Pera, R., et al. (2011). Endothelial Cells Derived From Human iPSCs Increase Capillary Density and Improve Perfusion in a Mouse Model of Peripheral Arterial Disease. *Arteriosclerosis Thrombosis Vasc Biology* 31, 1035.
- Rufaihah, A., Huang, N.F., Kim, J., Herold, J., Volz, K.S., Park, T., Lee, J.C., Zambidis, E.T., Reijo-Pera, R., and Cooke, J.P. (2013). Human induced pluripotent stem cell-derived endothelial cells exhibit functional heterogeneity. *American Journal of Translational Research* 5, 21–35.
- Sahara, M., Hansson, E.M., Wernet, O., Lui, K.O., Später, D., and Chien, K.R. (2014). Manipulation of a VEGF-Notch signaling circuit drives formation of functional vascular endothelial progenitors from human pluripotent stem cells. *Cell Res* 24, 820–841.
- Sarah, D., L, B. (2009). Transcriptional Control of Endothelial Cell Development *Developmental Cell* 16(2), 180-195.
- Saito, T., Bokhove, M., Croci, R., Zamora-Caballero, S., Han, L., Letarte, M., de Sanctis, D., and Jovine, L. (2017). Structural Basis of the Human Endoglin-BMP9 Interaction: Insights into BMP Signaling and HHT1. *Cell Reports* 19, 1917–1928.
- Scharpfenecker, M., van Dinther, M., Liu, Z., van Bezooijen, R., Zhao, Q., Pukac, L., Lowik, C., and ten Dijke, P. (2007). BMP-9 signals via ALK1 and inhibits bFGF-induced endothelial cell proliferation and VEGF-stimulated angiogenesis. *J Cell Sci* 120, 964–972.
- Schneidawind, C., Jeong, J., Schneidawind, D., Kim, I.-S., Duque-Afonso, J., Wong, S., Iwasaki, M., Breese, E.H., Zehnder, J.L., Porteus, M., et al. (2018). MLL leukemia induction by t(9;11) chromosomal translocation in human hematopoietic stem cells using genome editing. *Blood Adv* 2, 832–845.

- Schnoor, M., Lai, F.P., Zarbock, A., Kläver, R., Polaschegg, C., Schulte, D., Weich, H.A., Oelkers, M.J., Rottner, K., and Vestweber, D. (2011). Cortactin deficiency is associated with reduced neutrophil recruitment but increased vascular permeability in vivo. *J Exp Medicine* 208, 1721–1735.
- Schnoor, M., Alcaide, P., Voisin, M.-B., and van Buul, J.D. (2015). Crossing the Vascular Wall: Common and Unique Mechanisms Exploited by Different Leukocyte Subsets during Extravasation. *Mediat Inflamm* 2015, 1–23.
- Shaw, S.K., Ma, S., Kim, M.B., Rao, R.M., Hartman, C.U., Froio, R.M., Yang, L., Jones, T., Liu, Y., Nusrat, A., et al. (2004). Coordinated Redistribution of Leukocyte LFA-1 and Endothelial Cell ICAM-1 Accompany Neutrophil Transmigration. *J Exp Medicine* 200, 1571–1580.
- Shen, F., Degos, V., Chu, P.-L., Han, Z., Westbroek, E.M., Choi, E.-J., Marchuk, D., Kim, H., Lawton, M.T., Maze, M., et al. (2014). Endoglin Deficiency Impairs Stroke Recovery. *Stroke* 45, 2101–2106.
- Shovlin, C., Guttmacher, A., Buscarini, E., Faughnan, M., Hyland, R., Westermann, C., Kjeldsen, A., and Plauchu, H. (2000). Diagnostic criteria for hereditary hemorrhagic telangiectasia (Rendu-Osler-Weber syndrome). *American Journal of Medical Genetics* 91, 66–67.
- Singh, B.N., Kawakami, Y., Akiyama, R., Rasmussen, T.L., Garry, M.G., Gong, W., Das, S., Shi, X., Koyano-Nakagawa, N., and Garry, D.J. (2015). The Etv2-miR-130a Network Regulates Mesodermal Specification. *Cell Reports* 13, 915–923.
- Spiller, K.L., Vunjak-Novakovic, G., Ng, J., Anfang, R.R., Spiller, K.J., Nakazawa, K.R., and Daulton, J.W. (2014). The role of macrophage phenotype in vascularization of tissue engineering scaffolds. *Biomaterials* 35, 4477–4488.
- Stockmann, C., Kirmse, S., Helfrich, I., Weidemann, A., Takeda, N., Doedens, A., and Johnson, R.S. (2011). A Wound Size–Dependent Effect of Myeloid Cell–Derived Vascular Endothelial Growth Factor on Wound Healing. *J Invest Dermatol* 131, 797–801.
- Swift, M., and Weinstein, B. (2009). Arterial-Venous Specification During Development. *Circ Res* 104, 576–588.
- Takahashi, K., and Yamanaka, S. (2006). Induction of Pluripotent Stem Cells from Mouse Embryonic and Adult Fibroblast Cultures by Defined Factors. *Cell* 126, 663–676.
- Takahashi, K., Tanabe, K., Ohnuki, M., Narita, M., Ichisaka, T., Tomoda, K., and Yamanaka, S. (2007). Induction of Pluripotent Stem Cells from Adult Human Fibroblasts by Defined Factors. *Cell* 131, 861–872.
- Takata, K., Kozaki, T., Lee, C., Thion, and Otsuka, M. (2017). Induced-Pluripotent-Stem-Cell-Derived Primitive Macrophages Provide a Platform for Modeling Tissue-Resident Macrophage Differentiation and Function. *Immunity*.
- Tanaka, T., Takahashi, K., Yamane, M., Tomida, S., Nakamura, S., Oshima, K., Niwa, A., Nishikomori, R., Kambe, N., Hara, H., et al. (2012). Induced pluripotent stem cells from CINCA syndrome patients as a model for dissecting somatic mosaicism and drug discovery. *Blood* 120, 1299–1308.

- Taura, D., Sone, M., Homma, K., Oyamada, N., Takahashi, K., Tamura, N., Yamanaka, S., and Nakao, K. (2009). Induction and Isolation of Vascular Cells From Human Induced Pluripotent Stem Cells—Brief Report. *Arteriosclerosis Thrombosis Vasc Biology* 29, 1100–1103.
- Theocharides, A.P., Jin, L., Cheng, P.-Y., Prasolava, T.K., Malko, A.V., Ho, J.M., Poepl, A.G., van Rooijen, N., Minden, M.D., Danska, J.S., et al. (2012). Disruption of SIRP α signaling in macrophages eliminates human acute myeloid leukemia stem cells in xenografts. *J Exp Medicine* 209, 1883–1899.
- Thomas-Ecker, S., Lindecke, A., Hatzmann, W., Kaltschmidt, C., Zanker, K., and Dittmar, T. (2007). Alteration in the gene expression pattern of primary monocytes after adhesion to endothelial cells. *Proc National Acad Sci* 104, 5539–5544.
- Torres, R., Martin, M., Garcia, A., Cigudosa, J.C., Ramirez, J., and Rodriguez-Perales, S. (2014). Engineering human tumour-associated chromosomal translocations with the RNA-guided CRISPR–Cas9 system. *Nat Commun* 5, 233.
- Torres-Ruiz, R., Martinez-Lage, M., Martin, M.C., Garcia, A., Bueno, C., Castaño, J., Ramirez, J.C., Menendez, P., Cigudosa, J.C., and Rodriguez-Perales, S. (2017). Efficient Recreation of t(11;22) EWSR1-FLI1 + in Human Stem Cells Using CRISPR/Cas9. *Stem Cell Rep* 8, 1408–1420.
- Tørring, P.M., Larsen, M., Kjeldsen, A.D., Ousager, L., Tan, Q., and Brusgaard, K. (2015). Global gene expression profiling of telangiectasial tissue from patients with hereditary hemorrhagic telangiectasia. *Microvasc Res* 99, 118–126.
- Torsney, E., Charlton, R., Diamond, A.G., Burn, J., Soames, J.V., and Arthur, H.M. (2003). Mouse Model for Hereditary Hemorrhagic Telangiectasia Has a Generalized Vascular Abnormality. *Circulation* 107, 1653–1657.
- Tseng, D., Volkmer, J., Willingham, S., Contreras-Trujillo, H., Fathman, J., Fernhoff, N., Seita, J., Inlay, M., Weiskopf, K., Miyanishi, M., et al. (2013). Anti-CD47 antibody-mediated phagocytosis of cancer by macrophages primes an effective antitumor T-cell response. *Proc National Acad Sci* 110, 11103–11108.
- Urbich, C., Heeschen, C., Aicher, A., Dernbach, E., Zeiher, A.M., and Dimmeler, S. (2003). Relevance of Monocytic Features for Neovascularization Capacity of Circulating Endothelial Progenitor Cells. *Circulation* 108, 2511–2516.
- Uusi-Rauva, K., Blom, T., von Schantz-Fant, C., Blom, T., Jalanko, A., and Kyttälä, A. (2017). Induced Pluripotent Stem Cells Derived from a CLN5 Patient Manifest Phenotypic Characteristics of Neuronal Ceroid Lipofuscinoses. *Int J Mol Sci* 18, 955.
- Val, D.S. (2011). Key transcriptional regulators of early vascular development. *Arteriosclerosis Thrombosis Vasc Biology* 31, 1469–1475.
- Val, S., Chi, N.C., Meadows, S.M., Minovitsky, S., Anderson, J.P., Harris, I.S., Ehlers, M.L., Agarwal, P., Visel, A., Xu, S.-M., et al. (2008). Combinatorial Regulation of Endothelial Gene Expression by Ets and Forkhead Transcription Factors. *Cell* 135, 1053–1064.
- Valdimarsdottir, G., Goumans, M.-J., Rosendahl, A., Brugman, M., Itoh, S., Lebrin, F., Sideras, P.,

- and ten Dijke, P. (2002). Stimulation of Id1 expression by bone morphogenetic protein is sufficient and necessary for bone morphogenetic protein-induced activation of endothelial cells. *Circulation* *106*, 2263–2270.
- Vanoli, F., Tomishima, M., Feng, W., Lamribet, K., Babin, L., Brunet, E., and Jasin, M. (2017). CRISPR-Cas9–guided oncogenic chromosomal translocations with conditional fusion protein expression in human mesenchymal cells. *Proc National Acad Sci* *114*, 3696–3701.
- Walther, C., Tayebwa, J., Lilljebjörn, H., Magnusson, L., Nilsson, J., von Steyern, F., Øra, I., Domanski, H.A., Fioretos, T., Nord, K.H., et al. (2014). A novel SERPINE1-FOSB fusion gene results in transcriptional up-regulation of FOSB in pseudomyogenic haemangioendothelioma. *J Pathology* *232*, 534–540.
- Westermann, C.J., Rosina, A.F., Vries, V., and de Coteau, P.A. (2003). The prevalence and manifestations of hereditary hemorrhagic telangiectasia in the Afro-Caribbean population of the Netherlands Antilles: A family screening. *Am J Med Genet* *116A*, 324–328.
- White, M.P., Rufaihah, A.J., Liu, L., Ghebremariam, Y.T., Ivey, K.N., Cooke, J.P., and vastava, D. (2012). Limited Gene Expression Variation in Human Embryonic Stem Cell and Induced Pluripotent Stem Cell-Derived Endothelial Cells. *Stem Cells* *31*, 92–103.
- van Wilgenburg, B., Browne, C., Vowles, J., and Cowley, S.A. (2013). Efficient, Long Term Production of Monocyte-Derived Macrophages from Human Pluripotent Stem Cells under Partly-Defined and Fully-Defined Conditions. *Plos One* *8*, e71098.
- Willenborg, S., Lucas, T., van Loo, G., Knipper, J.A., Krieg, T., Haase, I., Brachvogel, B., Hammerschmidt, M., Nagy, A., Ferrara, N., et al. (2012). CCR2 recruits an inflammatory macrophage subpopulation critical for angiogenesis in tissue repair. *Blood* *120*, 613–625.
- Williams, M.R., Sakurai, Y., Zughaier, S.M., Eskin, S.G., and McIntire, L.V. (2009). Transmigration across activated endothelium induces transcriptional changes, inhibits apoptosis, and decreases antimicrobial protein expression in human monocytes. *J Leukocyte Biol* *86*, 1331–1343.
- Willingham, S., Volkmer, J., Gentles, A., Sahoo, D., Dalerba, P., Mitra, S., Wang, J., Contreras-Trujillo, H., Martin, R., Cohen, J., et al. (2012). The CD47-signal regulatory protein alpha (SIRPα) interaction is a therapeutic target for human solid tumors. *Proc National Acad Sci* *109*, 6662–6667.
- Wong, C., Heit, B., and Kubes, P. (2010). Molecular regulators of leucocyte chemotaxis during inflammation. *Cardiovasc Res* *86*, 183–191.
- Woodfin, A., Voisin, M.-B., Beyrau, M., Colom, B., Caille, D., Diapouli, F.-M., Nash, G.B., Chavakis, T., Albelda, S.M., Rainger, E.G., et al. (2011). The junctional adhesion molecule JAM-C regulates polarized transendothelial migration of neutrophils in vivo. *Nat Immunol* *12*, 761–769.
- Wynn, T., Chawla, A., and Pollard, J. (2013). Macrophage biology in development, homeostasis and disease. *Nature* *496*, 445–455.
- Xu, B., Wu, Y., Huey, M., Arthur, H.M., Marchuk, D.A., Hashimoto, T., Young, W.L., and Yang, G.-Y.

- (2016). Vascular Endothelial Growth Factor Induces Abnormal Microvasculature in the Endoglin Heterozygous Mouse Brain. *J Cereb Blood Flow Metabolism* 24, 237–244.
- Yanagimachi, M., Niwa, A., Tanaka, T., Honda-Ozaki, F., Nishimoto, S., Murata, Y., Yasumi, T., Ito, J., Tomida, S., Oshima, K., et al. (2013). Robust and highly-efficient differentiation of functional monocytic cells from human pluripotent stem cells under serum- and feeder cell-free conditions. *Plos One* 8, e59243.
- Yang, L., Kowalski, J.R., Zhan, X., Thomas, S.M., and Luscinskas, F.W. (2006). Endothelial Cell Cortactin Phosphorylation by Src Contributes to Polymorphonuclear Leukocyte Transmigration In Vitro. *Circ Res* 98, 394–402.
- Yoo, C., Na, H.-J., Lee, D.-S., Heo, S., An, Y., Cha, J., Choi, C., Kim, J., Park, J.-C., and Cho, Y. (2013). Endothelial progenitor cells from human dental pulp-derived iPS cells as a therapeutic target for ischemic vascular diseases. *Biomaterials* 34, 8149–8160.
- Zanotelli, M.R., Ardalani, H., Zhang, J., Hou, Z., Nguyen, E.H., Swanson, S., Nguyen, B., Bolin, J., Elwell, A., Bischel, L.L., et al. (2016). Stable engineered vascular networks from human induced pluripotent stem cell-derived endothelial cells cultured in synthetic hydrogels. *Acta Biomater* 35, 32–41.
- Zhang, H., Xue, C., Shah, R., Bermingham, K., Hinkle, C., Li, W., Rodrigues, A., Tabita-Martinez, J., Millar, J., Cuchel, M., et al. (2015). Functional analysis and transcriptomic profiling of iPSC-derived macrophages and their application in modeling Mendelian disease. *Circ Res* 117, 17–28.
- Zhang, J., Schwartz, M.P., Hou, Z., Bai, Y., Ardalani, H., Swanson, S., Steill, J., Ruotti, V., Elwell, A., Nguyen, B., et al. (2017). A Genome-wide Analysis of Human Pluripotent Stem Cell-Derived Endothelial Cells in 2D or 3D Culture. *Stem Cell Rep* 8, 907–918.



Chapter 2

Differentiation and Functional Comparison of Monocytes and Macrophages from hiPSCs with Peripheral Blood Derivatives

Xu Cao, Gopala Krishna Yakala, Francijna E. van den Hil, Amy Cochrane, Christine L. Mummery and Valeria V. Orlova*

Department of Anatomy and Embryology, Einthovenweg 20, 2333ZC
Leiden, The Netherlands

*Corresponding author

Published in Stem Cell Reports

Vol. 12, pages 1282–1297, June 11, 2019

Doi: 10.1016/j.stemcr.2019.05.003

ABSTRACT

A renewable source of human monocytes and macrophages would be a valuable alternative to primary cells from peripheral blood (PB) in biomedical research. We developed an efficient protocol to derive monocytes and macrophages from human induced pluripotent stem cells (hiPSCs) and performed functional comparison with PB-derived cells. hiPSC-derived monocytes were functional after cryopreservation and exhibited comparable gene expression profiles as PB-derived monocytes. Notably, hiPSC-derived monocytes were more activated with greater adhesion to endothelial cells under physiological flow. hiPSC-derived monocytes were successfully polarized to M1 and M2 macrophage subtypes that showed similar pan- and subtype-specific gene and surface protein expression and cytokine secretion to PB-derived macrophages. hiPSC-derived macrophages exhibited higher endocytosis and efferocytosis and similar bacterial and tumour cell phagocytosis functionality compared to PB-derived macrophages. In summary, we developed a robust protocol to generate hiPSC-monocytes and macrophages from independent hiPSC-lines that showed aspects of functional maturity comparable with those from PB.

INTRODUCTION

Human peripheral blood mononuclear cells (PBMCs) are routinely used to derive monocytes and macrophages for many areas of biomedical research but despite the relative simplicity of the isolation procedure, it is often difficult outside specialized clinical centres to obtain large, high-quality cell batches on a regular basis from different donors, especially when research requires these from patients with rare diseases. In addition, recent studies suggest that many tissues are populated by specialist macrophages distinct from peripheral blood-derived macrophages (PBDMs) that are formed from primitive erythro-myeloid progenitors (EMPs) originating from hemogenic endothelium (HE) in the yolk sac (Ginhoux and Jung, 2014). Yolk sac-derived EMPs are different from hematopoietic stem cells (HSCs) derived from the aorta-gonad-mesonephros (AGM) region that appears during the definitive stage of hematopoiesis, and can be distinguished from AGM derived hematopoietic progenitors by the absence of HOXA gene expression (Dou et al., 2016; Ivanovs et al., 2017; Ng et al., 2016). Studies using human pluripotent stem cells (hPSCs) showed that it is possible to differentiate yolk sac-like hemogenic endothelium, identified as vascular endothelial-cadherin (VEC)+, CD73- and CD34+ cells, and early hematopoietic progenitors that express hematopoietic marker CD43 (Choi et al., 2009; Choi et al., 2012). These CD43+ cells can give rise to EMP-like cells with broad erythroid and myeloid differentiation capacity, apparently reminiscent of EMPs found in the mouse embryo. Multiple protocols have shown that hPSCs could be a potent source of monocytes and macrophages (Choi et al., 2009; Happel et al., 2018; Karlsson et al., 2008; Lachmann et al., 2015; Lang et al., 2018;

Schwartz et al., 2015; Takata et al., 2017; Uenishi et al., 2014; Vanhee et al., 2015; Zhang et al., 2015). Importantly these hiPSC-derived macrophages (IPSDMs) are similar to yolk sac-derived EMPs, as they undergo MYB-independent myeloid differentiation (Buchrieser et al., 2017; Vanhee et al., 2015) and lack expression of HOXA genes (Dou et al., 2016; Ivanovs et al., 2017; Ng et al., 2016); this suggests they are more like tissue-resident macrophages than PBDMs. Furthermore, IPSDMs can be conditioned by the resident cells to acquire tissue-specific characteristics *in vitro* (Takata et al., 2017) and *in vivo* (Happle et al., 2018; Takata et al., 2017). hiPSCs, therefore, provide unique opportunities to study tissue-resident macrophages which are otherwise very difficult or impossible to access (Lee et al., 2018).

Previous protocols primarily utilized continuous harvesting of floating cells in culture over periods of up to 8 weeks, with average yields of 2-3 x10⁶ IPSDMs per week per plate (Happle et al., 2018; Lachmann et al., 2015; van Wilgenburg et al., 2013). “Continuous harvesting” was recently successfully translated into stirred tank bioreactors for the mass production of IPSDMs (Ackermann et al., 2018). Here, we describe a protocol that allows production of EMP-like cells that can be further differentiated towards hiPSC-derived monocytes (hiPSC-mono) with the yield of 15-20 x10⁶ from a single plate in just 15 days. These hiPSC-mono can be used immediately, or cryopreserved and used thereafter in functional assays or induced to differentiate into IPSDMs, and polarized to “classically activated” inflammatory (M1) or “alternatively activated” anti-inflammatory (M2) subtypes. We also performed a side-by-side comparison with PB-derived monocytes and macrophages using functional assays, including adhesion to endothelial cells under flow, phagocytosis of bacteria, apoptotic and tumor cells.

RESULTS

Differentiation of CD14⁺ monocytes from hiPSCs

To derive monocytes from hiPSCs, we adapted our previous differentiation protocol of non-hemogenic vascular endothelial-cadherin (VEC)+CD73⁺ endothelial cells (Orlova et al., 2014a; Orlova et al., 2014b) to conditions that allowed the derivation of VEC+CD73⁺ hemogenic endothelium (HE) as described by Slukvin and colleagues (Uenishi et al., 2014). All differentiation steps were performed in IF9S serum-free medium (Uenishi et al., 2014), with some adaptations, such as normoxia (21% O₂) and the timing of growth factor addition. Undifferentiated hiPSCs were maintained in E8 medium and switched to IF9S medium. We found that 2 days of mesoderm induction with BMP4, Activin A, CHIR99021, followed by 3 days inducing endothelial cell fate with vascular endothelial growth factor (VEGF), SB431542, basic fibroblast growth factor (bFGF) and stem cell factor (SCF) resulted in efficient differentiation of VEC+CD73⁺-CD34⁺ HE. From day 5, a combination of human recombinant IL-6, IL-3, TPO, SCF, FGF2 and VEGF was added to

induce hematopoietic progenitor cells (HPCs) that resemble EMPs and were defined by the expression of CD43 and CD45. EMP-like cells were further differentiated into monocytes by human M-CSF, IL-3 and IL-6 addition for another 6 days. The protocol was next tested in three independent hiPSC lines reprogrammed using non-integrating Sendai virus or episomal methods: LUMC0083 (LU83, from PB erythroblasts), LUMC0020 (LU20, from skin fibroblasts) and LUMC0054 (LU54, from kidney epithelial cells isolated from urine). After 2 days of mesoderm induction, more than 60% of cells were CD140a+ (Figure 1C, S1A-B). On day 5, around 40% of the cells expressed endothelial cell-specific markers VEC and CD34. Within the VEC+CD34+ population, most cells were also CD73- HE (Figure 1C, S1A, S1C). After another 4 days in the presence of hematopoietic growth factors and cytokines, many non-adherent HPCs emerged from adherent HE (Figure 1B, Movie S1-S2). On day 9, expression of an early HPC surface marker CD43 was examined in the total population (adherent and suspension culture). Overall, by day 9 all three hiPSC lines had been induced to form HPCs expressing CD43 with high efficiency (Figure 1C, S1A, S1D). At this stage, the majority of CD43+ cells were also CD41a+CD235a+ indicating they were erythro-megakaryocytic progenitors, with only a small percentage of the total cell population being CD43+CD45+CD41a-CD235a- myeloid progenitors (Figure 1C-D, S1A, S1E). The CFU assay showed that cells on day 9 had already acquired high myeloid cells differentiation potential but had also developed the ability to differentiate into erythroid and granulocyte lineages (Figure S1F).

At day 9, cells were dissociated and cultured in suspension in the presence of IL-3 and IL-6 to promote proliferation of CD43+CD45+ myeloid progenitors and human M-CSF to promote differentiation of CD14+ monocytes from these myeloid progenitors (Choi et al., 2009; Uenishi et al., 2014). Under these conditions, the percentage of CD43+CD45+CD41a-CD235a- myeloid lineage cells increased to 50-70% across the different hiPSC lines by day 15 (Figure 1D). Percentages of CD43+CD45-CD41a+CD235a+ erythro-megakaryocytic lineage cells rapidly decreased on day 13-15 (Figure S1E). By day 15, CD14+ cells represented more than half of the total population across three independent hiPSC lines (Figure 1C, S1A). CD14+ monocytes were then purified using immuno-magnetic beads (Figure 1E, S1G). Isolated CD14+ cells showed typical monocyte morphology (Figure 1G), although were larger in size, with the cytoplasm containing fine and coarse vacuoles, most probably reflecting a more activated state (Figure S2A-C). After initially seeding 400,000 hiPSCs on a 12-well culture plate, 18.7 ± 2.9 million (LU83), 10.5 ± 5.2 million (LU20) and 17.2 ± 4.5 million (LU54) CD14+ monocytes respectively were harvested on day 15 (Figure 1F), resulting in a yield of 36.83 ± 10.40 monocytes generated from one hiPSC initially seeded or $15.47 \pm 4.37 \times 10^6$ (average of three lines) CD14+ monocytes from each 12-well plate. The isolated hiPSC-mono were cryopreserved for further functional assessment or differentiation into macrophages.

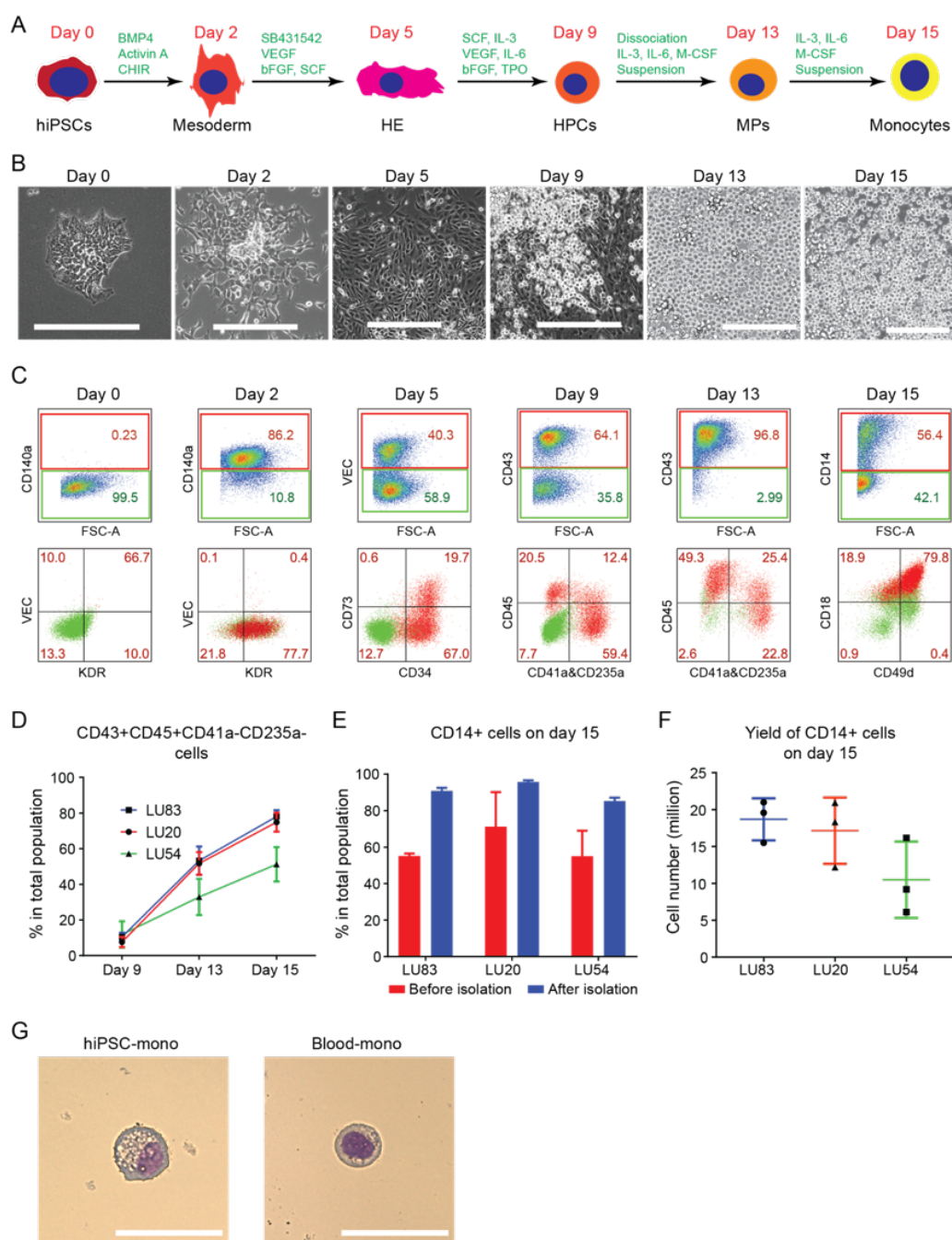


Figure 1. Differentiation of CD14+ monocytes from hiPSCs. (A) Schematic overview of CD14+ monocytes differentiation protocol from hiPSCs. (B) Bright field images of representative cellular morphology at day 0 (undifferentiated hiPSCs), day 2 (mesoderm), day 5 (HE), day 9 (HPCs), day 13 (MPs) and day 15 (CD14+ monocytes). Scale bar represents 200 μ m. (C) FACS analysis of stage-specific markers at day 0, day 2, day 5, day 9, day 13 and day 15 of differentiation from

representative hiPSC line (LU83). Positive populations are gated in upper panels and their percentages are shown in red in both upper and lower panels. (D) Quantification of percentage of myeloid lineage cells (CD43+CD45+CD41a-CD235a-) in the total cell population at day 9, day 13 and day 15 of differentiation. Quantification of three independent experiments from three hiPSC lines (LU83, LU20 and LU54) is shown. (E) Quantification of percentage of CD14+ cells at day 15 of differentiation before and after isolation using CD14+ MACS. Quantification of three independent experiments from three hiPSC lines (LU83, LU20 and LU54) is shown. (F) Yield of CD14+ monocytes at day 15 of differentiation from three hiPSC lines and three independent experiments. Yield of monocytes is equal to the total cell number multiplied by percentages of CD14+ cells. (G) Giemsa staining of hiPSC-mono isolated at day 15 of differentiation from one representative hiPSC line (LU83) and Blood-mono. Scale bar represents 50 μm . Error bars are $\pm\text{SD}$ of three independent experiments in (D-F). See also Figure S1 and Movie S1-S2.

Functional assessment of hiPSC-mono

Several cryopreserved batches of hiPSC-mono were thawed with a recovery of $43.2\pm9.9\%$, and were compared functionally with Blood-mono (Figure 2). Both cells expressed similar levels of monocyte surface markers CD14 and CD45 (Figure 2A). The monocytes were then compared functionally using a microfluidic monocyte adhesion assay to ECs we described previously (Halaidych et al., 2018) (Figure 2B). Briefly, hiPSC-mono or Blood-mono cells were inserted under flow into microfluidic chips coated with either primary human umbilical vein endothelial cells (HUVECs) or hiPSC-derived endothelial cells (hiPSC-ECs) stimulated with $\text{TNF}\alpha$. Adhesion of the monocytes to ECs was determined under flow at venous shear stress (0.5 dynes/cm^2). HUVECs expressed high levels of E-Selectin and VCAM-1 after $\text{TNF}\alpha$ treatment compared to hiPSC-ECs, although they expressed comparable levels of ICAM-1 and endothelial cell-specific markers, such as VE-cadherin, CD31 and CD105 (Figure 2F). Total number of hiPSC-mono and Blood-mono adherent to HUVECs were higher than to hiPSC-ECs, as observed previously (Halaidych et al., 2018). On the other hand, total number of hiPSC-mono adherent to ECs was higher than Blood-mono (Figure 2C-D). These differences correlated with increased expression of leukocyte integrin subunits CD49d and CD29 (VLA-4 integrin), the major ligands for the endothelial receptor VCAM-1, on hiPSC-mono compared to Blood-mono (Figure 2E).

Differentiation of macrophages from hiPSC-mono

To differentiate towards M0 macrophages (M0), cryopreserved CD14+ hiPSC-mono or CD14+ Blood-mono isolated from cryopreserved PBMCs were plated on fetal calf serum (FCS)-coated cell culture plates in the presence of M-CSF for 4 days. The M0 cells could be polarized towards M1 macrophages (M1) using LPS and $\text{IFN-}\gamma$ or M2 macrophages

(M2) using IL-4. The differentiation protocol is shown schematically in Figure 3A (Martinez and Gordon, 2014).

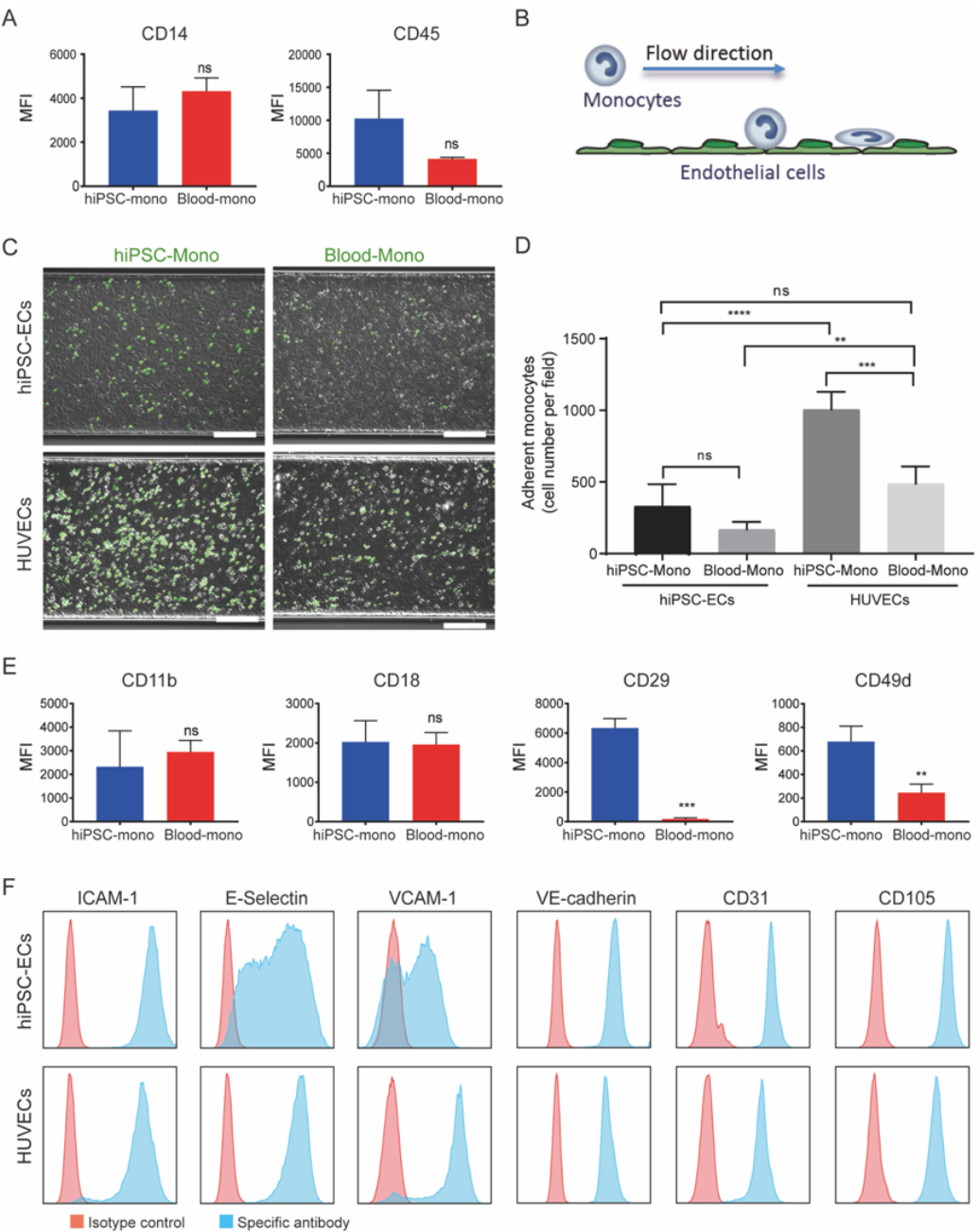


Figure 2. Functional comparison of hiPSC-mono and Blood-mono in microfluidic adhesion assay. (A) FACS analysis of surface expression of CD14 and CD45 on hiPSC-mono and Blood-mono after cryopreservation. Error bars are \pm SD of three independent experiments. Unpaired t-test. ns

= non-significant. (B) Schematic for microfluidic flow adhesion assay of monocytes and ECs. (C) Representative images taken at the end of the flow assay for each combination of ECs and monocytes. Monocytes were labelled with DiOC6 (green). Scale bar represents 200 μ m. (D) Quantification of the number of adhered monocytes: hiPSC-mono and hiPSC-ECs, Blood-mono and hiPSC-ECs, hiPSC-mono and HUVECs, Blood-mono and HUVECs. Error bars are \pm SD of four independent experiments. Uncorrected Fisher's LSD test. ns = non-significant, *** $p < 0.001$, **** $p < 0.0001$. (E) FACS analysis of surface expression of MAC-1 (CD11b and CD18) and VLA-4 (CD49d and CD29) integrin subunits on hiPSC-mono and Blood-mono. Error bars are \pm SD of three independent experiments. Unpaired t-test. ns = non-significant, ** $p < 0.01$, *** $p < 0.001$. (F) FACS analysis of ICAM-1, E-Selectin, VCAM-1, VE-Cadherin, CD31 and CD105 on hiPSC-ECs and HUVECs after TNF α treatment. Isotype control is shown in red and antigen-specific antibody is shown in blue. See also Figure S2.

Characterization of IPSDMs

Morphologically, IPSDMs were similar to PBDMs. Polarization towards M0 induced an elongated morphology. Polarization towards M1, resulted in a stellar shape with multiple protrusions and polarization towards M2, resulted in a more rounded morphology (Figure 3B-C). Oil Red O staining indicated that M0-IPSDMs and M2-IPSDMs had a higher intracellular lipid content compared to M1-IPSDMs and PBDMs (Figure 3C). FACS analysis of pan-specific macrophage surface markers CD11b, CD18 and CD45 showed comparable expression in all macrophage subtypes. IPSDMs expressed comparable level of CD11b but lower level of CD18 and CD45 compared to PBDMs. Subtype-specific macrophage markers CD80 (M1) and CD206 (M2) were highly expressed in the relevant IPSDM subsets and much like levels in PBDMs (Figure 3D, S3A-B). M0-IPSDMs and M0-PBDMs also expressed high levels of M2 macrophage markers CD206 and CD163, in agreement with previous reports (Gordon and Martinez, 2010; Vogel et al., 2014) where M0 macrophages were indicated as already showing high similarity to M2 identity (Figure 3D, S3A-B).

We next compared mRNA expression of macrophage pan-specific marker *CD68* and subset-specific markers (red text indicates M1 markers and blue text for M2 markers) in IPSDMs differentiated from three hiPSC lines to PBDMs. We also tested expression of toll-like receptors (TLRs) that are crucial for macrophage function, allowing the recognition of pathogens (Figure 3E). As expected, *CD68* was expressed by all macrophage subtypes. Expression of known pro-inflammatory cytokines and chemokines, including *IL1B*, *IL6*, *IL8*, *TNFA*, *CCL2*, *CCL5*, and *CXCL10* was the highest in the M1 subset of IPSDMs and PBDMs. Other known M1 markers, including *CD64*, *IDO1*, *NOX2*, were also highly expressed in M1-IPSDMs and M1-PBDMs. Gene expression of

M2 markers, *CD206* and *CD163*, were indeed expressed highest in M2 subsets and this matched well with surface protein levels (Figure 3D). M2-IPSDMs and M2-PBDMs subsets had the highest expression of M2 specific genes *CD200R* and *TGM2* and expressed the highest level of anti-inflammatory cytokines and chemokines, *IL1RA*, *CCL22*, and *CCL24*. TLRs, including *TLR1*, *TLR2*, *TLR4*, *TLR6* and *TLR8* were preferentially expressed by M1, in accordance with previous work (Schlaepfer et al., 2014). Overall, the genes tested were comparable between IPSDMs and PBDMs (Figure 3E).

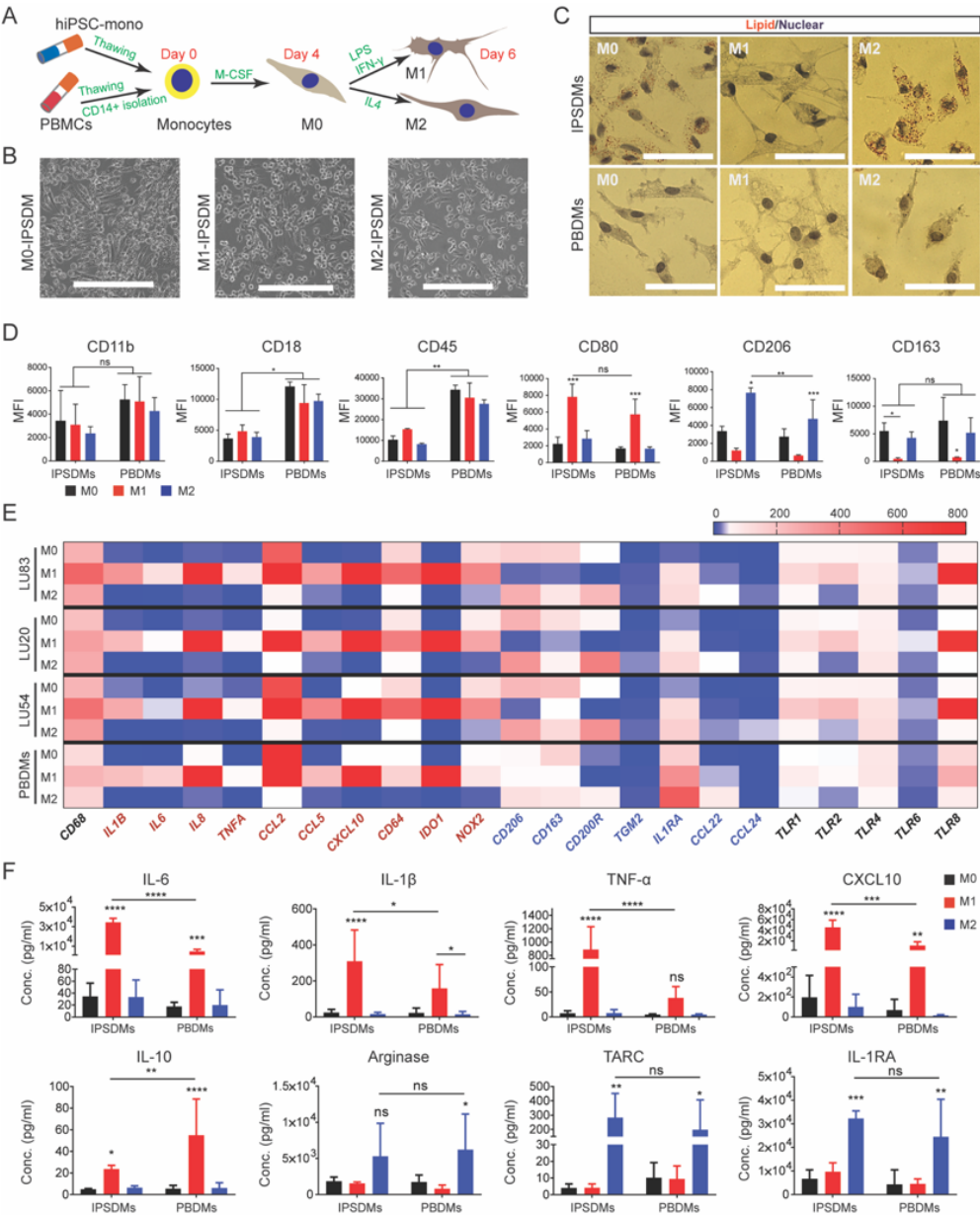


Figure 3. Characterization of IPSDMs. (A) Schematic overview of macrophage differentiation

protocol from cryopreserved hiPSC-mono and PBMCs. (B) Bright field images of representative cellular morphology of IPSDMs. Scale bar represents 200 μ m. (C) Oil red O staining of lipid (red) within M0, M1 and M2 subtypes of IPSDMs and PBDMs. Nuclei (purple) were stained with Haematoxylin. Scale bar represents 50 μ m. (D) Quantification of surface expression of pan-specific macrophage markers: CD11b, CD18 and CD45 and subtype-specific markers: CD80 (M1) and CD206 (M2) on IPSDMs (differentiated from LU83) and PBDMs. Error bars are \pm SD of three independent experiments. Uncorrected Fisher's LSD test. ns = non-significant, * $p < 0.05$, ** $p < 0.01$, *** $p < 0.001$. (E) Heatmap of gene expression analysis of macrophage specific markers by qPCR in IPSDMs differentiated from three hiPSC lines (LU83, LU20 and LU54) and PBDMs. Mean values of three independent experiments are shown. M1 specific genes are shown in red and M2 specific genes are shown in blue. (F) Quantification of secreted cytokines and chemokines by a Multiplex assay using supernatants from IPSDMs and PBDMs after 48 hours of polarization. Error bars are \pm SD of three independent experiments. Uncorrected Fisher's LSD test. ns = non-significant, * $p < 0.05$, ** $p < 0.01$, *** $p < 0.001$, **** $p < 0.0001$. # higher than the detection limit of Multiplex. See also Figure S3.

Cytokine and chemokine secretion were next examined in macrophage subtypes. The M1 subset of both IPSDMs and PBDMs secreted high levels of pro-inflammatory cytokines and chemokines, including IL-6, IL-1 β , TNF- α and CXCL10 (Figure 3F). The secretion of pro-inflammatory cytokines and chemokines were significantly higher in M1-IPSDMs than M1-PBDMs. Other pro-inflammatory cytokines and chemokines, including CCL2, IL-8 and IL-18, were also highly secreted by M1 subset derived from different hiPSC lines and PBMC donors (Figure S3C). Notably, an anti-inflammatory cytokine, IL-10 was highly secreted by M1-IPSDMs and M1-PBDMs, in accordance with previous finding (de Waal Malefyt et al., 1991; Murthy et al., 2000; Stanley et al., 2012). The M2 subset of both IPSDMs and PBDMs secreted high levels of anti-inflammatory cytokines and enzymes such as TARC, IL-1RA and Arginase (Figure 3F).

Functional characterization of IPSDMs

We next assessed the endocytic activity of IPSDMs using Dil-AcLDL uptake. All IPSDM subtypes had the ability to ingest Dil-AcLDL. M1-IPSDMs showed significantly lower Dil-AcLDL uptake compared to M0-IPSDMs and M2-IPSDMs (Figure 4A-B). Moreover, compared to PBDMs, IPSDMs showed higher uptake of Dil-AcLDL (Figure 4A-B).

Next, we compared the ability of the IPSDM to phagocytose bacteria. GFP labelled *E. coli* were incubated with IPSDMs and PBDMs and their phagocytic efficiency was

measured by FACS. M0-IPSDMs and M2-IPSDMs had the highest phagocytic activity compared to the pro-inflammatory M1-IPSDMs (Figure 4C-D). Furthermore, CD163, a crucial scavenger receptor mediating bacterial phagocytosis of macrophages, was mainly expressed by M0 and M2 macrophages and absent on M1, as shown in Figures 3D-E, S3A-B. There was no significant difference between IPSDMs and PBDMs (Figure 4C-D).

Assessment of efferocytosis activity of IPSDM

To determine whether IPSDMs can ingest apoptotic cells *in vitro*, we performed an efferocytosis assay. Apoptotic cells were obtained by exposing hiPSCs to UV-radiation (35J/cm²). More than half of the UV-treated cells became early apoptotic (Annexin V+PI-) with only 16.5% of the cells becoming necrotic (Annexin V+PI+) (Figure S4). CFSE-labelled apoptotic cells were then incubated with M0-IPSDMs and M0-PBDMs and their efferocytosis efficiency was measured by FACS. Both M0-IPSDMs and M0-PBDMs showed higher efficiencies apoptotic cell uptake than live cells without UV-radiation. M0-IPSDMs showed higher efferocytosis activity than M0-PBDMs (Figure 5A-B). Receptors which mediate the “find-me” or “eat-me” signals for efferocytosis, such as *CX3CR1*, *S1PR1*, *CD36* and *MERTK* were expressed at higher levels in M0-IPSDMs than M0-PBDMs (Figure 5C). Both M0- and M2- IPSDMs and PBDMs showed high efferocytosis capability whereas M1-IPSDMs and M1-PBDMs showed poor efferocytosis (Figure 5D-E). This was confirmed across three independent hiPSC lines (Figure 5E).

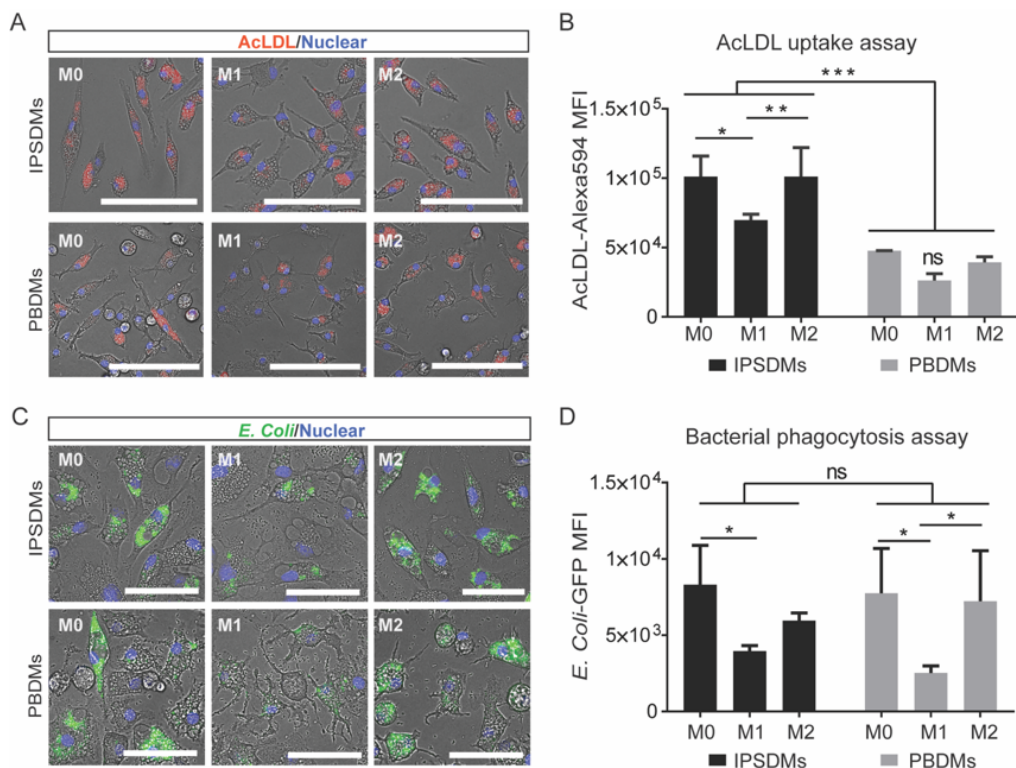


Figure 4. Endocytosis and phagocytosis of bacteria by IPSDMs and PBDMs. (A) Representative images of AcLDL-Alexa Fluor594 uptake assay by different subtypes of IPSDMs and PBDMs. AcLDL positive uptake is shown in red, cell nuclei are stained with Hoechst in blue. Scale bar represents 100 μ m. (B) Quantification of AcLDL-Alexa Fluor594 median fluorescence intensity of different macrophage subtypes by FACS. Error bars are \pm SD of three independent experiments. Uncorrected Fisher's LSD test: ns = non-significant, * p < 0.05, ** p < 0.01, *** p < 0.001. (C) Representative images of bacterial phagocytosis by different subtypes IPSDMs and PBDMs. Nuclei were stained with Hoechst in blue. GFP labelled (pHrodoTM Green) *E.coli* were pH sensitive and only show green fluorescence inside macrophages. Scale bar represents 100 μ m. (D) Quantification of *E.coli*-GFP median fluorescence intensities in macrophage subtypes by FACS. Error bars are \pm SD of three independent experiments. Uncorrected Fisher's LSD test: ns = non-significant, * p < 0.05. IPSDMs were differentiated from LU83 in (A-D).

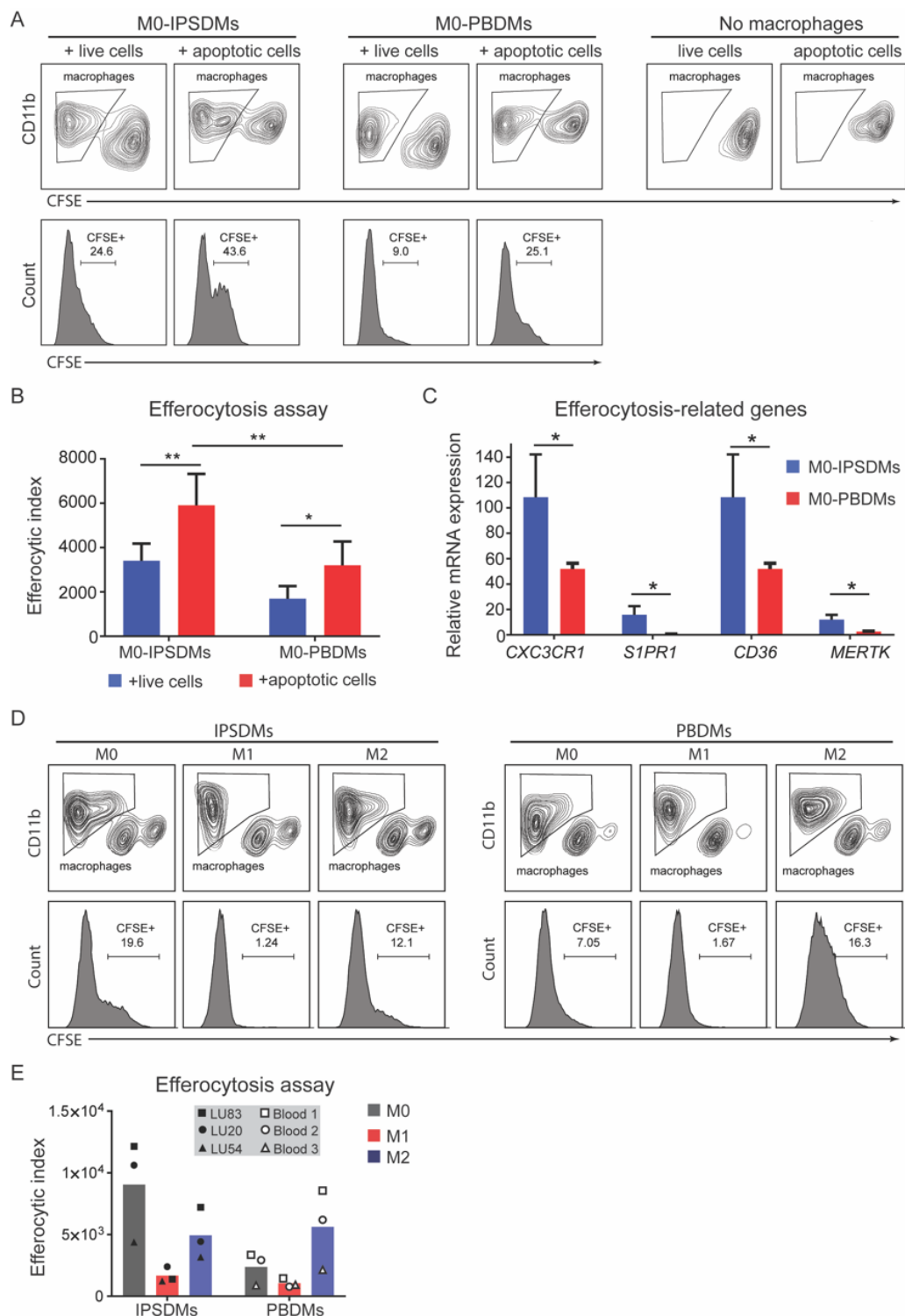


Figure 5. Characterization of efferocytosis activity of IPSDMs and PBDMs. (A) Efferocytosis assay of M0-IPSDMs and M0-PBDMs. Live cells (used as a negative control) and apoptotic cells were labelled with CFSE and macrophages were stained by anti-CD11b antibody. Histogram plot

of CFSE (lower panel) within CD11b+ population (upper panel) are shown. (B) Efferocytic index of M0-IPSDMs and M0-PBDMs. Percentage of CFSE+ macrophages was multiplied by MFI of CFSE in order to calculate the efferocytic index. Error bars are \pm SD of four independent experiments. Uncorrected Fisher's LSD test: * $p < 0.05$, ** $p < 0.01$. (C) Quantification of gene expression of efferocytosis-related genes *CX3CR1*, *S1PR1*, *CD36* and *MERTK* by qPCR in M0-IPSDMs and M0-PBDMs. Unpaired t-test: * $p < 0.05$. (D) Efferocytosis assay of different subtypes of IPSDMs and PBDMs. Live cells (used as a negative control) and apoptotic cells were labelled with CFSE and macrophages were stained by anti-CD11b antibody. Histogram plot of CFSE (lower panel) within CD11b+ population (upper panel) are shown. (E) Efferocytic index of different subtypes of IPSDMs and PBDMs. Percentage of CFSE+ macrophages was multiplied by MFI of CFSE in order to calculate the efferocytic index. Data are presented as mean of three biological replicates (three hiPSC lines or PBMC samples). IPSDMs were differentiated from LU83 in (A-D). See also Figure S4.

Assessment of tumour cell phagocytotic activity of IPSDMs

Previous studies demonstrated that macrophages show high infiltration in tumours; their ability to phagocytose tumour cells is currently being explored in cancer immunotherapy (Gul and van Egmond, 2015). CD47 overexpression on cancer cells often enables them to escape phagocytosis via the interaction with CD172a receptor on macrophages. This has led to the use of CD47 blocking antibody in multiple clinical trials to advance of cancer therapy (Chao et al., 2012; Weiskopf and Weissman, 2015). Here we compared the tumour cell phagocytosis ability of IPSDMs and PBDMs in the presence of a blocking CD47 antibody. Immortalized T-cell lymphoma cells (Jurkat) were used as target tumour cells as they express high levels of CD47 (Figure 6A). M0-IPSDMs and M0-PBDMs expressed high and comparable levels of CD172a (Figure 6B). Pre-incubation with anti-CD47 antibody, significantly increased engulfment of tumour cells by both IPSDMs (57.8%) and PBDMs (54.0%), compared to controls without CD47 blocking antibody (16.2% and 10.7%) (Figure 6C-D, Movie S3 and data not shown). The phagocytic index (the product of CFSE MFI and percentage of CFSE+ macrophages) of IPSDMs and PBDMs increased around 5-fold and 7-fold respectively due to the CD47 block (Figure 6E). M0-IPSDMs showed similar tumour phagocytosis activity compared to M0-PBDMs in the presence of CD47-blocking antibody (Figure 6D-E). Tumour phagocytosis activity in the presence of anti-CD47 was next determined on M0-, M1- and M2-IPSDMs and we show that M0 and M2-IPSDMs had the highest tumour phagocytosis activity (Figure S5A-B).

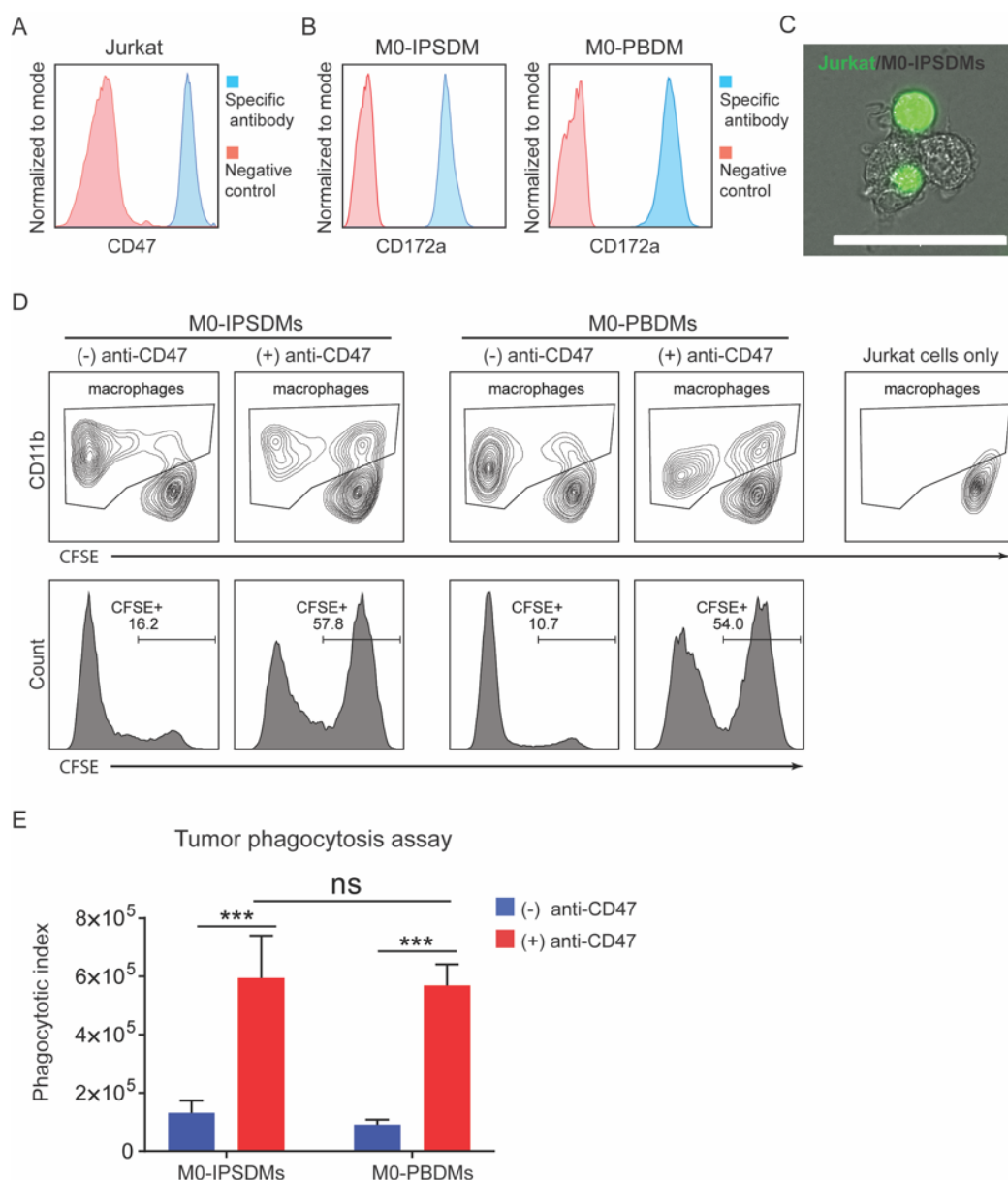


Figure 6. Phagocytosis of tumour cells by IPSDMs and PBDMs. (A) FACS analysis of CD47 on Jurkat cells. Secondary antibody only was used as a negative control. (B) FACS analysis of CD172a on M0-IPSDMs and M0-PBDMs. Non-stained cells were used as negative control. (C) A representative image of Jurkat cells (labelled with green fluorescent dye) phagocytized by M0-IPSDMs (phase contrast image). Scale bar represents 50 μ m. CFSE labelled Jurkat cells were incubated with anti-CD47 blocking antibody and co-cultured with M0-IPSDMs for 30 min. (D) FACS analysis of Jurkat cell phagocytosis by M0-IPSDMs and M0-PBDMs. CFSE-labelled Jurkat cells were incubated with or without anti-CD47 blocking antibody and added to macrophages for 2h. CD11b⁺ macrophages are gated (upper panel) and their CFSE intensity are shown as

histogram (lower panel). (E) Phagocytotic index of M0-IPSDMs and M0-PBDMs with and without CD47 blocking antibody. Percentage of CFSE+ macrophages was multiplied by MFI of CFSE to get phagocytotic index. Error bars are \pm SD of four independent experiments. Uncorrected Fisher's LSD test: ns = non-significant, *** $p < 0.001$. M0-IPSDMs were differentiated from LU83 in (B-E). See also Figure S5 and Movie S3.

DISCUSSION

PB-derived monocytes and macrophages have been widely used to study many diseases and tissue homeostasis. Recent studies, however, demonstrated that tissue-resident macrophages in mouse originate from yolk sac-derived EMPs that are different from PB or bone marrow-derived macrophages that originate from HSCs. hPSCs could be efficiently differentiated towards EMP-like cells that are reminiscent of yolk sac-derived EMPs found in mouse, and represent MYB and HOXA independent lineages (Buchrieser et al., 2017; Dou et al., 2016; Ivanovs et al., 2017; Ng et al., 2016; Vanhee et al., 2015). Therefore, hPSC-derived monocytes and macrophages could be potentially a useful source of patient-specific cells that otherwise are difficult or impossible to derive. hPSC-derived monocytes and macrophages, therefore, can be used to study tissue, organ and tumour-specific macrophages inaccessible through regular biopsies.

Here we describe an efficient protocol that was robust over three independent hiPSC lines: derivative monocytes and macrophage subtypes were obtained with comparable differentiation efficiencies and functional properties. hiPSCs were first directed to generate mesoderm with high efficiency, then to form HE and HPCs from which monocyte-like cells could be derived after 15 days. Similarly, to previous studies, present protocol likely resembles yolk sac-derived EMPs, although, we have not thoroughly investigated HOXA expression or MYB-dependence. Magnetic bead-based purification of CD14+ cells allowed efficient enrichment to a >90% pure cell population which could be cryopreserved, with post-thaw recovery rate of 30-50%. The additional magnetic bead-based purification step is the principle drawback of our protocol here to previously published protocols that involve continuous harvesting of macrophages (Ackermann et al., 2018; Buchrieser et al., 2017; Lachmann et al., 2015; van Wilgenburg et al., 2013; Zhang et al., 2015), and could limit scalability of the protocol. Continuous harvesting protocols have clear advantages when large numbers of cells are needed, for example for transplantation studies. However, for disease modelling applications a shorter protocol that allows cryopreservation of independent cell batches can have its own advantages. We found that the cell batches produced using our protocol are functionally indistinguishable, demonstrating the reproducibility of the production process as such.

Functional comparison with Blood-mono showed that hiPSC-mono apparently represent a more activated state, with cytoplasm containing fine and coarse vacuoles,

greater aggregation in suspension culture and increased surface expression of $\alpha 4\beta 1$ integrin (VLA-4 or CD49dCD29). The activated phenotype of hiPSC-mono might either be due to prolonged culture or to differences in developmental origin. Using an *in vitro* model of inflammation in a microfluidic device, we found that the hiPSC-mono could roll and adhere to ECs much like primary Blood-mono. The hiPSC-mono could adhere to both HUVECs and hiPSC-ECs. The hiPSC-mono showed higher adherence to ECs than Blood-mono due to their higher surface expression of integrins CD49b and CD29, which gives them a greater affinity for EC surface receptors.

These hiPSC-mono could be differentiated towards macrophage lineages; the M0-IPSDMs could be polarized to form pro-inflammatory M1-IPSDMs or anti-inflammatory M2-IPSDMs. We confirmed the IPSDMs phenotype through their morphology, surface markers, mRNA expression, cytokine secretion and responses in functional assays compared with PBDMs. M0-IPSDMs, M1-IPSDMs and M2-IPSDMs all acquired typical morphologies and marker expression of the respective PBDM subtypes, as demonstrated previously using either fully defined, or serum-based protocols (van Wilgenburg et al., 2013; Zhang et al., 2015). Importantly, M1-IPSDMs acquired a pro-inflammatory phenotype, and conversely, M0-IPSDMs and M2-IPSDMs showed an anti-inflammatory phenotype, bases on secreted and surface markers, and gene expression profiles. However, the endocytic activity of IPSDMs, determined by their ability to uptake acetylated low-density lipoprotein (AcLDL), was higher and the ability to phagocytose apoptotic cells (or efferocytosis) was more efficient than PBDMs, much as demonstrated previously for tissue-resident macrophages (A-Gonzalez et al., 2017; Roberts et al., 2017). This has great potential for their use in the study of diseases such as autoimmune or cardiovascular diseases in which this mechanism is impaired.

Increasing evidence has brought macrophages to the fore in tumour immunotherapy.

Like PBDMs, the IPSDMs here also expressed high levels of signal regulatory protein α (SIRP α , CD172a), the receptor for the “don’t eat me” signal, CD47, which is highly expressed on tumour cells (Chao et al., 2012; Weiskopf and Weissman, 2015). We demonstrated that blocking CD172a-CD47 signalling in IPSDMs and PBDMs comparably increased tumour cell phagocytosis. This indicates that IPSDMs could be an alternative to PBDMs in developing new cancer immunotherapies

In summary, we developed a highly robust protocol to derive monocytes from hiPSCs which could be cryopreserved, or differentiated towards M0-IPSDMs. These M0-IPSDMs could be further polarized to pro-inflammatory M1-IPSDMs and anti-inflammatory M2-IPSDMs. Again, these IPSDMs were phenotypically similar to PBDMs. The short differentiation time combined with serum-free media, autologous source, high cell output and reproducibility makes IPSDMs derived using the protocol here an attractive cell source for disease modelling and provide a more consistent and reliable

reference for downstream *in vivo* clinical trials.

EXPERIMENTAL PROCEDURES

hiPSC lines and maintenance

The following hiPSC lines were used in the present study: LUMC0020 (LU20, generated from skin fibroblasts) (Zhang et al., 2014); LUMC0054 (LU54, generated from kidney epithelial cells isolated from urine, <http://hpscereg.eu/cell-line/LUMCi001-A>) (Halaidych et al., 2018); LUMC0083 (LU83, from PB erythroblasts). hiPSCs were cultured in recombinant vitronectin (VN)-coated plates in TeSR-E8 all from STEMCELL Technologies (SCT) according to the manufacturer's instructions.

Differentiation of myeloid cells from hiPSCs

hiPSCs were maintained in mTeSR-E8 to reach 80% confluence. On day -1, hiPSCs were dissociated with Gentle Cell Dissociation Reagent (STEMCELL Technologies) for 5 min at room temperature to obtain small cell clumps. The cells were then seeded into Matrigel coated plates (75 µg/mL) at a density of ~10000 cell/cm² (1:30 split ratio). Cells were cultured in TeSR-E8 for 24 hours and switched to IF9S medium (Table S1), modified from (Uenishi et al., 2014), supplemented with 50 ng/mL BMP4 (R&D Systems), 15 ng/mL ACTIVIN A (Miltenyi Biotec) and 1.5 µM CHIR99021 (Axon Medchem) for the first two days (day 0 to day 2). On day 2, cells were refreshed with IF9S supplemented with 50 ng/ml VEGF (R&D Systems), 50 ng/ml bFGF (PeproTech), 50 ng/ml SCF (Miltenyi Biotec) and 10 µM SB431542 (Tocris Bioscience). On day 5 and day 7, cells were refreshed with IF9S supplemented with 50 ng/ml VEGF, 50 ng/ml bFGF, 50 ng/ml SCF, 50 ng/ml IL-6 (Miltenyi Biotec), 50 ng/ml TPO (Miltenyi Biotec) and 10 ng/ml IL-3 (Miltenyi Biotec). On day 9, floating cells were collected and adherent cells were dissociated with TrypLE (Life Technologies) for 10 minutes at 37°C. Then floating and adherent cell were combined and resuspended in IF9S medium supplemented with 50 ng/ml IL-6, 10 ng/ml IL-3 and 80 ng/ml M-CSF (Miltenyi Biotec). Cells collected from one 12 well plate were plated into one 24 well ultra-low attachment plate (CORNING). Medium was refreshed on day 13 and day 15 with IF9S medium containing 50 ng/ml IL-6, 10 ng/ml IL-3 and 80 ng/ml M-CSF. Cells were cultured at 37°C, 5% CO₂, normoxia conditions throughout the whole differentiation.

Isolation of CD14+ myeloid cells

On day 15 of differentiation, all cells in suspension were collected and washed once with FACS buffer (PBS, 0.5% BSA, 2 mM EDTA). Then, CD14+ cells were isolated using CD14 MicroBeads (Miltenyi Biotec) following the manufacturer's instructions. 60 µL Microbeads were used for 1X10⁷ of total cells. Isolated CD14+ cells were cryopreserved

in CryoStor CS10 medium (Stem Cell Technologies) or further differentiated into macrophages.

To isolate human blood monocytes, peripheral blood mononuclear cells (PBMCs) were first isolated using Ficoll-Paque™ PLUS (GE Healthcare) from healthy donors' blood. PBMCs were cryopreserved in CryoStor CS10 medium at a density of 20 million/ml. CD14⁺ monocytes were isolated from cryopreserved PBMCs using CD14 MicroBeads following the manufacturer's instructions.

Cryopreservation of hiPSC-mono

Isolated hiPSC-mono were centrifuged and suspended in CryoStor® CS10 cryopreservation medium at a concentration of 3.75×10^6 cells/ml, keeping the cell suspension on ice; 400 µl were aliquoted into each cryovial (1.5×10^6 cells per vial). Cryovials were next placed in prechilled Mr. Frosty™ Freezing Container and left at -80°C for 24 h, then transferred to liquid N₂ for prolonged storage. To thaw hiPSC-mono, cryovials were removed from liquid nitrogen and thawed in a water bath at 37°C. hiPSC-mono were next transferred into 15 ml tubes containing 10 ml of prewarmed IF9S medium. Cells were centrifuged at 1100 rpm (300 g) for 3 min and suspended in IF9S medium supplemented with 80 ng/ml M-CSF. Cells were finally plated in FCS-coated cell culture plates and placed in the cell culture incubator for 48 hours without disturbance.

Differentiation of macrophage subtypes

hiPSC-derived CD14⁺ cells or blood monocytes were plated on FCS-coated tissue culture plates at a density of 40,000 cells/cm² in IF9S medium supplemented with 80 ng/ml M-CSF. After 4 days of culture, all monocytes differentiated into macrophages (M0) with more than 90% confluency. M0 macrophages were then polarized to M1 or M2 macrophages for 48 hours in IF9S medium supplemented with different stimulus: 100 ng/ml LPS (SIGMA) and 20 ng/ml IFN-γ (Miltenyi Biotec) for M1; 20ng/ml IL4 (Miltenyi Biotec) for M2.

CFU assay

Hematopoietic CFU assay was performed using serum-free MethoCult™ SF H4636 (Stem Cell Technologies) following manufacturer's instructions.

Giemsa staining

Monocytes were immobilized on microscope slide using Cytospin, followed by the staining using Wright-Giemsa Stain (Sigma Aldrich) according to the manufacturer's instructions.

Differentiation of ECs from hiPSCs

hiPSCs were maintained in mTeSR-E8 and differentiated towards ECs using previously published protocols (Orlova et al., 2014a; Orlova et al., 2014b).

Microfluidic flow assay

Microfluidic flow assay was performed as previously described (Halaidych et al., 2018). Briefly, Vena8 Endothelia+ chips (Cellix) were coated with 50 µg/mL fibronectin overnight at 4°C. ECs were first treated with 10 ng/ml BMP9 (R&D) for 24 hours, then stimulated with TNFα (10 ng/ml) for 12 hours (overnight) in the presence of BMP9. Next day, ECs were collected and injected into the microfluidic channel. Then the chip was incubated at 37°C to facilitate cell attachment. Monocytes were collected and stained with DiOC6 (1:5000) (Sigma), then re-suspended in IF9S medium at the end concentration of 2.5×10^6 cells/ml. For flow experiment, monocytes were perfused for 5 minutes at 0.5 dyne/cm² through the microfluidic channel, followed by a 5 minutes wash with IF9S medium. The number of adherent fluorescently labelled monocytes on ECs was quantified using the open source software CellProfiler (Carpenter et al., 2006).

Oil red O staining

Macrophages were washed twice with DPBS and fixed with 4% PFA for 15 minutes. Then cells were washed 3 times with DPBS and stained with fresh Oil red O solution for 10 minutes followed by a wash with 75% ethanol for 15 seconds. After that cells were stained with Haematoxylin for 2 minutes and washed three times with DPBS.

Flow cytometry analysis

Cells were washed once with FACS buffer and stained with antibodies for 30 minutes at 4°C. Samples were washed once with FACS buffer and analyzed on MACSQuant VYB (Miltenyi Biotec). Results were analyzed using FlowJo v10 (FlowJo, LLC). Fluorochrome conjugated human antibodies are listed in Table S2. FACS analysis of CD47 was done using anti-CD47 antibody (BIO-RAD, MCA911, 1:25) and Alexa 488 conjugated donkey anti-mouse secondary antibody (ThermoFisher Scientific). Propidium Iodide Solution (Miltenyi Biotec, 130-093-233, 1:100) was also used in specific flow cytometry analysis.

Quantitative real-time polymerase chain reaction (qRT-PCR)

RNA was extracted from monocytes and macrophages using the NucleoSpin® RNA kit (Macherey-Nagel). cDNA was synthesized using iScript-cDNA Synthesis kit (Bio-Rad). iTaq Universal SYBR Green Supermixes (Bio-Rad) and Bio-Rad CFX384 real time system were used for the PCR reaction and detection. Primers used are listed in Table S3. Relative gene expression was determined according to the standard delta Ct calculation and normalized to housekeeping genes (mean of hARP and RPL37A).

Multiplex cytokine analysis

M0 macrophages were cultured in IF9S medium supplemented with 80 ng/ml M-CSF until reaching more than 90% confluence. Then cells were polarized toward different subtypes of macrophages in IF9S medium containing different stimuli indicated earlier. Cell culture supernatants were collected after 48 hours of polarization. Concentration of cytokines were measured using LEGENDplex™ Human Inflammation Panel kit and Human Macrophage/Microglia Panel kit (BioLengend) according to manufacturer's instructions.

AcLDL uptake and bacterial phagocytosis assay

M0 macrophages were dissociated and plated into 96 well plate (CORNING) at a density of 50,000 cells/well in IF9S medium supplemented with 80 ng/ml M-CSF. After reaching more than 90% confluence, cells were polarized towards M0, M1 and M2 in IF9S medium for 12 hours. Then cells were used for the AcLDL uptake or bacterial phagocytosis assay. Alexa Fluor™ 594 AcLDL (ThermoFisher Scientific) was used for AcLDL uptake assay following manufacturer's instructions. Bacterial phagocytosis assay was done with pHrodo™ Green *E. coli* BioParticles® Conjugate (Life Technologies) following manufacturer's instructions. Finally, macrophages were dissociated with accutase (Promocell) and fluorescence intensities of the macrophages were measured by FACS using MACSQuant VYB.

Efferocytosis assay

M0 macrophages were dissociated and plated into 96 well plates at a density of 50,000 cells/well in IF9S medium supplemented with 80 ng/ml M-CSF. After reaching more than 90% confluence, cells were polarized towards M0, M1 and M2 in IF9S medium for 48 hours. Then cells were ready for the efferocytosis assay. To obtain apoptotic cells, hiPSCs were dissociated and stained with 5 μ M CFSE (ThermoFisher Scientific) and exposed to 35 J/cm² UV light for 5 minutes, then retained in medium for 90 minutes at 37°C. 2X10⁵ apoptotic cells were added to each well of macrophages and incubated for 90 minutes at 37°C. Then each well was washed once with IF9S medium to remove apoptotic cells that had not been phagocytosed. Then macrophages were dissociated with accutase (Promocell) and stained with CD11b antibody. Fluorescence intensity of CFSE in macrophages was measured by FACS. Percentages of CFSE+ cells within the CD11b+ population were multiplied by the number of CFSE MFI to calculate the efferocytic index.

Tumour phagocytosis assay

M0 macrophages were plated into 96 well plates at a density of 50,000 cells/well and cultured in IF9S medium supplemented with 80 ng/ml M-CSF to reach more than 90% confluence. Jurkat tumour cells (kindly provided by Dr. Luuk Hawinkels, LUMC) were

stained with CFSE and pre-incubated with 2 µg/ml anti-CD47 (BIO-RAD, MCA911) for 30 minutes. 2X10⁵ Jurkat cells were then added to each well of macrophages and incubated for 2 hours at 37°C. Then each well was washed once with IF9S medium and macrophages were dissociated with accutase and stained with CD11b antibody. Fluorescence intensity of CFSE in macrophages was measured by FACS. Percentage of CFSE+ cells within CD11b+ population was multiplied by the CFSE MFI to obtain the phagocytic index.

Statistical analysis

Statistical analysis was conducted with GraphPad Prism 7 software. Two-way ANOVA with Uncorrected Fisher's LSD test was applied for the analysis of two independent variables. Comparison between two samples was done with unpaired t-test. More details are described in figure legends. Error bars are shown as mean ±SD. ns = non-significant, *p < 0.05, **p < 0.01, ***p < 0.001, ****p < 0.0001.

AUTHOR CONTRIBUTIONS

X.C. and **G.Y.** designed and performed research, analysed and interpreted results and wrote the manuscript, **F.E.vdH** performed real-time PCRs, **A.C.** analysed and interpreted results and wrote the manuscript, **C.L.M.** designed the research and edited the manuscript, **V.V.O.** designed the research, analysed and interpreted results and wrote the manuscript.

ACKNOWLEDGMENTS

We would like to thank Andreea Ioan-Facsinay, Joanneke Kwekkeboom and Hetty de Boer for cryopreserved PBMCs and help with primary human peripheral blood sample collection (LUMC), Christian Freund and the LUMC iPSC Hotel for providing hiPSC lines, the LUMC Flow Cytometry Core Facility and the LUMC Light and Electron Microscopy Facility.

This project received funding from the European Union's Horizon 2020 Framework Programme (668724); Netherlands Organ-on-Chip Initiative, an NWO Gravitation project funded by the Ministry of Education, Culture and Science of the government of the Netherlands (024.003.001); the European Union's Horizon 2020 and innovation programme under the Marie Skłodowska-Curie grant agreement No 707404.

CONFLICT OF INTERESTS

The authors have no conflicts of interests to declare.

REFERENCES

- A-Gonzalez, N., Quintana, J.A., Garcia-Silva, S., Mazariegos, M., Gonzalez de la Aleja, A., Nicolas-Avila, J.A., Walter, W., Adrover, J.M., Crainiciuc, G., Kuchroo, V.K., *et al.* (2017). Phagocytosis imprints heterogeneity in tissue-resident macrophages. *J Exp Med* 214, 1281-1296.
- Ackermann, M., Kempf, H., Hetzel, M., Hesse, C., Hashtchin, A.R., Brinkert, K., Schott, J.W., Haake, K., Kuhnel, M.P., Glage, S., *et al.* (2018). Bioreactor-based mass production of human iPSC-derived macrophages enables immunotherapies against bacterial airway infections. *Nat Commun* 9, 5088.
- Buchrieser, J., James, W., and Moore, M.D. (2017). Human Induced Pluripotent Stem Cell-Derived Macrophages Share Ontogeny with MYB-Independent Tissue-Resident Macrophages. *Stem Cell Reports* 8, 334-345.
- Carpenter, A.E., Jones, T.R., Lamprecht, M.R., Clarke, C., Kang, I.H., Friman, O., Guertin, D.A., Chang, J.H., Lindquist, R.A., Moffat, J., *et al.* (2006). CellProfiler: image analysis software for identifying and quantifying cell phenotypes. *Genome Biol* 7, R100.
- Chao, M.P., Weissman, I.L., and Majeti, R. (2012). The CD47-SIRPalpha pathway in cancer immune evasion and potential therapeutic implications. *Curr Opin Immunol* 24, 225-232.
- Choi, K.D., Vodyanik, M.A., and Slukvin, I. (2009). Generation of mature human myelomonocytic cells through expansion and differentiation of pluripotent stem cell-derived lin-CD34+CD43+CD45+ progenitors. *J Clin Invest* 119, 2818-2829.
- Choi, K.D., Vodyanik, M.A., Togarrati, P.P., Suknutha, K., Kumar, A., Samarjeet, F., Probasco, M.D., Tian, S., Stewart, R., Thomson, J.A., *et al.* (2012). Identification of the hemogenic endothelial progenitor and its direct precursor in human pluripotent stem cell differentiation cultures. *Cell Rep* 2, 553-567.
- de Waal Malefyt, R., Abrams, J., Bennett, B., Figdor, C.G., and de Vries, J.E. (1991). Interleukin 10(IL-10) inhibits cytokine synthesis by human monocytes: an autoregulatory role of IL-10 produced by monocytes. *J Exp Med* 174, 1209-1220.
- Dou, D.R., Calvanese, V., Sierra, M.I., Nguyen, A.T., Minasian, A., Saarikoski, P., Sasidharan, R., Ramirez, C.M., Zack, J.A., Crooks, G.M., *et al.* (2016). Medial HOXA genes demarcate haematopoietic stem cell fate during human development. *Nat Cell Biol* 18, 595-606.
- Ginhoux, F., and Jung, S. (2014). Monocytes and macrophages: developmental pathways and tissue homeostasis. *Nat Rev Immunol* 14, 392-404.
- Gordon, S., and Martinez, F.O. (2010). Alternative activation of macrophages: mechanism and functions. *Immunity* 32, 593-604.
- Gul, N., and van Egmond, M. (2015). Antibody-Dependent Phagocytosis of Tumor Cells by Macrophages: A Potent Effector Mechanism of Monoclonal Antibody Therapy of Cancer. *Cancer Res* 75, 5008-5013.

- Halaidych, O.V., Freund, C., van den Hil, F., Salvatori, D.C.F., Riminucci, M., Mummery, C.L., and Orlova, V.V. (2018). Inflammatory Responses and Barrier Function of Endothelial Cells Derived from Human Induced Pluripotent Stem Cells. *Stem Cell Reports* 10, 1642-1656.
- Happle, C., Lachmann, N., Ackermann, M., Mirenska, A., Gohring, G., Thomay, K., Mucci, A., Hetzel, M., Glomb, T., Suzuki, T., *et al.* (2018). Pulmonary Transplantation of Human Induced Pluripotent Stem Cell-derived Macrophages Ameliorates Pulmonary Alveolar Proteinosis. *Am J Respir Crit Care Med* 198, 350-360.
- Ivanovs, A., Rybtsov, S., Ng, E.S., Stanley, E.G., Elefanty, A.G., and Medvinsky, A. (2017). Human haematopoietic stem cell development: from the embryo to the dish. *Development* 144, 2323-2337.
- Karlsson, K.R., Cowley, S., Martinez, F.O., Shaw, M., Minger, S.L., and James, W. (2008). Homogeneous monocytes and macrophages from human embryonic stem cells following coculture-free differentiation in M-CSF and IL-3. *Exp Hematol* 36, 1167-1175.
- Lachmann, N., Ackermann, M., Frenzel, E., Liebhaber, S., Brenig, S., Happle, C., Hoffmann, D., Klimenkova, O., Luttge, D., Buchegger, T., *et al.* (2015). Large-scale hematopoietic differentiation of human induced pluripotent stem cells provides granulocytes or macrophages for cell replacement therapies. *Stem Cell Reports* 4, 282-296.
- Lang, J., Cheng, Y., Rolfe, A., Hammack, C., Vera, D., Kyle, K., Wang, J., Meissner, T.B., Ren, Y., Cowan, C., *et al.* (2018). An hPSC-Derived Tissue-Resident Macrophage Model Reveals Differential Responses of Macrophages to ZIKV and DENV Infection. *Stem Cell Reports* 11, 348-362.
- Lee, C.Z.W., Kozaki, T., and Ginhoux, F. (2018). Studying tissue macrophages in vitro: are iPSC-derived cells the answer? *Nat Rev Immunol* 18, 716-725.
- Martinez, F.O., and Gordon, S. (2014). The M1 and M2 paradigm of macrophage activation: time for reassessment. *F1000Prime Rep* 6, 13.
- Murthy, P.K., Dennis, V.A., Lasater, B.L., and Philipp, M.T. (2000). Interleukin-10 modulates proinflammatory cytokines in the human monocytic cell line THP-1 stimulated with *Borrelia burgdorferi* lipoproteins. *Infect Immun* 68, 6663-6669.
- Ng, E.S., Azzola, L., Bruveris, F.F., Calvanese, V., Phipson, B., Vlahos, K., Hirst, C., Jokubaitis, V.J., Yu, Q.C., Maksimovic, J., *et al.* (2016). Differentiation of human embryonic stem cells to HOXA(+) hemogenic vasculature that resembles the aorta-gonad-mesonephros. *Nat Biotechnol* 34, 1168-1179.
- Orlova, V.V., Drabsch, Y., Freund, C., Petrus-Reurer, S., van den Hil, F.E., Muenthaisong, S., Dijke, P.T., and Mummery, C.L. (2014a). Functionality of endothelial cells and pericytes from human pluripotent stem cells demonstrated in cultured vascular plexus and zebrafish xenografts. *Arterioscler Thromb Vasc Biol* 34, 177-186.
- Orlova, V.V., van den Hil, F.E., Petrus-Reurer, S., Drabsch, Y., Ten Dijke, P., and Mummery, C.L. (2014b). Generation, expansion and functional analysis of endothelial cells and pericytes derived from human pluripotent stem cells. *Nat Protoc* 9, 1514-1531.

- Roberts, A.W., Lee, B.L., Deguine, J., John, S., Shlomchik, M.J., and Barton, G.M. (2017). Tissue-Resident Macrophages Are Locally Programmed for Silent Clearance of Apoptotic Cells. *Immunity* 47, 913-927 e916.
- Schlaepfer, E., Rochat, M.A., Duo, L., and Speck, R.F. (2014). Triggering TLR2, -3, -4, -5, and -8 reinforces the restrictive nature of M1- and M2-polarized macrophages to HIV. *J Virol* 88, 9769-9781.
- Schwartz, M.P., Hou, Z., Propson, N.E., Zhang, J., Engstrom, C.J., Santos Costa, V., Jiang, P., Nguyen, B.K., Bolin, J.M., Daly, W., *et al.* (2015). Human pluripotent stem cell-derived neural constructs for predicting neural toxicity. *Proc Natl Acad Sci U S A* 112, 12516-12521.
- Stanley, A.C., Lieu, Z.Z., Wall, A.A., Venturato, J., Khromykh, T., Hamilton, N.A., Gleeson, P.A., and Stow, J.L. (2012). Recycling endosome-dependent and -independent mechanisms for IL-10 secretion in LPS-activated macrophages. *J Leukoc Biol* 92, 1227-1239.
- Takata, K., Kozaki, T., Lee, C.Z.W., Thion, M.S., Otsuka, M., Lim, S., Utami, K.H., Fidan, K., Park, D.S., Malleret, B., *et al.* (2017). Induced-Pluripotent-Stem-Cell-Derived Primitive Macrophages Provide a Platform for Modeling Tissue-Resident Macrophage Differentiation and Function. *Immunity* 47, 183-198 e186.
- Uenishi, G., Theisen, D., Lee, J.H., Kumar, A., Raymond, M., Vodyanik, M., Swanson, S., Stewart, R., Thomson, J., and Slukvin, I. (2014). Tenascin C promotes hematoendothelial development and T lymphoid commitment from human pluripotent stem cells in chemically defined conditions. *Stem Cell Reports* 3, 1073-1084.
- van Wilgenburg, B., Browne, C., Vowles, J., and Cowley, S.A. (2013). Efficient, long term production of monocyte-derived macrophages from human pluripotent stem cells under partly-defined and fully-defined conditions. *Plos One* 8, e71098.
- Vanhee, S., De Mulder, K., Van Caeneghem, Y., Verstichel, G., Van Roy, N., Menten, B., Velghe, I., Philippe, J., De Bleser, D., Lambrecht, B.N., *et al.* (2015). In vitro human embryonic stem cell hematopoiesis mimics MYB-independent yolk sac hematopoiesis. *Haematologica* 100, 157-166.
- Vogel, D.Y., Glim, J.E., Stavenuiter, A.W., Breur, M., Heijnen, P., Amor, S., Dijkstra, C.D., and Beelen, R.H. (2014). Human macrophage polarization in vitro: maturation and activation methods compared. *Immunobiology* 219, 695-703.
- Weiskopf, K., and Weissman, I.L. (2015). Macrophages are critical effectors of antibody therapies for cancer. *MAbs* 7, 303-310.
- Zhang, H., Xue, C., Shah, R., Bermingham, K., Hinkle, C.C., Li, W., Rodrigues, A., Tabita-Martinez, J., Millar, J.S., Cuchel, M., *et al.* (2015). Functional analysis and transcriptomic profiling of iPSC-derived macrophages and their application in modeling Mendelian disease. *Circ Res* 117, 17-28.
- Zhang, M., D'Aniello, C., Verkerk, A.O., Wrobel, E., Frank, S., Ward-van Oostwaard, D., Piccini, I., Freund, C., Rao, J., Seebohm, G., *et al.* (2014). Recessive cardiac phenotypes in induced

pluripotent stem cell models of Jervell and Lange-Nielsen syndrome: disease mechanisms and pharmacological rescue. *Proc Natl Acad Sci U S A* **111**, E5383-5392.

Inventory of Supplemental Information for Chapter 2

Supplemental Figures and Legends:

Figure S1. Differentiation of CD14+ monocytes from hiPSCs. Related to Figure 1.

Figure S2. Comparison of cell sizes of whole blood, PBMCs, Blood-mono and hiPSC-mono. Related to Figure 2.

Figure S3. Characterization of IPSDMs and PBDMs. Related to Figure 3.

Figure S4. Induction of Apoptosis by UV Radiation. Related to Figure 5.

Figure S5. Characterization IPSDMs tumor phagocytosis activity. Related to Figure 6.

Supplemental Tables

Table S1. Formulation for IF9S medium. Related to Experiment Procedures.

Table S2. List of conjugated antibodies. Related to Experiment Procedures.

Table S3. Sequence of primes used for qPCR. Related to Experiment Procedures.

Supplemental Videos (can be found in the Supplementary information that accompanies the article online)

Movie S1. Monocyte differentiation day 7 to day 9. Related to Figure 1.

Movie S2. Monocyte differentiation day 6 to day 8. Related to Figure 1.

Movie S3. Tumor phagocytosis by IPSDMs. Related to Figure 6.

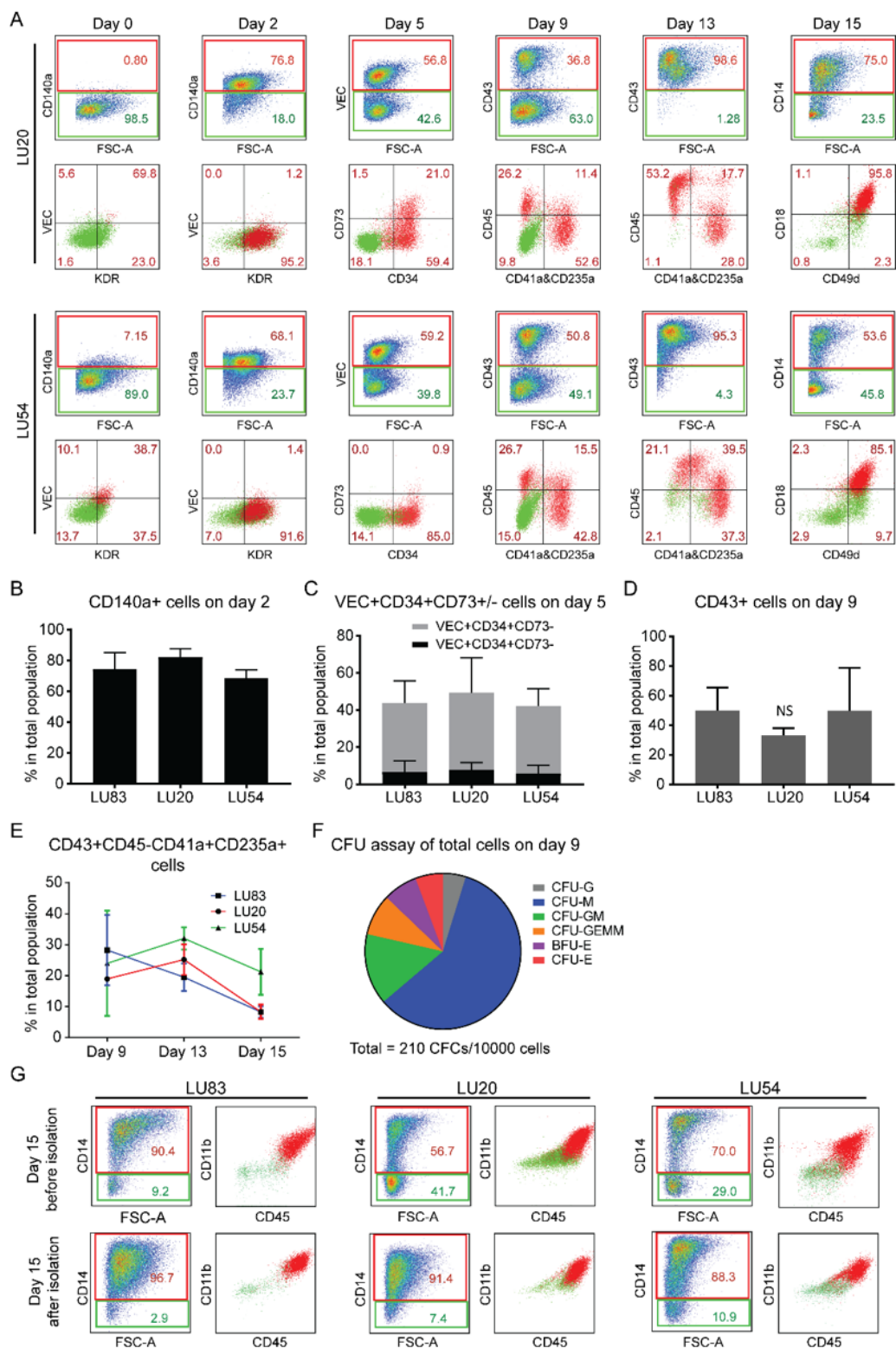


Figure S1. Differentiation of CD14⁺ monocytes from hiPSCs. Related to Figure 1.

(A) FACS analysis of stage-specific markers at day 0, day 2, day 5, day 9, day 13 and day 15 of differentiation from LU20 and LU54. Positive populations are gated in upper panels and their percentages are shown in red in both upper and lower panels. (B) Percentage of early pan-mesodermal cell marker (PDGFR α) on day 2 of differentiation from three hiPSC lines (LU83, LU20 and LU54). (C) Percentage of non-HE (VEC+CD34+CD73⁺) and HE (VEC+CD34+CD73⁻) subsets on day 5 of differentiation from three hiPSC lines (LU83, LU20 and LU54). (D) Percentage of early HPC marker CD43 on day 9 of differentiation from three hiPSC lines (LU83, LU20 and LU54). (E) Percentage of erythro-megakaryocytic lineage cells (CD43+CD45-CD41a+CD235a⁺) in total cell population on day 9, day 13 and day 15 of differentiation from three hiPSC lines (LU83, LU20 and LU54). (F) CFU assay of total cell population on day 9 of differentiation from LU83. (G) Representative FACS analysis of CD14⁺ monocytes before and after MACS isolation on day 15 of differentiation from three hiPSC lines (LU83, LU20 and LU54). Error bars are \pm SD of three independent experiments in (B-E).

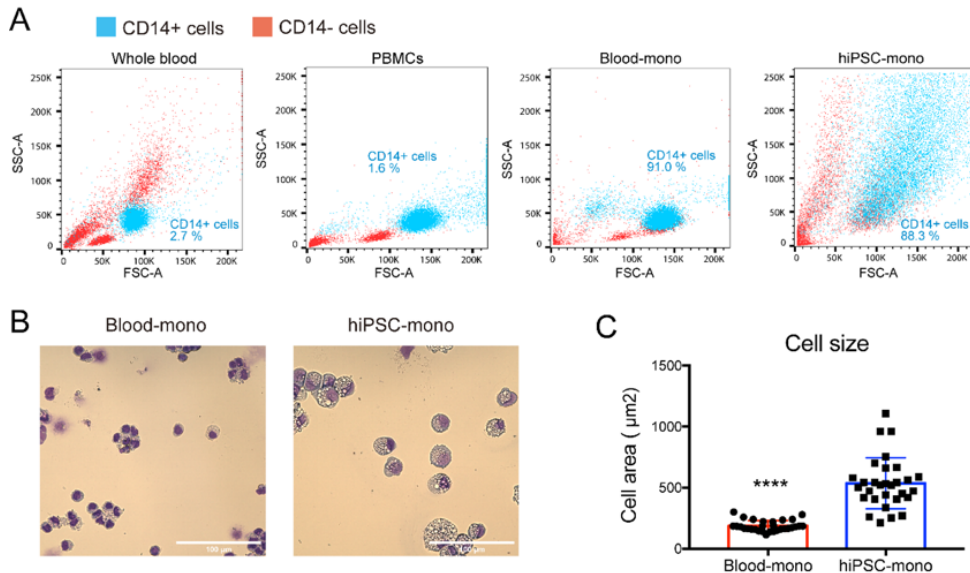


Figure S2. Comparison of cell sizes of whole blood, PBMCs, Blood-mono and hiPSC-mono. Related to Figure 2.

(A) FACS analysis of whole blood, PBMCs, Blood-mono from the same donor and hiPSC-mono on day 15 of differentiation from LU83 hiPSC line. (B) Giemsa staining of blood-mono isolated from

human PBMC and hiPSC-mono isolated on differentiation day 15. Scale bar 100 μ m. (C) Quantification of cell size of blood-mono and hiPSC-mono using Giemsa staining images. Cell area of 30 intact cells was measured from each cell type. Unpaired t-test. **** $p < 0.0001$.

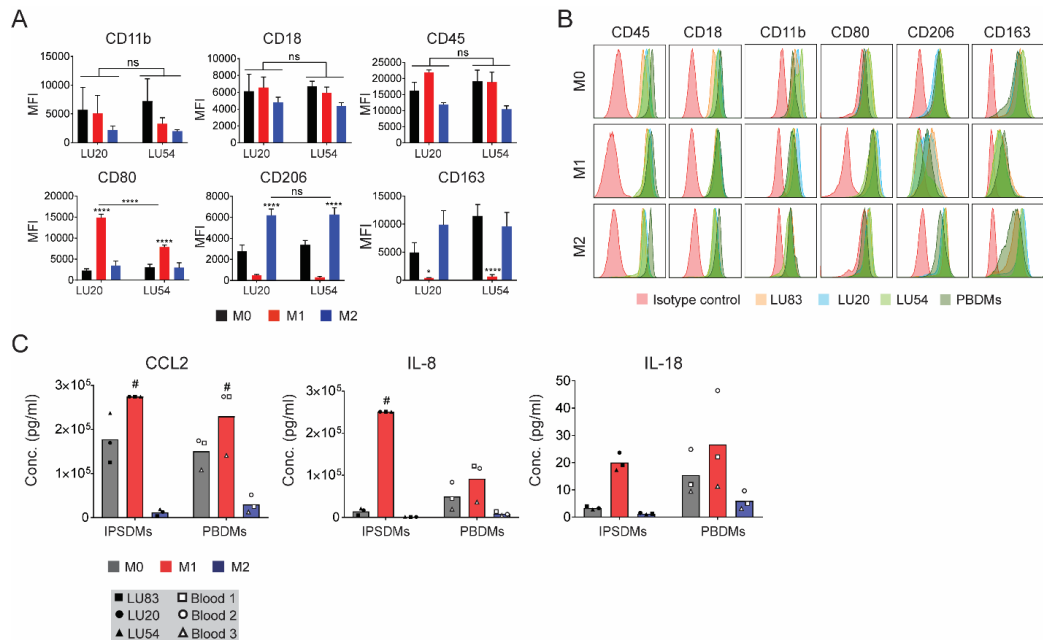


Figure S3. Characterization of IPSDMs and PBDMs. Related to Figure 3.

(A) Quantification of surface expression of pan-specific macrophage markers: CD11b, CD18 and CD45 and subtype-specific markers: CD80 (M1) and CD206 and CD163 (M2) on IPSDMs (differentiated from LU20 and LU54). Error bars are \pm SD of three independent experiments. Uncorrected Fisher's LSD test. ns = non-significant, * $p < 0.05$, **** $p < 0.0001$. (B) Representative FACS plots of pan-specific macrophage markers: CD11b, CD18 and CD45 and subtype-specific markers: CD80 (M1), CD206 and CD163 (M2) on IPSDMs (differentiated from LU20 and LU54) and PBDMs. (C) Quantification of secreted cytokines and chemokines by Multiplex assay using supernatants from IPSDMs and PBDMs after 48 hours of polarization. Data are presented as mean of three biological replicates (three hiPSC lines or PBMC samples). # higher than the detection limit of Multiplex.

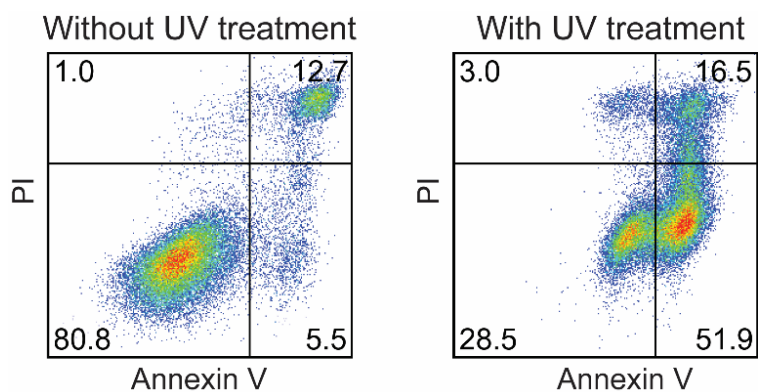


Figure S4. Induction of Apoptosis by UV Radiation. Related to Figure 5.

FACS analysis of apoptotic (Annexin V⁺ PI⁻) cells in hiPSCs without and with UV (35 J/cm²) treatment.

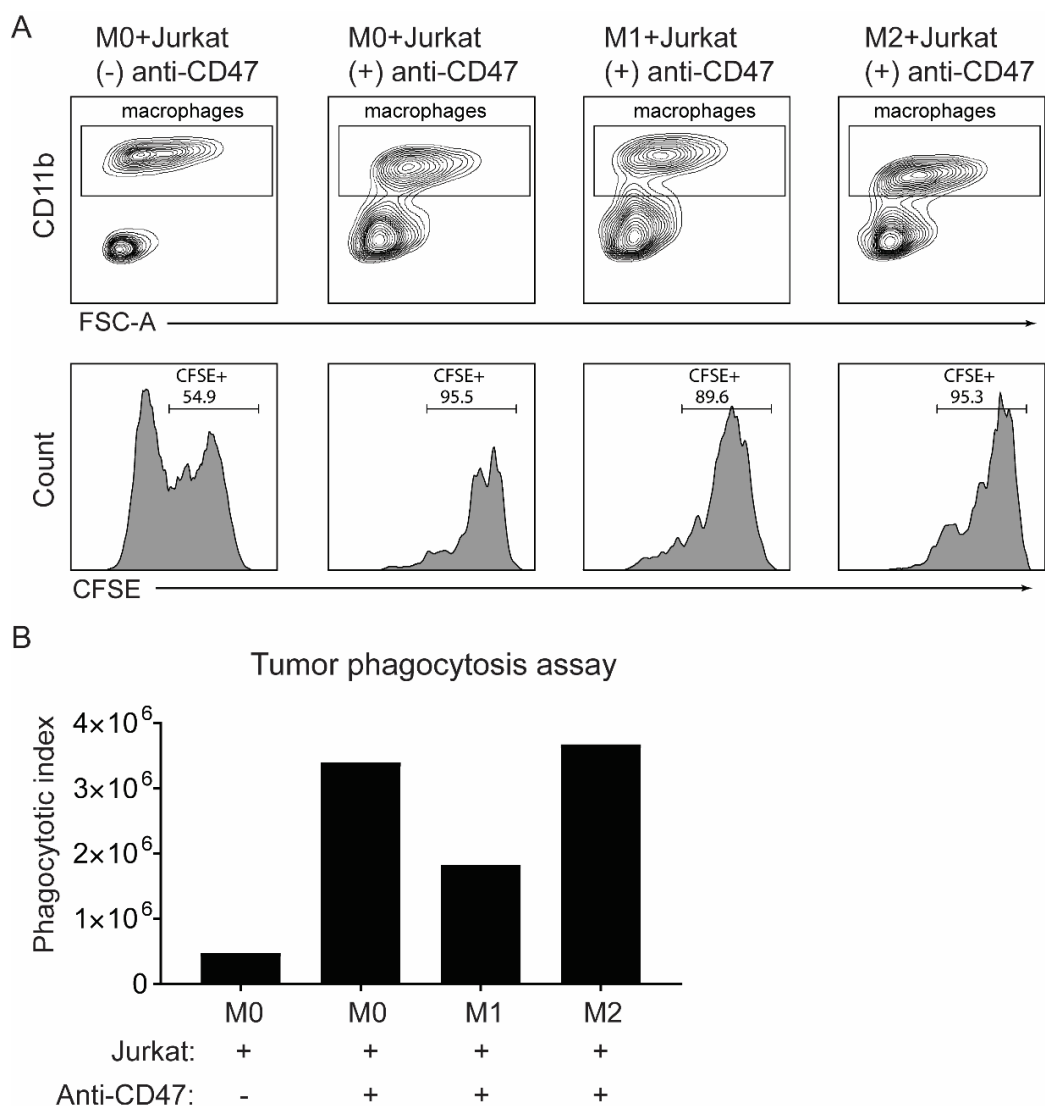


Figure S5. Characterization IPSDMs tumor phagocytosis activity. Related to Figure 6.

(A) FACS analysis of Jurkat cell phagocytosis by different subtypes of IPSDMs in the presence of CD47 blocking antibody. Jurkat cell phagocytosis by IPSDMs (M0) without CD47 blocking antibody is shown as a negative control. CD11b⁺ IPSDMs are gated (upper panel) and their CFSE intensities are shown as a histogram (lower panel). (B) Phagocytotic index of different subtypes of IPSDMs in the presence of CD47 blocking antibody. Jurkat cell phagocytosis by IPSDMs (M0) without CD47 blocking antibody is shown as a negative control. Percentage of CFSE⁺ macrophages was multiplied by MFI of CFSE to obtain the phagocytotic index. IPSDMs were differentiated from LU83 in (A-B).

Supplemental Tables

Medium component (stock concentration)	Source	Volume added (250ml final volume)	Final concentration
IMDM	Iscove's modified Dulbecco's medium (IMDM), no phenol red (Gibco, cat. no. 21056-023)	117.25 ml	--
F12	Ham's F-12 nutrient mix, GlutaMAX supplement (Gibco, cat. no. 31765-027)	117.25 ml	--
PVA (5%)	Poly vinyl alcohol (Sigma-Aldrich, cat. no. P8136-250G)	50 ul	10 mg/L
Lipids (100X)	Chemically defined lipid concentrate (Gibco, cat. no. 11905031)	250ul	0.1% (vol%)
ITS-X (100X)	Insulin-transferrin-selenium-ethanolamine (Gibco, cat. no. 51500-056)	5 ml	2% (vol%)
αMTG (1.3% in IMDM)	Mono-thio glycerol (Sigma-Aldrich, cat. no. M6145-25ml)	750 μ l	40 ul/L
AA2P (5 mg/ml)	Sigma-Aldrich, cat. no. A8960	3.2 ml	64 mg/L
GlutaMax (100X)	GlutaMAX-1 supplement (Gibco, cat. no. 35050-038)	2.5 ml	1% (vol%)
NEAA (100X)	MEM Non-Essential Amino Acids Solution (100X) (Gibco, Cat. No. 11140-035)	2.5 ml	1% (vol%)
Pen-strep (5,000 U/ml)	Gibco, cat no. 15070-063	1.25ml	0.5% (vol%)

Table S1. Formulation for IF9S medium. Related to Experiment Procedures.

Antibody	Fluorochrome	Source	Dilution	Catalog #
CD140a	BV421	BD Bioscience	1:100	562799
VE-Cadherin	Alexa488	eBioscience	1:50	53-1449-42
CD34	APC	Miltenyi Biotec	1:20	130-090-954
KDR	PE	R&D	1:20	FAB357P
CD73	PE	BD Pharmingen	1:20	550257
CD43	PE	BD Bioscience	1:20	560199
CD45	FITC	Miltenyi Biotec	1:20	130-080-202
CD41a	Vioblue	Miltenyi Biotec	1:20	130-105-610
CD235a	Vioblue	Miltenyi Biotec	1:20	130-100-273
CD14	PE	Miltenyi Biotec	1:20	130-091-242
CD11b	Vioblue	Miltenyi Biotec	1:20	130-097-336
CD18	FITC	Miltenyi Biotec	1:20	130-101-237
CD49d	PE-Vio770	Miltenyi Biotec	1:20	130-104-326
CD29	PE	eBioscience	1:50	12-0299-71
ICAM1	F	R&D	1:20	BBA20
E-Selectin	F	R&D	1:20	BBA21
VCAM1	PE	R&D	1:20	FAB5649P
CD31	APC	eBioscience	1:50	17-0319
CD105	Vioblue	Miltenyi Biotec	1:20	130-099-666
CD80	PE-Vio770	Miltenyi Biotec	1:20	130-101-218
CD206	FITC	Miltenyi Biotec	1:20	130-095-131
CD163	FITC	Miltenyi Biotec	1:100	130-112-290
CD172a	PE-Vio770	Miltenyi Biotec	1:20	130-099-793
Annexin-V	Pacific Blue	Thermofisher	1:20	A35122

Table S2. List of conjugated antibodies. Related to Experiment Procedures.

Gene	Forward sequence	Reverse sequence	Product size
CD68	GGAAATGCCACGGTTCATCCA	TGGGGTTCAGTACAGAGATGC	247
IL1B	ATGATGGCTTATTACAGTGGCAA	GTCGGAGATTCTGTAGCTGGA	132
IL6	ACTCACCTCTTCAGAACGAATTG	CCATCTTTGGAAGGTTTCAGGTTG	149
IL8	AGCACTCCTTGGCAAAAGT	CGGAAGGAACCATCTCACTG	116
TNFA	CCTCTCTCTAATCAGCCCTCTG	GAGGACCTGGGAGTAGATGAG	220
CCL2	CAGCCAGATGCAATCAATGCC	TGGAATCCTGAACCCACTTCT	190
CCL5	CCAGCAGTCGTCTTTGTCAC	CTCTGGGTTGGCACACACTT	54
CXCL10	GTGGCATTCAAGGAGTACCTC	TGATGGCCTTCGATTCTGGATT	198
CD64	AGCTGTGAAACAAAGTTGCTCT	GGTCTTGCTGCCCATGTAGA	75
IDO1	GCCAGCTTCGAGAAAGAGTTG	ATCCCAGAACTAGACGTGCAA	96
NOX2	ACCGGGTTTATGATATTCCACCT	GATTCGACAGACTGGCAAGA	135
CD206	TCCGGGTGCTGTTCTCCTA	CCAGTCTGTTTTTGATGGCACT	211
CD163	TTTGTCAACTTGAGTCCCTTCAC	TCCCGCTACACTTGTTTTTAC	127
CD200R	TGGTTGTTGAAAGTCAATGGCT	CTCAGATGCCTTCACCTTGTTT	153
TGM2	GAGGAGCTGGTCTTAGAGAGG	CGGTCACGACACTGAAGGTG	184
IL1RA	CATTGAGCCTCATGCTCTGTT	CGCTGTCTGAGCGGATGAA	167
CCL22	ATCGCCTACAGACTGCACTC	GACGGTAACGGACGTAATCAC	129
CCL24	ACATCATCCCTACGGGCTCT	CTTGGGGTCGCCACAGAAC	176
TLR1	CCACGTTCTCTAAAGACCTATCCC	CCAAGTGCTTGAGGTTTACAG	248
TLR2	ATCCTCCAATCAGGCTTCTCT	GGACAGGTCAAGGCTTTTTACA	118
TLR4	AGACCTGTCCCTGAACCCTAT	CGATGGACTTCTAAACCAGCCA	147
TLR6	TTCTCCGACGGAAATGAATTTGC	CAGCGGTAGGTCTTTTGAAC	75
TLR8	ATGTTCTTCAGTCGTCATGC	TTGCTGCACTCTGCAATAACT	143
CX3CR1	ACTTTGAGTACGATGATTGGCT	GGTAAATGTCGGTGACACTCTT	177
S1PR1	TTCCACCGACCCATGTACTAT	GCGAGGAGACTGAACACGG	185
CD36	GGCTGTGACCGGAACTGTG	AGGTCTCCAAGTGGCATTAGAA	92
MERTK	CTCTGGCGTAGAGCTATCACT	AGGCTGGGTTGGTGAAAACA	162
RPL37A	GTGGTTCCTGCATGAAGACAGTG	TTCTGATGGCGGACTTTACCG	84
HARP	CACCATTGAAATCCTGAGTGATGT	TGACCAGCCCAAAGGAGAAG	116

Table S3. Sequence of primes used for qPCR. Related to Experiment Procedures.

Supplemental Videos (can be found online, Doi: 10.1016/j.stemcr.2019.05.003)

Movie S1. Monocyte differentiation day 7 to day 9. Related to Figure 1.

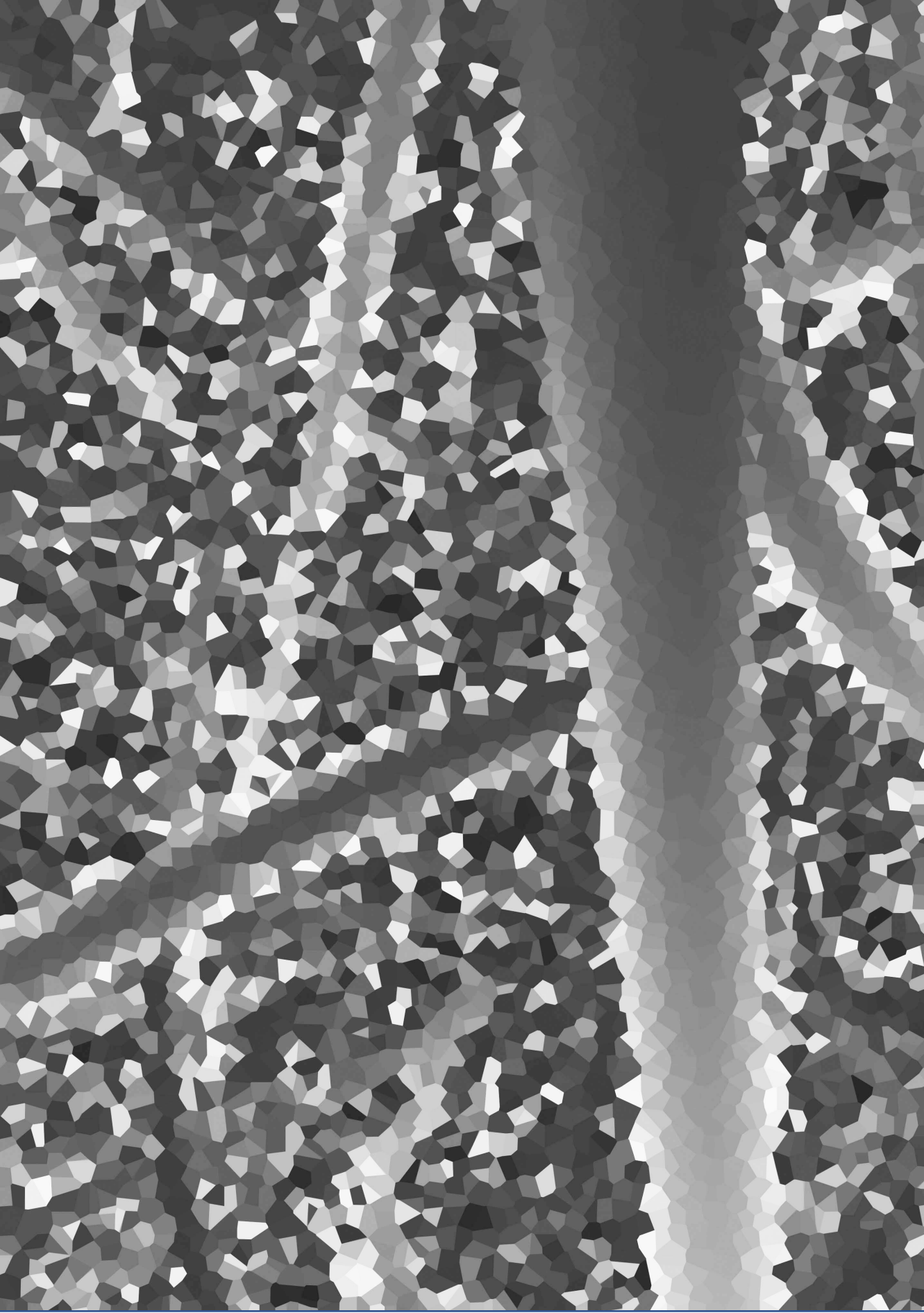
Time-lapse imaging of monocyte differentiation from LU83 hiPSC line. Video was taken from differentiation day 7 to day 9 in a timespan of ~50 hours. The video is 15 frames/second. The interval between each frame is 40 minutes in a real time. Scale bar represents 200 μm .

Movie S2. Monocyte differentiation day 6 to day 8. Related to Figure 1.

Time-lapse imaging of monocyte differentiation from LU83 hiPSC line. Video was taken from differentiation day 6 to day 8 in a timespan of ~48 hours. The video is 15 frames/second. The interval between each frame is 16 minutes in a real time. Scale bar represents 100 μm .

Movie S3. Tumor phagocytosis by IPSDMs. Related to Figure 6.

Tumor cell phagocytosis by M0-IPSDMs differentiated from LU83. Video was taken 30 minutes after co-culture of tumor cells with M0-IPSDMs. Video was made in the same field as Figure 6C. Video is 15 frames/second and interval between each frame is 30 seconds in a real time. Scale bar represents 50 μm .



Chapter 3

Generation and Functional Characterization of Monocytes and Macrophages Derived from Human Induced Pluripotent Stem Cells

Xu Cao, Francijna E. van den Hil, Christine L. Mummery and Valeria V. Orlova*

Department of Anatomy and Embryology, Einthovenweg 20, 2333ZC
Leiden, The Netherlands

*Corresponding author

Published in Current Protocols in Stem Cell Biology 2020

e108, Volume 52

Doi: 10.1002/cpsc.108

ABSTRACT

Monocytes and macrophages are essential for immune defense and tissue hemostasis. They are also the underlying trigger of many diseases. The availability of robust and short protocols to induce monocytes and macrophages from human induced pluripotent stem cells (hiPSCs) will benefit many applications of immune cells in biomedical research. Here we describe a protocol to derive and functionally characterize these cells. Large numbers of hiPSC-derived monocytes (hiPSC-mono) could be generated in just 15 days. These monocytes were fully functional after cryopreservation and could be polarized to M1 and M2 macrophage subtypes. hiPSC-derived macrophages (iPSDMs) showed high phagocytotic uptake of bacteria, apoptotic cells and tumor cells. The protocol was effective across multiple hiPSC lines. In summary, we developed a robust protocol to generate hiPSC-mono and iPSDMs which showed phenotypic features of macrophages and functional maturity in different bioassays.

Basic Protocol 1: Differentiation of hiPSCs toward monocytes

Support protocol 1: Isolation and cryopreservation of monocytes

Support Protocol 2: Characterization of monocytes

Basic Protocol 2: Differentiation of different subtypes of macrophages

Support Protocol 3: Characterization of iPSDMs

Support Protocol 4: Functional characterization of different subtypes of macrophages

KEYWORDS:

Induced pluripotent stem cells; monocytes; macrophages; differentiation; functional characterization

INTRODUCTION

Monocytes and macrophages play crucial roles in protective immunity and tissue hemostasis and trigger or exacerbate many pathological conditions, including diabetes, atherosclerosis, fibrosis and cancer (Wynn et al., 2013). Human peripheral blood mononuclear cells (PBMCs) are widely used as a source of human monocytes and macrophages for biomedical studies. However, their availability is often limited especially from patients with rare genetic diseases and there may be significant donor-to-donor variability. In addition, PBMC-derived macrophages (PBDMs) have a different developmental origin than tissue resident macrophages in many organs, which presents a shortcoming for their application in disease modeling *in vitro* (Ginhoux and Jung, 2014).

Previous studies have shown that human induced pluripotent stem cells (hiPSCs) can be induced to form hemogenic endothelium (HE), identified as CD144+CD34+ and CD73-, which could be further differentiated into CD43+ hematopoietic progenitors

(HPCs) and then to erythro-myeloid progenitors (EMPs); these are reminiscent of EMPs in the yolk sac during embryonic hematopoiesis. The differentiation process is MYB-independent and associated with HOXA expression (Buchrieser et al., 2017; Vanhee et al., 2015; Dou et al., 2016; Ivanovs et al., 2017; Ng et al., 2016), indicating this recapitulates primitive hematopoiesis *in vivo*. Other studies found that iPSDMs could acquire tissue-specific characteristics *in vitro* (Takata et al., 2017) and *in vivo* (Takata et al., 2017; Happle et al., 2018) by coculture with other tissue-resident cell types. All of these studies indicate that iPSDMs can be a unique source of patient-specific, tissue-resident macrophages given that they can be produced in unlimited cell numbers from a renewable donor source of choice and can adopt a tissue resident macrophage-like identity.

This unit describes two basic protocols: the efficient monolayer differentiation of monocytes from hiPSCs (Basic Protocol 1), and then induction of their differentiation to different macrophage subtypes from cryopreserved monocytes (Basic protocol 2); this is an adaption of our previous publication (Cao et al., 2019). Using our protocol, functional monocytes and polarized macrophage subtypes can be efficiently derived from hiPSCs within 2 and 3 weeks respectively.

All protocols described in this unit have been tested using at least three hiPSC lines and demonstrated as highly reproducible (Cao et al., 2019). Prior to the initiation of the differentiation process, hiPSCs are cultured in chemically defined E8™ medium on human recombinant vitronectin-coated plates and passaged routinely every week when ~90% confluent. For the passaging, hiPSCs are dissociated with Gentle Cell Dissociation Reagent (GCDR) at room temperature (RT) to obtain small cell clumps. Cells are passaged with a split ratio of 1:10 to 1:20 for maintenance. Cells are refreshed 48 hours after seeding and then every 24 hours. For the differentiation, hiPSCs are passaged similarly as for maintenance on Matrigel-coated plates in E8™ medium. Details of the differentiation process are described in Basic protocols 1 and 2. Isolation and cryopreservation of hiPSC-driven monocytes (hiPSC-mono) is described in Support Protocol 1. Support Protocol 2 describes methods for characterization of hiPSC-mono. Support Protocol 3 describes methods for characterization of iPSDMs. In Support Protocol 4, four different functional assays are described for the analysis of endocytosis, bacterial phagocytosis, efferocytosis and tumor phagocytosis activities of iPSDMs.

BASIC PROTOCOL 1

DIFFERENTIATION OF hiPSCs TOWARD MONOCYTES

This protocol describes methods for the efficient derivation hiPSC-mono in 14 to 15 days, which had been tested and proven robust with multiple hiPSC lines previously (Cao et al., 2019).

Monocyte differentiation from hiPSCs is divided into five steps (Fig. 1). The first is seeding and culture of hiPSCs. The seeding density determines the differentiation efficiency so needs to be optimal since higher seeding densities can suppress HPC induction from day 5 to day 9. The second step is mesoderm induction with BMP4, Activin A and CHIR99021 for 2 days, followed by HE induction for 3 days with VEGF, FGF2, SB431542 and SCF. On day 2 and 5, the differentiation efficiency can be determined by FACS for mesoderm (CD140a+) and HEs (CD144+CD34+CD73-), respectively. The fourth step is hematopoietic induction from day 5 to day 9 using VEGF, FGF2, SCF, IL-3, IL-6 and TPO. The differentiation efficiency can easily be estimated based on the number of round HPCs that emerge or quantified by FACS for the HPC specific marker CD43 on day 9. The last step is monocyte induction from HPCs uses IL-3, IL-6 and M-CSF in suspension culture. On day 9, the round HPCs are collected first before dissociation of adherent cells using TrypLE and accutase sequentially to minimize cell stress. Large numbers of dead cells and cell debris may lead to unintended monocyte activation. CD14+ monocytes can be harvested and isolated either on day 14 or 15 depending on differentiation efficiency and/or on hiPSC line, and optimal time can be determined either by FACS or by observing a small number of cells starting to adhere to the plate and differentiate towards macrophages.

Expected results are large numbers of round HPCs forming by day 9 of differentiation and more than 50% CD14+ monocytes before isolation. More details on expected results are described in the UNDERSTANDING RESULTS section.

Part- or all of the protocol can be tailored to specific End-user interests. For instance, the differentiation protocol for CD73- HEs from hiPSCs can be useful to study HE development *in vitro* and the subsequent endothelial- to hematopoietic transition (EHT). HPCs derived from this protocol on day 9 show multilineage differentiation potential in a colony forming-unit (CFU) assay, developing to erythroid, myeloid (granulocytes, monocytes, macrophages) and megakaryocyte lineages (Cao et al., 2019). Uenishi et al. showed that T lymphoid cells can also be generated from hiPSC-derived HPCs differentiated using a comparable method, even though Tenascin C was used as an extracellular matrix protein to promote lymphoid differentiation (Uenishi et al., 2014). These results suggest that HPCs derived using this protocol can also be used for the induction of other hematopoietic lineages, including granulocytes, erythrocytes, megakaryocytes and T lymphocytes.

Materials

hiPSCs: This protocol was developed using LUMC0020 (LU20, generated from skin fibroblasts) (Zhang et al., 2014); LUMC0054 (LU54, generated from kidney epithelial cells isolated from cells in urine, <http://hpscereg.eu/cell-line/LUMCi001-A>) (Halaidych et al., 2018); and LUMC0083 (LU83, generated

from skin fibroblasts by LUMC hiPSC Core Facility).

CellAdhere™ Dilution Buffer (Stemcell Technologies, cat. no. 07183)

Gentle Cell Dissociation Reagent (GCDR; Stemcell Technologies, cat. no. 07174)

TeSR™-E8™ Kit for hESC/hiPSC (Stemcell Technologies, cat. no. 05990)

Vitronectin-coated 6-well plate (see recipe)

Matrigel-coated 6-well plate (see recipe)

Tubes, 15 ml (Greiner Bio-One, cat. no. 188271)

IF9S medium (see recipe)

Mesoderm induction medium (see recipe)

Hemogenic endothelium induction medium (see recipe)

Hematopoietic induction medium (see recipe)

Monocyte induction medium (see recipe)

Accutase-Solution (PromoCell, cat. no. C-41310)

TrypLE™ Express Enzyme (1X), no phenol red (GIBCO, cat. no. 12604021)

FACSB-10 (see recipe)

Cell scraper, blue, 28 cm (Greiner Bio-One, cat. no. 541070)

Costar® 24-well Clear Flat Bottom Ultra-Low Attachment Multiple Well Plates (Corning, cat. no. 3473)

Passaging of hiPSCs for maintenance

1. Prewarm a Vitronectin-coated 6-well plate, CellAdhere™ Dilution Buffer, TeSR-E8 at RT for at least 30 min.
2. Remove differentiated parts of hiPSC colonies by scraping them with a 200 µl pipette tip.
3. Aspirate TeSR-E8 containing differentiated parts of the culture.
4. Add 1 ml GCDR to each well of a 6-well plate and incubate for 5 min at RT.

The timing of GCDR dissociation varies and it should be monitored carefully. A prolonged dissociation time may lead to cell detachment.

5. Aspirate GCDR and add 1 ml TeSR-E8 to each well of a 6-well plate.
6. Detach the cell colonies by scraping them with a cell scraper.
7. Transfer the cell colonies into a 15 ml tube and pipette up and down 1 to 2 times gently with a 1 ml pipette.

It is critical to break large pieces of colonies by pipetting to increase their adherence and survival after seeding.

8. Wash the Vitronectin-coated plate with 1 ml of Dilution Buffer for each well and add 2 ml of TeSR-E8.

9. Add 33 to 100 μ l of the cell suspension from step 7 into each well (with a splitting ratio 1:10 to 1:30). Distribute the cells evenly and place the plate with the cells in an incubator at 37 °C.

It is important to ensure that the cell suspension is well mixed, and the cells do not precipitate at the bottom of the tube. Gently tap the bottom of the tube before taking up the cell suspension from the tube.

10. Refresh the cells every day starting 48 h after passaging of the hPSCs.

More than 2 ml TeSR-E8 can be added when the cells become relatively dense 5 to 6 days after passaging of the hPSCs.

11. Passage the cells once a week when hiPSC colonies start to contact each other (~90% confluency).

Passaging of hiPSCs for myeloid differentiation

Passage hiPSCs when they reach 90% confluency, as for the passaging for maintenance.

12. Prewarm a Matrigel-coated 6-well plate (or use a freshly prepared Matrigel-coated plate), TeSR-E8 at RT for at least 30 min.
13. Dissociate hiPSC colonies, follow steps 2-7.
14. Remove Matrigel and add 2 ml TeSR-E8 in each well of the 6-well plate.
15. Add 20 to 30 μ l of the cell suspension into each well (with a split ratio 1:33 to 1:50). Distribute the cells evenly and place it in an incubator at 37 °C.

The seeding density of hiPSCs is of essential importance for the differentiation efficiency. Too high a density will inhibit the emergence of hematopoietic cells from hemogenic endothelium from day 5 to day 9. When the hiPSCs are dissociated from a confluent well, a higher split ratio (1:50) is recommended.

Differentiation of hiPSCs toward HPCs in 9 days

16. Mesoderm induction from day 0 to day 2. 24 h after the passaging from step 15 (day -1), replace TeSR-E8 medium with mesoderm induction medium (2 ml per well). Place the plate with the cells into an incubator at 37 °C.

Optimal density of hiPSC colonies on day 0 should be around 30 colonies per well. Always prewarm medium to RT and add growth factors to the medium right before refreshing.

17. Hemogenic endothelium induction from day 2 to day 5. On day 2, replace mesoderm induction medium with hemogenic endothelium induction medium (3 ml per well).

On day 5, the differentiation efficiency of hemogenic endothelium can be determined by FACS analysis. More than 30% of the total cell population should be CD34+CD144+CD73-.

18. Hematopoietic induction from day 5 to day 9. On day 5, replace hemogenic endothelium induction medium with hematopoietic induction medium. Refresh the cell culture on day 7 of differentiation. See video S1 for the morphology change from day 7 to day 9.

On day 5, multiple cell layers should appear in the central area of the colonies while the edges stay as a monolayer. Most colonies have a dark sphere in the middle. Round single hematopoietic cells should start to appear in the central area already from day 7. At first, they will stay attached to the colonies, but as more cells appear, they will partly be released into the supernatant. On day 9, the differentiation efficiency of hematopoietic progenitors can be determined by FACS. More than 50% of CD43+ cells can be obtained on day 9.

Monocyte induction from HPCs in 5-6 days

19. Prewarm Accutase® solution to 37 °C.
20. Gently detach loosely attached HPCs by flushing the colonies with the medium using a 5 ml pipette. Collect all floating cells and transfer cell suspension into a 50 ml tube.
21. Wash each well with 1 ml of DPBS and collect it into the same 50 ml tube from step 20. Add 0.5 ml of TrypLE to each well of a 6-well plate and incubate at 37 °C for 5 min. Tap the plate several times and collect all cell suspension into the same 50 ml tube from step 20.
22. Add 0.5 ml of Accutase® solution to each well of the 6-well plate and incubate at 37 °C for 5 min.

The incubation time needed may vary for different hiPSC lines and seeding densities. Prolonged dissociation (up to 8 min) may be needed to detach most of the colonies. Some cells might remain attached.

23. Add 1 ml IF9S medium to each well. Scrape off the cells using a cell scraper. Collect all cell suspension into the same 50 ml tube from step 20.

Avoid pipetting too vigorously and too often as it could damage the cells. Introducing too many dead cells and cell debris may be toxic and induce the activated phenotype

of monocytes.

24. Add 1 ml IF9S medium to each well. Pipette up and down 3-4 times to wash off the remaining cells and collect the whole cell suspension in the same 50 ml tube from step 20.
25. Centrifuge the cells collected in the 50 ml tube at 1100 rpm (300 g) for 3 min at RT, then resuspend the pellet in 12 ml of monocyte induction medium for each 6-well plate used to collect cells.
26. Distribute cell suspension over 12 wells of a 24-well low-attachment plate, adding 1 ml to each well.

Mix the cell suspension well before adding it to the 24-well plate.

27. Refresh cells on day 12 with monocyte induction medium. To refresh, slowly flip the plate 45 degrees and remove 0.5 ml of the old medium from each well using a 5 ml pipette, then add 1 ml fresh medium.

Avoid disturbing the plate in order to keep all cells at the bottom before refreshing. Aspirate only upper supernatant from the well.

28. On day 14 or 15, collect all floating cells and perform the isolation of CD14+ monocytes as described in Support Protocol 1.

The time of harvesting can be either day 14 or 15 depending on each differentiation and hiPSC line. Cells should be collected when a small number of cells start to adhere and differentiate into macrophages. It is highly recommended to check the differentiation efficiency by FACS. Efficient monocyte induction should result in more than 50 % of CD14+ cells.

SUPPORT PROTOCOL 1

ISOLATION AND CRYOPRESERVATION OF MONOCYTES

This protocol describes methods for both isolation and cryopreservation of hiPSC-mono which has proven robust using at least three hiPSC lines previously (Cao et al., 2019). CD14 expression can be determined by FACS before monocyte isolation to determine the differentiation efficiency. The isolation should be performed on day 14 to day 15 depending on the differentiation efficiency and adherence of monocytes to the plate. The aim is to get the highest percentage of CD14+ cells before large numbers of adherent monocytes are observed at the time isolation is performed. Expected results are more than 50% CD14+ monocytes before isolation, with a yield of $\sim 5 \times 10^6$ monocytes after isolation on day 14 or 15 from each 6-well plate of hiPSCs. More details on expected results are described in UNDERSTANDING RESULTS section.

Materials

Tubes, 15 ml (Greiner Bio-One, cat. no. 188271)

CD14 MicroBeads, human (Miltenyi Biotec, cat. no. 130-050-201)

CryoStor® CS10 (Stemcell Technologies, cat. no. 07930)

FACS buffer (see recipe)

Sterile filters, 100 µm (CellTrics, cat. no. 04-004-2328)

Costar® 24-well Clear Flat Bottom Ultra-Low Attachment Multiple Well Plates (Corning, cat. no. 3473)

QuadroMACS Starting Kit (LS) (Miltenyi, cat. no. 130-091-051)

Cryotubes (Greiner Bio-One, cat. no. 123263)

1. Before collecting cells on day 14/15, prechill a Mr. Frosty™ Freezing Container to 4 °C. Prewarm FACS buffer (FACSB) to RT.
2. Pipette the cell suspension up and down twice using a 5 ml pipette and collect the whole cell suspension in a 50 ml tube.
3. Wash each well with 0.5 ml FACSB and collect it into the same tube. Spin down at 1100 rpm (300 g) for 3 min.
4. Discard the supernatant and resuspend in 12 ml FACSB. Filter through a 100 µm CellTrics® filter to obtain a single cell suspension. Collect all cells in a 15 ml tube. Count total cell number and centrifuge at 1100 rpm (300 g) for 3 min at RT.

It is critical to remove cell clumps by filtering, as they can block the column during magnetic isolation. Total cell number varies per differentiation. Usually 20 to 40 million cells can be collected from one 24-well low-attachment plate.

5. Discard supernatant and resuspend cells in FACSB (80 µl for every 10 million cells). Then add 50 µl CD14 MicroBeads for every 10 million cells. Mix well by flicking the bottom of the tube and incubate the tube at 4 °C for 15 min.

Depending on the percentage of CD14+ cells (ranging from 40% to 80%) before isolation, 40 to 60 µl CD14 MicroBeads should be added for every 10 million cells.

6. Add 1.5 ml FACSB for every 10 million cells. Mix well by flicking the bottom of the tube and spin down at 1100 rpm (300 g) for 3 min at RT.
7. Discard supernatant and resuspend cells (up to 40 million) in 500 µl FACSB.
8. Assemble the QuadroMACS Separator according to the manufacturer's instruction. Place a LS column in the magnetic field. Wash the LS column with 3 ml FACS buffer. Collect the fluid into a 15 ml tube.

The QuadroMACS Separator is a very strong magnet and it should be kept away from all electrical devices.

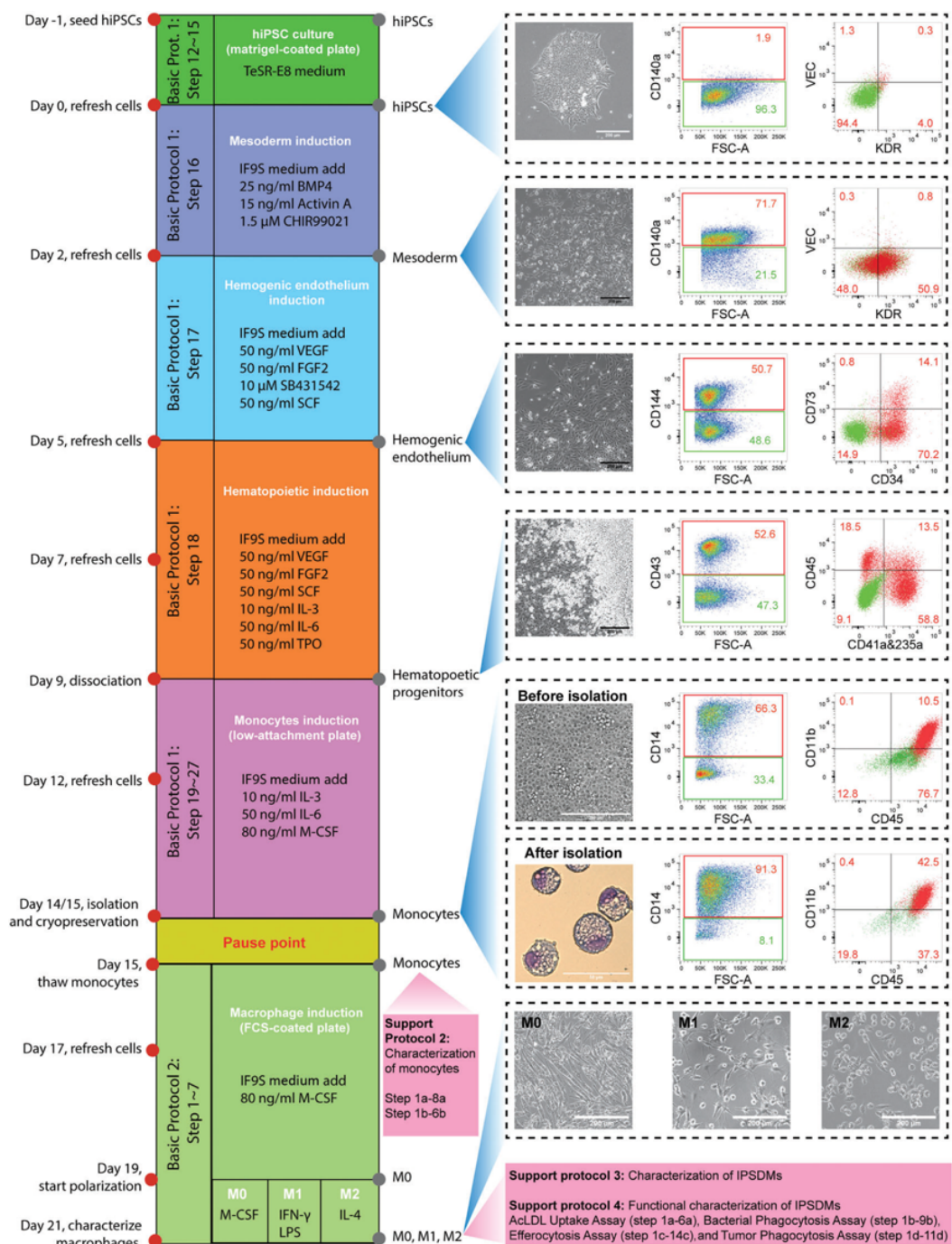


Figure 1 Timeline of all protocol procedures. Bright-field images of representative cellular morphology are shown for day 0 (undifferentiated hiPSCs), day 2 (mesoderm), day 5 (HE), day 9 (HPCs), day 14/15 (monocytes before isolation) and day 21 (M0, M1, M2 macrophages). FACS analysis of stage-specific markers at day 0, day 2, day 5, day 9 and day 15 of differentiation are shown. Wright-Giemsa staining of hiPSC-mono after isolation at day 15 is also shown. Scale bar

represents 200 μm in all bright-field images and 50 μm in Wright-Giemsa staining.

9. Wait until the reservoir of the column becomes empty, then add the 500 μl cell suspension into the reservoir. Collect unbound cells into a 15 ml tube.
10. Wait until the reservoir of the column becomes empty. Add 3 ml FACS buffer into the column to wash off the unbound cells. Collect unbound cells into a 15 ml tube. Repeat the washing for another two times (wash the column three times in total).
11. Remove the column from the magnet and put it on the top of a new 15 ml tube. Add 5 ml FACS buffer to the column. Immediately flush out the cells from the column by firmly pushing the plunger into the column.
12. Count number of cells in the collection tube. Take an aliquot for the characterization of purified monocytes.

More than 90% of CD14⁺ monocytes can be obtained after the isolation step.

13. Spin down monocytes at 1100 rpm (300 g) for 3 min at RT.
14. Cryopreservation of monocytes. Resuspend monocytes in CryoStor[®] CS10 cryopreservation medium to get a final concentration of 3.75 million/ml. Aliquot 400 μl into each cryovial (1.5 million cells per vial).

Monocytes and CS10 cryopreservation medium should be kept on ice. Cryovials should also be on ice during aliquoting of cells.

15. Place all cryovials into a Mr. Frosty[™] Freezing Container and leave it at -80°C for 24 h. Then transfer all cryovials into liquid N_2 for prolonged storage.

Monocytes can be stored in liquid N_2 for at least two years.

SUPPORT PROTOCOL 2

CHARACTERIZATION OF MONOCYTES

Isolated monocytes are characterized by Wright-Giemsa staining (Fig. 1) or FACS (Fig. 2A). Wright-Giemsa can be used to examine nucleus shape and cell size, and flow cytometry can be used to check for specific surface markers expressed on monocytes. Characterization can be done on either freshly isolated or cryopreserved monocytes after thawing. Cryopreserved hiPSC-mono can be compared with freshly isolated monocytes for the expression of monocyte-specific markers (Fig. 2A) as well as characterized functionally based on their ability to adhere to hiPSC-derived endothelial cells (hiPSC-ECs) or human umbilical vein endothelial cells (HUVECs) (Fig. 2B-D). The

flow assay had been described in detail in our earlier publication (Halaidych et al., 2018b) and only briefly introduced here. In this assay, hiPSC-mono should be highly adhesive to both hiPSC-ECs and HUVECs that are stimulated with TNF- α (Fig. 2C-D). Primary blood monocytes (Blood-mono) can serve as controls for the characterization and functional assays of hiPSC-mono.

Materials

hiPSCs-mono (isolated from Support Protocol 1)
Tubes, 15 ml (Greiner Bio-One, cat. no. 188271)
RPMI 1640 Medium (GIBCO, cat. no. 21875034)
Wright-Giemsa Stain, Modified (Sigma-Aldrich, cat. no. WG16)
FACS buffer (see recipe)
Round-bottom tube, 5 ml FACS tube (BD Biosciences, cat. no. 352058)
White filter cards (Thermo Scientific, cat. No. 5991022)
Cytocentrifuge (Thermo Scientific, cat.no. A78300003)
Microscope slides (VWR, cat. no. 631-1553)
MACSQuant® VYB Flow Cytometer (Miltenyi, cat. no. 130-096-116)

Wright-Giemsa staining of hiPSC-mono

- 1a. Centrifuge monocytes and resuspend in RPMI 1640 medium containing 10% FBS to reach a final concentration of 0.2×10^6 cells/ml.
- 2a. Label the slides then mount them with the paper pad and cuvette in the metal holder of the cytocentrifuge.

The protocol may need to be adjusted based on the model of cytocentrifuge used.

- 3a. Load 100 to 200 μ l of monocyte suspension in each cuvette.
- 4a. Spin at 800 rpm for 3 min at RT.
- 5a. Disassemble each metal holder. Remove the cuvette and paper pad carefully without disturbing cytocentrifuged cells. Label the cell area with a permanent marker pen.
- 6a. Dry slides at 37 °C in an incubator dryer for 1-2 h.
- 7a. Add 1 ml of Wright-Giemsa Stain solution to each slide to cover the cell area. After 30 s, add 1 ml deionized water and mix thoroughly with the dye by gently pipetting up and down with a 1 ml pipet tip.
- 8a. After 1 min, pick up the slide carefully with tweezers. Rinse the slide thoroughly by putting the back side of the slide under the water tab for 1 min and air dry.

Slides can be stored at RT for at least 3 years.

Flow cytometric analysis of hiPSC-mono

- 1b. Place a 100 μ m CellTrics filter on the top of a 5 ml FACS tube. Apply monocyte suspension through the filter and wash once with 2 ml FACSBS.
- 2b. Spin down at 1100 rpm (300 g) for 3 min at RT.
- 3b. Wash the cells once by resuspending them in 1 ml of FACSBS and spin down at 1100 rpm (300 g) for 3 min at RT.
- 4b. Aspirate supernatant but leave around 50 μ l inside. Add fluorescent-conjugated FACS antibodies to the cell suspension to the desired working concentration. Suspend cells by flicking the bottom of the tube and incubate in the dark for 30 min at 4 °C. Antibodies used for the characterization of monocytes include those for CD45, CD14, CD11b, CD18. Fc-R blocking antibody should be added to each tube to reduce non-specific binding of antibodies. Details of all antibodies are listed in the Reagents section.
- 5b. Turn off the light of the cell culture hood. Wash the cell suspension with 1 ml FACSBS and centrifuge at 1100 rpm (300 g) for 3 min at RT.

Stained cells can be analyzed using flow cytometry immediately or fixed with 1% (wt/vol) PFA and analyzed the next day.

- 6b. Analyze samples with a flow cytometer. We used the MACSQuant VYB (Miltenyi) with the following instrument settings: Blue/488 FITC, A488: 525/50; Yellow/561 PE: 586/15, APC: 661/20, APC-Cy7: 750LP. FlowJo software was used for data analysis.

The MACSQuant VYB laser setup may require additional compensation between PE and APC channels. For that, extra compensation tubes need to be prepared and run before the analysis. Please refer to the manual of the flow cytometer you are using for the setup and compensation procedures.

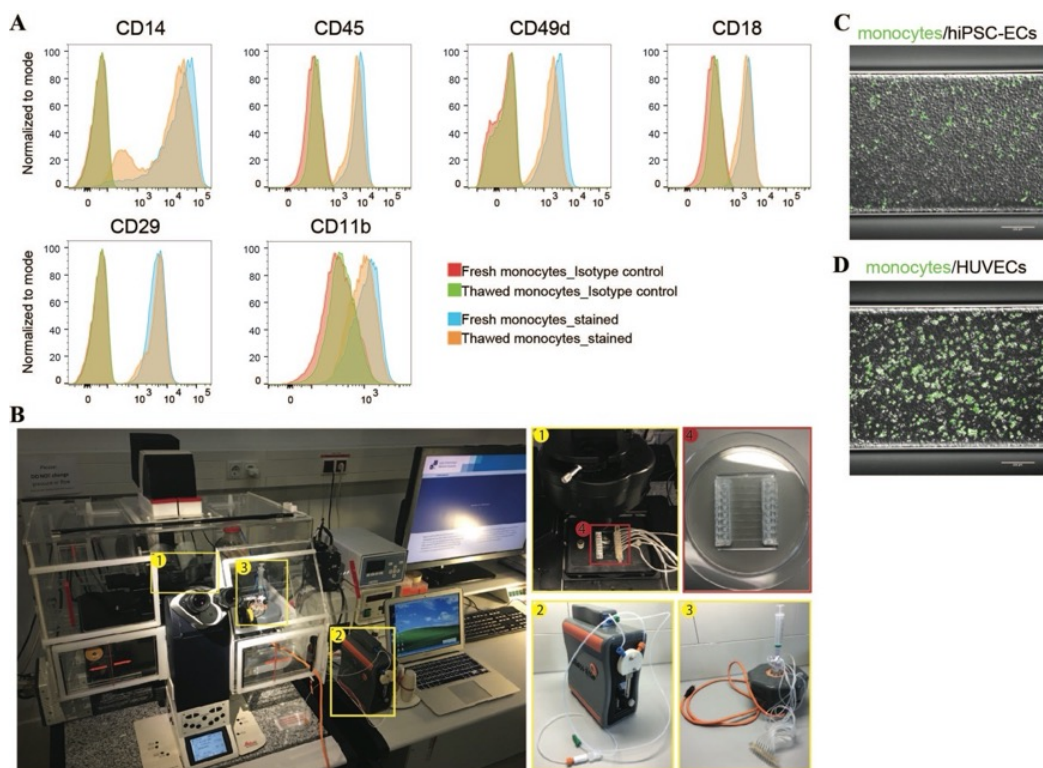


Figure 2 Functional characterization of hiPSC-mono in a Microfluidic Adhesion Assay
(A) FACS analysis of monocytes markers CD14, CD45 and integrins CD49d, CD18, CD29 and CD11b on freshly isolated and thawed monocytes. Isotype controls are shown in red.
(B) Bench setup for the microfluidic adhesion assay, including an inverted fluorescent microscope with mounted live imaging chamber (5% CO₂, 37 °C, humidified), (2) a microfluidic pump, (3) an 8-channel manifold, (4) an 8-channel microfluidic chip.
(C-D) Representative images taken at the end of the flow assay with hiPSC-ECs and HUVECs. Monocytes were labeled with DiOC6 (in green). Scale bar represents 200 μ m.

BASIC PROTOCOL 2

DIFFERENTIATION OF DIFFERENT SUBTYPES OF MACROPHAGES

This protocol describes methods for the induction of iPSDMs from freshly isolated or cryopreserved hiPSC-mono, which had been tested and proven robust with multiple hiPSC lines previously (Cao et al., 2019). Cryopreserved hiPSC-mono are thawed and seeded on Fetal Bovine Serum (FBS)-coated plates. An example of recovery is $43.2\% \pm 9.9\%$. Adherent monocytes are then further differentiated into M0 macrophage in the presence of M-CSF for 4 days in defined IF9S medium. One cryovial of hiPSC-mono (1.5×10^6 cells) are seeded either into 4 or 6 wells of a 6-well plate, in order to get a confluent monolayer of M0 macrophages in 4 and 6 days respectively.

Macrophages are highly heterogeneous due to the diverse stimuli and immune response induced by local tissue environment; they can be classified as pro-inflammatory M1 macrophages (M1) and anti-inflammatory M2 macrophages (M2) (Mantovani et al., 2004; R  s  r, 2015). In this protocol, we describe methods for the polarization of M1 using LPS and IFN-   or M2 using IL-4 for another 48 hours from M0 in IF9S medium. Identities of polarized macrophage subtypes can be examined based on the expression of macrophage-specific markers by FACS (Fig. 3). Alternatively, a multiplex cytokine assay can be used to quantify their protein secretion profile. Expected results are ~90% confluent monolayer of M0 macrophages 4/6 days after seeding. With this protocol, a confluent monolayer of polarized M1 and M2 iPSDMs can be derived from thawed hiPSC-mono in 6 days, which could easily provide enough iPSDMs for multiple characterization and functional assays *in vitro*. More details on expected results are described in UNDERSTANDING RESULTS section.

The major factor requiring optimization in Basic Protocol 2 is the seeding density of thawed hiPSC-mono and the induction time of M0 macrophages. The quality of cryopreserved hiPSC-mono may vary across different batches and hiPSC lines, which could affect their recovery rate and proliferation after thawing. In general, a confluent monolayer of M0 macrophages can still be obtained from a relatively low-quality batch of cryopreserved hiPSC-mono by a longer culture (up to 7 days) or a higher seeding density in M0 medium.

Materials

Cryopreserved monocytes (from Support Protocol 1)

IF9S medium (see recipe)

M0 Medium (see recipe)

M1 Medium (see recipe)

M2 Medium (see recipe)

Fetal Bovine Serum (FBS) South America, ultra-low endotoxin (Biowest, cat. no. S1860)

Accutase-Solution (PromoCell, cat. no. C-41310)

TrypLETM Express Enzyme (1X), no phenol red (GIBCO, cat. no. 12604021)

Culture plates, six wells (Greiner Bio-One, cat. no. 657160)

Tubes, 15 ml (Greiner Bio-One, cat. no. 188271)

MACSQuant^{  } VYB Flow Cytometer (Miltenyi, cat. no. 130-096-116)

Imaging plate, 96-well (Corning, cat. no. 353219)

Differentiation of monocytes into different subtypes of macrophages in 6 days

1. Coat 4 wells of a 6-well plate with FBS overnight at 37 °C (prepare one plate for each cryovial of monocytes). Prewarm IF9S medium to RT. Turn on the water bath and set it to 37 °C.
2. Take out a cryovial with monocytes from liquid nitrogen and thaw it in the water bath right away. Transfer all cell suspension in the cryovial into a 15 ml tube that contains 10 ml IF9S medium. Wash the cryovial once with medium to collect remaining cells.

The thawing procedure should be performed as quickly as possible to minimize the time of monocytes staying in cryopreservation medium. Move the cryovial in the water bath in a circle to thaw. Pipet cells gently to reduce mechanical stress.

3. Centrifuge the 15 ml tube at 1100 rpm (300 g) for 3 min. Discard supernatant.
4. Resuspend monocytes from each cryovial in 8 ml M0 medium.
5. Remove FCS from the 6-well plate and add 2 ml cell suspension into each well. Place the plate back into the incubator and move the plate in a cross-like pattern to distribute cells evenly.

Alternatively, cells can be seeded into 6 wells instead of 4 wells of a 6-well plate so that they become confluent in 6 days, in order to harvest more M0 macrophages at the expense of two additional days of culture.

6. Refresh cells with M0 medium 2 days post thawing.

Do not disturb cells during the first two days. Only a small number of cells adhere after 2 days (around 10%), which is normal and cells at this stage are still proliferating so that 80 % confluency should be reached on day 4 (when starting with 4 wells of a 6-well plate) or on day 6 (when starting with 6 wells of a 6-well plate). An additional day may be needed for both starting formats to allow cells to become confluent before starting polarization.

Polarization of iPSDMs

Polarization of M1 and M2 from M0 can be performed either in 6-well plate directly without dissociation or in 96-well plate for functional assays described in Support Protocol 4. For the polarization in 96-well plate, M0 are first dissociated and seeded in a new 96-well plates.

7. Two days before the assay, dissociate confluent M0 macrophages with Accutase solution at 37 °C for 10 min.
8. Resuspend cells in M0 medium to reach 0.5×10^6 cells/ml.
9. Seed 50×10^3 cells (in 100 μ l) into each well of a 96-well black imaging plate.

To obtain enough cells for analysis, seed 2 wells for each sample of the assay.

10. Start the polarization 24h after seeding. Refresh cells with M0, M1 and M2 medium respectively for polarization of M0, M1 and M2. Polarization last for overnight (~12h) for functional assays (in 96-well format) and 48h for other analysis (in 6-well format).

It is critical to reach more than 80% confluency for M0 macrophages before polarization.

SUPPORT PROTOCOL 3

CHARACTERIZATION OF iPSDMs

iPSDMs that have been polarized can be characterized by flow cytometry and the multiplex cytokine assay. Flow cytometry can be used to determine specific surface marker expression on each macrophage subtype (Fig. 3). The multiplex cytokine assay is used to measure cytokine and chemokine secretion by macrophages. The major factor requiring optimization in this protocol is the dissociation time of polarized iPSDMs for FACS. In some cases, a longer dissociation time (10 to 20 minutes) may be required to detach iPSDMs from the plate. For the supernatant collected for multiplex cytokine assay, we recommend diluting 3 times for the first trial and adjusting it later based on the result. Clear M1 and M2 specific signatures of polarized M1 and M2 macrophages should be observed by both FACS (Fig. 3) and multiplex cytokine assay (Cao et al., 2019).

Materials

- iPSDMs subtypes (from Basic Protocol 2)
- IF9S medium (see recipe)
- Accutase-Solution (PromoCell, cat. no. C-41310)
- FACS buffer (see recipe)
- FACSB-10 (see recipe)
- Tubes, 15 ml (Greiner Bio-One, cat. no. 188271)
- Round-bottom tube, 5 ml FACS tube (BD Biosciences, cat. no. 352058)
- MACSQuant® VYB Flow Cytometer (Miltenyi, cat. no. 130-096-116)
- LSR-II flow cytometer (BD Biosciences)
- Centrifuge 5810 R (Eppendorf)
- 96-well round bottom plate (Greiner Bio-One, cat. no. 651161)
- LEGENDplex™ Human Inflammation Panel, 13-plex (BioLegend, cat. no. 740809)
- LEGENDplex™ Human Macrophage/Microglia Panel, 13-plex (BioLegend, cat. no. 740503)

Flow cytometric analysis of iPSDMs

- 1a. Prewarm Accutase solution to 37 °C. Add 1 ml of Accutase solution to each well of a 6-well plate of iPSDMs at 37 °C for 10 min.
- 2a. Add 1 ml FACS-B-10 to each well to stop the dissociation and wash off cells by pipetting 3-4 times using a P1000.

Do not pipette more than 4 times as this may increase cell death. Check cells under the microscope after pipetting and continue with cell scraping if more than 1/3 of cells did not come off the substrate.

- 3a. Collect all of the cell suspension in a 50 ml tube. Add 2 ml IF9S medium to each well and wash off cells by pipetting 3-4 times using a P1000 pipette.

Check the culture under the microscope after pipetting and if a large number of cells is still attached, scrape them off using a cell scraper.

- 4a. Collect all of the cell suspension into the same 50 ml tube. Transfer an aliquot into a 5 ml FACS tube for analysis. Centrifuge at 1100 rpm (300 g) for 3 min at RT.
- 5a. Wash cells once with FACS-B and spin down at 1100 rpm (300 g) for 3 min at RT.
- 6a. Staining of FACS antibodies and analysis by flow cytometry should be done the same way as for monocytes, as described in Support Protocol 2.

Multiplex cytokine assay of iPSDMs

- 1b. Collect supernatant of polarized macrophages. Centrifuge at 1800 rpm (803 g) for 5 min to remove debris.

Cell culture supernatant can be aliquoted and stored at -20 °C for at least 1 year. Avoid multiple (>2) freeze-thaw cycles.

- 2b. The day before the assay, read the manual of the LEGENDplex™ kit carefully. Design the plate layout of the assay. Prepare Wash Buffer and assay Standard Cocktail. Aliquot 80 µl Standard Cocktail into each Eppendorf tube and store in -80 °C.
- 3b. On the day of the assay, warm up all reagents in the LEGENDplex™ kit and the cell culture supernatant to RT.
- 4b. Dilute the supernatant 3 times in Assay Buffer. Load 15 µl standard or diluted supernatant into the 96-well round bottom plate. Then add 15 µl Assay Buffer and 15 µl mixed beads into each well. Assays should be performed in duplicate.

We added 15 µl of each component instead of 25 µl which was recommended by the kit instructions. This may save samples and reagents used and does not affect the readout. However, less than 15 µl is not recommended.

- 5b. Seal the plate with a plate sealer and cover the plate with aluminum foil. Shake the plate at 800 rpm on a plate shaker for 2 hours at room temperature.
- 6b. Centrifuge the plate at 1050 rpm (273 g) for 5 minutes. Remove the plate seal and remove supernatant using a multichannel pipette. Do not disturb the blue pellet (beads) at the bottom.
- 7b. Wash the bead pellet with 200 μ l Wash Buffer. Centrifuge again at 1050 rpm (273 g) for 5 minutes and remove the supernatant.
- 8b. Add 15 μ l Detection Antibodies to each well. Seal the plate with the plate sealer and cover the plate with aluminum foil. Shake the plate at 800 rpm on a plate shaker for 1 hour at RT.
- 9b. Add 15 μ l SA-PE to each well. Seal the plate with plate sealer and cover the plate with aluminum foil. Shake the plate at 800 rpm on a plate shaker for 30 minutes at RT.
- 10b. Centrifuge at 1050 rpm (273 g) for 5 minutes and remove the supernatant.
- 11b. Add 150 μ l Wash Buffer to each well and resuspend the beads.
- 12b. Analyze samples with flow cytometer. We used the LSR-II (BD) with the following instrument settings: Blue laser: 575/26, Voltage: 360 V; Red laser: 660/20, Voltage: 400 V. Data was analyzed using LEGENDplex™ Data Analysis Software

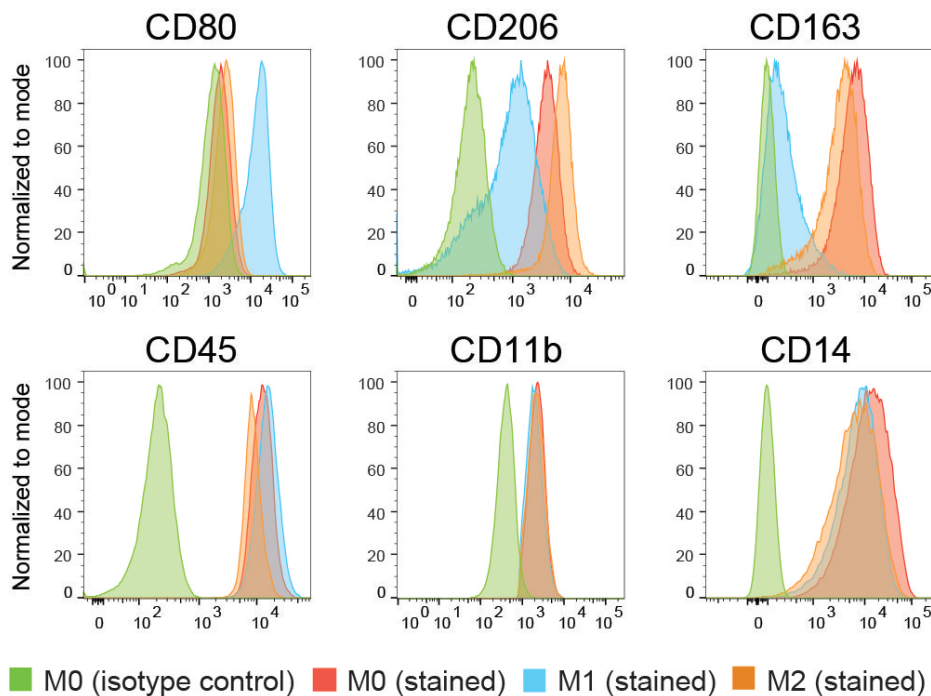


Figure 3 FACS analysis of macrophage subtype-specific markers CD80 (M1), CD206 and CD163 (M2) and pan-specific macrophage markers CD45, CD11b and CD14 on iPSDMs.

SUPPORT PROTOCOL 4

FUNCTIONAL CHARACTERIZATION OF DIFFERENT SUBTYPES OF MACROPHAGES

This protocol is designed to establish different assays for the functional characterization of iPSDMs, including Dil-acetylated low-density lipoprotein (AcLDL) Uptake Assay (Fig. 4A-B), Bacterial Phagocytosis Assay (Fig. 4C-D) and Efferocytosis Assay to examine their ability to clear up apoptotic cells (Fig. 5A) or the Tumor Phagocytosis assay to examine tumoricidal activity (Fig. 5B). These assays could be used to check the quality of iPSDMs produced with this and other published differentiation protocols. Similarities and differences could be observed when PBDMs and iPSDMs were compared using different assays as we previously observed (Cao et al., 2019).

Materials

- iPSDM subtypes (from Basic Protocol 2)
- IF9S medium (see recipe)
- Lipid-free IF9S medium (see recipe)
- PS-free IF9S medium (see recipe)
- Jurkat Medium (see recipe)
- Accutase-Solution (PromoCell, cat. no. C-41310)
- Alexa Fluor™ 594 AcLDL (Invitrogen, cat. no. L35353)
- NucBlue™ Live ReadyProbes™ Reagent (Invitrogen, cat. no. R37605)
- pHrodo™ Green E. coli BioParticles™ Conjugate for Phagocytosis (Invitrogen, cat. no. P35366)
- CellTrace™ CFSE Cell Proliferation Kit, for flow cytometry (Invitrogen, cat. no. C34554)
- Jurkat tumour cells (kindly provided by Dr. Luuk Hawinkels, LUMC)
- anti-human CD47 1:200 (Bio-rad, cat. no. MCA911)
- Annexin V, Pacific Blue™ conjugate, for flow cytometry (Invitrogen, cat. no. A35122)
- Annexin Binding Buffer (5X), for flow cytometry (Invitrogen, cat. no. V13246)
- Propidium Iodide Solution (Miltyen Biotec, cat. no. 130-093-233)
- Culture plates, six wells (Greiner Bio-One, cat. no. 657160)
- Imaging plate, 96-well (Corning, cat. no. 353219)
- MACSQuant® VYB Flow Cytometer (Miltyen Biotec, cat. no. 130-096-116)

AcLDL Uptake Assay

For the AcLDL assay, it is essential to use Lipid-free IF9S medium to deplete LDL during the polarization of iPSDMs.

- 1a. On the day of the assay, dilute Alexa Fluor 594 AcLDL in Lipid-free IF9S medium to a final concentration of 5 µg/ml (1 µL in 199 µL, 1:200 dilution). Add 100 µl to each well of macrophages and incubate at 37 °C for 4 h. Leave two wells without adding AcLDL as a negative control.
- 2a. Wash cells once with 100 µl Lipid-free IF9S medium.
- 3a. Prepare NucBlue solution by adding two drops of NucBlue™ Live ReadyProbes™ Reagent into 1 ml of Lipid-free IF9S medium. Add 100 µl to each well of macrophages and incubate at 37 °C for 20 min.
- 4a. Optionally, take images with the microscope during the incubation of NucBlue. Set the incubation chamber of the microscope to 37 °C and 5% CO₂.
- 5a. Remove NucBlue solution and dissociate macrophages with Accutase for 10 min at 37 °C.
- 6a. Collect cells from duplicate wells in a 5 ml FACS tube. Wash once with FACSB and analyze with a flow cytometer right away to measure Alexa Fluor 594 intensity in cells.

Bacterial Phagocytosis Assay

The bacterial phagocytosis assay should be performed in a molecular biology lab and not in the cell culture room to avoid bacterial contamination of cultured cells (all reagents, cells and equipment should be kept out of the cell culture lab).

- 1b. On the day of the assay, take one vial of pHrodo Green *E. coli* BioParticles Conjugate for all 30 wells to be tested. Add 1 ml of PS-free IF9S medium. Vortex for 30 s and transfer suspension into a clean glass tube. Add another 2 ml of PS-free IF9S medium. And incubate for 30 min at RT.
- 2b. Sonicate pHrodo Green *E. coli* BioParticles in PS-free IF9S medium for 15 min and incubate for 30 min at RT.
- 3b. Vortex pHrodo Green *E. coli* BioParticles in PS-free IF9S medium for 30 s and transfer to a 15-ml tube. Centrifuge at 200 rpm (1.8 g) for 1 min at RT. Transfer supernatant to a new tube.

It is crucial to obtain a homogenous single cell suspension. Cell clumps can be avoided by low-speed centrifugation. Take a small aliquot diluted in medium and check under a microscope to make sure all clumps are depleted.

- 4b. Add 70 µl pHrodo Green *E. coli* BioParticles (supernatant from the previous step 3b) per one well of 96-well plate containing macrophages (from Basic Protocol 2). Incubate for 30 min at 37 °C.
- 5b. Prepare NucBlue solution and add 100 µl to each well. Incubate at 37 °C for 20 min.

- 6b. Optionally, take images with the microscope during the incubation of NucBlue. Set the incubation chamber of the microscope to 37 °C and 5% CO₂.
- 7b. Remove NucBlue solution and dissociate macrophages with Accutase solution for 10 min at 37 °C.
- 8b. Collect cells from duplicate wells into a 5 ml FACS tube. Wash once with FACS buffer. Fix cells with 4% PFA and wash once with DPBS.

It is important to fix the cells in order to kill bacteria and avoid contamination of other reagents and equipment. Fixed cells can be stored in DPBS in the dark for up to 48 h at 4 °C.

- 9b. Analyze with a flow cytometer to measure Alexa Fluor 488 intensity in cells.

Efferocytosis Assay

This assay can be used to examine the capability of iPSCs for taking-up apoptotic cells. Live hiPSCs are also needed in this assay as a negative control.

- 1c. Culture hiPSCs in a normal manner as described in Basic Protocol 1, as a source of apoptotic cells for the assay.

To obtain enough hiPSCs, perform the assay when hiPSCs are confluent. Usually one well of confluent hiPSCs in 6-well plate are sufficient for 15-20 wells of the assay in a 96-well plate format. Prepare one extra well of hiPSCs for live cell control (non-apoptotic cells).

- 2c. On the day of the assay, dissociate hiPSCs with Accutase solution at 37 °C for 5 min. Then add 2 ml TeSR-E8 medium and pipette 3-4 times with a P1000 to obtain a single cell suspension. Centrifuge at 1100 rpm (300 g) for 3 min at RT.
- 3c. Spin down hiPSCs and resuspend in 3 ml TeSR-E8. Transfer the cell suspension into a 35x10 mm dish.
- 4c. Place the dish under the UV lamp at ~3 cm distance. Set the light intensity to 35 J/cm². Remove the lid and expose cells to UV light for 5 min.

It is necessary to optimize the UV light intensity and exposure time depending on the UV lamp used. Cells are more sensitive to the change of exposure time rather than the change of UV light intensity. Be aware that UV light exposure may cause eye and skin damage and carcinogenesis. Perform the experiment in an enclosed space or wear protective mask and clothes.

- 5c. Place the dish with cells back in the incubator for 1 h. During this incubation time, start to dissociate another well of hiPSCs using Accutase solution for the negative control without UV treatment.
- 6c. Spin down both apoptotic (UV treated) and live hiPSCs at 1100 rpm (300 g) for 3 min.

Take an aliquot of both apoptotic and live hiPSCs to determine the percentage of apoptotic cells. Apoptotic cells should be Annexin V+ and PI-. More than half of hiPSCs should be apoptotic due to the UV-treatment.

- 7c. Add 2 µl CFSE dye into 2 ml PBS to get a 5 µM CFSE working solution. Resuspend both tubes of hiPSCs in 1 ml of CFSE solution. Incubate at 37 °C for 20 min.
- 8c. Add 5 ml FACS-B-10 to each tube of hiPSCs and count cell number of each tube. Centrifuge at 1100 rpm (300 g) for 3 min.
- 9c. Resuspend cells in IF9S medium to a final cell concentration of 4 million/ml.
- 10c. Add 50 µl cell suspension to each well of iPSDMs. Incubate at 37 °C for 1 h.
- 11c. Wash each well of iPSDMs with 100 µl IF9S medium.
- 12c. Dissociate iPSDMs with Accutase at 37 °C for 10 min. Collect cells from duplicate wells in a 5 ml FACS tube. Wash once with FACS-B.
- 13c. Stain cells with anti-CD11b fluorescent-conjugated antibody for 30 min at 4 °C.
- 14c. Wash once with FACS-B and analyze with the flow cytometer immediately to measure the CFSE intensity within the population of CD11b+ iPSDMs.

Tumor Phagocytosis Assay

Jurkat cells (an immortalized line of human T lymphocyte cells) are used in this assay as targeted tumor cells to be phagocytosed by iPSDMs. Jurkat cells without anti-CD47 antibody treatment serve as a negative control. Jurkat cells are cultured in Jurkat Medium in a T75 flask and passaged every 4 days with 1:10 ratio.

- 1d. On the day of the assay, collect Jurkat cells and count cell number.
- 2d. Calculate the volume of Jurkat cell suspension needed (200K cells per well). Centrifuge at 1100 rpm (300 g) for 3 min.
- 3d. Resuspend cells in 1 ml CFSE working solution (5 µM in PBS, 1 µL in 999 µL, 1:1000 dilution). Incubate at 37 °C for 20 min.
- 4d. Add 5 ml FACS-B-10 to the tube. Aliquot the cell suspension into two tubes. One for the negative control without anti-CD47 treatment and the other for the experimental group with anti-CD47 treatment. Centrifuge both tubes at 1100 rpm (300 g) for 3 min.
- 5d. Suspend cells in both tubes in 50 µl FACS-B. Add 3 µl anti-CD47 (3 µg) for every million Jurkat cells in the experimental tube. Leave the negative control tube untreated. Incubate at 4 °C for 30 min.
- 6d. Wash once with FACS-B and resuspend cells in both tubes in IF9S medium to a final concentration of 4 million/ml.
- 7d. Add 50 µl cell suspension to each well of iPSDMs. Incubate at 37 °C for 2 h.
- 8d. Wash each well of iPSDMs with 100 µl IF9S medium.

- 9d. Dissociate iPSDMs with Accutase at 37 °C for 10 min. Collect cells from duplicate wells into a 5 ml FACS tube. Wash once with FACS B.
- 10d. Stain cells with anti-CD11b fluorescent-conjugated antibody for 30 min at 4 °C.
- 11d. Wash once with FACS B and analyze with the flow cytometer right away to measure CFSE intensity within CD11b+ iPSDMs.

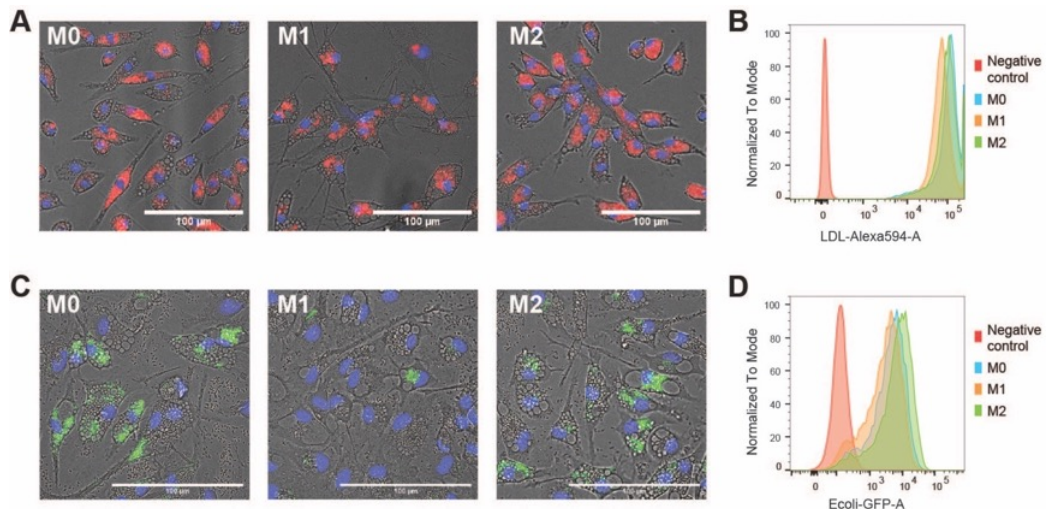


Figure 4 Endocytosis and phagocytosis of bacteria by iPSDMs. **(A)** Representative images of the AcLDL-Alexa Fluor 594 uptake assay by different subtypes of iPSDMs. AcLDL positive uptake is shown in red; cell nuclei are stained with Hoechst in blue. Scale bar represents 100 μ m. **(B)** FACS analysis of AcLDL-Alexa Fluor 594 median fluorescence intensity of different macrophage subtypes. M0 macrophages only is included as negative control. **(C)** Representative images of bacterial phagocytosis by different subtypes of iPSDMs. Nuclei were stained with Hoechst in blue. GFP-labeled (pHrodo green) *E. coli* were pH sensitive and only show green fluorescence inside macrophages. Scale bar represents 100 μ m. **(D)** FACS analysis of *E. coli*-GFP median fluorescence intensities in macrophage subtypes. M0 macrophages only is included as negative control.

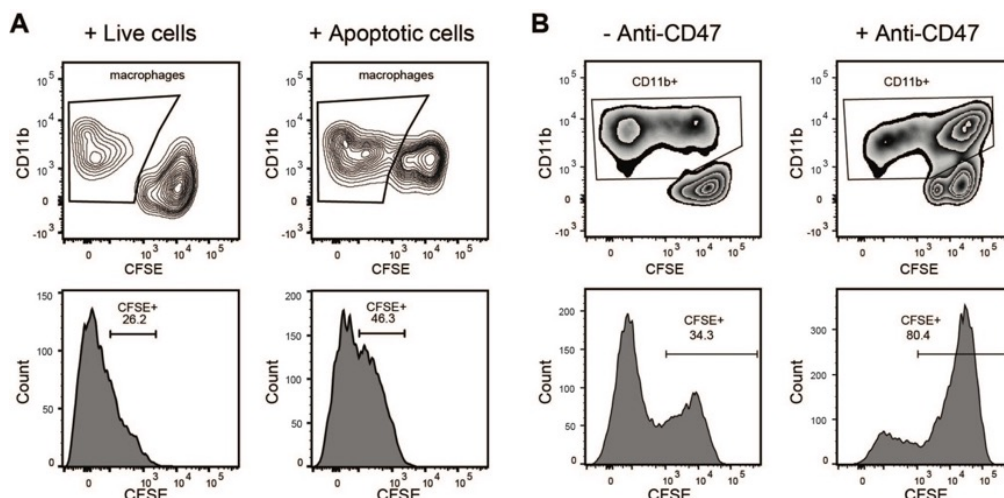


Figure 5 Efferocytosis and tumor phagocytosis assay of iPSDMs **(A)** Efferocytosis assay of M0-iPSDMs. Live cells (negative control) and apoptotic cells were labeled with CFSE and incubated with M0-iPSDMs. CD11b⁺ macrophages are gated (upper panel) and their CFSE intensity is shown in histograms (lower panel). **(B)** Phagocytosis of Jurkat cells by M0-iPSDMs. CFSE-labeled Jurkat cells were incubated with or without anti-CD47 blocking antibody and incubated with macrophages for 2 h. CD11b⁺ macrophages are gated (upper panel) and their CFSE intensity is shown in histograms (lower panel).

REAGENTS AND SOLUTIONS

AA2P (5 mg ml⁻¹)

Add 250 mg of AA2P to 50 ml of distilled water, non-sterile. Store at -20°C for up to 1 year.

Activin A (25 µg ml⁻¹ stock solution)

Reconstitute at a concentration of 25 µg ml⁻¹ in PBS containing 1% (wt/vol) BSA. Prepare aliquots and store for up to 1 year at -80 °C.

αMTG (1.3% (vol/vol))

Add 130 µl αMTG to 9,87 ml IMDM and store it at 4 °C protected from light.

BMP-4 (25 µg ml⁻¹ stock solution)

First reconstitute at a concentration of 100 µg ml⁻¹ in 4 mM HCl containing 1% (wt/vol) BSA. Then dilute further to 25 µg ml⁻¹ in PBS containing 0.1% (wt/vol) BSA. Prepare aliquots and store for up to 1 year at -80°C.

BSA, 1% (wt/vol) in PBS

Dissolve 0.5 g of BSA in 50 ml of PBS. Sterilize the solution by filtration by using a 0.22-µm membrane filter, and store it for up to 4 weeks at 4 °C.

CHIR99021 (CHIR) solution, 4mM

Reconstitute 10 mg in 5.37 ml in DMSO. Prepare aliquots and store at -20 °C.

CFSE dye

Take one vial of CFSE dye in the kit and reconstitute it in 18 μ l DMSO (provided in the kit) to prepare a 5 mM CFSE stock solution and store protected from light at -20 °C for up to 1 year.

EDTA, 0.5 M (pH 8.0)

Add 186.1 g of EDTA to 800 ml of distilled water. Adjust the pH to 8.0 with NaOH and add distilled water to a final volume of 1 liter. Filter the solution through a 0.22- μ m membrane filter and sterilize it by autoclaving. Store the solution for up to 1 year at room temperature (RT; 20 °C).

FACS buffer

Dissolve 1.25 g of BSA in 250 ml of PBS and add 1 ml of 0.5 M EDTA (pH 8.0). Sterilize the medium by using a Stericup filter (0.22 μ m) and store it for up to 4 weeks at 4 °C.

FACSB-10 (FACS buffer–10% (vol/vol) FBS)

Add 5 ml of FBS to 45 ml of FACS buffer, and sterilize it by filtration by using a 0.22- μ m membrane filter. Store the buffer for 4 weeks at 4 °C.

FGF2 (100 μ g ml⁻¹ stock solution)

Reconstitute at 100 μ g ml⁻¹ in PBS containing 0.1% (wt/vol) BSA. Prepare aliquots and store at -80 °C for up to 1 year. Avoid repeated freeze-thaw cycles.

SCF (50 μ g ml⁻¹ stock solution)

Reconstitute at 50 μ g ml⁻¹ in PBS containing 0.1% (wt/vol) BSA. Prepare aliquots and store them at -20 °C or below. Avoid repeated freeze-thaw cycles.

IFN- γ (40 μ g ml⁻¹ stock solution)

Reconstitute at 40 μ g ml⁻¹ in PBS containing 0.1% (wt/vol) BSA. Prepare aliquots and store them at -20 °C or below for up to 1 year. Avoid repeated freeze-thaw cycles.

IL-3 (20 μ g ml⁻¹ stock solution)

Reconstitute at 20 μ g ml⁻¹ in PBS containing 0.1% (wt/vol) BSA. Prepare aliquots and store at -20 °C or below for up to 1 year. Avoid repeated freeze-thaw cycles.

IL-4 (20 μ g ml⁻¹ stock solution)

Reconstitute at 20 μ g ml⁻¹ in PBS containing 0.1% (wt/vol) BSA. Prepare aliquots and store them at -20 °C or below for up to 1 year. Avoid repeated freeze-thaw cycles.

IL-6 (100 μ g ml⁻¹ stock solution)

Reconstitute at 100 μ g ml⁻¹ in PBS containing 0.1% (wt/vol) BSA. Prepare aliquots and store them at -20 °C or below for up to 1 year. Avoid repeated freeze-thaw cycles.

IL-10 (20 μ g ml⁻¹ stock solution)

Reconstitute at 20 μ g ml⁻¹ in PBS containing 0.1% (wt/vol) BSA. Prepare

aliquots and store them at $-20\text{ }^{\circ}\text{C}$ or below for up to 1 year. Avoid repeated freeze-thaw cycles.

LPS ($100\text{ }\mu\text{g ml}^{-1}$ stock solution)

Reconstitute at $100\text{ }\mu\text{g ml}^{-1}$ in PBS containing 0.1% (wt/vol) BSA. Prepare aliquots and store them at $-20\text{ }^{\circ}\text{C}$ or below for up to 1 year. Avoid repeated freeze-thaw cycles.

M-CSF ($80\text{ }\mu\text{g ml}^{-1}$ stock solution)

Reconstitute at $80\text{ }\mu\text{g ml}^{-1}$ in PBS containing 0.1% (wt/vol) BSA. Prepare aliquots and store them at $-20\text{ }^{\circ}\text{C}$ or below for up to 1 year. Avoid repeated freeze-thaw cycles.

PFA (4%, wt/vol)

Add 1 volume of PFA (8%, wt/vol) to 1 volume of 0.2 M phosphate buffer (pH 7.4). Cover the mixture with foil and keep it at $4\text{ }^{\circ}\text{C}$ for up to 2 weeks.

PFA (8%, wt/vol)

Add 40 g of PFA to 400 ml of Milli-Q water. Heat PFA up to $60\text{ }^{\circ}\text{C}$ and stir it at medium speed. After a few minutes, add ~ 10 drops of 1 N NaOH to dissolve the PFA granules. Eventually, the solution will become translucent. Let the solution cool down and add Milli-Q water to a total volume of 500 ml. Store the solution at $4\text{ }^{\circ}\text{C}$ for up to 2 months.

Phosphate buffer, 0.2 M (pH 7.4)

To prepare solution 1, dissolve 8.28 g of $\text{NaH}_2\text{PO}_4 \cdot \text{H}_2\text{O}$ in 300 ml of Milli-Q water. To prepare solution 2, dissolve 10.78 g of $\text{Na}_2\text{HPO}_4 \cdot 2\text{H}_2\text{O}$ in 300 ml of Milli-Q water. Add solution 1 to solution 2 until a pH of 7.4 is obtained, to make 0.2 M phosphate buffer (pH 7.4). This buffer can be stored at RT indefinitely (no expiration date).

PVA (5% (wt/vol))

Add 2 g of PVA to 40 ml of distilled water in a 50 ml tube. Leave the tube for 2 days on a roller bank at RT. Heat the tube for 10 min at $75\text{ }^{\circ}\text{C}$ to completely dissolve the PVA. Prepare aliquots and store at $4\text{ }^{\circ}\text{C}$, non-sterile.

SB431542 (20mM)

Reconstitute 10 mg in 1.3 ml in DMSO. Prepare aliquots and store at $-20\text{ }^{\circ}\text{C}$.

TGF β 3 ($5\text{ }\mu\text{g ml}^{-1}$)

Reconstitute the content of the vial to a concentration of $5\text{ }\mu\text{g ml}^{-1}$ in 4mM HCl containing 0.1% (wt/vol) BSA. Prepare aliquots and store up to 1 year at $-80\text{ }^{\circ}\text{C}$.

TPO ($50\text{ }\mu\text{g ml}^{-1}$ stock solution)

Reconstitute at $50\text{ }\mu\text{g ml}^{-1}$ in PBS containing 0.1% (wt/vol) BSA. Prepare aliquots and store them at $-20\text{ }^{\circ}\text{C}$ or below. Avoid repeated freeze-thaw cycles.

VEGF ($50\text{ }\mu\text{g ml}^{-1}$ stock solution)

Reconstitute at $50\text{ }\mu\text{g ml}^{-1}$ in PBS containing 0.1% (wt/vol) BSA. Prepare

aliquots and store them for up to 1 year at -80°C .

0.1% (vol/vol) TX-100 in PBS

Add 50 μl of TX-100 to 50 ml of PBS. Sterilize the solution by filtration using a 0.22- μm membrane filter. Store it for up to 1 year at RT.

IF9S medium

Prepare 250 ml of IF9S medium as shown. Sterilize the medium using a Stericup filter and store at 4°C for up to 3 weeks. The formulation is based on previously described IF9S medium (Uenishi et al., 2014).

Composition	Volume	Final concentration
IMDM	117.25 ml	
F12	117.25 ml	
PVA (5%)	50 μl	10 mg ml^{-1}
Lipids (100X)	250 μl	0.1%
ITS-X (100X)	5 ml	2%
αMTG (1.3%)	750 μl	40 $\mu\text{l l}^{-1}$
AA2P (5 mg ml^{-1})	3.2 ml	64 mg l^{-1}
Glutamax (200 mM)	2.5 ml	2 mM
NEAA (100X)	2.5 ml	1%
Pen/Strep (5,000 U ml^{-1})	1.25 ml	0.5%

Lipid-free IF9S medium

Prepare IF9S medium without Lipids (100X).

PS-free IF9S medium

Prepare IF9S medium without Pen/Strep (5,000 U ml^{-1}).

Mesoderm induction medium

Prepare mesoderm induction medium as shown. Always freshly prepare the medium.

Composition	Volume	Final concentration
IF9S	25 ml	
Activin A (25 $\mu\text{g ml}^{-1}$)	15 μl	15 ng ml^{-1}
BMP4 (25 $\mu\text{g ml}^{-1}$)	40 μl	40 ng ml^{-1}
CHIR (4 mM)	9,4 μl	1.5 μM

Hemogenic endothelium induction medium

Prepare hemogenic endothelium induction medium as shown. Always prepare the medium freshly.

Composition	Volume	Final concentration
IF9S	25 ml	
VEGF (50 $\mu\text{g ml}^{-1}$)	25 μl	50 ng ml^{-1}

SB431542 (20 nM)	12,5 µl	10 µM
FGF2 (100 µg ml ⁻¹)	12,5 µl	50 ng ml ⁻¹
SCF (50 µg ml ⁻¹)	25 µl	50 ng ml ⁻¹

Hematopoietic induction medium

Prepare hematopoietic induction medium as shown. Always prepare the medium freshly.

Composition	Volume	Final concentration
IF9S	25 ml	
IL-6 (100 µg ml ⁻¹)	12.5 µl	50 ng ml ⁻¹
IL-3 (20 µg ml ⁻¹)	12.5 µl	10 ng ml ⁻¹
TPO (50 µg ml ⁻¹)	25 µl	50 ng ml ⁻¹
FGF2 (100 µg ml ⁻¹)	12.5 µl	50 ng ml ⁻¹
SCF (50 µg ml ⁻¹)	25 µl	50 ng ml ⁻¹
VEGF (50 µg ml ⁻¹)	25 µl	50 ng ml ⁻¹

Monocyte induction medium

Prepare monocyte induction medium as shown. Always prepare the medium freshly.

Composition	Volume	Final concentration
IF9S	25 ml	
M-CSF (80 µg ml ⁻¹)	25 µl	80 ng ml ⁻¹
IL-6 (100 µg ml ⁻¹)	12.5 µl	50 ng ml ⁻¹
IL-3 (20 µg ml ⁻¹)	12.5 µl	10 ng ml ⁻¹

M0 medium

Prepare M0 medium as shown. Always prepare the medium freshly.

Composition	Volume	Final concentration
IF9S	25 ml	
M-CSF (80 µg ml ⁻¹)	25 µl	80 ng ml ⁻¹

M1 Medium

Prepare M1 medium as shown. Always prepare the medium freshly.

Composition	Volume	Final concentration
IF9S	25 ml	
LPS (100 µg ml ⁻¹)	2.5 µl	10 ng ml ⁻¹
IFN-γ (40 µg ml ⁻¹)	12.5 µl	20 ng ml ⁻¹

M2 Medium

Prepare M2 medium as shown. Always prepare the medium freshly.

Composition	Volume	Final concentration
IF9S	25 ml	
IL-4 (20 $\mu\text{g ml}^{-1}$)	25 μl	20 ng ml^{-1}

Jurkat Medium

Prepare 250 ml of Jurkat medium as shown. Sterilize the medium using a Stericup filter and store for up to 3 weeks 4°C.

Composition	Volume	Final concentration
RPMI 1640	250 ml	
FBS	25 ml	10%
Glutamax (200 mM)	2.5 ml	2 mM
BME (50 mM)	250 μl	50 μM
Pen/Strep (5,000 U ml^{-1})	2.5 ml	1%

Vitronectin-coated 6-well plate

Warm-up CellAdhere™ Dilution Buffer to room temperature (RT). Thaw 80 μl Vitronectin XF™ at RT and add it to 2.42 ml Dilution Buffer. Mix well and add 1.25 ml to each well of 6-well Cell Suspension Plates. Distribute Vitronectin to cover the whole well and incubate in RT for 1 hour. The plate can be used right away. Otherwise it can be sealed with Parafilm and stored at 4 °C for up to 2 weeks.

Matrigel-coated six-well plate

Thaw 100 μl Matrigel on ice for each 6-well cell culture plate. Aliquot 12 ml cold (4 °C) DMEM/F12 medium into a 50 ml tube. Cool a pipette tip by pipetting up and down the cold DMEM/F12 medium several times and use it to transfer thawed Matrigel into the medium. Mix with a cold (4 °C) pipette and add 2 ml to each well. Leave the plate at RT for 1 h and use it right away. Otherwise it can be sealed with Parafilm and stored at 4 °C for up to 2 weeks.

COMMENTARY

BACKGROUND INFORMATION

During embryo hematopoiesis, HPCs are generated from HEs in the aorta-gonad-mesonephros (AGM) region of the embryo which forms from the mesoderm lineage. Several protocols have been reported for the induction of monocytes and macrophages from hPSCs that rely on mimicking the hematopoiesis *in vivo*. In 2009, Choi et al. successfully differentiated hiPSCs into CD43+CD45+ hematopoietic progenitors through

the coculture with OP9 stromal cells; these could later be differentiated into mature macrophages using M-CSF and IL-1 β (Choi et al., 2009; 2011). In 2008, an embryoid body (EB)-based differentiation method was reported to induce monocyte-like cells from hPSCs using M-CSF and IL-3 (Karlsson et al., 2008; Wilgenburg et al., 2013). In 2015, a similar EB-based method was described, which can be used to derive granulocytes, monocytes and macrophages from hPSCs (Lachmann et al., 2015). Recently, this continuous harvesting method was successfully translated into bioreactors for mass production of iPSCs (Ackermann et al., 2018). Also, in 2015, Zhang et al. published another EB-based protocol which used single-time point harvesting instead of continuous harvesting. They induced mesoderm, HPCs and myeloid cells from hiPSCs sequentially, although the presence of HEs were not examined in their differentiation system (Zhang et al., 2015). More recently, monolayer differentiation protocols have been reported by several groups. Uenishi et al. established an elegant hematopoietic induction method from hPSCs using a stepwise strategy. Mesoderm cells were first induced with BMP4, Activin A, LiCl and FGF2, which were further differentiated into HEs using VEGF and FGF2. Then HPCs were induced from HEs with SCF, IL-6, IL-3, TPO, FGF2 and VEGF, which showed multilineage differentiation potential toward lymphoid and myeloid cells (Uenishi et al., 2014). In 2017, Takata et al. reported a comparable stepwise method to derive primitive macrophages from hiPSCs (Takata et al., 2017). Hypoxia conditions were utilized for hematopoietic induction in both monolayer protocols.

Our protocol described here utilizes the monolayer differentiation approach rather than EBs. It has the particular advantage that it is more efficient and robust than EB-based methods. For the induction of HPCs from hiPSCs (day 0-9), our method is similar to that of Uenishi et al. (Uenishi et al., 2014), although different growth factors were used for the induction of mesoderm and HEs (Cao et al., 2019). Mesoderm cells are first induced from hiPSCs in 2 days and then into CD144+CD73- HEs for another 3 days, using our previously established EC induction method (Orlova et al., 2014a; 2014b). To induce CD43+ HPCs from HEs, SCF, IL-6, IL-3, TPO, FGF2 and VEGF are applied from day 5 to day 9, much like the previously published protocol by Uenishi et al. (Uenishi et al., 2014) with the exception that we use normoxic conditions. Next, we induced the formation of CD14+ monocytes from HPCs. All cells were dissociated on day 9 and cultured in the presence of IL-3, IL-6 and M-CSF in suspension. After 5 to 6 days culture, more than half of the cells became CD14+ monocytes which could be purified and cryopreserved and later thawed for functional analysis or further polarization toward different macrophages subtypes. A unique feature of this protocol compared to other differentiation methods is the dissociation step for HPCs on day 9, followed by suspension culture which notably maximizes differentiation efficiency compared with collecting only the floating cells continuously (Karlsson et al., 2008; Lachmann et al.,

2015) or at a single time point (Takata et al., 2017; Wilgenburg et al., 2013; Zhang et al., 2015).

Compared to continuous harvesting, single-time point harvesting has a relatively lower total cell yield but with higher reproducibility across different lines and batches which is critical for disease modeling. hiPSC-mono from this protocol could be cryopreserved and still preserve their phenotype (Fig. 2A) and functionalities (Fig. 2C-D), which greatly facilitates their application in disease modeling *in vitro*. However, this protocol is not ideal for mass production of cells within bioreactors compared to continuous harvesting methods. Another limitation of this protocol is that the isolation step for CD14⁺ monocytes using magnetic beads, which is relatively labor intensive and expensive. Lastly, although defined and xeno-free medium is used throughout the protocol, the extracellular matrix used for coating is of animal origin and includes Matrigel and FBS. This may introduce batch-to-batch variations and need to be optimized or defined for application in regenerative medicine or clinical studies.

Functionality of hiPSC-mono can be examined via their adhesion to immobilized recombinant proteins that mediate the leukocyte recruitment cascade during inflammation, such as fibronectin, E-selectin, intercellular adhesion molecule-1 (ICAM-1), and vascular cell adhesion molecule-1 (VCAM-1). Alternatively, adhesion to activated, TNF- α , lipopolysaccharide (LPS) or IL-1 β stimulated endothelial cells (ECs) can be used. Traditionally, static assays are used, however they lack the physiological flow that is important for leukocyte adhesion and is essential in shear-induced activation of leukocyte integrins. Therefore, leukocyte adhesion in a microfluidic flow assay is a more physiologically relevant way of assessing functionality of hiPSC-mono and cross compare them with primary cells. Previously we described a detailed protocol to study adhesion of monocytes to hiPSC-ECs in a microfluidic chip (Halaidych et al., 2018b). The protocol was applied to study adhesion of human monocytic cell line (THP1) (Halaidych et al., 2018a), blood-mono and hiPSC-mono (Cao et al., 2019). We have previously shown that hiPSC-ECs when compared to primary HUVECs exhibit lower induction of leukocyte pro-adhesive receptors, such as E-selectin and ICAM-1, and lack upregulation of VCAM-1 upon treatments with various pro-inflammatory cytokines (TNF- α , LPS and IL-1 β) (Halaidych et al., 2018a). Pre-conditioning of hiPSC-ECs with bone morphogenetic protein 9 (BMP9) enhances inflammatory responses and results in an increase in VCAM-1 expression (Cao et al., 2019), which is an important receptor for very late antigen 4 (VLA-4, α 4 β 1, CD49d and CD29) integrin on leukocytes. VLA-4 is highly expressed on T-cells and neutrophils and is absent on blood-mono. hiPSC-mono show increased VLA-4 expression so that use of optimal stimulation conditions that facilitate VCAM-1 upregulation on hiPSC-ECs is recommended. Alternatively, HUVECs can be used, as they are known to express high levels of VCAM-1 after TNF- α treatment. hiPSC-ECs used in this assay were differentiated and cultured as previously described (Orlova et al., 2014a;

2014b).

Macrophages show diverse functions *in vivo* including phagocytosis, microbicidal killing, cytokine production, antigen presentation and antitumor activity (Woods et al., 2000). Functional activities of iPSDM subtypes can be assessed using various cell type specific assays. Endocytotic activity of iPSDMs can be determined using AcLDL uptake (Fig. 4A-B). Phagocytosis of bacteria is studied by adding GFP-labeled *Escherichia coli* (*E. coli*) to iPSDMs and the phagocytic efficiency is quantified by FACS (Fig. 4C-D). The capacity for uptake apoptotic cells (efferocytosis) can also be measured. Target cells induced to undergo apoptosis by UV light exposure are added to iPSDMs and the efferocytosis efficiency quantified by FACS (Fig. 5A). Different target cell types can be used for efferocytosis including hiPSCs and blood neutrophils although cancer cells are best avoided due to high tumor phagocytosis by macrophages. Lastly, tumor phagocytosis can be measured to investigate the anti-tumor activity of iPSDMs. Jurkat cells are often used as target cells for this; they are incubated with iPSDMs in the presence or absence of CD47 blocking antibody (anti-CD47) and the phagocytic efficiency is quantified by FACS (Fig. 5B). Other cancer cell types which express high levels of CD47 can also be used in the assay. PBDMs that differentiate and polarize in the same way as iPSDMs can be included as controls for the characterization and functional assays of iPSDMs.

iPSDMs derived from this protocol showed higher endocytosis and efferocytosis capacities than PBDMs (Cao et al., 2019), indicating a more tissue-resident macrophages-like identity (A-Gonzalez et al., 2017; Swirski et al., 2016). In addition, it has been shown that iPSDMs can be conditioned by neuronal cells to acquire a microglia identity *in vitro* (Takata et al., 2017; Haenseler et al., 2017). IL-34 could also drive the microglia differentiation from hiPSCs (Brownjohn et al., 2018; Muffat et al., 2016). These results suggest that the iPSDMs we obtain can be a source of tissue resident macrophages, especially for microglia cells. The characterization methods and functional assays described in this protocol could also be applicable also for other source of monocytes and macrophages, as they had been tested with both iPSDMs and PBDMs previously (Cao et al., 2019).

CRITICAL PARAMETERS:

hiPSCs used for the differentiation in this protocol are cultured on Vitronectin-coated plates in defined TeSR-E8 medium. Compared to other methods using irradiated mouse embryonic fibroblast (MEF) feeders or FBS, this defined protocol is simpler and more robust. Spontaneous differentiation of hiPSCs should be avoided as an undifferentiated state of hiPSCs is required for the successful differentiation of monocytes and macrophages. Cells should be passaged regularly every week and successful

maintenance of hiPSCs should yield uniform and compact colonies with more than 90% confluency after one week of passaging.

The whole differentiation process consists of two parts: the derivation of monocytes from hiPSCs in 14-15 days and the differentiation of mature macrophage subtypes from cryopreserved monocytes in 6-7 days (Fig. 1). Compared to the protocol published originally, we included a flexible time for the induction of HPCs to monocytes, as well as for the differentiation of M0 macrophages from monocytes; this can be adjusted depending on each differentiation and hiPSC line used. The monocyte induction from day 9 should last 5 to 6 days in order to get enough CD14⁺ monocytes with more than 50% purity before isolation. However, a longer induction time than 6 days should be avoided as monocytes usually start to adhere and differentiate into macrophages from day 14/15.

The initial seeding density of hiPSCs on Matrigel is absolutely crucial for the efficient differentiation of hematopoietic cells from hiPSCs. Too high seeding densities could inhibit or abolish completely the production of roundish HPCs from day 5 to day 9. At the beginning, we recommend testing different seeding densities with split ratios ranging from 1:30 to 1:50, in order to find out the optimal seeding density of the hiPSC line used.

The dissociation step on day 9 of the differentiation is one of the most labor intensive and critical steps during the whole differentiation process. Cells on day 9 contain multilayers including roundish HPCs on the top and other stromal or progenitor cells at the bottom. We recommend dissociating and collecting the majority of the cells by dissociation with enzyme and scraping. However, the whole procedure should be gentle to avoid too much cell death, as dead cells could inhibit differentiation and lead to activation of monocytes and reduction of the yield.

Both freshly isolated and cryopreserved monocytes can be used for the induction of functional macrophages on FBS-coated plates. We strongly recommend using fresh monocytes when large quantity of macrophages are needed, due to a much higher proliferative and recovery rate of fresh monocytes after seeding compared to cryopreserved monocytes. However, cryopreserved monocytes are excellent for disease modeling and other biological studies where macrophages from multiple batches and hiPSC lines are needed for experiments.

With regards to supplementation with M-CSF during the differentiation, we used 80 ng/ml for both monocyte induction from day 9 to day 14/15 and later the macrophage differentiation from monocytes. We observed higher M-CSF concentrations (up to 80 ng/ml) improved the differentiation efficiency of CD14⁺ monocytes. However, lower concentrations of M-CSF (40-80 ng/ml) can be used for macrophage induction from monocytes without affecting the yield and cell activity.

During the development of our protocols for the polarization of M1 and M2

macrophages, we found a higher starting density of M0 could benefit the survival of polarized M1 and M2 macrophages. So, a higher seeding density of monocytes and longer differentiation time for M0 are recommended when large numbers of polarized M1 and M2 are needed. The optimal polarization time is 24-48 hours. M2 macrophages start to undergo apoptosis after 48 hours of polarization. So, we recommend polarizing M1 and M2 macrophages from M0 for not more than 48 hours.

TROUBLESHOOTING:

The detailed troubleshooting guidelines can be found in Table 1.

Table 1. Troubleshooting

Step	Problem	Possible reason	Solution
Basic Protocol 1 (step 18)	Very few roundish hematopoietic cells	Too high starting seeding density of hiPSCs	Reduce hiPSC seeding density
Basic Protocol 1 (step 28)	Most monocytes adhere to the plate	Too many dead cells introduced on day 9 by dissociation	During dissociation, pipette cells gently and reduce incubation time with Accutase solution; Harvest monocytes on day 14 instead of day 15
Support Protocol 1 (step 10)	Liquid doesn't flow through the column	Column gets blocked by cell clumps	Filter cells with CellTrics® filter to get single cell suspension
Support Protocol 2 (step 8a)	Too high or low cell density	Cell suspension is not mixed well before loading; Too much or few cell suspensions loaded	Mix cells well before loading; Optimize volume of cell suspension loaded
Basic Protocol 2 (step 6)	No cells adhere two days after thawing	Old IF9S medium; Cell death during thawing procedure	Prepare fresh IF9S; Avoid vigorous pipetting and minimize the time of thawing procedure

Support Protocol 4 (step 6c)	Too few apoptotic cells or too many necrotic cells	UV exposure time not optimal; Incubation time after UV treatment is not optimal	Adjust UV exposure time from 3 to 7 min; Adjust incubation time from 1 h to 2 h
------------------------------	--	--	--

UNDERSTANDING RESULTS:

As the initial step of the differentiation protocol, seeding of hiPSCs at an optimal density is crucial for the efficient induction of hematopoietic cells. Around 60,000 hiPSCs should be seeded in each well of the 6-well plate which should give rise to 30-40 small size colonies the next day. These colonies expand continuously from day 0 to day 5 (Fig. 1). More than 60% of CD140a+ mesoderm cells on day 2 and 40% VEC+ endothelium on day 5 should be obtained and most of these VEC+ endothelium on day 5 should also be CD73- HEs (Fig.1). Non-adherent, roundish hematopoietic cells should appear from the center of colonies from around day 7 and their number grow continuously until day 9 (Fig. 1 and video S1). The number of roundish HPCs on day 9 is an easy and reliable way to assess the hematopoietic differentiation efficiency. More than 50% of the cells on day 9 should be CD43+ HPCs. Differentiations with few or no HPCs on day 9 are regarded as failed and should not be continued (see table 1 for troubleshooting). On day 9, all floating cells and adherent cells are collected and seeded in the low-attachment plate. Large numbers of single roundish cells and dark spheres can be observed under the microscope. During suspension culture from day 9 to day 14/15, the total cell number and cell morphology hardly change. In some differentiations, adherent cells can already be observed on day 14, indicating activation and maturation of monocytes that are ready to be harvested. For most differentiations, cells should be ready for harvest on day 15 when more than 50% have become CD14+ monocytes. More than 10 million CD14+ monocytes should be obtained from each 24-well low-attachment plate, and the purity of CD14+ cells should be higher than 90% after isolation (Fig. 1) (Cao et al., 2019).

An advantage of this protocol is that hiPSC-mono can be cryopreserved yet retain their phenotype and functionality. The recovery rate of cryopreserved hiPSC-mono should be higher than 40%. Thawed monocytes express similar levels of CD14, CD45, CD49d, CD18, CD29 and CD11b as newly isolated hiPSC-derived monocytes (Fig. 2A). To assess their functionality, a microfluidic assay can be performed with thawed hiPSC-mono (Fig. 2B). Thawed hiPSC-mono should adhere to both hiPSC-ECs and HUVECs activated by TNF- α , while greater adhesion should be observed with HUVECs than hiPSC-EC (Fig. 2C-D).

Thawed hiPSC-mono can also be polarized and give rise to M0, M1 and M2 macrophages. After 48 hours of seeding on FBS-coated plates, only a minority of thawed

monocytes will adhere with a roundish morphology. After refreshing on day 2, cells proliferate rapidly and reach around 80% confluence on day 4 or day 5 depending on the performance of differentiation and cryopreservation. After polarization for another 2 days, M0 should show an elongated morphology while M1 have a stellar shape with multiple protrusions, and M2 have a more rounded morphology with a lower cell density compared to M0 and M1 (Fig. 1). All subtypes should express comparable levels of specific pan-macrophage markers CD11b, CD18, and CD45 by FACS. M0 and M2 express higher CD206 and CD163, while M1 have the highest CD80 expression (Fig. 3). Optionally, qPCR and Multiplex cytokine assay can be performed for further characterization of derivative macrophage subtypes (Cao et al., 2019).

To investigate the functional activities of iPSDMs, several assays described in this protocol can be applied based on individual research interests. In the endocytosis assay, all iPSDM subtypes should show high levels of DiI-AcLDL uptake and higher endocytosis activity should be observed in M0 and M2 than M1 (Fig. 4A-B). In the bacterial phagocytosis assay, anti-inflammatory M0 and M2 should show higher phagocytic activity of *E. coli* than the pro-inflammatory M1 subtype (Fig. 4C-D). For the efferocytosis assay, iPSDMs should take up more apoptotic cells than live cells that have not undergone UV-treatment (Fig. 5A). Regarding the apoptotic target cells used in the efferocytosis assay, a more than 50% Annexin V+PI- apoptotic cells should be induced by the UV treatment (Cao et al., 2019). To investigate tumor phagocytotic activity of iPSDMs, CFSE-labeled Jurkat cells can be added to iPSDMs. After incubation, CFSE-labeled Jurkat cells should be observed within iPSDMs cell bodies under the microscope. iPSDMs should show significantly higher phagocytosis of Jurkat cells in the presence of anti-CD47 compared to the control group without anti-CD47 blocking antibody (Fig. 5B).

TIME CONSIDERATION

Basic Protocol 1: The differentiation of monocytes from hiPSCs takes 14 to 15 days in total.

(step 1-11) ~20 min will be need for passaging of hiPSCs for maintenance.

(step 12-15) ~20 min will be needed for passaging of hiPSCs to Matrigel-coated plate for differentiation;

(step 16-18) ~15 min will be needed on each day of day 0, 2, 5, 7 to change the media;

(step 19-26) ~1 h will be needed to collect floating hematopoietic cells and dissociation of adherent cells;

(step 27) ~15 min will be needed to change media for the suspension culture;

Support protocol 1:

(step 1-15) ~1.5 h will be needed to collect all cells, perform CD14+ cell isolation and cryopreservation of isolated cells.

Support Protocol 2:

(step 1a-8a) ~3 h will be needed to do Wright-Giemsa staining (include 2 h drying of slide);

(step 1b-6b) ~1 h will be needed for FACS of monocytes (include 30 min incubation);

Basic Protocol 2: The differentiation of macrophage subtypes from monocytes takes 6 to 7 days in total.

(step 1-5) ~15 min will be needed to thaw cryopreserved monocytes and seed into FCS-coated plate;

(step 6) ~ 10 min will be needed to change the media 2 days after seeding;

(step 8-10) ~20 min will be needed for the dissociation and seeding of M0 macrophages

(step 11) ~10 min will be needed to change the media

Support Protocol 3:

(step 1a-6a) ~1.5 h will be needed for FACS of iPSCMs (include 30 min incubation);

(step 1b-12b) ~6 h will be needed for Multiplex cytokine assay (include 3 h incubation);

Support Protocol 4:

(step 1a-6a) ~5.5 h will be needed to perform the AcLDL uptake assay (include 4 h incubation);

(step 1b-9b) ~2.5 h will be needed to perform the Bacterial phagocytosis assay;

(step 1c-14c) ~4 h will be needed to perform the Efferocytosis assay (include two times 1 h incubation);

(step 1d-11d) ~5 h will be needed to perform the Tumor phagocytosis assay (include 2 h incubation).

ACKNOWLEDGEMENTS:

We thank Christian Freund and LUMC hiPSC Hotel for providing LUMC0020, LUMC0054 and LUM0083 hiPSC lines, and the LUMC Flow Cytometry Core Facility and the LUMC Light and Electron Microscopy Facility. We are grateful for financial support from the Netherlands Science Foundation (NWO) under the Gravitation Grant ‘NOCI’ (# 024.003.001) and the European Union’s Horizon 2020 research and innovation Programme under grant agreement No. 668724.

LITERATURE CITED:

- A-Gonzalez, N., Quintana, J. A., García-Silva, S., Mazariegos, M., González de la Aleja, A., Nicolás-Ávila, J. A., Walter, W., Adrover, J. M., Crainiciuc, G., Kuchroo, V. K., et al. 2017. Phagocytosis imprints heterogeneity in tissue-resident macrophages. 214:1281.
- Ackermann, M., Kempf, H., Hetzel, M., Hesse, C., Hashtchin, A. R., Brinkert, K., Schott, J. W., Haake, K., Kühnel, M. P., Glage, S., et al. 2018. Bioreactor-based mass production of human iPSC-derived macrophages enables immunotherapies against bacterial airway infections. *Nature Communications* 9:5088–5013.

- Brownjohn, P. W., Smith, J., Solanki, R., Lohmann, E., Houlden, H., Hardy, J., Dietmann, S., and Livesey, F. J. 2018. Functional Studies of Missense TREM2 Mutations in Human Stem Cell-Derived Microglia. *Stem Cell Reports* 10:1294–1307.
- Buchrieser, J., James, W., and Moore, M. D. 2017. Human Induced Pluripotent Stem Cell-Derived Macrophages Share Ontogeny with MYB-Independent Tissue-Resident Macrophages. *Stem Cell Reports* 8:334–345.
- Cao, X., Yakala, G. K., van den Hil, F. E., Cochrane, A., Mummery, C. L., and Orlova, V. V. 2019. Differentiation and Functional Comparison of Monocytes and Macrophages from hiPSCs with Peripheral Blood Derivatives. *Stem Cell Reports* 12:1282–1297.
- Choi, K.-D., Vodyanik, M. A., and Slukvin, I. I. 2009. Generation of mature human myelomonocytic cells through expansion and differentiation of pluripotent stem cell-derived lin[−]CD34⁺CD43⁺CD45⁺ progenitors. *Journal of Clinical Investigation* 119:2818–2829.
- Choi, K.-D., Vodyanik, M., and Slukvin, I. I. 2011. Hematopoietic differentiation and production of mature myeloid cells from human pluripotent stem cells. *Nature Protocols* 6:296–313.
- Dou, D. R., Calvanese, V., Sierra, M. I., Nguyen, A. T., Minasian, A., Saarikoski, P., Sasidharan, R., Ramirez, C. M., Zack, J. A., Crooks, G. M., et al. 2016. Medial HOXA genes demarcate haematopoietic stem cell fate during human development. *Nature Cell Biology* 18:595–606.
- Ginhoux, F., and Jung, S. 2014. Monocytes and macrophages: developmental pathways and tissue homeostasis. *Nature Reviews Immunology* 14:392–404.
- Haenseler, W., Sansom, S. N., Buchrieser, J., Newey, S. E., Moore, C. S., Nicholls, F. J., Chintawar, S., Schnell, C., Antel, J. P., Allen, N. D., et al. 2017. A Highly Efficient Human Pluripotent Stem Cell Microglia Model Displays a Neuronal-Co-culture-Specific Expression Profile and Inflammatory Response. *Stem Cell Reports* 8:1727–1742.
- Halaidych, O. V., Freund, C., van den Hil, F., Salvatori, D. C. F., Riminucci, M., Mummery, C. L., and Orlova, V. V. 2018a. Inflammatory Responses and Barrier Function of Endothelial Cells Derived from Human Induced Pluripotent Stem Cells. *Stem Cell Reports* 10:1642–1656.
- Halaidych, O. V., van den Hil, F., Mummery, C. L., and Orlova, V. V. 2018b. Microfluidic Assay for the Assessment of Leukocyte Adhesion to Human Induced Pluripotent Stem Cell-derived Endothelial Cells (hiPSC-ECs). *Journal of Visualized Experiments*.
- Happle, C., Lachmann, N., Ackermann, M., Mirenska, A., Göhring, G., Thomay, K., Mucci, A., Hetzel, M., Glomb, T., Suzuki, T., et al. 2018. Pulmonary Transplantation of Human Induced Pluripotent Stem Cell-derived Macrophages Ameliorates Pulmonary Alveolar Proteinosis. *American Journal of Respiratory and Critical Care Medicine* 198:350–360.
- Ivanovs, A., Rybtsov, S., Ng, E. S., Stanley, E. G., Elefanty, A. G., and Medvinsky, A. 2017. Human haematopoietic stem cell development: from the embryo to the dish. *Development* 144:2323–2337.
- Karlsson, K. R., Cowley, S., Martinez, F. O., Shaw, M., Minger, S. L., and James, W. 2008. Homogeneous monocytes and macrophages from human embryonic stem cells following coculture-free differentiation in M-CSF and IL-3. *Experimental Hematology* 36:1167–1175.

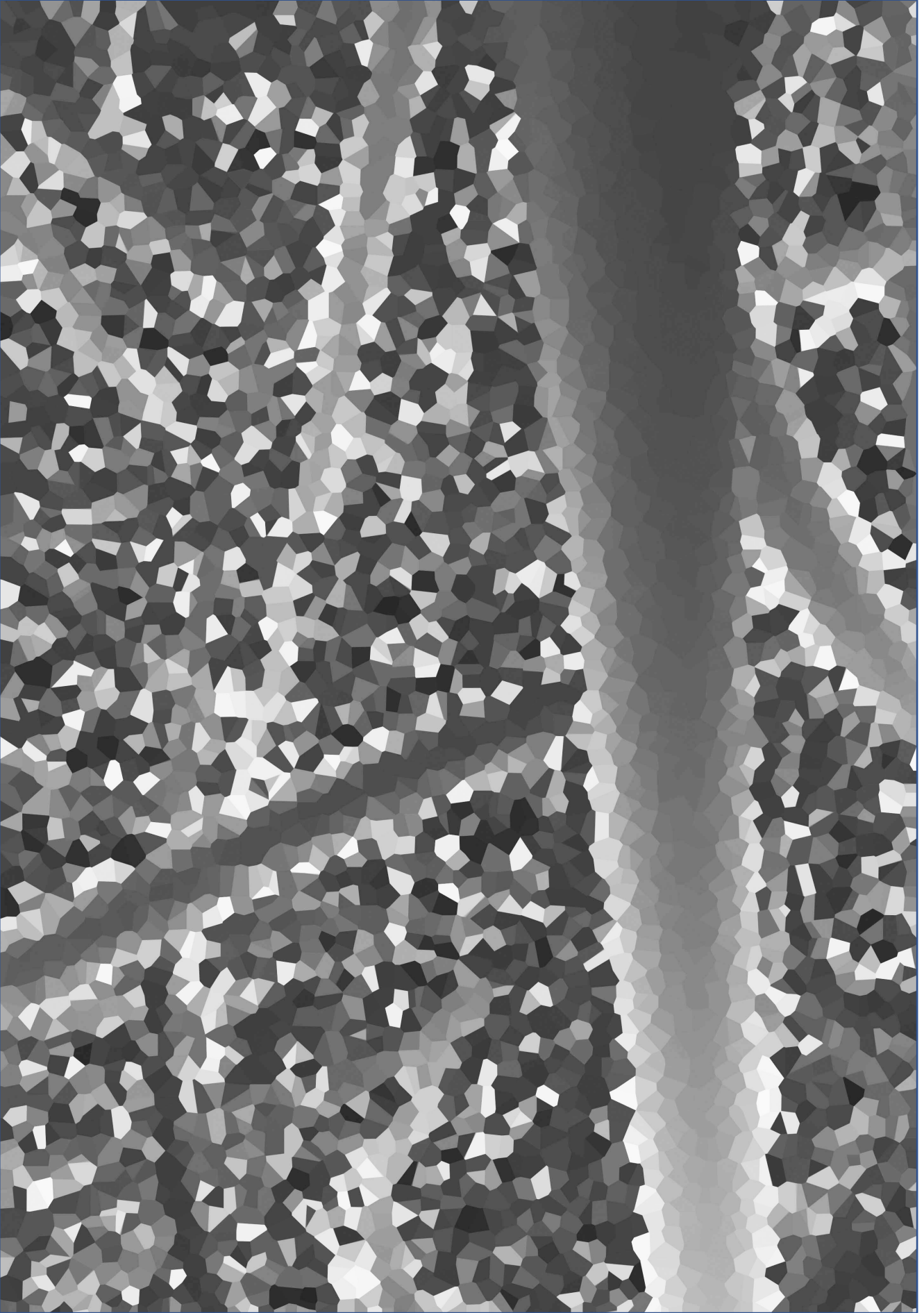
- Lachmann, N., Ackermann, M., Frenzel, E., Liebhaber, S., Brenning, S., Happle, C., Hoffmann, D., Klimenkova, O., Lüttge, D., Buchegger, T., et al. 2015. Large-Scale Hematopoietic Differentiation of Human Induced Pluripotent Stem Cells Provides Granulocytes or Macrophages for Cell Replacement Therapies. *Stem Cell Reports* 4:282–296.
- Mantovani, A., SICA, A., SOZZANI, S., ALLAVENA, P., VECCHI, A., and Locati, M. 2004. The chemokine system in diverse forms of macrophage activation and polarization. *Trends in Immunology* 25:677–686.
- Muffat, J., Li, Y., Yuan, B., Mitalipova, M., Omer, A., Corcoran, S., Bakiasi, G., Tsai, L.-H., Aubourg, P., Ransohoff, R. M., et al. 2016. Efficient derivation of microglia-like cells from human pluripotent stem cells. *Nature Medicine* 22:1358–1367.
- Ng, E. S., Azzola, L., Bruveris, F. F., Calvanese, V., Phipson, B., Vlahos, K., Hirst, C., Jokubaitis, V. J., Yu, Q. C., Maksimovic, J., et al. 2016. Differentiation of human embryonic stem cells to HOXA+ hemogenic vasculature that resembles the aorta-gonad-mesonephros. *Nature Biotechnology* 34:1168–1179.
- Orlova, V. V., Drabsch, Y., Freund, C., Petrus-Reurer, S., van den Hil, F. E., Muenthaisong, S., Dijke, P. T., and Mummery, C. L. 2014a. Functionality of Endothelial Cells and Pericytes From Human Pluripotent Stem Cells Demonstrated in Cultured Vascular Plexus and Zebrafish Xenografts. *Arterioscler Thromb Vasc Biol* 34:177–186.
- Orlova, V. V., van den Hil, F. E., Petrus-Reurer, S., Drabsch, Y., Dijke, ten, P., and Mummery, C. L. 2014b. Generation, expansion and functional analysis of endothelial cells and pericytes derived from human pluripotent stem cells. *Nature Protocols* 9:1514–1531.
- Rószter, T. 2015. Understanding the Mysterious M2 Macrophage through Activation Markers and Effector Mechanisms. *Mediators of Inflammation* 2015:1–16.
- Swirski, F. K., Robbins, C. S., and Nahrendorf, M. 2016. Development and Function of Arterial and Cardiac Macrophages. *Trends in Immunology* 37:32–40.
- Takata, K., Kozaki, T., Lee, C. Z. W., Thion, M. S., Otsuka, M., Lim, S., Utami, K. H., Fidan, K., Park, D. S., Malleret, B., et al. 2017. Induced-Pluripotent-Stem-Cell-Derived Primitive Macrophages Provide a Platform for Modeling Tissue-Resident Macrophage Differentiation and Function. *Immunity* 47:183–198.e6.
- Uenishi, G., Theisen, D., Lee, J.-H., Kumar, A., Raymond, M., Vodyanik, M., Swanson, S., Stewart, R., Thomson, J., and Slukvin, I. 2014. Tenascin C Promotes Hematoendothelial Development and T Lymphoid Commitment from Human Pluripotent Stem Cells in Chemically Defined Conditions. *Stem Cell Reports* 3:1073–1084.
- Vanhee, S., De Mulder, K., Van Caeneghem, Y., Verstichel, G., Van Roy, N., Menten, B., Velghe, I., Philippé, J., De Bleser, D., Lambrecht, B. N., et al. 2015. In vitro human embryonic stem cell hematopoiesis mimics MYB-independent yolk sac hematopoiesis. 100:157–166.
- Wilgenburg, B. V., Browne, C., Vowles, J., and Cowley, S. A. 2013. Efficient, Long Term Production of Monocyte-Derived Macrophages from Human Pluripotent Stem Cells under Partly-Defined and Fully-Defined Conditions. *PLoS ONE* 8:e71098.

- Woods, J., Lu, Q., Ceddia, M. A., and Lowder, T. 2000. Special feature for the Olympics: effects of exercise on the immune system: exercise-induced modulation of macrophage function. *Immunology and cell biology* 78:545–553.
- Wynn, T. A., Chawla, A., and Pollard, J. W. 2013. Macrophage biology in development, homeostasis and disease. *Nature* 496:445–455.
- Zhang, H., Xue, C., Shah, R., Bermingham, K., Hinkle, C. C., Li, W., Rodrigues, A., Tabita-Martinez, J., Millar, J. S., Cuchel, M., et al. 2015. Functional Analysis and Transcriptomic Profiling of iPSC-Derived Macrophages and Their Application in Modeling Mendelian Disease. *Circulation research* 117:17–28.
- Zhang, M., D'Aniello, C., Verkerk, A. O., Wrobel, E., Frank, S., Ward-van Oostwaard, D., Piccini, I., Freund, C., Rao, J., Seeböhm, G., et al. 2014. Recessive cardiac phenotypes in induced pluripotent stem cell models of Jervell and Lange-Nielsen syndrome: disease mechanisms and pharmacological rescue. *PNAS* 111:E5383–92.

Video Legend

Video S1: Time-lapse video from differentiation day 7 to day 9 (can be found online Doi: 10.1002/cpsc.108)

Video legend: Time lapse take from differentiation day 7 to day 9 at a frequency of 30 minutes each frame. This video plays at 10 frames per seconds. Scale bar represents 200 μm .



Chapter 4

Transcriptional Dynamics During Segregation of Endothelial and Myocardial Lineages from Cardiac Mesoderm

Xu Cao¹, Maria Mircea², Gopala Krishna Yakala¹, Francijna E. van den Hil¹, Hailiang Mei³, Konstantinos Anastassiadis⁴, Christine L. Mummery¹, Stefan Semrau² and Valeria V. Orlova^{1, *}

¹Department of Anatomy and Embryology, Einthovenweg 20, 2333ZC Leiden, The Netherlands

²Leiden Institute of Physics, Leiden University, 2333 RA, Leiden, The Netherlands

³Sequencing analysis support core, Leiden University Medical Center, Leiden, 2333ZA, The Netherlands

⁴Stem Cell Engineering, Biotechnology Center, Center for Molecular and Cellular Bioengineering, Technische Universität Dresden, Dresden, 01307, Germany

*Corresponding author

Manuscript in preparation

ABSTRACT

We previously showed that two major cellular components of the human heart, cardiac endothelial cells and cardiomyocytes, could be derived simultaneously from human induced pluripotent stem cells (hiPSCs). *In vivo* studies in mice have shown these lineages derive from a common MESP1+ mesoderm progenitor. Although this has been investigated using whole transcriptome sequencing, the transcriptional control and dynamics of their segregation from cardiac mesoderm are not yet fully understood. In addition, the same transgenic approach cannot be used in human. Here, we used bulk and single cell RNA sequencing (RNAseq) to investigate EC and cardiomyocytes co-differentiation in hiPSC. We confirmed segregation of these two cardiac lineages from common cardiac mesoderm precursors but more importantly, revealed a critical role of transient expression of the transcription factor ETV2 for endothelial fate specification and showed unexpectedly that functional cardiomyocytes could also originate from ETV2+ progenitors.

INTRODUCTION

The ability to obtain different cardiac lineages derived from human induced pluripotent stem cells (hiPSCs) can facilitate studies of human heart development and modeling of cardiovascular diseases *in vitro*. Cardiomyocytes and endothelial cells (ECs) are two major cell types in the heart and their crosstalk through physical interactions and paracrine, autocrine and endocrine factors (Tirziu et al., 2010) has allowed the generation of physiologically relevant cardiac (micro)tissues, organoids and engineered heart tissues *in vitro* (Caspi et al., 2007; Giacomelli et al., 2017; Goldfracht et al., 2020; Masumoto et al., 2016; Mills et al., 2017; Narmoneva et al., 2004; Ravenscroft et al., 2016; Stevens et al., 2009; Tulloch et al., 2011).

Cardiomyocytes and ECs originate from *Mesp1*+ progenitors specified during gastrulation. In mice, these cells are first located in primitive streak and then migrate toward lateral plate mesoderm at ~E6.5 (Devine et al., 2014; Lescroart et al., 2014; Meilhac et al., 2014; Saga et al., 1999). It is still controversial when the segregation of cardiomyocytes and ECs from common progenitors actually occurs. scRNAseq of mouse *Mesp1*+ progenitors collected at E6.75 and E7.25 showed that these cells were already segregated into distinct cardiovascular lineages, including cardiomyocytes and ECs (Lescroart et al., 2018). However, some studies showed multipotential progenitors were still present in lateral plate mesoderm which originates in the primitive streak and expresses *Flk-1* (Ema et al., 2006; Garry and Olson, 2006). These cells were initially recognized as multipotent cardiac progenitor cells (CPCs) (Tam et al., 1997). However, in human heart development, there is limited knowledge on the timing and transcriptional control for segregation of cardiac endothelial and myocardial lineages from multipotent CPCs.

Studies in mouse and chick showed heart mainly develops from two sources of progenitors (Buckingham et al., 2005; Vincent and Buckingham, 2010): the first heart field (FHF) in the cardiac crescent contributes to the primitive heart tube which serves as a scaffold into which second heart field (SHF) cells can migrate before heart chamber morphogenesis. It had already been shown that cells from SHF were patterned before migration in to give rise to different parts of heart (Galli et al., 2008; Zaffran et al., 2004). CPCs from FHF and SHF could be distinguished by expression of *ISL1*, which was specifically expressed in SHF (Cai et al., 2003). *NKX2-5* expressing CPCs in both FHF and SHF from E7.5 to E7.75 could contribute to both the cardiomyocytes and ECs in the heart (Paffett-Lugassy et al., 2013). As a direct target of *NKX2-5*, *ETV2* was found to be expressed in all ECs but not myocardium by E8.5 (Ferdous et al., 2009). *ETV2* was required for the development of endothelial and hematopoietic lineages and directly targets *TAL1*, *GATA2*, *LMO2*, *TEK*, *NOTCH1*, *NOTCH4*, *CDH5* (De Val et al., 2008; Ferdous et al., 2009; Lee et al., 2008; Liu et al., 2015). Overexpression of *ETV2* itself could convert human fibroblasts into endothelial-like cells (Morita et al., 2015). In mouse embryonic stem cells (ESCs), *ETV2* could initiate the hemangiogenic specification in a threshold-dependent manner instructed by VEGF signaling (Zhao et al., 2017). Later, *ETV2* expression was also found to direct the segregation of hemangioblasts and smooth muscle cells (SMCs) in mouse ESCs (Zhao and Choi, 2019). However, it is still unclear whether *ETV2* also plays a role in the segregation of ECs and cardiomyocytes from CPCs during human heart development.

Previously we found that *MESP1*⁺ progenitors derived from human ESCs could give rise to cardiomyocytes, ECs and SMCs (Hartogh et al., 2015). *Flk-1*⁺ cardiovascular progenitors generated from ESCs resembled CPCs *in vivo* (Moretti et al., 2006). Recently we developed a co-differentiation system for ECs and cardiomyocytes from hiPSCs through a common cardiac mesoderm (CM) stage (Giacomelli et al., 2017). ECs thus derived showed a cardiac specific identity, evidenced by high expression of cardiac markers *MEOX2*, *GATA4*, *GATA6* and *ISL1*. The developmental path and transcriptional dynamics during differentiation of endothelial and myocardial lineages in this protocol have, however, not yet been characterized.

Droplet-based single cell RNA sequencing (scRNAseq) greatly facilitates the study of global transcriptional dynamics at single cell resolution. Paik et al. performed scRNAseq analysis of hiPSC-derived ECs (hiPSC-ECs) which were less than 10% of the total population among cells expressing the cardiac marker *TNNT2*. The developmental process of EC and cardiac lineages as such were not further studied (Paik et al., 2018). In another scRNAseq study on hiPSC-ECs from a different differentiation method, pseudotime analysis of ECs collected at different time points showed that endothelial and mesenchymal lineages had a common developmental origin in mesoderm cells (McCracken et al., 2019), although the identity and differentiation potential of these

mesenchymal cells was not characterized.

Here, we performed both scRNAseq and bulk RNAseq on cells from our co-differentiation system. scRNAseq analysis identified CM as the common developmental origin of cardiomyocytes and ECs. *ETV2* expression was observed principally in the endothelial lineage but also in a subpopulation of the myocardial lineage. An *ETV2*^{mCherry} hiPSC reporter line was generated and used to study real-time expression dynamics and the role of *ETV2* during endothelial and myocardial lineage segregation and development. We found that different subpopulations of *ETV2*⁺ progenitors showed distinct differentiation potentials toward cardiomyocytes and ECs. The segregation of endothelial and myocardial fates was controlled in an *ETV2*-threshold dependent manner. scRNAseq analysis described the transcriptional dynamics during cardiomyocytes and ECs development and maturation, which correlated with the time-course of bulk RNAseq analysis. Early and late progenitors for both lineages were also identified. In summary, this study depicted the developmental path and segregation of human cardiomyocytes and ECs from CM in hiPSC.

RESULTS

Single-cell profiling of co-differentiation of cardiomyocytes and endothelial cells from hiPSCs

To investigate the developmental path of ECs and cardiomyocytes from hiPSC (Figure 1A), we carried out scRNAseq on day 6 of differentiation. A total 5107 and 3743 cells were analysed from two independent differentiations (Figure S1A-B) and visualized using Uniform Manifold Approximation and Projection (UMAP). Unsupervised cell clustering resulted in 5 clusters (Figure S1C). Cells in cluster 4 showed high expression of pluripotent markers, such as *POU5F1* and *NANOG* (Figure S1D) and were therefore excluded from downstream analysis (Figure S1E). Cells from two independent differentiations clustered similarly, although replicate 2 had fewer cells in cluster 1 (Figure S1F). Cells in clusters 3 and 5 mainly differed in the expression of cell-cycle- and proliferation-related genes (data not shown), with the highest G2M- and Proliferation scores found in cluster 5 compared to cluster 3 (Figure S1G-H). We therefore further reduced the number of clusters to three (C1, C2, C3) by combining clusters 3 and 5 (Figure 1B).

Next, marker genes of each cell cluster were identified in order to determine their identities (Table S1). Cluster C1 was characterized by increased expression of CM and cardiac progenitor genes, such as *MESP1*, *ISL1*, *DKK1*, *SMARCD3*, *ABLIM1*, *TMEM88* as well as cell cycle genes *CDK6* and *NEK2* (C1: CM (Figure 1C, F). Cluster C2 was characterized by increased expression of early cardiomyocyte-specific genes, including *MYL4*, *TNNI1*, *MYL7*, *ACTA2*, *TNNT2*, *HAND2* and *NKX2-5* (C2: Cardiac progenitors (CPs))(Figure 1D, G). Cluster C3 was characterized by increased expression of EC-specific

genes, such as *CDH5*, *CD34*, *KDR*, *HEY2*, *TEK*, *TIE1*, *ACVRL1*, *SOX17*, *ENG*, *ICAM2*, *PECAM1* (Endothelial progenitors) (EPs)) (Figure 1E, H). Notably, the *ETV2* transcription factor, a master regulator of hematoendothelial specification, was highly expressed in the EP cell cluster and a small fraction of cells in the CM and CP cell clusters (Figure 1I).

Pseudotime analysis of co-differentiation of endothelial cells and cardiomyocytes from hiPSCs

Diffusion pseudotime analysis (Haghverdi et al., 2016) at day 6 of differentiation showed segregation into three developmental branches that corresponded to CM, CP and EP cell clusters (Figure 2A). Developmental trajectories of CPs and EPs originating at the CM branch. Based on the pseudotime analysis, the EP branch progressed further in development compared to the CP branch. *MESP1* was highly expressed in the CM branch and at an early time-point of the EP and CP branches (Figure 2B). Cardiac makers *MYL4*, *TNNI1* and EC markers *CDH5*, *PECAM1* were expressed specifically in the CP and EP branches respectively (Figure 2B). Genes related to cardiac or muscle functionalities, like *ACTC1*, *GATA4*, *PKP2*, *HAND1* and *PDLIM5* were expressed at the end of CM branch and further increased in the CP branch (Figure S2A). Endothelial specific genes *CDH5*, *PECAM1*, *CD34*, *KDR* and *SOX17* increased in pseudotime from the CM branch to the EP branch (Figure S2B). *ETV2* was highly expressed in the early EP branch and in a small number of cells across CPs and the late CM branch (Figure 2B). *ETV2* showed transient expression around 2.19 to 2.49 pseudotime time label with peak expression around 2.25 pseudotime time label (Figure 2C, S2A-B). Analysis of *ETV2* expression in the period of 2.19 to 2.49 pseudotime time label showed highest *ETV2* expression and percentage of *ETV2*⁺ cells in the EP branch (Figure 2D and Figure S2C). *ETV2* expression was comparable in *ETV2*⁺ cells in all three developmental branches (Figure S2D). Expression of *ETV2* downstream target genes, such as *TAL1*, *GATA2* and *LMO2* (Liu et al., 2015) was induced after *ETV2* and correlated with the increased *ETV2* expression (Figure 2E, F). Analysis of DEGs in *ETV2*⁺ cells in CP and EP developmental branches showed enrichment in cardiomyocyte and endothelial cell specific genes indicating that the cells acquired these respective identities (Figure 2G, Table S2) and have further segregated from *ETV2*⁺ cells in the CM developmental branch (Figure S2E-F).

Generation and characterization of genetically encoded *ETV2*^{mCherry} fluorescent hiPSC reporter line

In order to follow *ETV2* expression during co-differentiation of endothelial cell- and cardiomyocytes differentiation of hiPSCs in real-time, a P2A-mCherry fluorescence reporter with nuclear localization signal (NLS) and neomycin selection cassette was inserted into the endogenous *ETV2* locus before the stop codon using CRISPR/Cas9-facilitated homologous recombination (Figure S3A). Targeted hiPSC clones after

Neomycin selection and excision of the selection cassette were confirmed by PCR (Figure S3A, B) and Sanger sequencing. Clones with ETV2^{mCherry} targeted into both alleles were selected for downstream analysis (Figure S3C). Time-lapse imaging of differentiating cultures showed the appearance of nuclear mCherry from day 4 of differentiation followed by the appearance of endothelial cell markers, such as VE-cadherin (CD144) and lectin (Figure S3D-E and Video S1). mCherry protein remained for a longer period than the endogenous *ETV2* mRNA expression (Figure S3F-G).

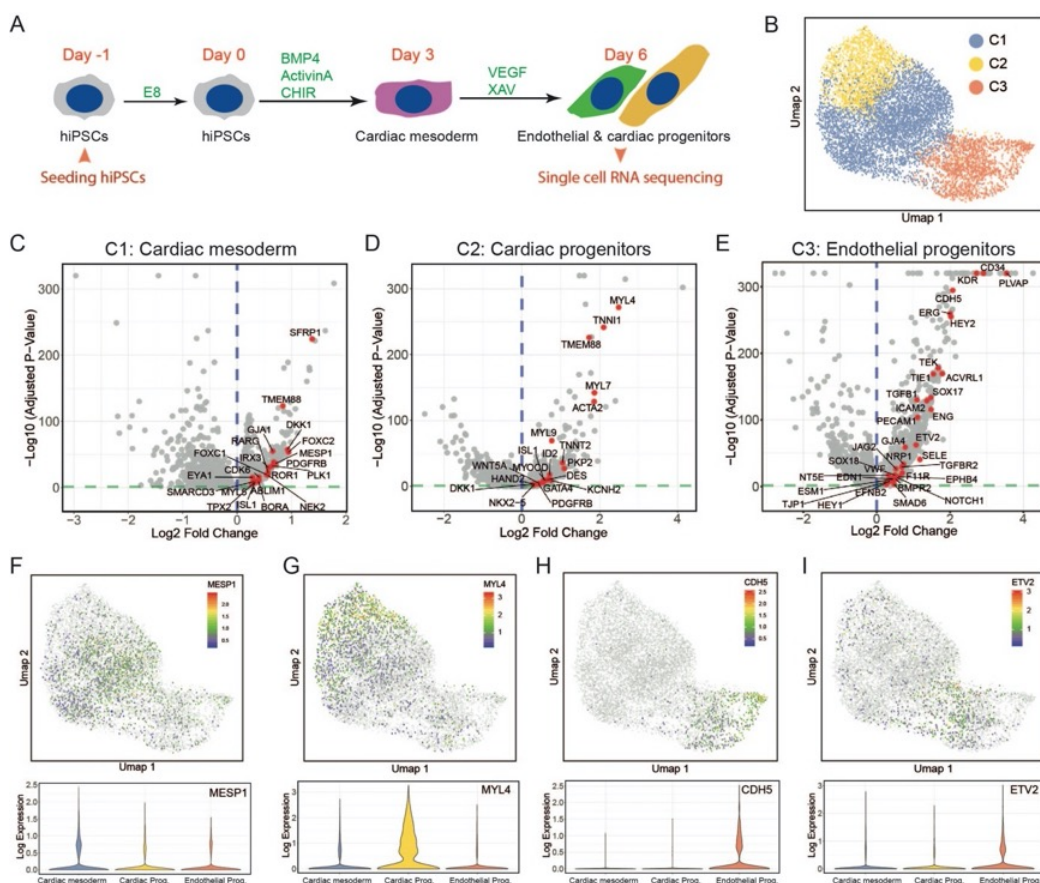


Figure 1. Single-cell RNA sequencing analysis of endothelial and cardiac lineages during co-differentiation of hiPSCs (A) Schematic overview of CMEC differentiation protocol from day -1 to day 6. Cells were collected for scRNAseq on day 6. (B) scRNAseq data of day 6 visualized using UMAP. Three clusters (C1-C3) of cells were identified. (C-E) Volcano plots show fold change and p values of all genes in each cluster compared to background (all the rest of cells). Representative significant up-regulated genes ($P_{\text{adjusted}} < 0.05$ & fold change > 1.2) are labelled in red. (F-G) *MESP1*, *MYL4*, *CDH5* and *ETV2* expression (log₂ transformed) in individual cells (UMAPs) and three clusters (violin plots).

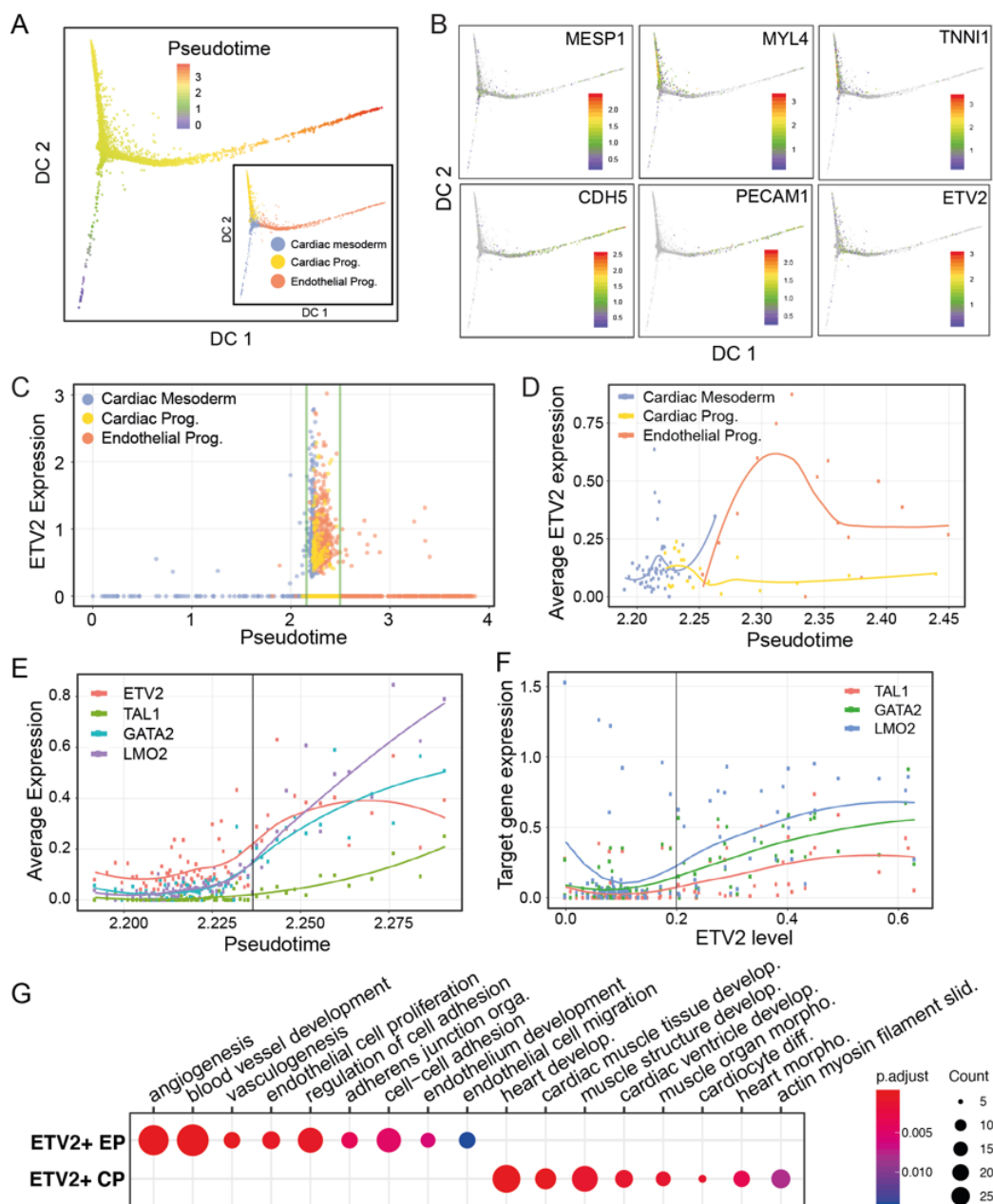


Figure 2. Pseudotime analysis for EC and cardiomyocytes co-differentiation from hiPSCs (A) Dimensionality reduction of scRNAseq data of day 6 using diffusion map. Cell identities are labeled with different colors (bottom right) based on clusters identified in Figure 1B. (B) Diffusion maps show expression patterns of *MESP1*, *MYL4*, *TNNI1*, *CDH5*, *PECAM1* and *ETV2*. (C) Expression (\log_2 transformed) of *ETV2* following pseudotime in CM, CPs and EPs branches. Pseudotime 2.19 and 2.49 were labeled with green lines to show main *ETV2* expression time window. (D) Average expression of *ETV2* of each branch between pseudotime 2.19 to 2.49. Bins

of pseudo time with equal number of cells (50 cells) were constructed and the average expression was calculated among these cells. (E) Average expression of *ETV2* and its direct target genes *TAL1*, *GATA2*, *LMO* in CM and EPs cells between pseudotime 2.19 to 2.49. Bins of pseudo time with equal number of cells (50 cells) were constructed and the average expression was calculated among these cells. (F) Correlation of *ETV2* level with *ETV2* target genes' expression in CM and EPs cells between pseudotime 2.19 to 2.49. Bins of pseudo time with equal number of cells (50) were constructed and the average expression was calculated among these cells. (G) GO enrichment analysis of differentially expressed genes (DEGs) between *ETV2*+ EPs and *ETV2*+ CPs. 128 and 136 genes were upregulated in *ETV2*+ EPs and CPs respectively ($P_{\text{adjusted}} < 0.05$). A complete list of GOs can be found in Table S2. Color represents the P_{adjusted} of enrichment analysis and dot size represents count of genes mapped to the GO.

***ETV2*^{mCherry} fluorescent reporter line recapitulates developmental trajectories during co-differentiation of endothelial cells and cardiomyocytes from hiPSCs**

Bulk RNA sequencing was next performed on *ETV2*^{mCherry}+CD144+ (DP) and *ETV2*^{mCherry}+CD144- (SP) cells sorted on day 4, 5, 6 and 8 of endothelial cell- and cardiomyocyte co-differentiation from at least 3 independent differentiations (Figure 3A). Principal component (PC) analysis showed separate clustering of DP and SP cells with progressive change over the time (Figure 3B). Mapping of bulk RNAseq samples on scRNAseq diffusion pseudotime plot resulted in co-aligning of DP cells on the EP branch and SP cells on the CP branch (Figure 3C). Notably day 8 SP cells clustered further away from the differentiating cells in the CP branch suggesting a more advanced differentiation state (Figure 3C).

Consensus clustering of the most variable genes across DP or SP cells (3000 genes for each cell type) resulted in three gene clusters with distinct gene expression profiles D1-D3 (DP cells) and S1-S3 (SP cells) (Figure S4A-B, Table S3). Cluster D1 (1226 genes) was characterized by increased expression of of respective genes over time, cluster D2 (1127 genes) was characterized by decreased expression of of respective genes at day 5 of differentiation and cluster D3 (647 genes) was characterized by the decreased expression of of respective genes on day 8 of differentiation (Figure 3D). Gene Ontology (GO) analysis of cluster D1 showed enrichment in terms for angiogenesis, Notch signalling pathway, transforming growth factor beta receptor signalling pathway, receptor-mediated endocytosis and developmental maturation (Figure 4F, Table S4). Specifically, angiogenesis-related genes (*CDH5*, *TIE1*, *TEK*, *EFNB2*, *SOX18*, *VEGFB*, *LEPR*), Notch and transforming growth factor beta receptor signalling pathway related genes (*COL1A2*, *NOTCH1*, *HES4*, *DLL4*, *JAG2*, *HEY1*, *NOTCH3*, *NOTCH4*, *TGFBR2*, *EGF*) and heart valve morphogenesis related genes (*SMAD6*, *EFNA1*, *GATA5*, *HEY2*, *EMILIN1*, *NOS3*, *GATA3*) were upregulated over the course of differentiation in DP cells (Figure 3H, S4C).

Cell cycle related genes were enriched in cluster D2 (*ITGB1*, *CDK4*, *CCND1*, *CDK2AP2*, *MYC*, *CDC6*) (Figure S4D). Cell proliferation related genes and fatty-acyl-CoA biosynthetic process genes were enriched in cluster D3 (*ACLY*, *FASN*, *ELOVL1*, *SLC25A1*, *ACSL3*, *ACSL4*) (Figure S4E).

Cluster S1 (936 genes) was characterized by the increased expression of respective genes over the time, cluster S2 (746 genes) was characterized by the decreased expression of respective genes at day 8 of differentiation and cluster S3 (1318 genes) was characterized by the decreased expression of cell type specific genes later on day 5 of differentiation (Figure 3E). GO analysis of genes in cluster S1 showed enrichment in terms for related to the heart development and function (Figure 3G, Table S4). Specifically, cardiac chamber and cardiac muscle development related genes were upregulated over the course of differentiation in SP cells (*MYH6*, *HAND1*, *MYH10*, *TNNT2*, *NKX2-5*, *ISL1*, *TNNC1*, *MYOD*, *LMO4* and *HEY1*, *MYL7*, *MYL4*, *ACTA2*, *KCNH2*) (Figure 3I, S4F). Mitotic nuclear division genes (*TPX2*, *CDC20*, *NEK2*, *PLK1*, *PRC1* and *CDC25C*) were enriched in cluster S2 (Figure S4F). Transcription and translation process related genes (*SF1*, *SNRPE*, *DDX23*, *RRP1B* and *PRMT5*) were enriched in cluster S3 (Figure S4G).

Next, mean gene expression per cell for each gene cluster (D1-D3 and S1-S3) from the bulk RNA sequencing were calculated and mapped on scRNAseq UMAP and diffusion pseudotime plots (Figure 3J-M, S4H-K). Genes in cluster D1 were specifically expressed in the EP cluster (Figure 3J) and showed increased expression along the pseudotime EP branch (Figure 3L). Genes in cluster S1 were highly expressed in the CM and CP clusters (Figure 3K) and showed increased expression along the pseudotime CP branch (Figure 3M). Genes in clusters D2-D3 and S2-S3 showed similar patterns of expression with the highest expression in the CM cluster (Figure S4H, I) and early pseudotime EP branch (Figure S4J-K).

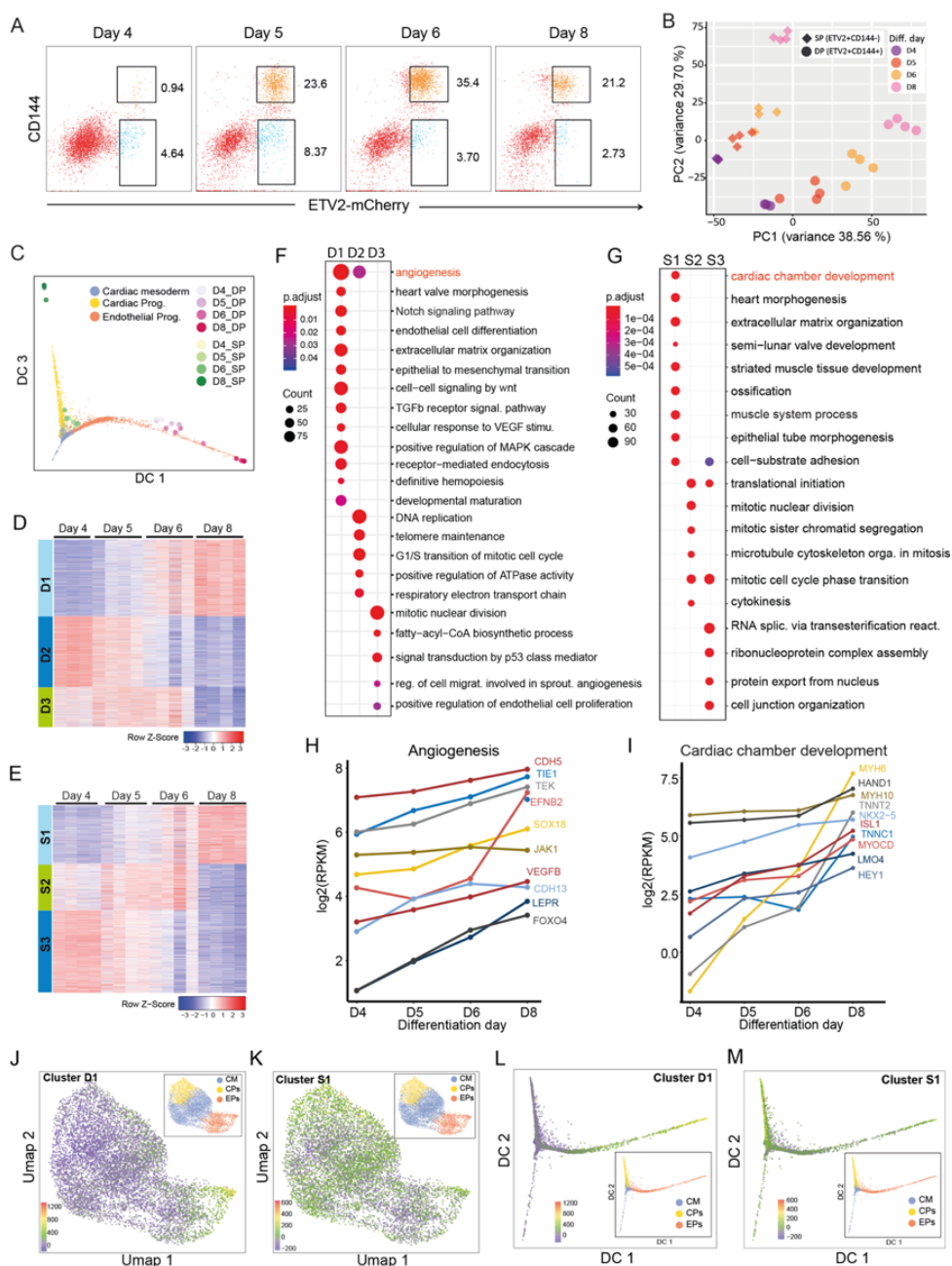


Figure 3. Transcriptomic analysis of EC and cardiac cell development from hiPSCs using a hiPSC ETV2^{mCherry} reporter line (A) FACS analysis of CD144 and ETV2^{mCherry} expression at day 4, 5, 6 and 8 of differentiation. ETV2+CD144+ (DP) and ETV2+CD144- (SP) cells were sorted on each day for bulk RNA sequencing. (B) PCA of all sorted DP and SP samples collected from three or four independent differentiations. (C) Diffusion maps of scRNAseq analysis and its overlay with all bulk RNAseq samples collected on day 4, 5, 6 and 8. Different clusters of cells or bulk samples are labelled with different colours. (D-E) Gene expression pattern in all DP (D) and SP (E) cells.

3000 most variable genes across all DP or SP samples were identified and grouped into three clusters by Consensus clustering. Genes in each cluster can be found in Table S3. Color scale represents relative expression (row z-score). (F-G) GO enrichment analysis of each gene cluster of DP (C) and SP (D) samples. Representative GOs are shown, while complete list of GO can be found in Table S4. Color represents the P_{adjusted} of enrichment analysis and dot size represents count of genes mapped to the GO. (H-I) Representative genes mapped to representative GOs of cluster D1 (E) and S1 (F) and their expression levels from day 4 to day 8 are shown. (J-K) Standardized sum of expression of genes in cluster D1 (F) and S1 (G) was calculated for each cell based on scRNAseq data and visualized in UMAPs. Color represents standardized sum of expression value. (L-M) Standardized sum of expression of genes in cluster D1 (I) and S1 (J) was calculated for each cell based on scRNAseq data and displayed in diffusion maps. Color represents standardized sum of expression value.

Diversification of endothelial and cardiomyocyte cell lineages during simultaneous co-differentiation from hiPSCs

To validate ETV2^{mCherry} reporter, ETV2^{mCherry+} and ETV2^{mCherry-} cells were sorted on day 5 of differentiation and differentiated toward ECs in the presence of VEGF (Figure 4A-B). FACS analysis on day 5 after sort resulted in pure population of CD144+CD31+ ECs (>90%) from ETV2^{mCherry+} cells with a small fraction of ECs (10-15%) developed from ETV2^{mCherry-} cells (Figure 4C-D). Cells derived from ETV2^{mCherry+} cells expressed endothelial-specific markers, as observed by qPCR and immunofluorescence analysis (Figure 4E-H). Functionally, ECs differentiated from ETV2^{mCherry+} cells upregulated pro-inflammatory markers, such as ICAM-1 and E-Selectin upon TNF- α stimulation (Figure 4I-L), as shown previously for hiPSC-ECs (Halaidych et al, 2018, SCR).

ETV2^{mCherry} DP, SP and double negative (DN) cells were next sorted at day 7 of differentiation and further cultured in the presence of VEGF until day 18 (Figure 4A-M). DP cells differentiated into CD144+CD31+ ECs (>80%) (Figure 4N-O). In contrast, SP and DN cells differentiated into cTnT+ cardiomyocytes (>50%) with very few ECs being detected (Figure 4N-O). Interestingly, cardiomyocytes derived from SP cells seem to proliferate more and formed a monolayer composed of a contracting cell sheet, while cardiomyocytes from DN cells proliferated to a less extent and with only a number of separated cell clusters contracting (Video S2). Almost all DP cells on day 18 expressed EC marker CD31, while only few numbers of cells derived from SP and DP cells were positive for CD31 (Figure 4P-R). Most cells derived from SP and DN expressed cardiomyocyte-specific α -Actinin and cTnT and showed typical sarcomeric structures (Figure 4Q-R). A small number of SP and DN-derived cells were also positive for the smooth muscle cell marker SM22 while negative for cardiac markers (data not shown).

Furthermore, SP cell fraction-derived α -Actinin positive cardiomyocytes were positive for SM22 indicating possibly their immaturity (Figure 4R).

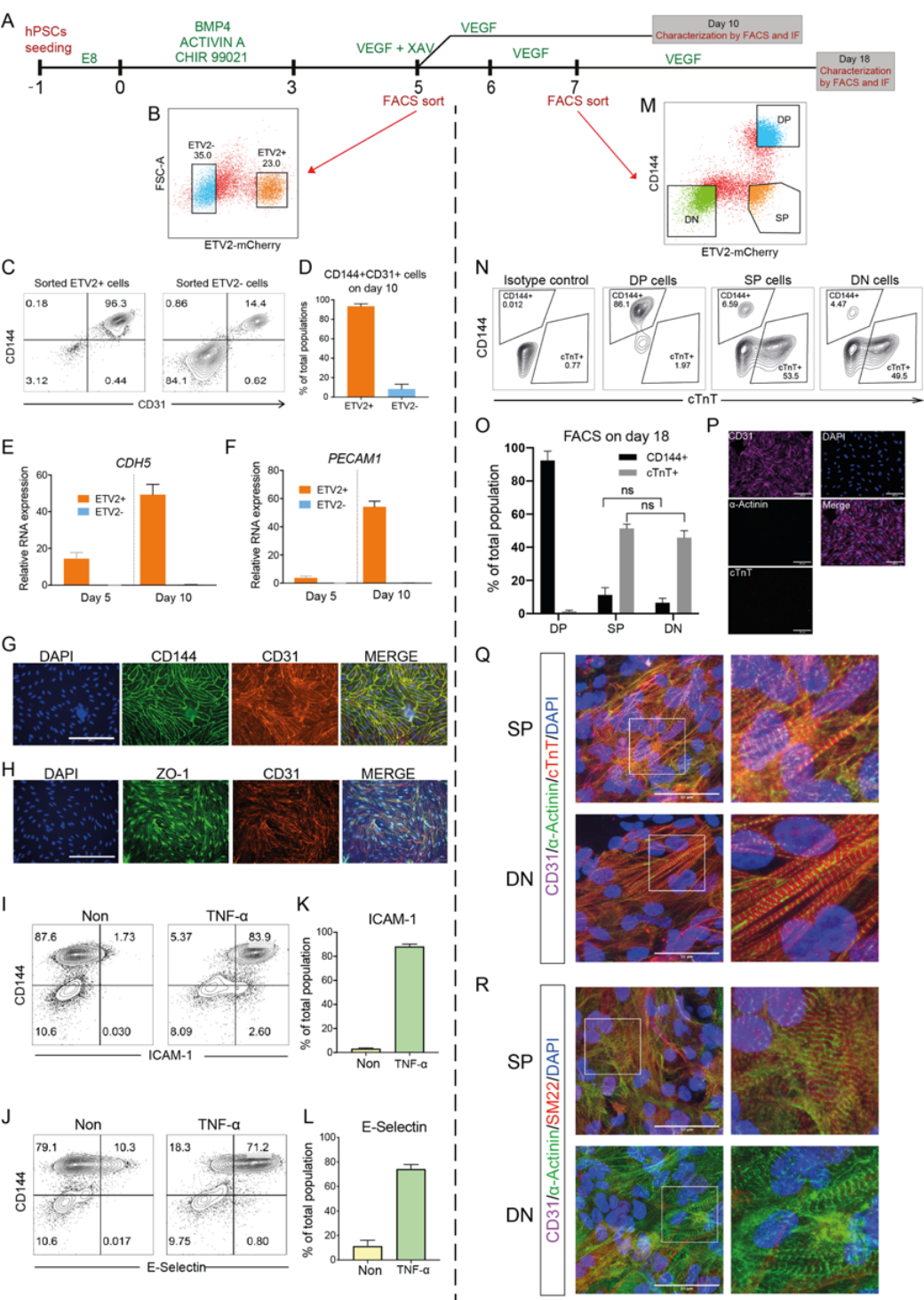


Figure 4. Diversification of endothelial and cardiomyocyte cell lineages during simultaneous

co-differentiation from hiPSCs (A) Schematic of CMEC differentiation protocol and FACS sort. ETV⁺ and ETV²⁻ cells were sorted on day 5 and cultured in VEGF until day 10. DP, SP, DN were sorted on day 7 and cultured in VEGF until day 18. (B) Representative FACS analysis ETV²⁻-mCherry on day 5 and gates for FACS sort of ETV²⁺ and ETV²⁻ cells are shown. (C) FACS analysis of endothelial markers CD144 and CD31 on day 10 of sorted ETV²⁺ and ETV²⁻ cells. (D) Quantification of the percentage of CD144⁺CD31⁺ cells in total populations on day 10 of sorted ETV²⁺ and ETV²⁻ cells. (E-F) Quantification of gene expression of *CDH5* and *PECAM1* in sorted ETV²⁺ and ETV²⁻ cells on day 5 and day 10. (G-H) Immuno-staining of CD144, CD31 and cell-cell junctional marker ZO-1 on day 10. Scale bar 200 μ m. (I-J) FACS analysis of ICAM1, E-Selectin and CD144 for sorted ETV²⁺ cells on day 10. Cells were stimulated with TNF- α for 24 h before FACS. (K-L) Quantification of percentage of CD144⁺ICAM-1⁺ (K) and CD144⁺E-Selectin⁺ (L) cells in total population on day 10. (M) FACS analysis of CD144 and ETV²-mCherry expression on day 7. DP, SP and DN cells were gated and sorted. (N) FACS analysis of CD144 and cardiomyocytes marker cTnT on day 18 of sorted DP, SP and DN cells. Isotype antibodies were included as control. (O) Quantification of CD144⁺ ECs and cTnT⁺ cardiomyocytes on day 18 of DP, SP and DN cells. (E) Immuno-staining of CD31, α -Actinin, cTnT and DAPI on day 18 of DP cells. Scale bar 50 μ m. (F) Immuno-staining of CD31, α -Actinin, cTnT, SM22 and DAPI on day 18 of SP and DN cells. Scale bar 50 μ m. Error bars are \pm SD of three independent experiments in (D-F, K-L, O).

DISCUSSION

In this study, we characterized the development of ECs and cardiomyocytes during their co-differentiation from hiPSC (Giacomelli et al., 2017) using their bulk- and scRNAseq profiles. Our major question was whether the ECs and cardiomyocytes actually had a common precursor as assumed previously on the basis of studies in mice or whether they differentiated in parallel.

Analysis showed that all cells could be divided into three principal clusters on day 6 of differentiation, corresponding to mesodermal, early myocardial and endothelial identities. Myocardial and endothelial lineages had a common origin in *MESP1*⁺ mesoderm cells in this *in vitro* system, in agreement with previous *in vivo* studies (Lescroart et al., 2018; 2014). Genes involved in early cardiomyocytes specification, including *SMARCD3* (Devine et al., 2014), *TMEM88* (Palpant et al., 2013) and *ISL1* (Quaranta et al., 2018) were highly expressed in CMs. Specifically, *TMEM88* was shown previously to promote cardiomyocyte but inhibit EC differentiation from multipotent cardiac mesoderm (Palpant et al., 2013), which was indeed absent in the endothelial lineage here. EPs differentiated from hiPSCs showed a clear EC identity and were fully functional based on their inflammatory response upon TNF α stimulation and endocytosis of Dil-AcLDL. Notably, they also expressed a number of cardiac markers like *MEOX2*, *GATA4*, *GATA6* and *ISL1*, suggesting an cardiac specific EC identity, which

corelated with our previous findings (Giacomelli et al., 2017). Myocardial cells, on the other hand, were still early progenitors on day 6 of the differentiation as no functionally contracting cardiomyocytes were observed yet at this stage.

ETV2 was identified as a specific marker of EP cluster in our scRNAseq dataset, corresponding to its fundamental role in hemagiogenic development (Garry et al., 2017). Interestingly, *ETV2* expression was also observed in a small population of CM and CP cell clusters. Moreover, the *ETV2*⁺ population on day 6 of differentiation were highly heterogenous, being composed of mesoderm, cardiac and endothelial lineages. Pseudotime analysis suggested that *ETV2*⁺ cardiomyocytes and endothelial cells both originated from *ETV2*⁺ CM. ECs had higher percentage of *ETV2*⁺ cells as well as average *ETV2* expression than the other two lineages. Although average *ETV2* levels in the *ETV2*⁺ subpopulation from different lineages were comparable over the whole time period, a short pulse of *ETV2* upregulation was specifically observed in endothelial *ETV2*⁺ cells during the differentiation (Figure S2D). In addition, expression of direct target genes of *ETV2* were triggered once an *ETV2* expression threshold was reached. This was also observed in previous reports during hemagiogenic specification (Zhao and Choi, 2019; 2017). These results suggested an *ETV2* pulse- and threshold dependent segregation of cardiomyocytes and ECs from their common mesoderm precursors.

An *ETV2*^{mCherry} hiPSC reporter line generated to track, isolate and characterize *ETV2*⁺ cells during CMEC differentiation showed that *ETV2*^{mCherry}⁺ cells could give rise to both Lectin⁺ ECs and Lectin⁻ non-ECs on day 8 (Figure 2C), suggesting that not all *ETV2* expressing cells could give rise ECs. Through the bulk RNAseq analysis for *ETV2*^{mCherry}⁺ ECs (DP) and non-ECs (SP) on different days of the differentiation, DP and SP cells were found to acquire more specific endothelial and myocardial identities as well as downregulate cell cycle-related genes from day 4 to day 8, indicating further development and maturation of these cells. Notably, although *CDH5* was expressed as early as day 4, several key angiogenesis and Notch signaling pathway genes, like *LEPR*, *FOXO4*, *DLL4*, *NOTCH4* and *EGF*, only started to be expressed after day 4 indicating a specified EC fate but immature progenitor identity on day 4. These relatively late expressed genes could potentially be used as markers to distinguish early and late ECs during development *in vitro* or *in vivo*. Genes involved in heart development and definitive hematopoiesis were also upregulated during ECs development (Figure 3B), suggesting cardiac endothelial- and probably a mixture of hemogenic endothelial identity of these ECs, while their hematopoietic potential should be further studied although this is beyond the scope of this study. In terms of SP cells, cardiac and muscle development related genes were highly enriched and upregulated during its development, suggesting a myocardial fate of these cells. Although SP cells had already committed to a cardiac fate by upregulation of cardiac genes *HAND1*, *MYH10*, *NKX2-5*, *ISL1*, *TNNC1*, *MYOCD* and *LMO4*, some crucial genes for cardiomyocytes were still

absent on day 4, including *MYH6* and *TNNT2*. *MYH6* encodes the major cardiomyocyte thick filament protein MHC- α and *TNNT2* was routinely used as a cardiomyocyte marker. Both genes are essential for cardiomyocyte contractility and started to be expressed after day 4. Their relatively late expression could allow us to identify early and late cardiac progenitors during cardiac development in future studies.

scRNAseq data on day 6 showed that endothelial and cardiac specific genes were upregulated along the EP- and CP development routes using unbiased pseudotime analysis, which correlated with the bulk RNAseq analysis and confirmed the specification and maturation process of these two lineages. Most importantly, DP and SP samples from bulk RNAseq were overlaid well with the EP and CP branches according to their differentiation times within the diffusion plot of pseudotime analysis. This further confirmed the endothelial and myocardial fates of DP and SP cells, respectively. However, it is worth mentioning that DP and SP did not fully correspond to EP and CP clusters. The large number of *CDH5* negative cells identified in the early EP branch was not present in sorted DP population. Therefore, all DP samples were mapped to the latter half of the EP branch (Figure 3F). Although all SP samples were mapped to the CP branch due to their common myocardial identities, day 8 SP cells were developed further beyond the end of CPs branch. This suggested that cardiac cells on day 8 were more mature and could not be captured by scRNAseq on day 6, which correlated well with the dramatic increase of cardiac genes from day 6 to day 8 in SP samples (Figure 4B).

Interestingly, we found there were two subpopulations of ETV2⁺ progenitors with different differentiation potentials. DP cells sorted on day 7 gave rise to endothelial cells only in the presence of VEGF, as expected. However, the majority of SP cells, also sorted on day 7, consistently gave rise to contracting cardiomyocytes under the same culture conditions. This provided direct evidence that the SP cells were cardiomyocyte progenitors. More importantly, it demonstrated that both ECs and cardiomyocytes could be derived from ETV2⁺ progenitors, confirming the presence of a common precursor implied by our earlier studies (Giacomelli et al, 2017). Notably, though, only a few (~5%) ECs could be derived from SP and DN cells, which could be derived from multipotent progenitors with delayed differentiation. Although SP and DN cells had similar differentiation potentials with similar efficiencies, the SP population had a higher cell growth after sorting (data not shown). Cardiomyocytes derived from SP cells also showed higher contractility compared to DN-derived cells (Video S2). This difference could be due to either the different cell densities (growth rates) or their different development origins (FHF vs. SHF). More work is needed to establish the identity of cardiomyocytes from SP and DN populations definitively.

In summary, this study used time-course bulk RNAseq and scRNAseq analysis to investigate the co-differentiation of cardiomyocytes and ECs from hiPSCs. scRNAseq

revealed transcriptional dynamics during early myocardial and endothelial lineage segregation from their common *MESP1*⁺ CM progenitors. We found that both cardiomyocytes and ECs could be specified from ETV2⁺ precursors in an ETV2-threshold-dependent manner, which may reflect differentiation *in vivo* process from multipotent CPCs. Overall, this study provides insights into the developmental of different human cardiac lineages and a rich data set for comparison with lineage reporters in mice.

MATERIAL AND METHODS

hiPSC culture

The NCRM1 hiPSC line (NIH) was used in this study. This hiPSC control line was cultured in TeSR-E8 on Vitronectin XF and was routinely passaged once a week using Gentle Cell Dissociation Reagent (all from Stem Cell Technologies). Prior to targeting NCRM1 hiPSCs were passaged as a bulk on feeders in hESC-food medium. RevitaCell (Life Technologies) was added to the medium (1:200) after every passage to enhance viability after single cell passaging with TrypLE (Life technologies).

Generation of hiPSC reporter line using CRISPR/Cas9

The p15a-cm-hETV2-P2A-NLS-mCherry-neo repair template plasmid was generated using overlap PCR and restriction-based cloning and ligation. The ETV2 homology arms were amplified from genomic DNA and the neomycin cassette flanked by FRT sites was amplified from the p15A-cm-PAX3-venus-neo-1kb plasmid (from Konstantinos Anastassiadis). P2A-NLS-mCherry double-stranded DNA fragment was ordered from IDT. The sgRNA/Cas9 plasmid was modified from SpCas9-2A-Puro V2.0 plasmid (Addgene, Feng Zang).

NCRM1 hiPSCs were passaged with ratio 1:2 or 1:3 into 60 mm dishes to reach 60-70% confluency the next day for transfection. 20 µl lipofectamine (Invitrogen), 8 µg of repair template and 8 µg of sgRNA/Cas9 plasmid were diluted in 600 µl of Opti-MEM and added to each 60 mm dish. After 18 hours the medium was changed to hESC-food. After another 6 hours G-418 (50 µg/ml) selection was started and was kept for 1 week. Survived cells were cultured in hESC-food and passage into 6-well plate for the transfection of Flp recombinase expression vector to remove the neomycin cassette. 300 µl of Opti-MEM containing 10 µl lipofectamine and 4 µg CAGGs-Flpo-IRES-puro plasmid was added per well for 18 hours. Puromycin (0,5 µg/ml) selection was started 24 hours post transfection and lasted for 2 days. Once recovered, cells were passage into 96-well format for clonal expansion via limited dilution. Targeted clones were identified by PCR and sequencing. Primers outside the ETV2 homology arms and primers inside the targeting construct were used to confirm on-target integration. The absence of mutation within inserted sequence and untargeted allele were confirmed by Sanger

sequencing (BaseClear).

Endothelial and myocardial lineages co-differentiation from hiPSCs

Endothelial and cardiac cells were induced from hiPSCs in a monolayer using CMEC protocol as described previously (Giacomelli et al., 2017). Briefly hiPSCs were split with a 1:12 ratio and seeded on 6-well plates coated with 75 µg/mL (growth factor reduced) Matrigel (Corning) on day -1. At day 0, cardiac mesoderm was induced by changing TeSR-E8 to BPEL medium (Ng et al., 2008), supplemented with 20 ng/mL BMP4 (R&D Systems), 20 ng/mL ACTIVIN A (Miltenyi Biotec) and 1.5 µM CHIR99021 (Axon Medchem). At day 3, cells were refreshed with BPEL supplemented 5 µM XAV939 (Tocris Bioscience) and 50 ng/ml VEGF (R&D Systems). From day 6 onwards, cells were refreshed every 3 days with BPEL medium supplemented with 50 ng/ml VEGF.

Fluorescence-activated cell sorting

For FACS sorting on day 5 of CMEC protocol, ETV2-mCherry positive and negative cells were sorted using FACSARIA III (BD-Biosciences). Around 20k cells/cm² were seeded on Fibronectin (from bovine plasma, 5µg/ml, Sigma Aldrich) coated plates. Cells were cultured in BPEL supplemented with VEGF (50 ng/ml) until day 10. The medium was refreshed every 3 days.

For FACS sorting on day 7 of CMEC protocol, VEC+mCherry+ (DP), VEC-mCherry+ (SP) and VEC-mCherry- (DN) cells were sorted using FACSARIA III. 1 million cells were seeded in each well of Matrigel-coated 12-well plate in BPEL supplemented with VEGF (50 ng/ml) and RevitaCell (1:200). Cells were refreshed 24 h after seeding and every three days afterwards with BPEL supplemented with VEGF (50 ng/ml).

Immunofluorescence staining and imaging

Cultured cells were fixed in 4% paraformaldehyde for 15 min, permeabilized for 10 min with PBS containing 0.1% Triton-X 100 (Sigma-Aldrich) and blocked for 1h with PBS containing 5% BSA (Sigma-Aldrich). Then cells were stained with primary antibody overnight at 4°C. The next day cells were washed three times (20 min each time) with PBS. After that cells were incubated with fluorochrome-conjugated secondary antibodies for 1h at room temperature and washed three times (20 min each time) with PBS. Then cells were stained with DAPI (Life Technologies) for 10 min at room temperature and washed once with PBS for 10min. Both primary and secondary antibodies were diluted in 5% BSA/PBS. Images were taken with EVOS FL AUTO2 imaging system (ThermoFischer Scientific) with 20x objective. For staining of ECs and cardiomyocytes on day 18, images were taken with a Leica SP8WLL confocal laser-scanning microscope using a 63x magnification objective and Z-stack acquisition. Details of all antibodies that were used are provided in Table S5.

AcLDL uptake assay

Alexa Fluor™ 594 AcLDL (ThermoFisher Scientific) was diluted in lipid-free BPEL to a final concentration of 5 µg/ml and added to ECs on differentiation day 10. After 4 hours incubation in 37 °C, wash cells once with lipid-free BPEL medium. Stain nucleus with NucBlue™ Live ReadyProbes™ for 20 min in 37 °C and then take images.

FACS analysis

Cells were washed once with FACS buffer (PBS containing 0.5% BSA and 2 mM EDTA) and stained with FACS antibodies for 30 min at 4°C. Samples were washed once with FACS buffer and analyzed on MACSQuant VYB (Miltenyi Biotech) equipped with a violet (405 nm), blue (488 nm) and yellow (561 nm) laser. The results were analyzed using FlowJo v10 (FlowJo, LLC). Details of all fluorochrome conjugated FACS antibodies are provided in Table S5.

Quantitative Real-Time Polymerase Chain Reaction (qPCR)

Total RNA was extracted using the NucleoSpin® RNA kit (Macherey-Nagel) according to the manufacturer's protocol. cDNA was synthesized using an iScript-cDNA Synthesis kit (Bio-Rad). iTaq Universal SYBR Green Supermixes (Bio-Rad) and Bio-Rad CFX384 real-time system were used for the PCR reaction and detection. Relative gene expression was determined according to the standard $\Delta\Delta CT$ calculation and normalized to housekeeping genes (mean of HARP and RPL37A). Details of all primers used are provided in Table S6.

Bulk RNA sequencing and analysis

Cells were sorted on differentiation day 4, 5, 6 and 8 for bulk RNA-Seq. Total RNA was extracted using the NucleoSpin® RNA kit (Macherey-Nagel). Whole transcriptome data were generated at BGI (Shenzhen, China) using the Illumina HiSeq4000 (100bp paired end reads). Raw data was processed using the LUMC BIOPET Gentrap pipeline (<https://github.com/biopet/biopet>), which comprises FASTQ preprocessing, alignment and read quantification. Sickle (v1.2) was used to trim low-quality read ends (<https://github.com/najoshi/sickle>). Cutadapt (v1.1) was used for adapter clipping (Martin, 2011), reads were aligned to the human reference genome GRCh38 using GSNAP (gmap-2014-12-23) (Wu and Nacu, 2010) (Wu and Watanabe, 2005) and gene read quantification with htseq-count (v0.6.1p1) against the Ensembl v87 annotation (Yates et al., 2016). Gene length and GC content bias were normalized using the R package cqn (v1.28.1) (Hansen et al., 2012). Genes were excluded if the number of reads was below 5 reads in ≥90% of the samples. The final dataset comprised gene expression levels of 31 samples and 22,419 genes.

Differentially expressed genes were identified using generalized linear models as implemented in edgeR (3.24.3) (Robinson et al., 2010). P-values were adjusted using the Benjamini-Hochberg procedure and $FDR \leq 0.05$ was considered significant. Analyses were performed using R (version 3.5.2). PCA plot was generated with the built-in R functions `prcomp` using transposed normalized RPKM matrix. Correlation among samples was calculated using `cor` function with spearman method and the correlation heatmap was generated with `aheatmap` function (NMF package).

Gene clusters were calculated with CancerSubtypes package (Xu et al., 2017). The top 3000 most variable genes across all chosen samples were identified based on the most variant Median Absolute Deviation (MAD) using `FSbyMAD` function, then `z_score` normalization was performed for each gene. K clusters were calculated using the K-means clustering of euclidean distance. Clustering was iterated 1000 times for K clusters in the range 2 to 10. Heatmap of genes in all clusters was generated using R basic heatmap function. Gene ontology enrichment for each cluster of genes was performed using `compareCluster` function of clusterProfiler package (v3.10.1) (Yu et al., 2012) and $q \leq 0.05$ was considered significant.

Single-cell RNA sequencing and analysis

Sample preparation and sequencing

Cells were dissociated into single cells on day 6 of CMEC differentiation and loaded into the 10X Chromium Controller for library construction using the Single-Cell 3' Library Kit. Next, indexed cDNA libraries were sequenced on the HiSeq4000 platform. The mean reads per cell were reported as 28,499 in the first replicate and 29,388 in the second replicate.

Pre-processing, clustering and UMAP

Both replicates of day 6 CMEC differentiation were merged into one data set. The average number of detected genes is 2643 and the average total expression per cell is 10382 (Figure S1A-B). Then, undetected genes (> 1 UMI count detected in less than two cells) and cells with low number of transcripts were removed from further analysis (Figure S1A-B). This resulted in 5107 cells for the first replicate, and 3743 cells for the second replicate with 13243 genes each. Expression profiles were normalized with the `scrn` package in R (V 1.10.2) using the method described in (Lun et al., 2016). The 10% most highly variable genes (HVG) for each replicate were calculated with `scrn` after excluding ribosomal genes (obtained from the HGNC website without any filtering for minimum gene expression), stressed genes (van den Brink et al., 2017) and mitochondrial genes. Batch effect correction between replicates was performed with a mutual nearest neighbours (MNN)- based approach (Haghverdi et al., 2018) implemented in the `scrn` package. (Here we used log-transformed and normalized count data with the 10% most HVG that were present in all replicates). The MNN

algorithm was run with $d = 30$ and $k = 20$.

Louvain clustering was performed on the shared-nearest-neighbours graph with $k = 100$ and $d = 30$, which resulted in 5 clusters. One of the 5 clusters was identified by marker genes as undifferentiated iPSCs and was excluded from further analysis.

Uniform Manifold Approximation and Projection (UMAP) was performed on the principal component scores of the MNN corrected counts using the R package `umap` (V 0.2.3.1) with 10 nearest neighbours, $\text{min_dist} = 0.7$ and cosine metric.

Cell Cycle and Proliferation Analysis

Cell cycle analysis was performed with the `scrn` package using the `cyclone` function on normalized counts. For the proliferation analysis a list of known proliferation genes (Whitfield et al., 2006) was used and the average scaled expression per cell was calculated. Based on the cell cycle results two of the four remaining clusters were merged.

Differential expression analysis and identification of cluster maker genes

The R package `edgeR` (V 3.24.3, 31) (Robinson et al., 2010) was used to perform differential expression analysis. We used raw counts and a negative binomial distribution to fit the generalized linear model. The covariates were comprised of 6 binary dummy variables that indicate the three remaining clusters per replicate and a variable that corresponds to the total number of counts per cell. Finally, p-values for each cluster considering both replicates were obtained and adjusted for multiple hypothesis testing with the Benjamini-Hochberg method.

Pseudo Time Analysis

For the pseudo time analysis, the first 30 principal component scores of the above described MNN corrected normalized counts were used to calculate a diffusion map (R package `destiny`, V 2.12.0) using default parameters. Then, diffusion pseudo time was calculated with the same package. The root cell was chosen from the cluster identified as cardiac mesoderm via literature markers. In order to display genes in pseudo time the first branch was extracted, which led to two tip cells, one within the endothelial progenitors and the other within cardiac progenitors. In order to display the trend of genes in some plots, bins of pseudo time with equal number of cells were constructed. For each bin the average expression or the average expression percentage was calculated among the cells.

Comparison to bulk RNA-sequencing data

Both replicates of normalized single cell counts were combined with bulk RNA-sequencing data. The MNN approach was used to correct between the two single-cell replicates using the 10% HVG per replicate and the bulk RNA-sequencing data, with $d = 30$ and $k = 20$. After batch correction a diffusion map was calculated on the MNN corrected values with default parameters.

Statistics

Statistical analysis was conducted with GraphPad Prism 7 software. Data are represented as mean \pm SD.

Acknowledgements

S.L. Kloet and E. de Meijer (Leiden Genome Technology Center) for help with 10X Genomics experiments (cell encapsulation, library preparation, single-cell sequencing, primary data mapping, and quality control).

Funding

This project received funding from the European Union's Horizon 2020 Framework Programme (668724); European Research Council (ERCAdG 323182 STEMCARDIOVASC); Netherlands Organ-on-Chip Initiative, an NWO Gravitation project funded by the Ministry of Education, Culture and Science of the government of the Netherlands (024.003.001).

REFERENCES

- Buckingham, M., Meilhac, S., Zaffran, S., 2005. Building the mammalian heart from two sources of myocardial cells. *Nat. Rev. Genet.* 6, 826–835. doi:10.1038/nrg1710
- Cai, C.-L., Liang, X., Shi, Y., Chu, P.-H., Pfaff, S.L., Chen, J., Evans, S., 2003. Isl1 identifies a cardiac progenitor population that proliferates prior to differentiation and contributes a majority of cells to the heart. *Developmental Cell* 5, 877–889. doi:10.1016/s1534-5807(03)00363-0
- Caspi, O., Lesman, A., Basevitch, Y., Gepstein, A., Arbel, G., Habib, I.H.M., Gepstein, L., Levenberg, S., 2007. Tissue engineering of vascularized cardiac muscle from human embryonic stem cells. *Circ. Res.* 100, 263–272. doi:10.1161/01.RES.0000257776.05673.ff
- De Val, S., Chi, N.C., Meadows, S.M., Minovitsky, S., Anderson, J.P., Harris, I.S., Ehlers, M.L., Agarwal, P., Visel, A., Xu, S.-M., Pennacchio, L.A., Dubchak, I., Krieg, P.A., Stainier, D.Y.R., Black, B.L., 2008. Combinatorial Regulation of Endothelial Gene Expression by Ets and Forkhead Transcription Factors. *Cell* 135, 1053–1064. doi:10.1016/j.cell.2008.10.049
- Devine, W.P., Wythe, J.D., George, M., Koshiba-Takeuchi, K., Bruneau, B.G., 2014. Early patterning and specification of cardiac progenitors in gastrulating mesoderm. *Elife* 3, 508. doi:10.7554/eLife.03848
- Ema, M., Takahashi, S., Rossant, J., 2006. Deletion of the selection cassette, but not cis-acting elements, in targeted Flk1-lacZ allele reveals Flk1 expression in multipotent mesodermal progenitors. *Blood* 107, 111–117. doi:10.1182/blood-2005-05-1970
- Ferdous, A., Caprioli, A., Iacovino, M., Martin, C.M., Morris, J., Richardson, J.A., Latif, S., Hammer, R.E., Harvey, R.P., Olson, E.N., Kyba, M., Garry, D.J., 2009. Nkx2-5 transactivates the Ets-related protein 71 gene and specifies an endothelial/endocardial fate in the developing embryo. *Proc. Natl. Acad. Sci. U.S.A.* 106, 814–819. doi:10.1073/pnas.0807583106

- Galli, D., Domínguez, J.N., Zaffran, S., Munk, A., Brown, N.A., Buckingham, M.E., 2008. Atrial myocardium derives from the posterior region of the second heart field, which acquires left-right identity as *Pitx2c* is expressed. *Development* 135, 1157–1167. doi:10.1242/dev.014563
- Garry, D.J., Olson, E.N., 2006. A common progenitor at the heart of development. *Cell* 127, 1101–1104. doi:10.1016/j.cell.2006.11.031
- Giacomelli, E., Bellin, M., Sala, L., van Meer, B.J., Tertoolen, L.G.J., Orlova, V.V., Mummery, C.L., 2017. Three-dimensional cardiac microtissues composed of cardiomyocytes and endothelial cells co-differentiated from human pluripotent stem cells. *Development* 144, 1008–1017. doi:10.1242/dev.143438
- Goldfracht, I., Protze, S., Shiti, A., Setter, N., Gruber, A., Shaheen, N., Nartiss, Y., Keller, G., Gepstein, L., 2020. Generating ring-shaped engineered heart tissues from ventricular and atrial human pluripotent stem cell-derived cardiomyocytes. *Nat. communications* 11(1), 75. doi:10.1038/s41467-019-13868-x
- Haghverdi, L., Lun, A.T.L., Morgan, M.D., Marioni, J.C., 2018. Batch effects in single-cell RNA-sequencing data are corrected by matching mutual nearest neighbors. *Nat Biotechnol* 36, 421–427. doi:10.1038/nbt.4091
- Hansen, K.D., Irizarry, R.A., WU, Z., 2012. Removing technical variability in RNA-seq data using conditional quantile normalization. *Biostatistics* 13, 204–216. doi:10.1093/biostatistics/kxr054
- Hartogh, den, S.C., Schreurs, C., Monshouwer-Kloots, J.J., Davis, R.P., Elliott, D.A., Mummery, C.L., Passier, R., 2015. Dual reporter MESP1 mCherry/w-NKX2-5 eGFP/w hESCs enable studying early human cardiac differentiation. *Stem Cells* 33, 56–67. doi:10.1002/stem.1842
- Lee, D., Park, C., Lee, H., Lugus, J.J., Kim, S.H., Arentson, E., Chung, Y.S., Gomez, G., Kyba, M., Lin, S., Janknecht, R., Lim, D.-S., Choi, K., 2008. ER71 Acts Downstream of BMP, Notch, and Wnt Signaling in Blood and Vessel Progenitor Specification. *Cell Stem Cell* 2, 497–507. doi:10.1016/j.stem.2008.03.008
- Lescroart, F., Chabab, S., Lin, X., Rulands, S., Paulissen, C., Rodolosse, A., Auer, H., Achouri, Y., Dubois, C., Bondue, A., Simons, B.D., Blanpain, C., 2014. Early lineage restriction in temporally distinct populations of *Mesp1* progenitors during mammalian heart development. *Nat Cell Biol* 16, 829–840. doi:10.1038/ncb3024
- Lescroart, F., Wang, X., Lin, X., Swedlund, B., Gargouri, S., Sánchez-Dànes, A., Moignard, V., Dubois, C., Paulissen, C., Kinston, S., Göttgens, B., Blanpain, C., 2018. Defining the earliest step of cardiovascular lineage segregation by single-cell RNA-seq. *Science* 359, 1177–1181. doi:10.1126/science.aao4174
- Liu, F., Li, D., Yu, Y.Y.L., Kang, I., Cha, M.-J., Kim, J.Y., Park, C., Watson, D.K., Wang, T., Choi, K., 2015. Induction of hematopoietic and endothelial cell program orchestrated by ETStranscription factor ER71/ ETV2. *EMBO Rep* 16, 654–669. doi:10.15252/embr.201439939
- Lun, A.T.L., Bach, K., Marioni, J.C., 2016. Pooling across cells to normalize single-cell RNA

- sequencing data with many zero counts. 17, 75–14. doi:10.1186/s13059-016-0947-7
- Martin, M., 2011. Cutadapt removes adapter sequences from high-throughput sequencing reads. *EMBnet j.* 17, 10. doi:10.14806/ej.17.1.200
- Masumoto, H., Nakane, T., Tinney, J.P., Yuan, F., Ye, F., Kowalski, W.J., Minakata, K., Sakata, R., Yamashita, J.K., Keller, B.B., 2016. The myocardial regenerative potential of three-dimensional engineered cardiac tissues composed of multiple human iPS cell-derived cardiovascular cell lineages. *Sci. Rep.* 6, 29933–29910. doi:10.1038/srep29933
- McCracken, I.R., Taylor, R.S., Kok, F.O., la Cuesta, de, F., Dobie, R., Henderson, B.E.P., Mountford, J.C., Caudrillier, A., Henderson, N.C., Ponting, C.P., Baker, A.H., 2019. Transcriptional dynamics of pluripotent stem cell-derived endothelial cell differentiation revealed by single-cell RNA sequencing. *Eur. Heart J.* 385, 9963117. doi:10.1093/eurheartj/ehz351
- Meilhac, S.M., Lescroart, F., Blanpain, C., Buckingham, M.E., 2014. Cardiac cell lineages that form the heart. *Cold Spring Harb Perspect Med* 4, a013888–a013888. doi:10.1101/cshperspect.a013888
- Mills, R., Titmarsh, D., Koenig, X., Parker, B., Ryall, J., Quaife-Ryan, G., Voges, H., Hodson, M., Ferguson, C., Drowley, L., Plowright, A., Needham, E., Wang, Q., Gregorevic, P., Xin, M., Thomas, W., Parton, R., Nielsen, L., Launikonis, B., James, D., Elliott, D., Porrello, E., Hudson, J., 2017. Functional screening in human cardiac organoids reveals a metabolic mechanism for cardiomyocyte cell cycle arrest. *Proc. Natl. Acad. Sci. U.S.A.* 114(40), E8372-E8381. doi:10.1073/pnas.1707316114
- Moretti, A., Caron, L., Nakano, A., Lam, J.T., Bernshausen, A., Chen, Y., Qyang, Y., Bu, L., Sasaki, M., Martin-Puig, S., Sun, Y., Evans, S.M., Laugwitz, K.-L., Chien, K.R., 2006. Multipotent embryonic isl1+ progenitor cells lead to cardiac, smooth muscle, and endothelial cell diversification. *Cell* 127, 1151–1165. doi:10.1016/j.cell.2006.10.029
- Morita, R., Suzuki, M., Kasahara, H., Shimizu, N., Shichita, T., Sekiya, T., Kimura, A., Sasaki, K.-I., Yasukawa, H., Yoshimura, A., 2015. ETS transcription factor ETV2 directly converts human fibroblasts into functional endothelial cells. *Proc. Natl. Acad. Sci. U.S.A.* 112, 160–165. doi:10.1073/pnas.1413234112
- Narmoneva, D.A., Vukmirovic, R., Davis, M.E., Kamm, R.D., Lee, R.T., 2004. Endothelial cells promote cardiac myocyte survival and spatial reorganization: implications for cardiac regeneration. *Circulation* 110, 962–968. doi:10.1161/01.CIR.0000140667.37070.07
- Ng, E.S., Davis, R., Stanley, E.G., Elefanty, A.G., 2008. A protocol describing the use of a recombinant protein-based, animal product-free medium (APEL) for human embryonic stem cell differentiation as spin embryoid bodies. *Nat Protoc* 3, 768–776. doi:10.1038/nprot.2008.42
- Paffett-Lugassy, N., Singh, R., Nevis, K.R., Guner-Ataman, B., O'Loughlin, E., Jahangiri, L., Harvey, R.P., Burns, C.G., Burns, C.E., 2013. Heart field origin of great vessel precursors relies on nkx2.5-mediated vasculogenesis. *Nat Cell Biol* 15, 1362–1369. doi:10.1038/ncb2862
- Paik, D.T., Tian, L., Lee, J., Sayed, N., Chen, I.Y., Rhee, S., Rhee, J.-W., Kim, Y., Wirka, R.C., Buikema,

- J.W., Wu, S.M., Red-Horse, K., Quertermous, T., Wu, J.C., 2018. Large-Scale Single-Cell RNA-Seq Reveals Molecular Signatures of Heterogeneous Populations of Human Induced Pluripotent Stem Cell-Derived Endothelial Cells. *Circ. Res.* 123, 443–450. doi:10.1161/CIRCRESAHA.118.312913
- Palpant, N.J., Pabon, L., Rabinowitz, J.S., Hadland, B.K., Stoick-Cooper, C.L., Paige, S.L., Bernstein, I.D., Moon, R.T., Murry, C.E., 2013. Transmembrane protein 88: a Wnt regulatory protein that specifies cardiomyocyte development. *Development* 140, 3799–3808. doi:10.1242/dev.094789
- Quaranta, R., Fell, J., Rühle, F., Rao, J., Piccini, I., Araúzo-Bravo, M.J., Verkerk, A.O., Stoll, M., Greber, B., 2018. Revised roles of ISL1 in a hES cell-based model of human heart chamber specification. *Elife* 7, 12209. doi:10.7554/eLife.31706
- Ravenscroft, S.M., Pointon, A., Williams, A.W., Cross, M.J., Sidaway, J.E., 2016. Cardiac Non-myocyte Cells Show Enhanced Pharmacological Function Suggestive of Contractile Maturity in Stem Cell Derived Cardiomyocyte Microtissues. *Toxicol. Sci.* 152, 99–112. doi:10.1093/toxsci/kfw069
- Robinson, M.D., McCarthy, D.J., Smyth, G.K., 2010. edgeR: a Bioconductor package for differential expression analysis of digital gene expression data. *Bioinformatics* 26, 139–140. doi:10.1093/bioinformatics/btp616
- Saga, Y., Miyagawa-Tomita, S., Takagi, A., Kitajima, S., Miyazaki, J.I., Inoue, T., 1999. MesP1 is expressed in the heart precursor cells and required for the formation of a single heart tube. *Development* 126, 3437–3447.
- Stevens, K.R., Kreutziger, K.L., Dupras, S.K., Korte, F.S., Regnier, M., Muskheli, V., Nourse, M.B., Bendixen, K., Reinecke, H., Murry, C.E., 2009. Physiological function and transplantation of scaffold-free and vascularized human cardiac muscle tissue. *Proc Natl Acad Sci U S A* 106, 16568–16573. doi:10.1073/pnas.0908381106
- Tam, P.P., Parameswaran, M., Kinder, S.J., Weinberger, R.P., 1997. The allocation of epiblast cells to the embryonic heart and other mesodermal lineages: the role of ingression and tissue movement during gastrulation. *Development* 124, 1631–1642.
- Tirziu, D., Giordano, F.J., Simons, M., 2010. Cell Communications in the Heart. *Circulation* 122, 928–937. doi:10.1161/CIRCULATIONAHA.108.847731
- Tulloch, N.L., Muskheli, V., Razumova, M.V., Korte, F.S., Regnier, M., Hauch, K.D., Pabon, L., Reinecke, H., Murry, C.E., 2011. Growth of engineered human myocardium with mechanical loading and vascular coculture. *Circ. Res.* 109, 47–59. doi:10.1161/CIRCRESAHA.110.237206
- van den Brink, S.C., Sage, F., Vértessy, Á., Spanjaard, B., Peterson-Maduro, J., Baron, C.S., Robin, C., van Oudenaarden, A., 2017. Single-cell sequencing reveals dissociation-induced gene expression in tissue subpopulations. *Nat. Methods* 14, 935–936. doi:10.1038/nmeth.4437
- Vincent, S.D., Buckingham, M.E., 2010. How to make a heart: the origin and regulation of cardiac progenitor cells. *Curr. Top. Dev. Biol.* 90, 1–41. doi:10.1016/S0070-2153(10)90001-X
- Whitfield, M.L., George, L.K., Grant, G.D., Perou, C.M., 2006. Common markers of proliferation.

- Nat. Rev. Cancer 6, 99–106. doi:10.1038/nrc1802
- Wu, T.D., Nacu, S., 2010. Fast and SNP-tolerant detection of complex variants and splicing in short reads. *Bioinformatics* 26, 873–881. doi:10.1093/bioinformatics/btq057
- Wu, T.D., Watanabe, C.K., 2005. GMAP: a genomic mapping and alignment program for mRNA and EST sequences. *Bioinformatics* 21, 1859–1875. doi:10.1093/bioinformatics/bti310
- Xu, T., Le, T.D., Liu, L., Su, N., Wang, R., Sun, B., Colaprico, A., Bontempi, G., Li, J., 2017. CancerSubtypes: an R/Bioconductor package for molecular cancer subtype identification, validation and visualization. *Bioinformatics* 33, 3131–3133. doi:10.1093/bioinformatics/btx378
- Yates, A., Akanni, W., Amode, M.R., Barrell, D., Billis, K., Carvalho-Silva, D., Cummins, C., Clapham, P., Fitzgerald, S., Gil, L., Girón, C.G., Gordon, L., Hourlier, T., Hunt, S.E., Janacek, S.H., Johnson, N., Juettemann, T., Keenan, S., Lavidas, I., Martin, F.J., Maurel, T., McLaren, W., Murphy, D.N., Nag, R., Nuhn, M., Parker, A., Patricio, M., Pignatelli, M., Rahtz, M., Riat, H.S., Sheppard, D., Taylor, K., Thormann, A., Vullo, A., Wilder, S.P., Zadissa, A., Birney, E., Harrow, J., Muffato, M., Perry, E., Ruffier, M., Spudich, G., Trevanion, S.J., Cunningham, F., Aken, B.L., Zerbino, D.R., Flicek, P., 2016. Ensembl 2016. *Nucleic Acids Res.* 44, D710–D716. doi:10.1093/nar/gkv1157
- Yu, G., Wang, L.-G., Han, Y., He, Q.-Y., 2012. clusterProfiler: an R Package for Comparing Biological Themes Among Gene Clusters. *OMICS: A Journal of Integrative Biology* 16, 284–287. doi:10.1089/omi.2011.0118
- Zaffran, S., Kelly, R.G., Meilhac, S.M., Buckingham, M.E., Brown, N.A., 2004. Right ventricular myocardium derives from the anterior heart field. *Circ. Res.* 95, 261–268. doi:10.1161/01.RES.0000136815.73623.BE
- Zhao, H., Choi, K., 2019. Single cell transcriptome dynamics from pluripotency to FLK1+ mesoderm. *Development* 146, dev.182097. doi:10.1242/dev.182097
- Zhao, H., Choi, K., 2017. A CRISPR screen identifies genes controlling Etv2 threshold expression in murine hemangiogenic fate commitment. *Nat Comms* 8, 541–512. doi:10.1038/s41467-017-00667-5

SUPPLEMENTARY INFORMATION

Supplemental figures S1-S7

Supplemental tables S1-S6

Supplemental Videos S1, S2

(Table S1-S4, Videos S1, S2 can be found online:

<https://www.dropbox.com/sh/z96w86rp8insusk/AACzcYkq4eMufhe2UmQkia8Ca?dl=0>)

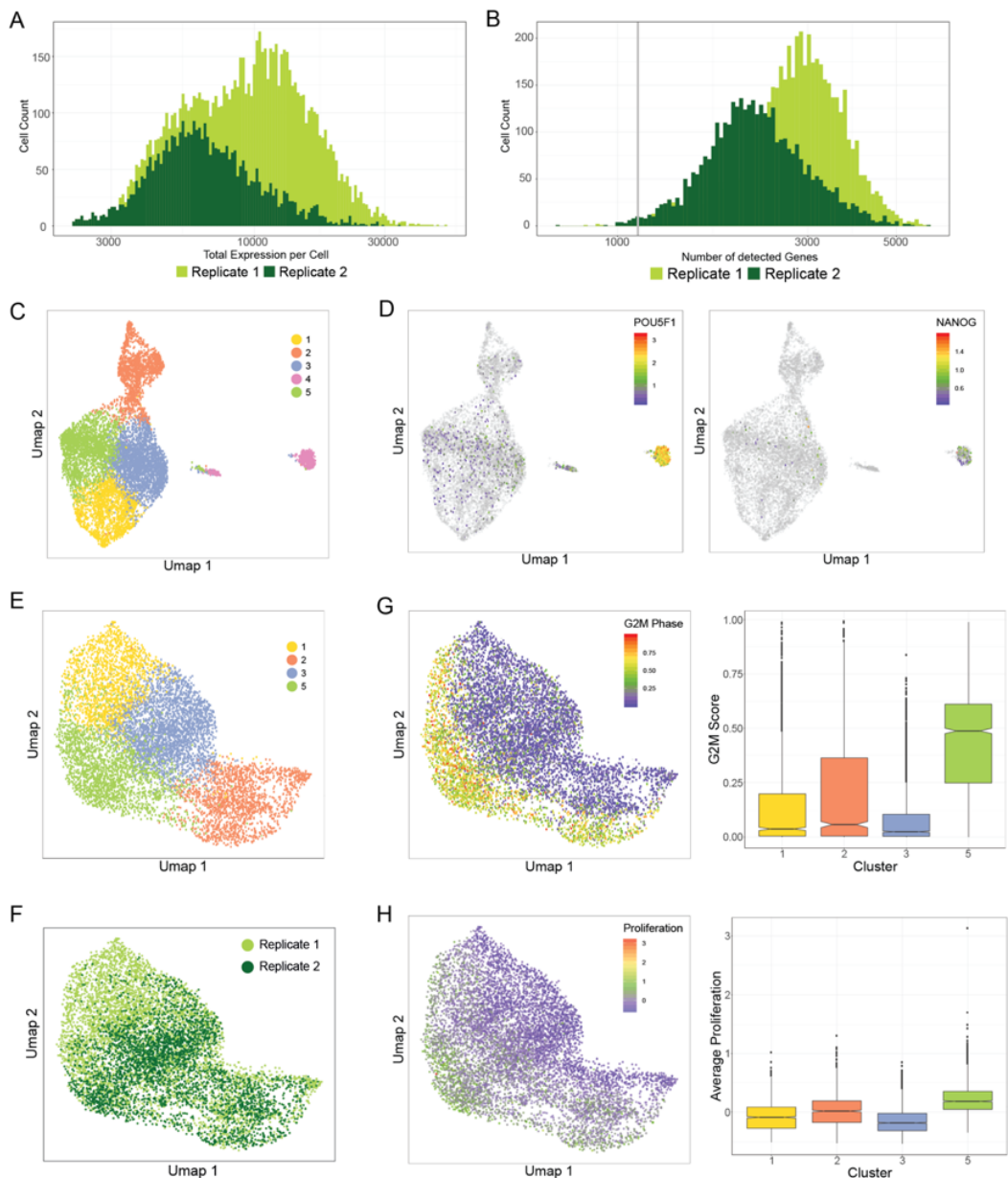


Figure S1. Single-cell RNA sequencing analysis for day 6 of CMEC differentiation from hiPSCs

(A-B) Distribution of total expression and number of detected genes in each cell of the scRNAseq dataset. Undetected genes (> 1 UMI count detected in less than two cells) and cells with low number of transcripts were removed from further analysis.

(C) scRNAseq data collected on day 6 is visualized using UMAP. Five clusters (1-5) of cells were identified.

(D) Expression of pluripotency markers *POU5F1* and *NANOG* in all cells shown in UMAP.

(E) UMAP after exclusion of pluripotent stem cell cluster (cluster 4).

(F) Overlay of two different batches of cells collected for scRNAseq on day 6 of CMEC

differentiation.

(G-H) G2M score (G) and standardized mean expression of proliferation-related genes (H) in all cells and in individual clusters.

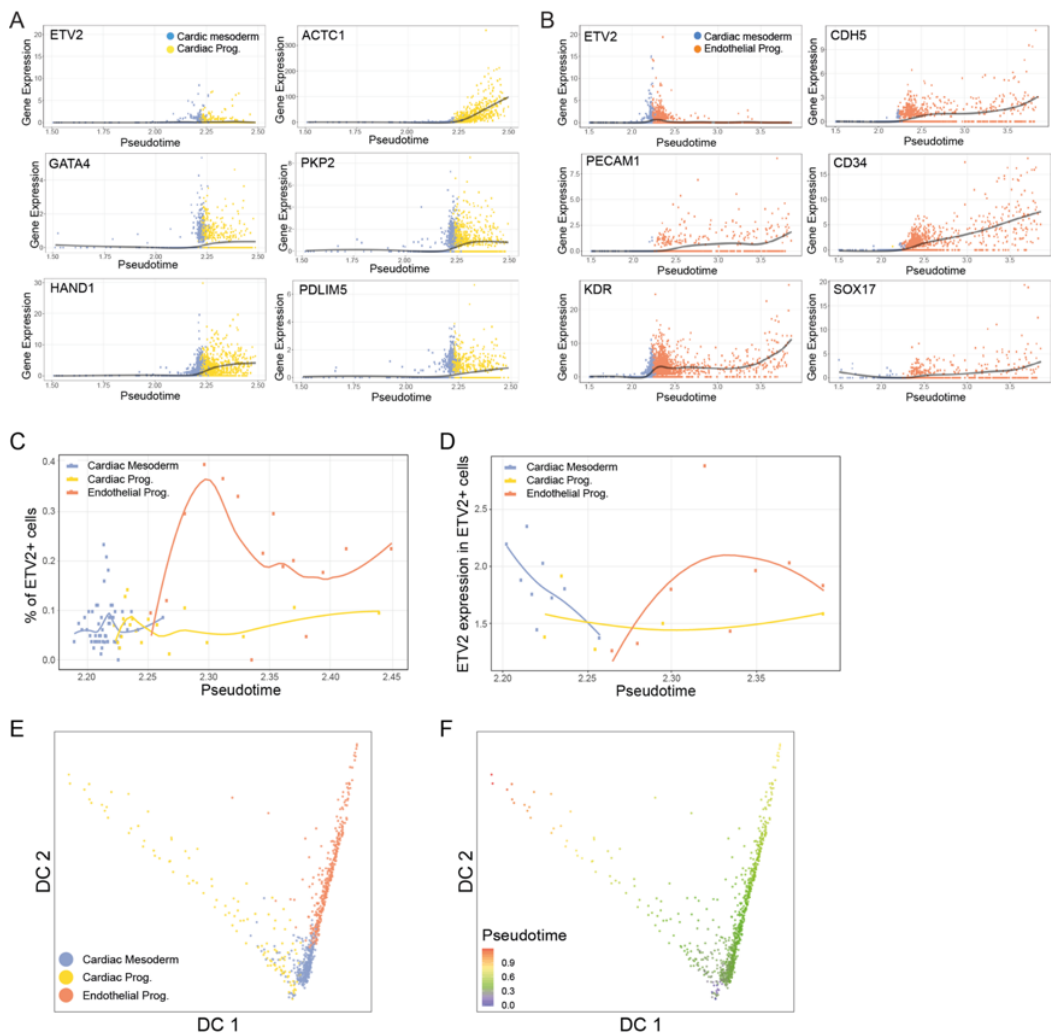


Figure S2. Pseudotime analysis of CMEC differentiation from hiPSCs

(A) Expression of *ETV2* and cardiac markers *ACTC1*, *GATA4*, *PKP2*, *HAND1* and *PDLIM5* following pseudotime in CM and CPs development route.

(B) Expression of *ETV2* and endothelial markers *CDH5*, *PECAM1*, *CD34*, *KDR* and *SOX17* following pseudotime in CM and EPs development route.

(C) Percentage of *ETV2* expressing cells within each branch between pseudotime 2.19 to 2.49. Bins of pseudo time with equal number of cells (50 cells) were constructed and the percentage of *ETV2* expressing cells was calculated among these cells.

(D) Average expression of *ETV2* in *ETV2* expressing cells within each branch between pseudotime 2.19 to 2.49. Bins of pseudo time with equal number of cells (50 cells) were constructed and the

average expression was calculated among these cells.

(E-F) Dimensionality reduction of scRNAseq data for all *ETV2*⁺ population using diffusion map. Cell identities are labeled with different colors in (E). Color scale indicates the pseudotime in (F).

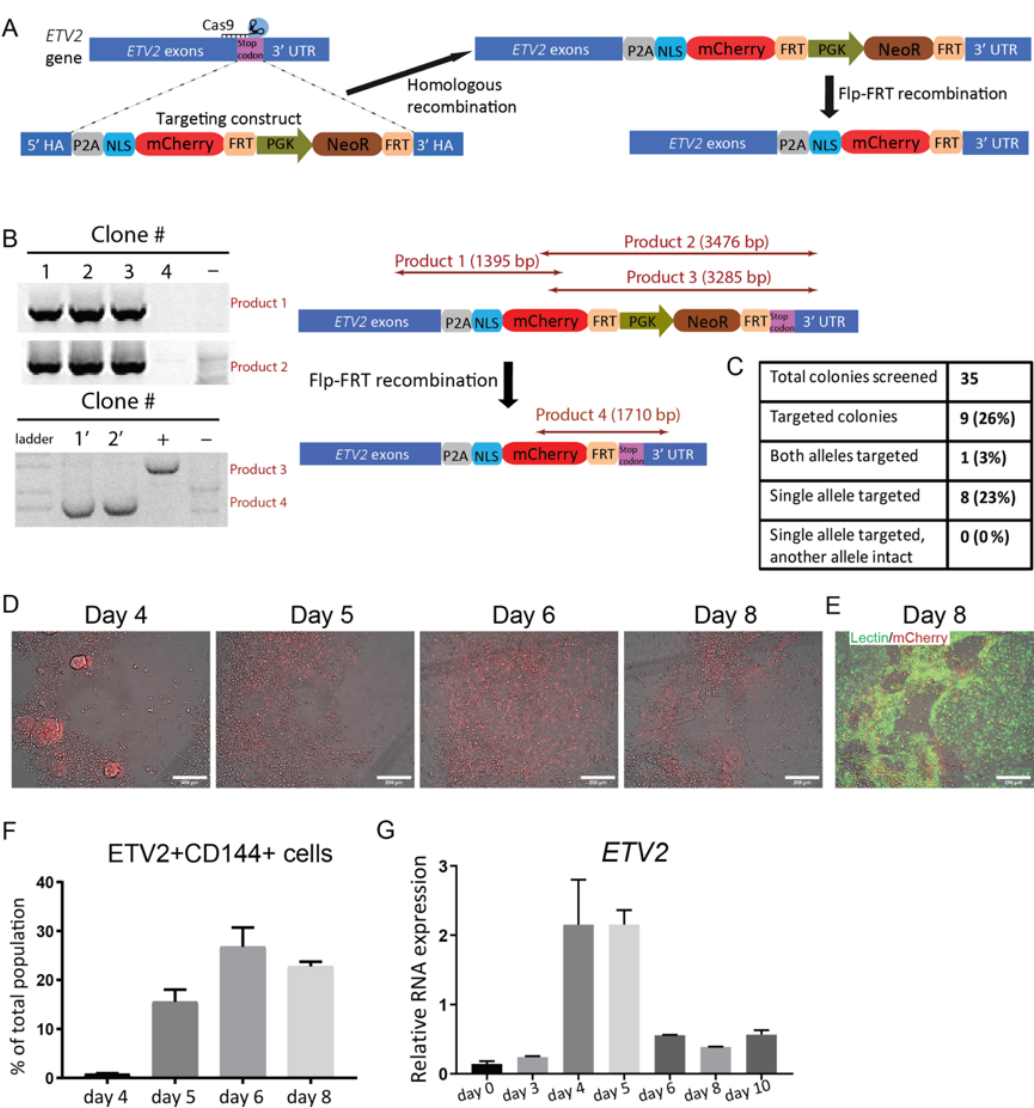


Figure S3. Generation and characterization of ETV2-mCherry reporter hiPSC line

(A) Schematic overview of CRISPR/Cas9-Mediated Knock-in of mCherry reporter into *ETV2* locus of hiPSCs. mCherry and Neomycin Resistance (NeoR) was inserted into *ETV2* gene locus through Homologous recombination. Then NeoR cassette was removed by flpo recombinase as shown on the right.

(B) PCR screening of targeted clones with correct insertion at *ETV2* locus. Two pairs of primers (for product 1 and product 2) were used to confirm the integration of construct into the genome.

Clone 1, 2, 3 were correctly targeted and clone 4 was not targeted. non-targeted hiPSCs (-) were included as negative control. Lower panel: Excision of neomycin-resistance cassette was confirmed using one pair of PCR primer (product 3 and 4 for before and after excision). Clone 1' ad 2' were successfully excised by FLPO recombinase. Genomic DNA before excision (+) and non-targeted hiPSCs (-) were included as positive and negative control.

(C) Summary of CRISPR targeting efficiency. Out of 35 colonies screened, 1 colony was targeted on both alleles. 8 colonies were targeted on only one allele, but the other allele showed undesired mutations.

(D) Overlay of bright-field and mCherry fluorescence images on differentiation day 4, 5, 6 and 8 of CMEC differentiation using ETV2-mCherry reporter line. Scale bar 200 μ m.

(E) Lectin staining of cells at the same location as shown in (B) on day 8 of differentiation. mCherry is in red and Lectin is in green. Scale bar 200 μ m.

(F) Quantification of percentages of ETV2+CD144+ cells by FACS on differentiation day 4, 5, 6 and 8.

(F) Quantification of *ETV2* expression by qPCR on different days of CMEC differentiation.

Error bars are \pm SD of three independent experiments in (F-G).

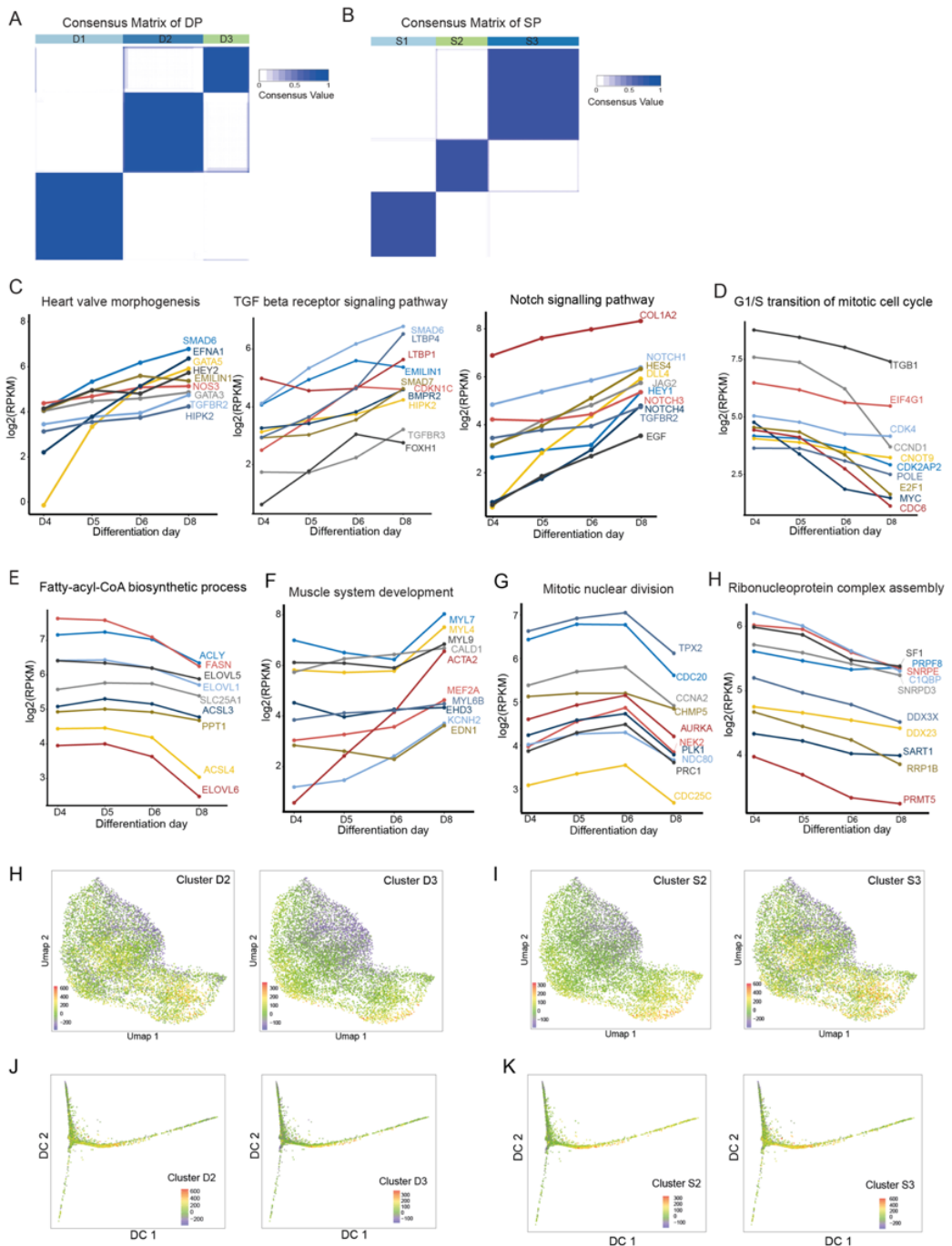


Figure S4. Time-course transcriptomic analysis of DP and SP cells during CMEC differentiation

(A) Consensus clustering for 3000 most variant genes across all DP samples (A) and all SP samples (B). All genes were divided into 3 clusters D1-D3 for DP (A) and S1-S3 for SP (B). Consensus value indicates similarity between two genes.

(C-H) Representative GOs enriched in cluster D1 (C), D2 (D), D3 (E), S1 (F), S2 (G) and S3 (H). Representative genes mapped to these GOs and their expression levels from day 4 to day 8 are

shown.

(H-I) Standardized sum of expression of genes in cluster D2, D3 (H) and S2, S3 (I) was calculated for each cell based on scRNAseq data and visualized in UMAPs. Color represents standardized sum of expression value.

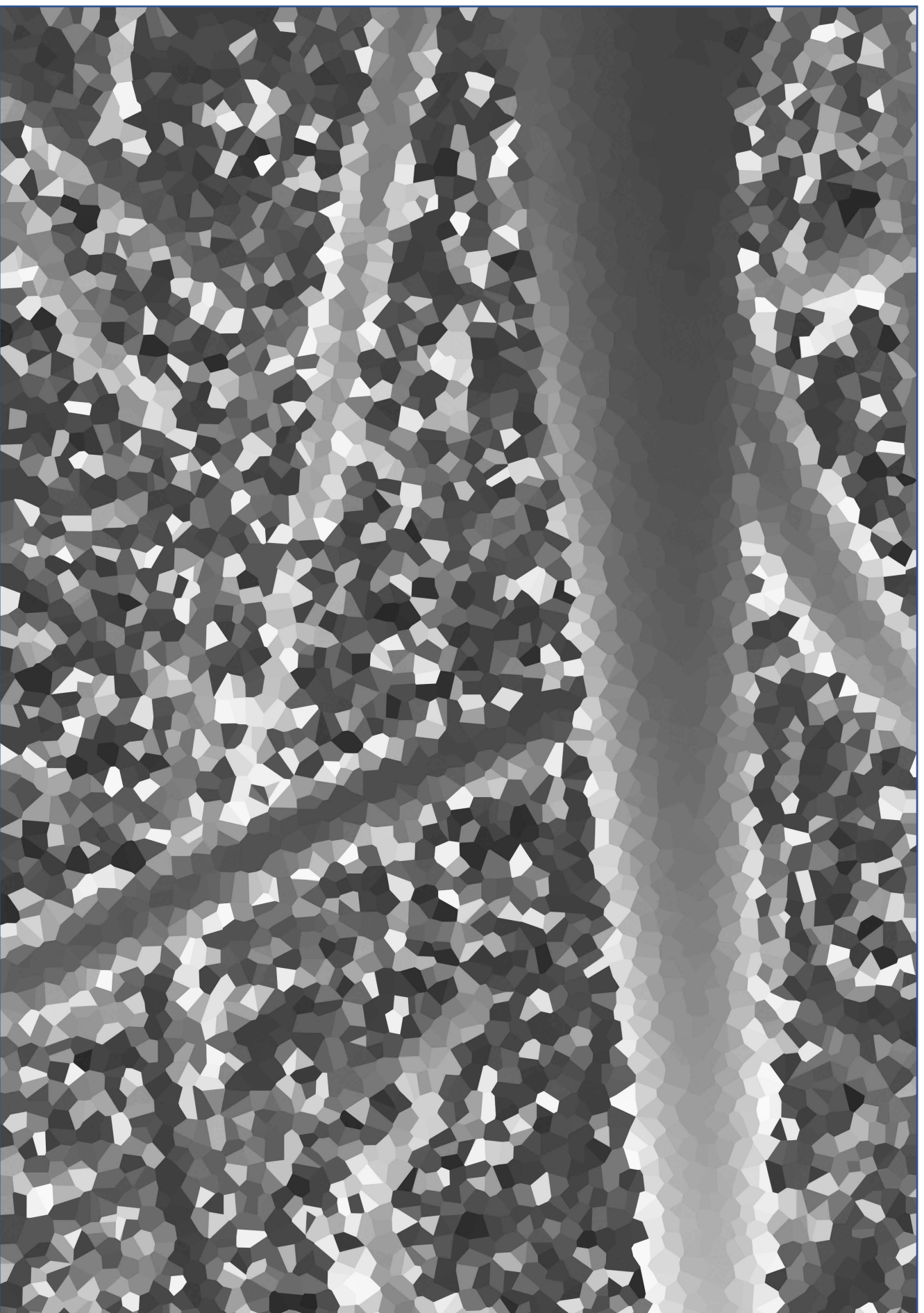
(J-K) Standardized sum of expression of genes in cluster D2, D3 (J) and S2, S3 (K) was calculated for each cell based on scRNAseq data and displayed in diffusion maps. Color represents standardized sum of expression value.

Antibody	Application	Source	Dilution	Catalog #
CD144	FACS	eBioscience	1:50	53-1449-42
ICAM1	FACS	R&D	1:20	BBA20
E-Selectin	FACS	R&D	1:20	BBA21
α -ACTININ	IF	Sigma–Aldrich	1:800	A7811
cTnT	IF			
CD31	IF	R&D	1:200	AF806
ZO-1	IF	eBioscience	1:200	61-7300
CD144	IF	CellSignaling	1:200	2158
SM22	IF	Abcam	1:400	ab14106
AF488	IF	Invitrogen	1:200	A21206
AF594	IF	Termo Fisher	1:200	
AF647	IF	Termo Fisher	1:200	A21448

Table S4. List of antibodies

Gene	Forward sequence	Reverse sequence	Product size
<i>hARP</i>	CACCATTGAAATCCTGAGTGATGT	TGACCAGCCCAAAGGAGAAG	116
<i>RPL37A</i>	GTGGTTCCTGCATGAAGACAGTG	TTCTGATGGCGGACTTTACCG	84
<i>ETV2</i>	CAGCTCTCACCGTTTGCTC	AGGAACTGCCACAGCTGAAT	106
<i>CDH5</i>	GGCATCATCAAGCCCATGAA	TCATGTATCGGAGGTCGATGGT	100
<i>CD31</i>	GCATCGTGGTCAACATAACAGAA	GATGGAGCAGGACAGGTTTCAG	101
<i>PDGFRA</i>	ATTGCGGAATAACATCGGAG	GCTCAGCCCTGTGAGAAGAC	95
<i>NKX2-5</i>	TTCCCGCCGCCCGCCTTCTAT	CGCTCCGCGTTGTCCGCCTCTGT	138
<i>TBX5</i>	ACATGGAGCTGCACAGAATG	TGCTGAAAGGACTGTGGTTG	104
<i>GATA4</i>	GACAATCTGGTTAGGGGAAGC	GAGAGATGCAGTGTGCTCGT	105
<i>BMP10</i>	CCTCTGCCAACATCATTAGGAG	TTTTCGGAGCCCATTAAACTGA	77
<i>HAND2</i>	ACATCGCCTACCTCATGGAC	TGGTTTTCTTGTCGTTGCTG	162

Table S5. Sequence of primes used for qPCR



Chapter 5

Vascular defects associated with Hereditary Hemorrhagic Telangiectasia revealed in patient-derived isogenic iPSCs

Valeria V. Orlova^{1*}, Xu Cao¹, Amy Cochraine¹, Roderick C. Slieker^{2,3}, Christian Freund¹, Francijna van den Hil¹, David Lemmonier⁴, Gonzalo Sánchez-Duffhues², Hailiang Mei⁵, Cornelius J.J. Westermann⁶, Repke J. Snijder⁶, Frans Disch⁶, Johannes Kristian Ploos van Amstel⁸, Peter ten Dijke², Franck Lebrin^{4,7}, Hans-Jurgen Mager⁶, Christine L. Mummery^{1,9*}

¹Department of Anatomy and Embryology, Leiden University Medical Center, Leiden, 2333ZA, The Netherlands

²Department of Cell and Chemical Biology, Leiden University Medical Center, Leiden, 2333ZA, The Netherlands

³Department of Epidemiology and Biostatistics, Amsterdam Public Health Institute, VU University Medical Center, Amsterdam, 1007MB, The Netherlands

⁴Eindhoven Laboratory for Experimental Vascular Medicine, Department of Internal Medicine (Nephrology), Leiden University Medical Center, Leiden, The Netherlands

⁵Sequencing analysis support core, Leiden University Medical Center, Leiden, 2333ZA, The Netherlands

⁶St Antonius Hospital, Nieuwegein, The Netherlands

⁷CNRS UMR 7241, INSERM U1050, Collège de France, Paris, France

⁸Department of Medical Genetics, University Medical Center Utrecht, Utrecht, The Netherlands

⁹Department of Applied Stem Cell Technologies, University of Twente, Enschede, 7500AE, The Netherlands

*Corresponding authors' e-mail address: v.orlova@lumc.nl and c.l.mummery@lumc.nl

Under revision

ABSTRACT

Hereditary Hemorrhagic Telangiectasia (HHT) is a genetic disease characterized by weak blood vessels and exacerbated by inflammation. Here, we generated induced pluripotent stem cells (hiPSC) from patients with *ENDOGLIN* (*ENG*) mutations (HHT1) and showed reduced *ENG* expression in HHT1-endothelial cells (HHT1-hiPSC-ECs), reflecting haploinsufficiency (Paquet et al., 2001). From one mosaic patient (*ENG*^{c.1678C>T}), we derived diseased and healthy hiPSCs. HHT1^{c.1678C>T}-hiPSC-ECs showed increased inflammatory responses and defective vascular organisation specifically when grown in 3D organ-on-chip devices under microfluidic flow. RNA-seq comparison with HHT1^{WT}-hiPSC-ECs showed inflammation-induced imbalance in TGFβ and BMP signalling pathways accompanying *ENG* deficiency and involvement of WNT-signalling; this was confirmed by small-molecule rescue (Avior et al., 2016; Cunha et al., 2017; Esch et al., 2015) of the *in vitro* HHT1 phenotype. The patient-based hiPSC model thus showed key roles for inflammation and the WNT-signalling pathway in HHT1, in line with established mouse models and reported symptoms in HHT1 patients (Lebrin et al., 2010; Mahmoud et al., 2010; Tørring et al., 2015) and suggested new target cells and pathways for therapy.

MAIN TEXT

Many mutations causing HHT have been identified which are widely used for diagnosis (Letteboer et al., 2004; McDonald et al., 2015), but understanding mechanisms underlying the phenotype is confounded by complex adaptive processes that occur *in vivo* in mutant mice (El-Brolosy and Stainier, 2017). Genetic background also contributes to the differences in phenotype in different mouse strains, perhaps to a larger extent than in patients (Benzinou et al., 2012; Letteboer et al., 2015; Tang, 2003; Tang et al., 2005). Anti-angiogenic, anti-inflammatory, immunomodulator drugs are all currently in clinical trial for treating HHT (Cunha et al., 2017) but their mechanism of action is not always well understood. Most notably, thalidomide that was successfully tested in the patients (Lebrin et al., 2010) may have both anti-inflammatory and anti-angiogenic activity but its cellular targets are unknown. To develop human model for HHT *in vitro*, we generated hiPSC lines from somatic tissue of three HHT1 patients with different *ENG* mutations (Extended Data Fig. 1a, b), where all three mutations were predicted to cause haploinsufficiency. One patient was identified as being a genetic mosaic allowing generation of isogenic pairs of hiPSC lines, with and without the mutation (HHT1^{c.1678C>T} and HHT1^{WT}). The genetic identity of the lines was confirmed by DNA fingerprinting. HHT1-hiPSC clones showed normal karyotypes and were verified as pluripotent using standard methods (PluriTest, expression of pluripotency markers and spontaneous

differentiation towards three germ cell lineages; Extended Data Fig. 1 and Fig. 2). HHT1-hiPSCs were then induced to differentiate to endothelial cells (ECs) (Halaidych et al., 2018; Orlova et al., 2014b; 2014a). Surface ENG (CD105) was significantly downregulated in HHT1-hiPSC-ECs (Fig. 1b and Extended Data Fig. 3e), as found in HHT1 patients. By contrast, surface expression of other major EC markers such as vascular endothelial cadherin (VEC), platelet and endothelial adhesion molecule (CD31/PECAM1) and kinase insert domain receptor (KDR), also known as vascular endothelial growth factor receptor 2, and CD34 was similar among lines (Fig. 1b and Extended Data Fig. 3e). ENG haploinsufficiency thus had no effect on the differentiation efficiency towards ECs (Extended Data Fig. 3c, d). Whole transcriptome sequencing (RNA-seq) on HHT1 patient-derived isogenic hiPSC-ECs confirmed that HHT1^{WT}- and HHT1^{c.1678C>T}-hiPSC-ECs expressed comparable levels of well-established pan-ECs markers and additionally that there were no differences in expression of arterial or venous-EC markers (Extended Data Fig. 4a, b, c). ENG haploinsufficiency also had no apparent effect on functionality of HHT1-hiPSC-ECs in a set of standard assays. HHT1-hiPSC-ECs showed similar responses upon short-term stimulation with bone morphogenetic protein 9 (BMP9) and transforming growth factor- β (TGF β) with no difference in downstream signalling, barrier function or migration rates (Extended Data Fig. 5). Furthermore, EC junctional organisation, proliferation and angiogenic sprouting in 2D assays were similar in control and HHT1-hiPSC-ECs (Extended Data Fig. 6). However, blood flow and inflammation are thought to contribute to initiating the development of the vascular lesions in HHT (Mahmoud et al., 2010; Sugden et al., 2017). We therefore hypothesised that additional triggers might be required by ECs to promote vascular phenotypes evident in some, but not all, vascular beds in HHT1 patients with ENG haploinsufficiency. The ability of hiPSC-ECs to form a perfused microvascular network was therefore examined using 3D cultures in microfluidic chips. Primary human brain vascular pericytes (HBVPs) were used to support microvascular network formation. The vascular network developed around day 3-4 of culture; luminized microvessels were observed around day 5-6 and the presence of lumen confirmed by confocal microscopy (Extended Data Fig. 7). To visualize ECs and HBVP, we immunostained post-fixed (day 6) 3D microfluidic cultures with antibodies against CD31/PECAM1 EC surface protein and SOX17 EC nuclei (Fig. 2c) and a pericyte/vascular smooth muscle cell marker (SM22) (Fig 2h). Proliferation was assessed using an EdU assay (Fig. 2f). Remarkably, we found that in contrast to 2D microvascular cultures, the ability to form microvessels in microfluidic chips was strikingly compromised in HHT1^{c.1678C>T}-hiPSC-ECs compared to HHT1^{WT}-hiPSC-ECs (Fig. 1c), despite similar initial seeding densities (Extended Data Fig. 8). Quantification of the vascular networks confirmed reduced vascular density and diameter of the vessels but showed no difference in the total length of the vessels, number of branching points or branching point density (Fig. 1d). The overall number of ECs, determined by

quantification of EC-specific (SOX17+) nuclei was however decreased in the networks formed by HHT1^{c.1678C>T}-hiPSC-ECs (Fig. 1c, e). Proliferation of HHT1^{c.1678C>T}-hiPSC-ECs was reduced, as evidenced by fewer EdU positive nuclei (Figure 1f, g). Furthermore, HBVPs exhibited strikingly longer protrusions when cultured in the vascular networks formed with HHT1^{c.1678C>T}hiPSC-ECs compared to HHT1^{WT}-hiPSC-ECs (Fig. 1h, i). ENG is an accessory receptor involved in regulating TGFβ-mediated signal transduction via enhancing TGFβ/activin receptor-like kinase 1 (ALK1) and inhibiting TGFβ/ALK5 signaling (Goumans et al., 2002; 2003; Lebrin et al., 2004). ENG binds TGFβ ligands (TGFβ1 and TGFβ3) only in a complex with TGFβ type II receptor (TGFBRII) (Lebrin et al., 2005).

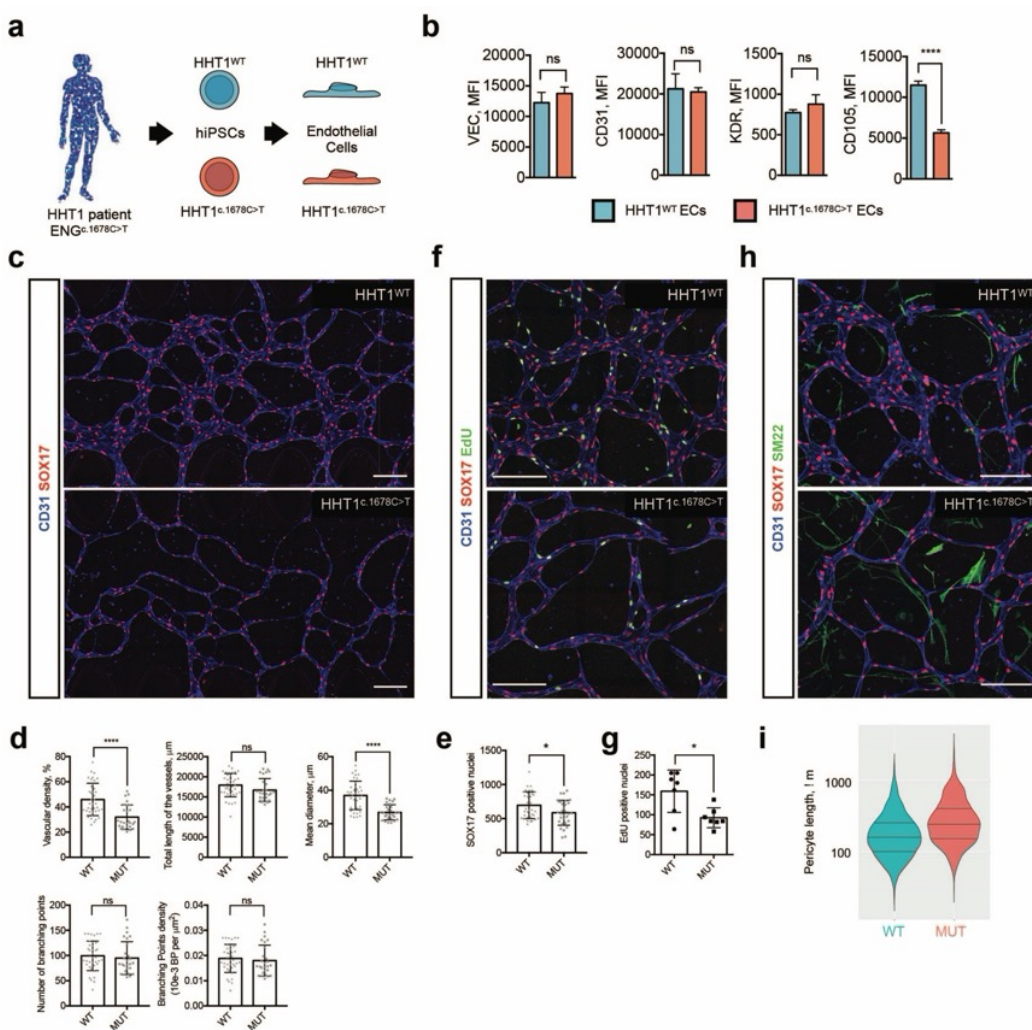


Figure 1. 3D culture in microfluidic organ on chips reveals functional differences in ECs from HHT1 patient-derived isogenic hiPSCs. **(a)** Schematic overview of ECs differentiated from HHT1 patient-derived isogenic hiPSCs. **(b)** FACS analysis of surface VEC, CD31, KDR and ENG (CD105) expression on isolated ECs (P2) from HHT1^{WT} and HHT1^{c.1678C>T} hiPSC lines. ECs differentiated from three independent hiPSC clones were analysed. Median fluorescent intensity values are shown. Error bars are \pm SD. Unpaired t-test. **** p<0.001. **(c)** Representative images of perfused microvascular networks of ECs differentiated from HHT1^{WT} and HHT1^{c.1678C>T} hiPSC lines and HBVPs in 3D microfluidic chips. ECs are stained with anti-CD31 (blue) and anti-SOX17 (red). Scale bar represents 200 μ m. **(d)** Quantification of EC sprouting network at day 6 of the microfluidic culture: vascular density, total length of the microvessels, mean diameter, number of branching points and branching points density. Error bars are \pm SD of microfluidic cultures from four independent experiments. Unpaired t-test. **** p<0.001. **(e)** Quantification of SOX17+ EC nuclei. Error bars are \pm SD of microfluidic cultures from three independent experiment. Unpaired t-test. * p<0.01. **(f)** Representative images showing proliferative (EdU positive) (green) ECs in the co-cultures. Scale bar represents 200 μ m. **(g)** Quantification of proliferative (EdU positive) ECs in the co-cultures. Error bars are \pm SD of four microfluidic cultures (one independent experiment). Unpaired t-test. * p<0.05. **(h)** Representative images showing contractile HBVPs with anti-SM22 (green). Scale bar represents 200 μ m. **(i)** Violin plot of HBVP length. Black vertical lines indicate 25%, 50% (median) and 75% quartiles. Quantification of pericyte length were performed on microfluidic cultures from three independent experiment.

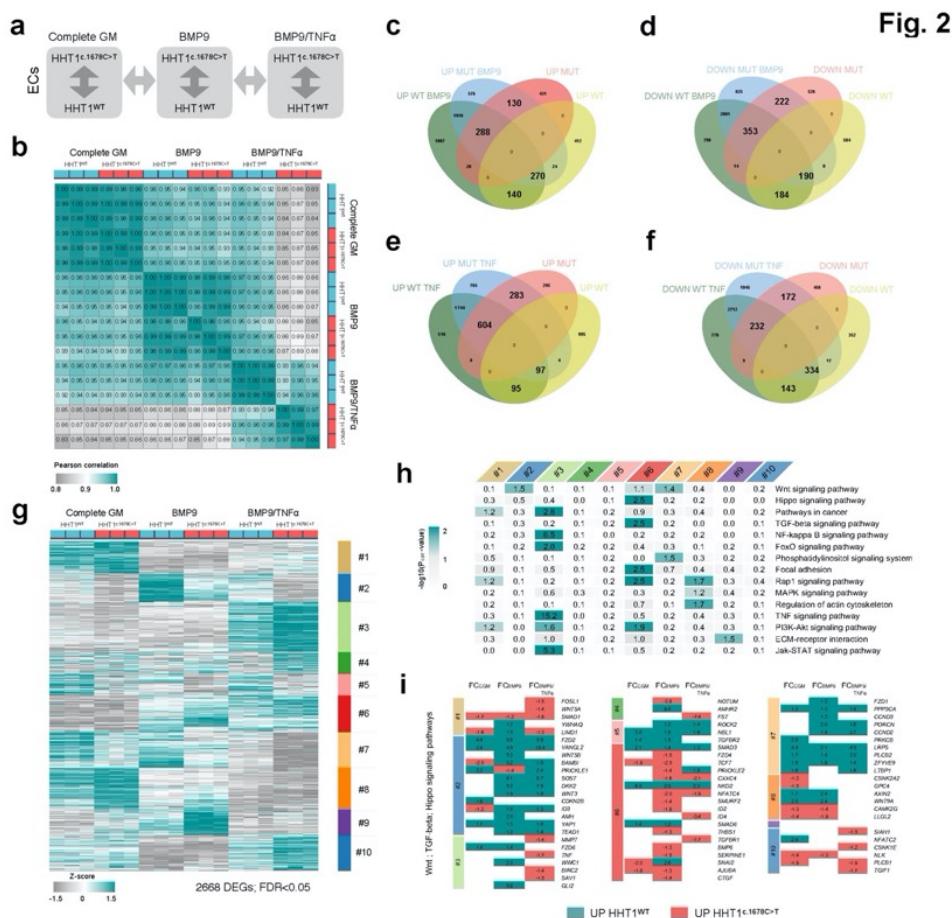


Figure 2. Identification of dysregulated pathways in ECs from HHT1 patient-derived isogenic hiPSCs upon inflammatory stimulus. (a) Schematic overview of the RNA-seq samples (three independent batches of ECs per experiments per group were used). (b) Heatmap showing Pearson correlation coefficients of ECs based on RNA-seq profiles using all genes after QC and normalization (total 19423 genes). (c,d,e,f) Venn diagrams of commonly upregulated (UP) (c,e) or downregulated (DOWN) (d,f) genes upon BMP9 and TNFα treatment in HHT1^{WT}-hiPSC-ECs (UP and DOWN WT BMP9 or TNF) and HHT1^{c.1678C>T}-hiPSC-ECs (UP and DOWN MUT BMP9 or TNF) and genes that are upregulated (UP) or downregulated (DOWN) in HHT1^{c.1678C>T}-hiPSC-ECs (UP and DOWN) vs HHT1^{WT}-hiPSC-ECs (UP and DOWN WT). (g) Heatmap showing hierarchical clustering of the 2668 UP and DOWN DEGs from Venn diagrams. (h) GO analysis of signalling pathways (KEGG's signalling pathway database) enriched in specified gene clusters. P-values (p_{corr}) were adjusted using Benjamini–Hochberg correction for multiple hypothesis testing. GO terms with $p_{corr}<0.1$ are shown. (i) Fold change (FC) of gene expression between HHT1^{WT}-hiPSC-ECs vs HHT1^{c.1678C>T}-hiPSC-ECs cultured in complete medium (FC_{FULL}), upon treatment with BMP9 (FC_{BMP9}), or upon treatment with BMP9 and TNFα (FC_{TNF}) of genes enriched in terms TGFβ, WNT and Hippo signalling pathway.

In addition to TGF β , ENG has been shown to bind BMP9 independent of ALK1 and TGFBR11 (Castonguay et al., 2011; Saito et al., 2017). BMP9 was initially identified as a “quiescence factor” for EC (David et al., 2006) but more recently it was also shown to exacerbate inflammatory responses in primary ECs (Appleby et al., 2016; Mitrofan et al., 2017), contrasting with the anti-inflammatory and immunosuppressive function of TGF β (Chen and ten Dijke, 2016; Walshe et al., 2009). We also observed that BMP9 reduced EC barrier function in hiPSC-ECs (Extended Data Fig. 5c, e). We therefore examined the expression of E-selectin, intercellular adhesion molecule-1 (ICAM-1) and vascular cell adhesion molecule-1 (VCAM-1) in hiPSC-ECs upon TNF α treatment in the presence or absence of BMP9. We found that BMP9 increased the expression of E-selectin and VCAM-1 in hiPSC-ECs treated with TNF α compared to hiPSC-ECs stimulated with TNF α alone (Extended Data Fig. 9a, b). We therefore next examined HHT1^{WT} and HHT1^{c.1678C>T} hiPSC-ECs using these optimised pro-inflammatory conditions. HHT1^{c.1678C>T} hiPSC-ECs also showed increased surface expression of E-selectin, ICAM-1 and VCAM-1, and reduced surface expression of ENG and KDR (Extended Data Fig. 9c) whilst as in controls expression of other EC markers, such as VEC, CD31 and CD34 was unchanged. Furthermore, HHT1^{c.1678C>T} hiPSC-ECs showed increased expression of proinflammatory cytokines (IL-6 and GM-CSF), and reduced barrier function upon BMP9 and TNF α addition (Extended Data Fig. 9d-g). In order to identify signaling pathways that might be dysregulated, we compared HHT1^{c.1678C>T} hiPSC-ECs and isogenic HHT1^{WT}-ECs by RNA-seq, cultured in complete growth medium, or in the medium with BMP9 or BMP9 and TNF α addition (Fig. 3a). We first examined differentially expressed genes (DEGs) commonly upregulated in HHT1^{WT} and HHT1^{c.1678C>T} hiPSC-ECs in response to BMP9 or BMP9 and TNF α (Extended Data Fig. 10a). In total, 4029 DEGs [FDR<0.05] were identified. Hierarchical clustering showed distinct gene clusters that shared common expression patterns in HHT1-hiPSC-ECs and were either downregulated by BMP9 (cluster #1), upregulated by BMP9 and downregulated by TNF α (cluster #2 and #4) or upregulated by TNF α (cluster #3). Gene ontology (GO) analysis indicated Pathways in cancer, Lysosomes, TNF α and TGF β signaling pathways among top 5 upregulated terms in cluster #1, #2, #3 and #4 respectively (Extended Data Fig. 10b). TGF β and WNT signaling pathways were identified among the top-ten enriched pathways in gene clusters #2 and #4 that were upregulated upon BMP9 treatment (Extended Data Fig. 10c). HHT1-hiPSC-ECs showed the highest segregation upon TNF α treatment, indicating that the inflammatory component might indeed exacerbate the phenotype in HHT1-hiPSC-ECs in culture (Fig. 3b). To identify dysregulated signaling pathways, we next identified DEGs between HHT1^{c.1678C>T} and HHT1^{WT} hiPSC-ECs cultured in complete growth medium, or in the medium with BMP9 or BMP9 and TNF α [FDR<0.05]. Enrichment analysis of genes commonly up- or downregulated by BMP9 or BMP9 and TNF α as well as those differentially expressed between HHT1^{c.1678C>T} and HHT1^{WT} hiPSC-

ECs (Fig. 2c-f) identified in total 2668 genes, with 604 more strongly upregulated in HHT1^{c.1678C>T}-hiPSC-ECs versus 97 genes in HHT1^{WT}-hiPSC-ECs following TNF α treatment (Fig. 2e). Similar numbers of genes were upregulated upon BMP9 treatment or downregulated upon BMP9 and BMP9 with TNF α treatment in HHT1^{c.1678C>T} and HHT1^{WT} hiPSC-ECs (Fig. 2c, d, f). Hierarchical clustering of the DEGs and gene enrichment analysis identified distinct gene clusters with the WNT signaling pathway being enriched in clusters #2 and #7, and the TGF β and Hippo signaling pathways enriched in cluster #6 (Fig. 2h, i). BMP9 upregulated both SMAD2/3 and SMAD1/5 target genes, and the canonical WNT signaling pathway (Extended Data Fig.11). The SMAD2/3 targets were more upregulated and both the SMAD1/5 targets and canonical WNT pathway more downregulated in HHT1^{c.1678C>T}-hiPSC-ECs versus HHT1^{WT}-hiPSC-ECs. Furthermore, inflammatory pathways, such as NF-kappaB, TNF α and Jak-STAT were the most enriched in the cluster #3, and more strongly upregulated in HHT1^{c.1678C>T}-hiPSC-ECs (Fig. 2h). TNF α treatment further resulted in downregulation of SMAD1/5 and canonical WNT signaling, and upregulation of SMAD2/3 signaling in HHT1-hiPSC-ECs. HHT1^{c.1678C>T}-hiPSC-ECs showed further decreased canonical WNT and upregulated SMAD2/3 signaling when compared to HHT1^{WT}-hiPSC-ECs. *ALK5* (*TGFBR1*) and *ALK1* (*ACVRL1*) for example, were significantly up- and downregulated respectively in HHT1^{c.1678C>T}-hiPSC-ECs upon TNF α treatment resulting in increased *ALK5* to *ALK1* ratios (Extended Data Fig.11d). Interplay of BMP9 and TNF α pathways was evidenced by exacerbated reduction in barrier function in HHT1^{c.1678C>T}-hiPSC-ECs, illustrating the likely importance of BMP9 and TNF α in manifestation of HHT (Fig. 3 a, b). Interplay between TGF β /BMP and WNT signaling pathways has already been well established in different model systems (Attisano and Wrana, 2013; Fuentealba et al., 2007) and WNT was also recently identified as one potentially dysregulated signaling pathway in biopsies from HHT1 patients (Tørring et al., 2015). We therefore examined whether dysregulated WNT signaling might cause the abnormal vascular networks formed by HHT1^{c.1678C>T}-hiPSC-ECs in microfluidic chips. Addition of the small molecular inhibitor (XAV 939) or activator of WNT signaling (CHIR99021, CHIR) between day 1 to day 3 of EC self-organization in the 3D chip either inhibited (data not shown) or promoted vascular network formation by HHT1^{c.1678C>T}-hiPSC-ECs respectively (Fig. 3c). Quantification of the vascular networks confirmed increased vascular density and diameter of the vessels, and increased overall numbers of ECs, but showed no difference in the total length of the vessels, number of branching points or branching points density (Fig. 3d).

In this study we thus developed a human *in vitro* model for the genetic vascular disorder HHT using hiPSCs derived from patients with mutations in the *ENG* gene (HHT1). The results showed that we likely capture the direct effects of reduced ENG protein on the EC surface without compensation or adaption mechanisms thought to be present in mutant mice. As such, the results in the HHT1-hiPSC-EC model here may be more

similar to earlier studies in which siRNA was used to knock down *Eng* in mouse embryonic ECs (Lebrin et al., 2004), although they would not capture genetic background differences that can contribute to the severity of the phenotypes observed in patients. Interestingly but unexpectedly, *ENG* haploinsufficiency in HHT1-hiPSC-ECs had no effect on multiple aspects of EC function in 2D, with differentiation, proliferation, barrier function and sprouting in HHT1-hiPSC lines being undistinguishable from that in isogenic controls. This is reflected in the phenotype in patients where only some, but not all, vascular beds are affected, other factors such as blood flow rates and inflammatory cells likely contributing to the development of the vascular lesions. We have previously demonstrated that hiPSC-ECs have lower inflammatory responses than for example human umbilical vein ECs (HUVECs) (Halaidych et al., 2018). BMP9 enhanced the inflammatory responses in hiPSC-ECs, and since it is present in circulating blood, it is conceivable that it not only contributes to ECs becoming quiescent but also increases EC responsiveness to inflammatory stimuli, in accordance with recent data on transcriptomic and epigenetic changes that occur upon EC quiescence *in vivo*³². Our transcriptome profiling of hiPSC-ECs following BMP9 exposure showed its importance in balancing both the SMAD1/5 and SMAD2/3 pathways in ECs (Fig. 3e), but also in priming the cells for inflammatory insults that cause upregulation of SMAD2/3 and downregulation of both SMAD1/5 and canonical WNT signaling (Fig. 3f). Despite having no evident effect on their function in standard 2D culture conditions, 3D culture under fluid flow *ENG* haploinsufficiency makes ECs much more sensitive to inflammatory conditions, causing far more profound imbalances in SMAD2/3 and SMAD1/5 signaling due to changes in the ALK5 to ALK1 ratio, as we reported previously (Lebrin et al., 2004), and further downregulation of the canonical WNT pathway (Fig. 3g). Our work here not only shows that HHT1 patient-derived hiPSC-ECs can be used to study the role of *ENG* *in vitro*, but also provides the first experimental evidence on the contribution of WNT and TNF α signaling pathways in the pathology of HHT1. This is revealed specifically in 3D culture under microfluidic flow. Together, the study suggests new avenues for drug discovery using mechanism-based approaches with opportunities for validation using ECs from patients-derived hiPSCs.

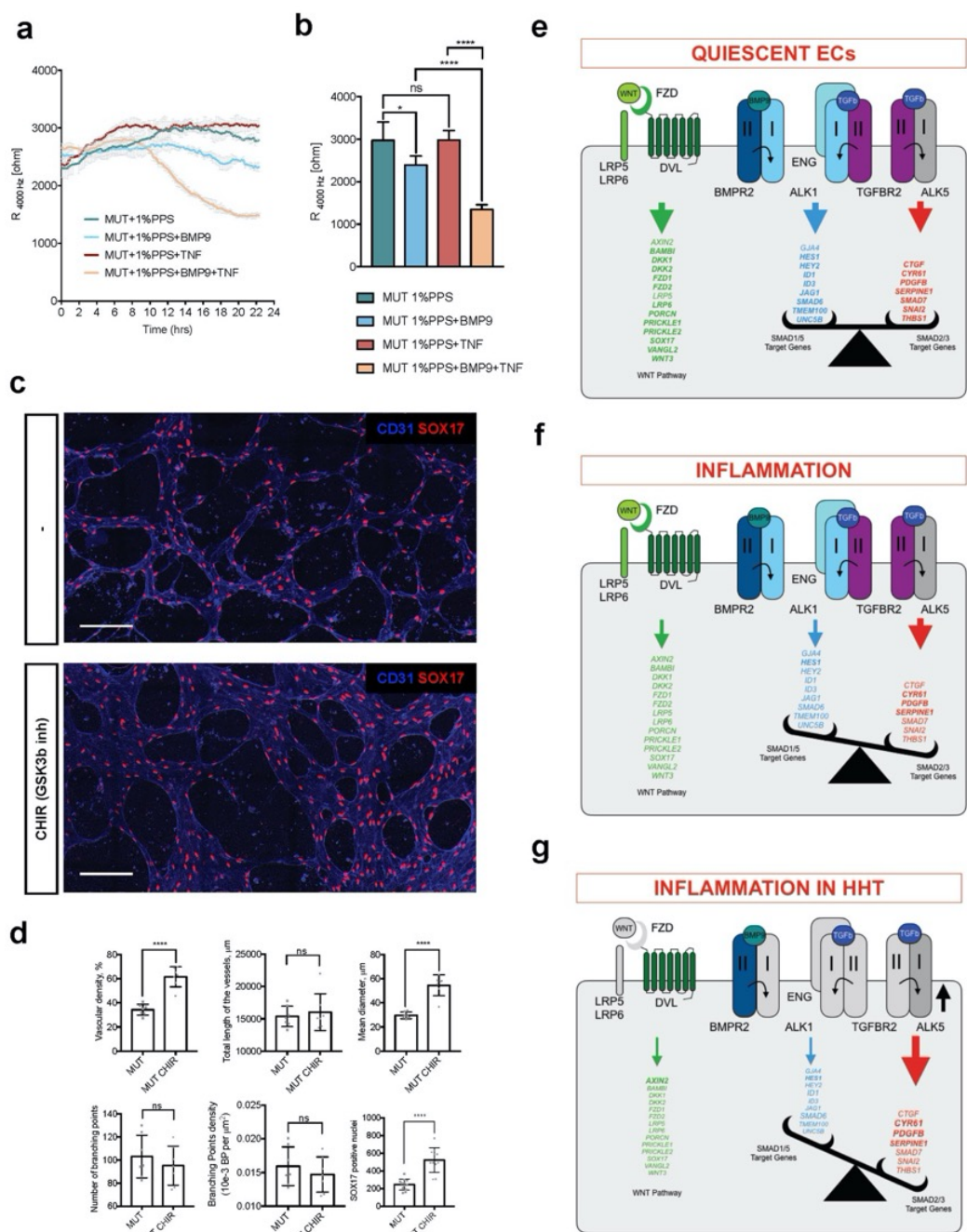


Figure 3. Interplay between TGF β , WNT and inflammation causes vascular defects associated with HHT. (a) Absolute resistance of the EC monolayer at 4000 Hz in HHT1^{c.1678C>T}-hiPSC-ECs cultured in growth factor-free medium with 1% platelet poor serum (1% PPS) or 1% PPS and BMP9 or 1%PPS with TNF α or 1%PPS with BMP9 and TNF α supplementation is shown. Error bars are \pm SD one representative biological experiment. **(b)** Quantification of absolute resistance values at 4000 Hz in HHT1^{c.1678C>T}-hiPSC-ECs cultured in growth factor-free medium with 1% PPS

or 1% PPS and BMP9 or 1%PPS with TNF α or 1%PPS with BMP9 and TNF α supplementation is shown. Error bars are shown as \pm SD of three independent biological experiments. One-way ANOVA. ****p<0.0001, *p<0.01. **(c)** Representative images of perfused microvascular networks of ECs differentiated from HHT1^{c.1678C>T} hiPSCs in 3D microfluidic chips upon supplementation with activator of WNT signaling (CHIR99021, CHIR). ECs are stained with anti-CD31 (grey). Scale bar represents 200 μ m. **(d)** Quantification of EC sprouting network at day 6 of the microfluidic culture: vascular density, total length of the microvessels, mean diameter, number of branching points, branching points density and number of SOX17+ EC nuclei. Error bars are \pm SD of microfluidic cultures from three independent experiments. Unpaired t-test. **** p<0.0001. **(e-g)** Schematic showing dysregulated pathways in HHT: **(e)** BMP9 balances SMAD1/5 and SMAD2/3 signalling pathways in ECs. **(f)** Inflammation dysregulates the balance towards activation of SMAD2/3 signalling. **(g)** SMAD2/3 signalling is further exuberated in upon ENG deficiency in HHT which results in decreased ALK1 expression and increased ALK5 promoting SMAD2/3.

METHODS

Methods and associated references are described in supplementary information of this chapter.

Accession codes.

RNA-seq data are deposited into GEO: **GSE116467**

Acknowledgements

The LUMC human iPSC Hotel for generation and initial characterization of hiPSC lines; LUMC confocal imaging facility and Annelies Boonzaier - van der Laan for help with imaging; Karoly Szuhai and Danielle de Jong for help with COBRA-FISH; LUMC flow cytometry facility; patients for their contribution to the basic research on HHT; Sandra Petrus-Reurer and Ana Melo Bernardo for help with imaging and quantification of 2D cocultures; Lucas Hawikels for useful discussion; Douwe Astma for collecting patient samples.

This project was funded by the following grants: European Research Council (ERCAdG 323182 STEMCARDIOVASC); the Association Maladie de Rendu-Osler (AMRO) and the Kees Westermann Fund; Netherlands Organ-on-Chip Initiative, an NWO Gravitation

project funded by the Ministry of Education, Culture and Science of the government of the Netherlands (024.003.001).

Author contributions

VO: designed the research, established functional assays, performed experiments, performed RNA sequencing analysis and wrote the manuscript; XC: conducted EC differentiation, qRT-PCR, FACS and cytokine array experiments; AC: conducted immunofluorescence staining of ECs and imaging of microfluidic chips; RCS: performed RNA sequencing analysis; C.F.: performed reprogramming experiments; FEvdH: conducted EC differentiation and isolation, qRT-PCR, FACS; DL and FL: assisted with quantification of microfluidic experiments; GSD and PT: assisted with signal transduction experiments; H.M. assisted with RNA sequencing; K.J.J.W, F.D., R.J.S., J.J.M. provided HHT patient samples; K.J.PvA: conducted genetic analysis; CLM: designed the research and wrote the manuscript.

REFERENCES

- Appleby, S.L., Mitrofan, C.-G., Crosby, A., Hoenderdos, K., Lodge, K., Upton, P.D., Yates, C.M., Nash, G.B., Chilvers, E.R., and Morrell, N.W. (2016). Bone Morphogenetic Protein 9 Enhances Lipopolysaccharide-Induced Leukocyte Recruitment to the Vascular Endothelium. *J Immunol* 197, 3302–3314.
- Attisano, L., and Wrana, J.L. (2013). Signal integration in TGF- β , WNT, and Hippo pathways. *F1000prime Reports* 5, 17.
- Avior, Y., Sagi, I., and Benvenisty, N. (2016). Pluripotent stem cells in disease modelling and drug discovery. *Nat Rev Mol Cell Bio* 17, 170–182.
- Benzinou, M., Clermont, F.F., Letteboer, T.G., Kim, J.-H., Espejel, S., Harradine, K.A., Arbelaez, J., Luu, M., Roy, R., Quigley, D., et al. (2012). Mouse and human strategies identify PTPN14 as a modifier of angiogenesis and hereditary haemorrhagic telangiectasia. *Nat Commun* 3, 616.
- Castonguay, R., Werner, E., Matthews, R., Presman, E., Mulivor, A., Solban, N., Sako, D., Pearsall, R., Underwood, K., Sehra, J., et al. (2011). Soluble endoglin specifically binds bone morphogenetic proteins 9 and 10 via its orphan domain, inhibits blood vessel formation, and suppresses tumor growth. *J Biol Chem* 286, 30034–30046.
- Chen, W., and ten Dijke, P. (2016). Immunoregulation by members of the TGF β superfamily. *Nat Rev Immunol* 16, 723–740.
- Cunha, S.I., Magnusson, P.U., Dejana, E., and Lampugnani, M. (2017). Deregulated TGF- β /BMP Signaling in Vascular Malformations. *Circ Res* 121, 981–999.
- David, L., Mallet, C., Mazerbourg, S., Feige, J.-J., and Bailly, S. (2006). Identification of BMP9 and

- BMP10 as functional activators of the orphan activin receptor-like kinase 1 (ALK1) in endothelial cells. *Blood* **109**, 1953–1961.
- El-Brolosy, M.A., and Stainier, D.Y. (2017). Genetic compensation: A phenomenon in search of mechanisms. *Plos Genet* **13**, e1006780.
- Esch, E.W., Bahinski, A., and Huh, D. (2015). Organs-on-chips at the frontiers of drug discovery. *Nat Rev Drug Discov* **14**, 248–260.
- Fuentealba, L., Eivers, E., Ikeda, A., Hurtado, C., Kuroda, H., Pera, E., and Robertis, D.E. (2007). Integrating patterning signals: Wnt/GSK3 regulates the duration of the BMP/Smad1 signal. *Cell* **131**, 980–993.
- Goumans, M., Valdimarsdottir, G., Itoh, S., Rosendahl, A., Sideras, P., and ten Dijke, P. (2002). Balancing the activation state of the endothelium via two distinct TGF-beta type I receptors. *Embo J* **21**, 1743–1753.
- Goumans, M., Valdimarsdottir, G., Itoh, S., Lebrin, F., Larsson, J., Mummery, C., Karlsson, S., and ten Dijke, P. (2003). Activin receptor-like kinase (ALK)1 is an antagonistic mediator of lateral TGFbeta/ALK5 signaling. *Mol Cell* **12**, 817–828.
- Halaïdych, O., Freund, C., van den Hil, F., Salvatori, D., Riminucci, M., Mummery, C., and Orlova, V. (2018). Inflammatory Responses and Barrier Function of Endothelial Cells Derived from Human Induced Pluripotent Stem Cells. *Stem Cell Rep* **10**, 1642–1656.
- Lebrin, F., Goumans, M.-J., Jonker, L., Carvalho, R.L., Valdimarsdottir, G., Thorikay, M., Mummery, C., Arthur, H.M., and ten Dijke, P. (2004). Endoglin promotes endothelial cell proliferation and TGF- β /ALK1 signal transduction. *Embo J* **23**, 4018–4028.
- Lebrin, F., DECKERS, M., BERTOLINO, P., and TENDIJE, P. (2005). TGF- β receptor function in the endothelium. *Cardiovasc Res* **65**, 599–608.
- Lebrin, F., n, S., Raymond, K., Martin, S., van den Brink, S., Freitas, C., Bréant, C., Mathivet, T., Larrivée, B., Thomas, J.-L., et al. (2010). Thalidomide stimulates vessel maturation and reduces epistaxis in individuals with hereditary hemorrhagic telangiectasia. *Nat Med* **16**, 420–428.
- Letteboer, T., Zewald, R., Kamping, E., de Haas, G., Mager, J., Snijder, R., Lindhout, D., Hennekam, F., Westermann, C., and van Amstel, P.J. (2004). Hereditary hemorrhagic telangiectasia: ENG and ALK-1 mutations in Dutch patients. *Hum Genet* **116**, 8–16.
- Letteboer, T.G., Benzinou, M., Merrick, C.B., Quigley, D.A., Zhau, K., Kim, I.-J., To, M.D., Jablons, D.M., van Amstel, J.K., Westermann, C.J., et al. (2015). Genetic variation in the functional ENG allele inherited from the non-affected parent associates with presence of pulmonary arteriovenous malformation in hereditary hemorrhagic telangiectasia 1 (HHT1) and may influence expression of PTPN14. *Frontiers Genetics* **6**, 919.
- Mahmoud, M., Allinson, K., Zhai, Z., Oakenfull, R., Ghandi, P., Adams, R., Fruttiger, M., and Arthur, H. (2010). Pathogenesis of Arteriovenous Malformations in the Absence of Endoglin. *Circ Res* **106**, 1425–1433.
- Mitrofan, C.-G., Appleby, S.L., Nash, G.B., Mallat, Z., Chilvers, E.R., Upton, P.D., an

- Morrell, N.W. (2017). Bone morphogenetic protein 9 (BMP9) and BMP10 enhance tumor necrosis factor- α -induced monocyte recruitment to the vascular endothelium mainly via activin receptor-like kinase 2. *J Biol Chem* 292, 13714–13726.
- McDonald, J., Wooderchak-Donahue, W., Webb, C., Whitehead, K., Stevenson, D.A., and Bayrak-Toydemir, P. (2015). Hereditary hemorrhagic telangiectasia: genetics and molecular diagnostics in a new era. *Frontiers Genetics* 6, 1.
- Orlova, V., van den Hil, F., Petrus-Reurer, S., Drabsch, Y., Dijke, T.P., and Mummery, C. (2014a). Generation, expansion and functional analysis of endothelial cells and pericytes derived from human pluripotent stem cells. *Nat Protoc* 9, 1514–1531.
- Orlova, V., Drabsch, Y., Freund, C., Petrus-Reurer, S., van den Hil, F., Muenthaisong, S., Dijke, P., and Mummery, C. (2014b). Functionality of endothelial cells and pericytes from human pluripotent stem cells demonstrated in cultured vascular plexus and zebrafish xenografts. *Arteriosclerosis Thrombosis Vasc Biology* 34, 177–186.
- Paquet, M.-E., Pece-Barbara, N., Vera, S., Cymerman, U., Karabegovic, A., Shovlin, C., and Letarte, M. (2001). Analysis of several endoglin mutants reveals no endogenous mature or secreted protein capable of interfering with normal endoglin function. *Hum Mol Genet* 10, 1347–1357.
- Saito, T., Bokhove, M., Croci, R., Zamora-Caballero, S., Han, L., Letarte, M., de Sanctis, D., and Jovine, L. (2017). Structural Basis of the Human Endoglin-BMP9 Interaction: Insights into BMP Signaling and HHT1. *Cell Reports* 19, 1917–1928.
- Sugden, W.W., Meissner, R., Aegerter-Wilmsen, T., Tsaryk, R., Leonard, E.V., Bussmann, J., Hamm, M.J., Herzog, W., Jin, Y., Jakobsson, L., et al. (2017). Endoglin controls blood vessel diameter through endothelial cell shape changes in response to haemodynamic cues. *Nat Cell Biol* 19, 653–665.
- Tang, Y. (2003). Genetic modifiers interact with maternal determinants in vascular development of *Tgfb1*^{-/-} mice. *Hum Mol Genet* 12, 1579–1589.
- Tang, Y., Lee, K., Yang, H., Logan, D.W., Wang, S., McKinnon, M.L., Holt, L.J., Condie, A., Luu, M., and Akhurst, R.J. (2005). Epistatic interactions between modifier genes confer strain-specific redundancy for *Tgfb1* in developmental angiogenesis. *Genomics* 85, 60–70.
- Tørring, P.M., Larsen, M., Kjeldsen, A.D., Ousager, L., Tan, Q., and Brusgaard, K. (2015). Global gene expression profiling of telangiectasial tissue from patients with hereditary hemorrhagic telangiectasia. *Microvasc Res* 99, 118–126.
- Walshe, T.E., Dole, V.S., Maharaj, A.S., Patten, I.S., Wagner, D.D., and D'Amore, P.A. (2009). Inhibition of VEGF or TGF- β signaling activates endothelium and increases leukocyte rolling. *Arteriosclerosis Thrombosis Vasc Biology* 29, 1185–1192.

SUPPLEMENTARY INFORMATION

Supplemental Figures S1-S11

Supplemental Tables S1-S3

Methods

Supplemental References

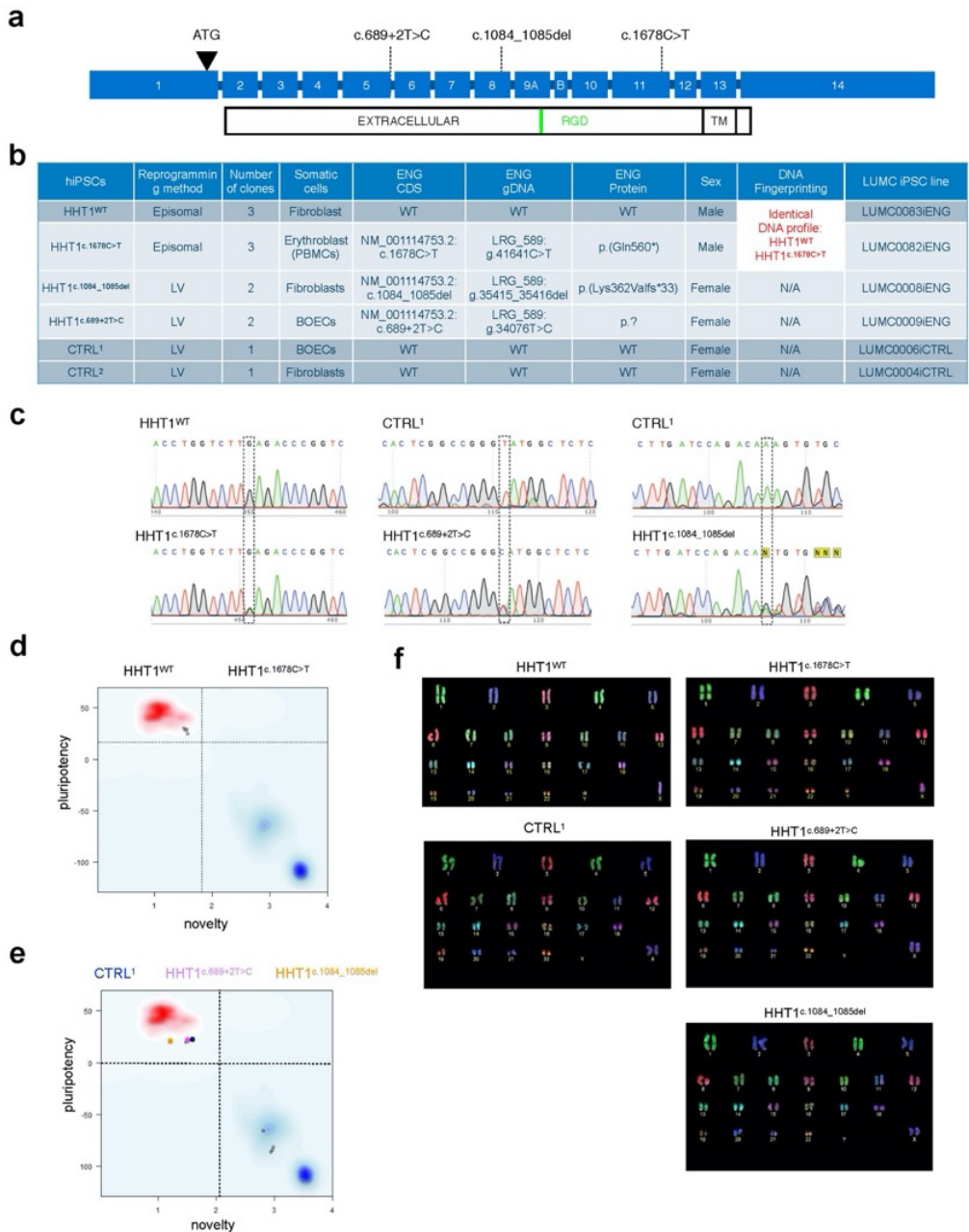


Figure S1. Characterization of HHT1 patient-derived hiPSCs. (a) Schematic overview of *ENG* genomic map, protein map and location of the mutations. **(b)** Overview of HHT1 patient and control hiPSC lines. **(c)** Sanger sequencing of the genomic DNA from control and HHT1 patient-derived hiPSC lines to confirm mutations. **(d,e)** Bioinformatics assessment of pluripotency of control and HHT1 patient-derived hiPSCs (PluriTest). **(f)** COBRA-FISH analysis of karyotype of control and HHT1 patient-derived hiPSC lines.

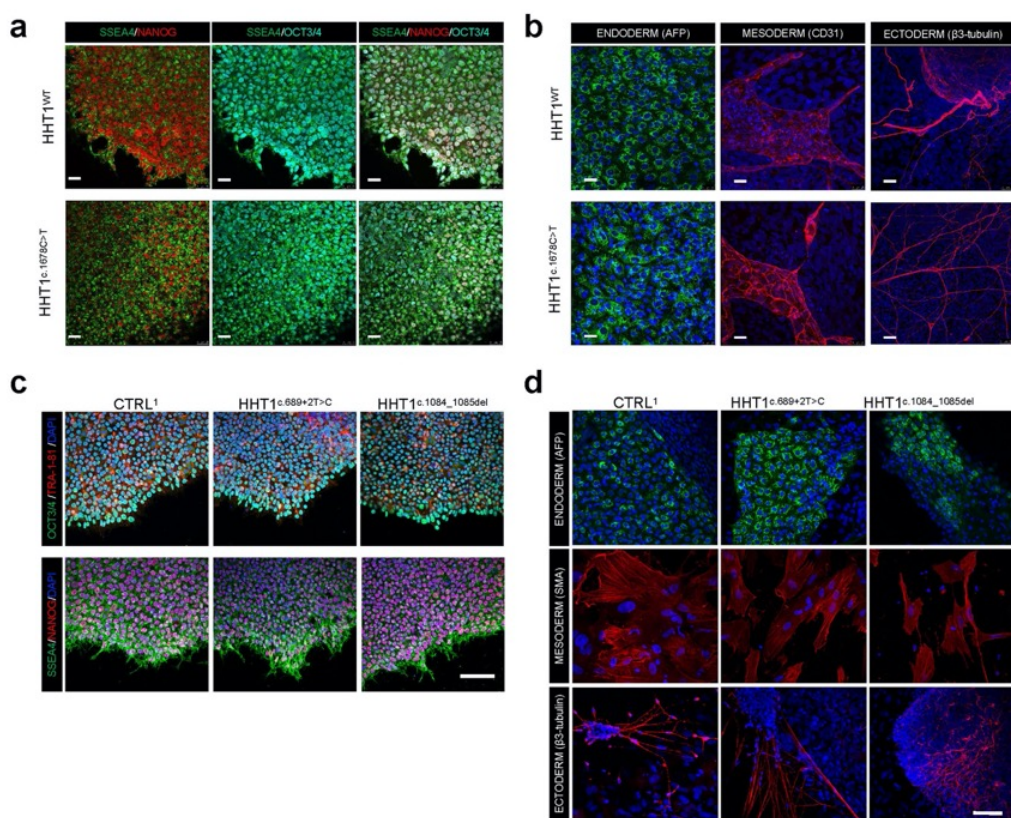


Figure S2. Characterization of HHT1 patient-derived hiPSCs. (a, c) Characterization of control and HHT1 patient-derived hiPSC lines: **(a)** immunofluorescent images for OCT3/4, SSEA4 and Nanog. Scale bar 25 μm; **(c)** immunofluorescent images for OCT3/4, TRA-1-81, SSEA4 and NANOG. Scale bar 75 μm. **(b, d)** Immunofluorescent images of the spontaneous differentiation demonstrating derivatives of all three germ layers: **(b)** βIII-tubulin for neuroectoderm, CD31 for mesoderm, AFP for endoderm. Scale bar 25μm; **(d)** βIII-tubulin for neuroectoderm, SMA for mesoderm and AFP for endoderm. Scale bar 75μm.

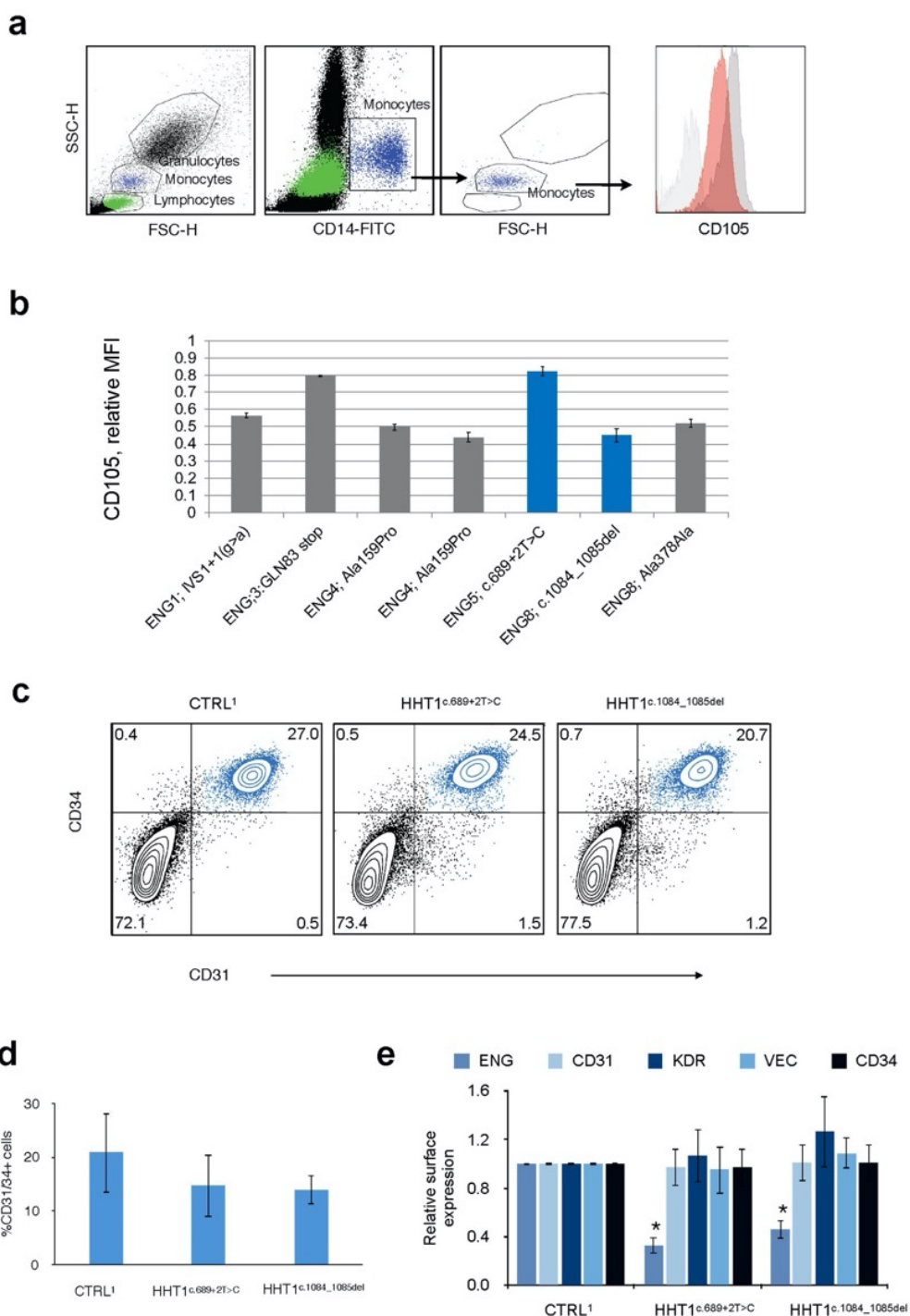


Figure S3. Characterization of ECs from HHT1 patient-derived hiPSCs. (a, b) Characterization of ENG expression on HHT1 patient-derived PBMCs: **(a)** Gating strategy to identify monocyte subset based on FSC and SSC scatters. Back gating of CD14+ monocytes to confirm the cell size of the population. Representative ENG histogram to demonstrate reduced ENG expression levels in

HHT1 monocytes (red) compared to control monocytes (grey); **(b)** relative ENG surface expression in HHT1 patient-derived PBMCs shown as mean fluorescence intensity (MFI) of ENG expression levels in HHT1 normalized to control PBMCs. Data are shown \pm SD from three independent measurements. **(c)** FACS analysis of CD34 and CD31 expression at differentiation day 10 in control and HHT1 patient-derived hiPSC-ECs. **(d)** Quantification of the yield of CD31+/CD34+ endothelial cells at day 10 of differentiation. Data are shown \pm SD from three to five independent experiments. **(e)** FACS analysis of surface expression levels of ENG, CD31, KDR, VEC and CD34 on hiPSC-ECs isolated from control and HHT1 patient-derived hiPSC lines. Data were normalized to CTRL. Data are shown \pm SD from three independent experiments. One-way ANOVA. * p <0.05.

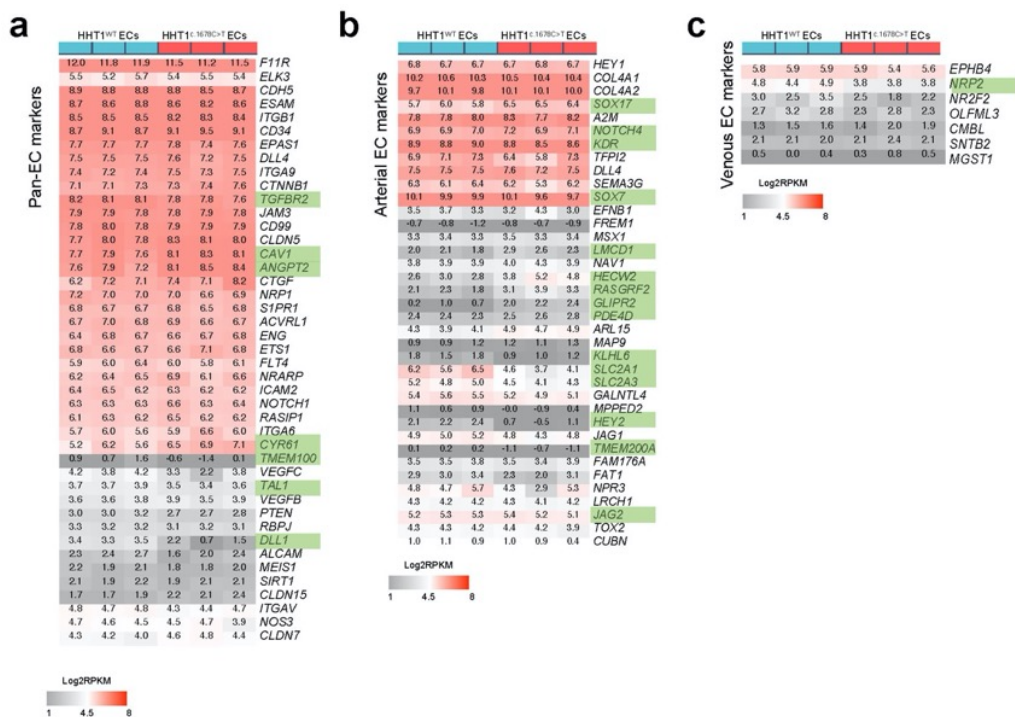


Figure S4. Characterization of ECs differentiated from HHT1 patient-derived isogenic hiPSCs. **(a)** Heatmap showing hierarchical clustering of pan-EC markers from RNA-seq. **(b, c)** Heatmap showing hierarchical clustering of arterial **(b)** and venous EC **(c)** markers from RNA-seq. DEGs with FDR<0.5 are highlighted in green.

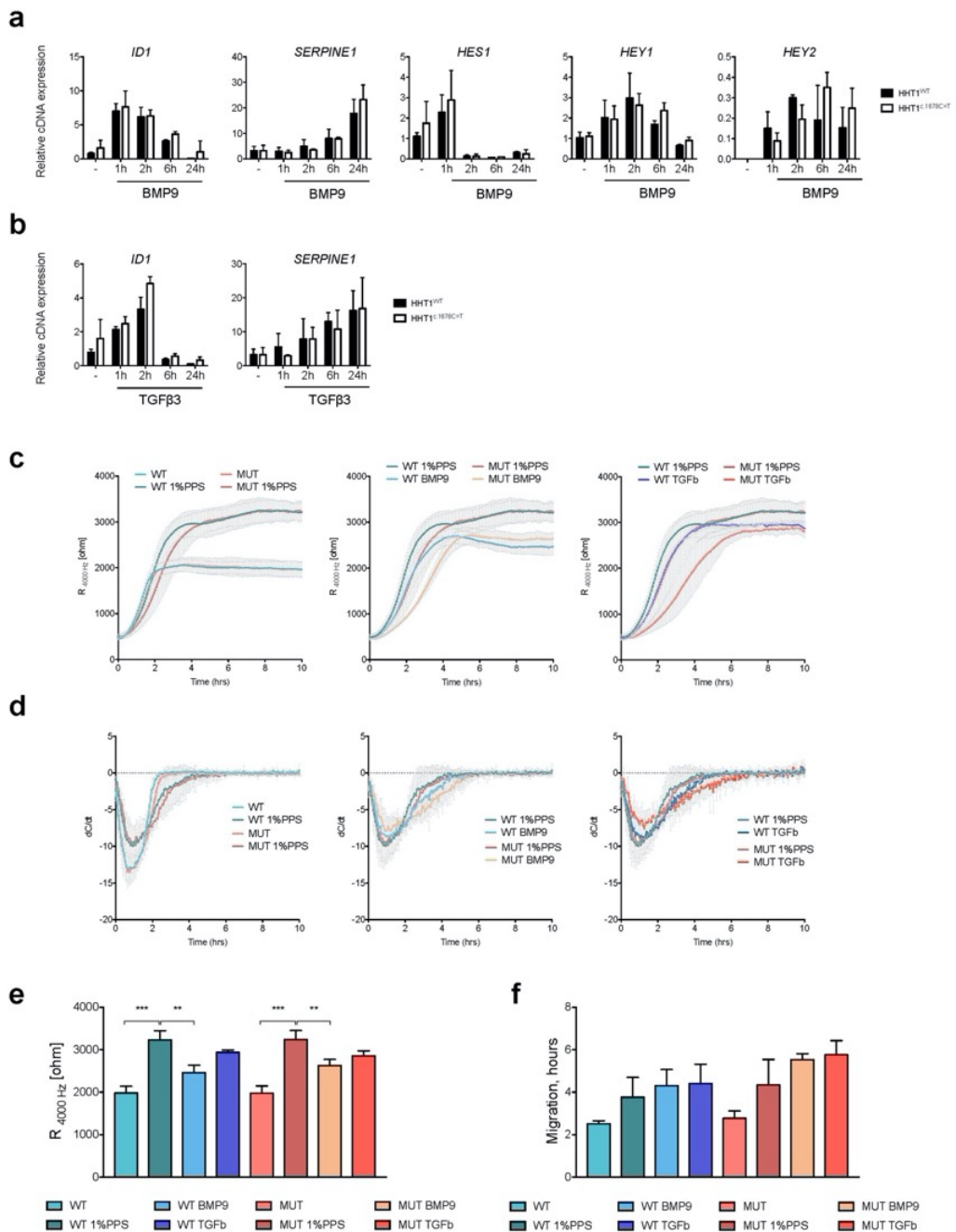


Figure S5. ECs from HHT1 patient-derived isogenic hiPSCs respond normally to TGFβ and BMP9. (a, b) Gene expression analysis of expression of *ID1*, *SERPINE1*, *HES1*, *HEY1* and *HEY2* (upon BMP9 1ng/ml stimulation) (a); and *ID1*, *SERPINE1* (upon TGFβ 1ng/ml stimulation)(b). Data are shown ±SD from three independent experiments. (c) Absolute resistance of the EC monolayer at 4000 Hz in complete EC growth medium, or growth factor-free medium supplemented with 1% PPS, or 1% PPS supplemented with BMP9 or TGFβ is shown. ECs were differentiated from

HHT1 patient-derived isogenic hiPSCs (P2). Error bars are \pm SD of three independent biological experiments. **(d)** Mean speed of migration (dC/dt) determined as a change in capacitance at 64000Hz over the time after electric wound healing in EC growth medium, or growth factor-free medium supplemented with 1% PPS, or 1% PPS supplemented with BMP9 (2 ng/ml) or TGF β (1 ng/ml). Error bars are shown as \pm SD of average values from three independent biological experiments. **(e)** Quantification of absolute resistance values at 4000 Hz in complete EC growth medium. Error bars are shown as \pm SD of three to five independent biological experiments. **(f)** Quantification of migration rates determined as a time upon closing the wound ($dC/dt > (-0,1 \text{ nF/h})$) of hiPSC-ECs in real-time wound healing assay in EC growth medium, or growth factor-free medium supplemented with 1% PPS, or 1% PPS supplemented with BMP9 or TGF β is shown. Error bars are shown as \pm SD of three independent biological experiments. One-way ANOVA. *** $p \leq 0.0001$, ** $p \leq 0.005$.

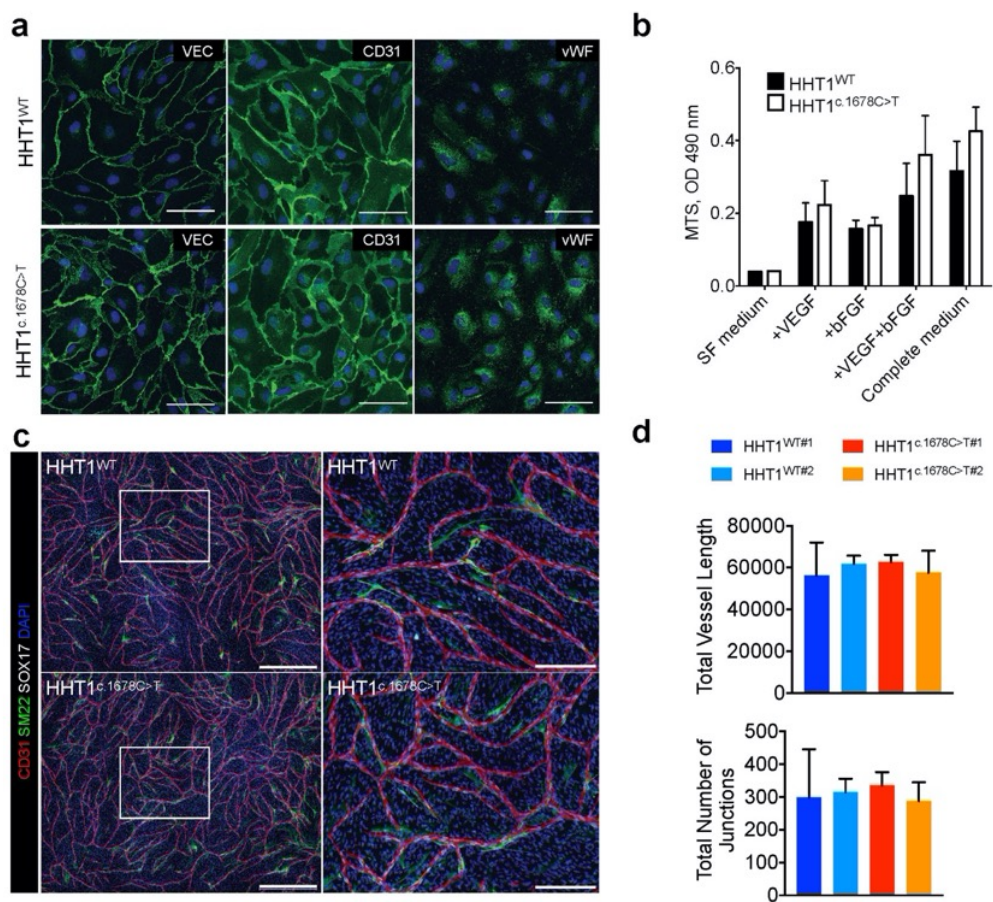


Figure S6. ECs from HHT1 patient-derived isogenic hiPSCs show no disease phenotype in standard functional EC assays in 2D. (a) Immunofluorescent analysis of EC markers VEC, CD31

and vWF on isolated ECs from HHT1 patient-derived isogenic hiPSCs (P2). Scale bar 75 μ m. **(b)** Assessment of EC proliferation in serum-free medium (SF medium), SF medium + VEGF (+VEGF), SF medium + bFGF (+FGF), SF medium VEGF + bFGF (+VEGF+FGF) or complete EC growth medium (Complete medium) at 72h after medium change. The analysis was performed on ECs differentiated from three independent clones of HHT1 patient-derived isogenic hiPSCs. Error bars are \pm SD. **(c)** Representative immunofluorescent images of an *in vitro* vasculogenesis sprouting assay at day 10 of the co-culture of ECs differentiated from two independent clones of HHT1 patient-derived isogenic hiPSCs and CD31- cells differentiated from an independent control hiPSC line. ECs are stained with anti-CD31 (red) and anti-SOX17 (grey), contractile CD31- cells with anti-SM22 (green) and nuclei stained with DAPI (blue). Left panels: automatically stitched images (10x objective, 4 x 4 focus planes) are shown; scale bar represents 750 μ m. Right panels: magnification of the framed area in the left panel, scale bar represents 250 μ m. **(d)** Quantification of EC sprouting network at day 10 of the co-culture. The total vessel length and total number of junctions are shown. Data are shown as \pm SD of three independent biological experiments.

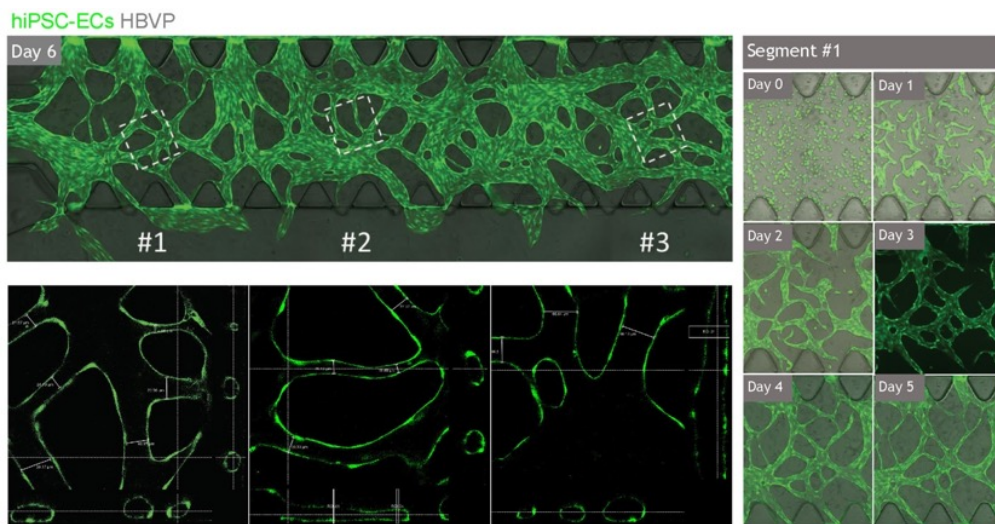


Figure S7. 3D microvessels in microfluidic organ on chip. Representative immunofluorescent images of microvascular networks formed in microfluidic chips by hiPSC-derived ECs (hiPSC-ECs GFP) (green). Images were taken every 24h from day 0 (after seeding) till day 6. Dashed boxes (in white) were imaged on WLL1 confocal microscope and Z-sections of lumens are shown in the panels below.

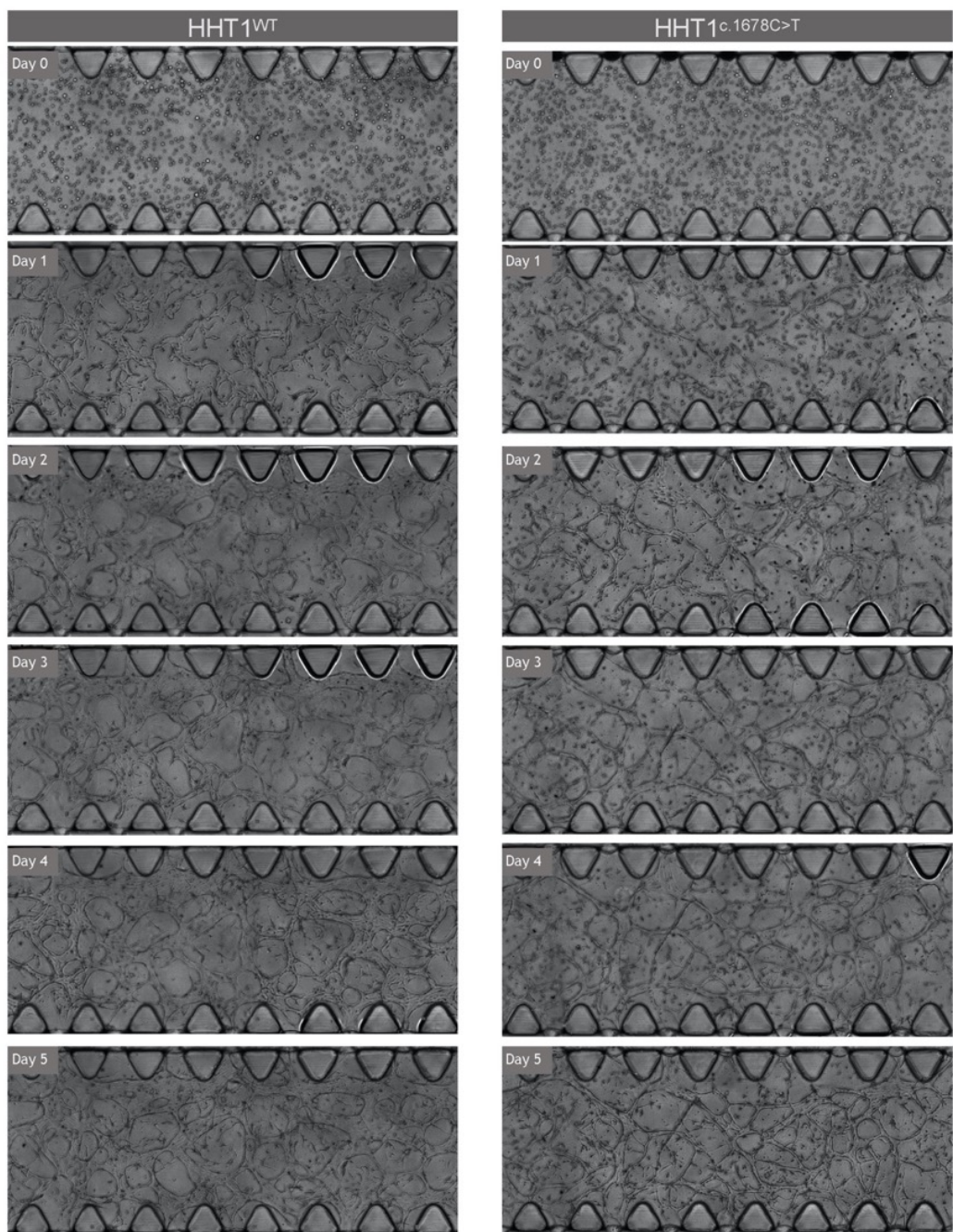


Figure S8. Representative images of microfluidic chips seeded with ECs from HHT1 patient-derived isogenic hiPSCs. Images were taken every 24h from day 0 (after seeding) till day 5.

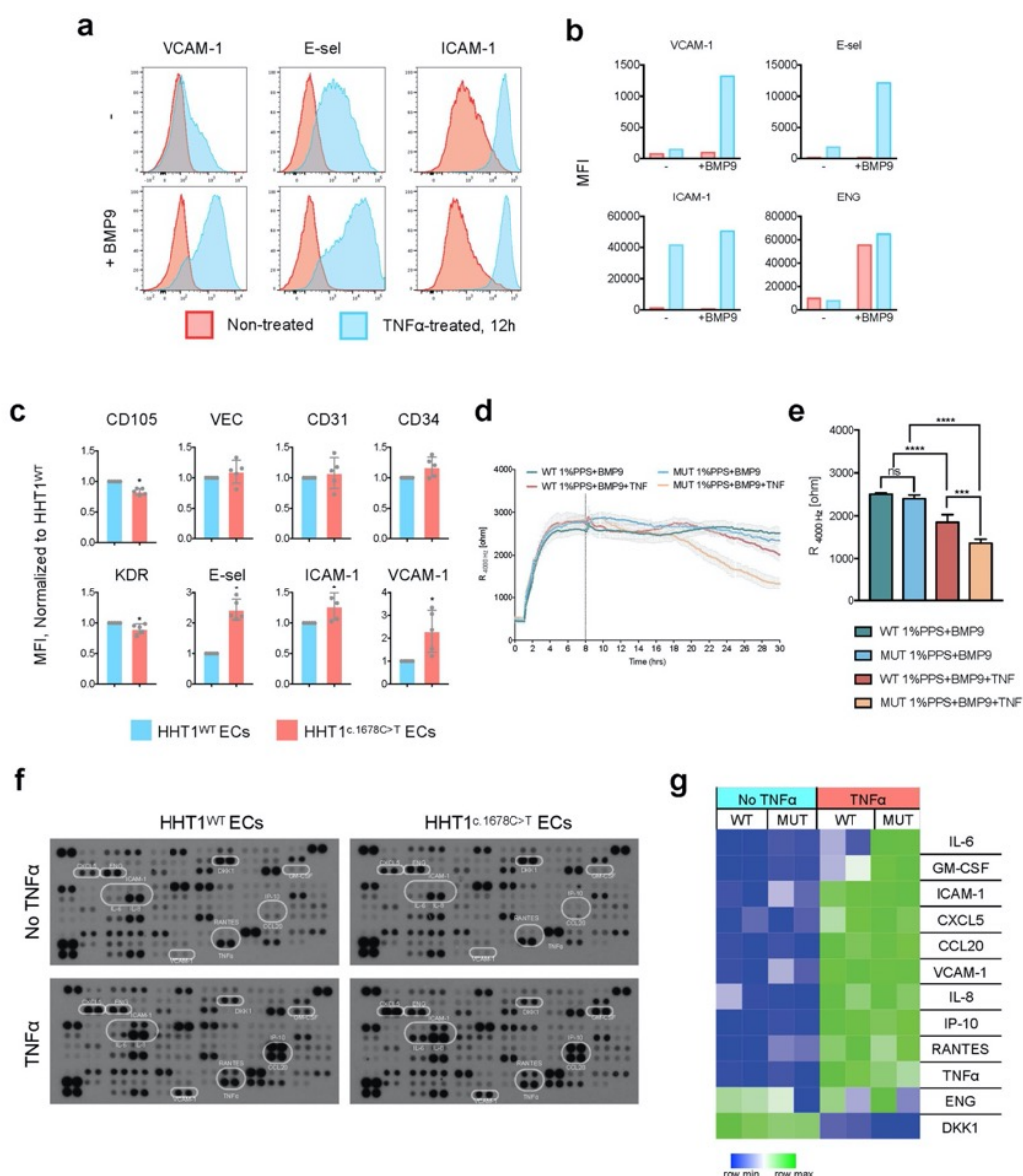


Figure S9. Inflammatory responses in ECs from HHT1 patient-derived isogenic hiPSCs. (a) FACS showing expression of VCAM-1, E-selectin and ICAM-1 in hiPSC-ECs in complete EC growth medium (-) and in 1% PPS medium with BMP9 (+BMP9) (non-treated, red filled histograms) or treated with TNF α (12h) (TNF α -treated, blue filled histograms). (b) Quantification of VCAM-1, E-selectin, ICAM-1 and ENG median fluorescent intensity (MFI). (c) Quantification of ENG (CD105), VEC, CD31, CD34, KDR, E-selectin, ICAM-1 and VCAM-1 median fluorescent intensity (MFI) in ECs from HHT1 patient-derived isogenic hiPSCs cultured in growth factor-free medium with 1% PPS treated with BMP9 and TNF α . (d) Absolute resistance of the EC monolayer at 4000 Hz in HHT1^{WT} and HHT1^{c.1678C>T} ECs cultured in growth factor-free medium with 1% PPS and BMP9 or 1% PPS with BMP9 and TNF α is shown. ECs were differentiated from HHT1 patient-derived isogenic

hiPSCs (P2). Error bars are \pm SD of four independent wells from one biological experiment. **(e)** Quantification of absolute resistance values at 4000 Hz in HHT1^{WT} and HHT1^{c.1678C>T} ECs cultured in growth factor-free medium with 1% PPS and BMP9 or 1% PPS with BMP9 and TNF α . Error bars are shown as \pm SD of three to five independent biological experiments. One-way ANOVA. **** p <0.0001, ** p <0.0005. **(f)** Representative photomicrographs of cytokine protein arrays incubated with supernatants of ECs from HHT1 patient-derived isogenic hiPSCs after 12h incubation in 1% PPS without or with TNF α . **(g)** Quantification of pixels intensities of depicted proteins (white circles in panel **(f)**) from two independent experiments.

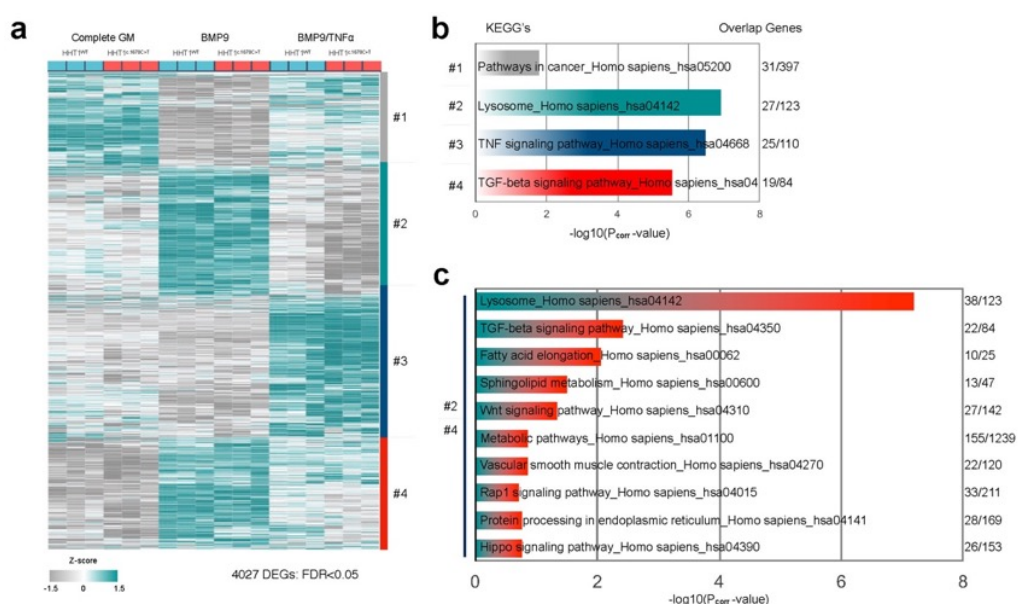


Figure S10. Identification of dysregulated pathways in ECs from HHT1 patient-derived isogenic hiPSCs upon introduction of inflammatory component. (a) Heatmap showing hierarchical clustering of 4027 DEGs [FDR<0.05] that are commonly upregulated in ECs from HHT1 patient-derived isogenic hiPSCs upon BMP9 or TNF α . **(b)** Top signalling pathways (KEGG's signalling pathway database) that are enriched in clusters #1, #2, #3 and #4. **(c)** Top ten signalling pathways (KEGG's signalling pathway database) that are enriched in clusters #2 and #4.

		FC CGM	FC BMP9	FC BMP9/TNFα	FCWT BMP9	FCWT BMP9/TNFα	FCMUT BMP9	FCMUT BMP9/TNFα
TGFβ Pathway Ligands/Receptors	ACVR1	1.3			1.7		2.2	
	ACVR1B				1.3		1.5	
	ACVR2A						-1.4	1.3
	ACVRL1				1.4		1.8	-1.4
	BMP2					3.9	-1.5	4.7
	BMP4	2.1					1.8	
	BMP6		-1.3		4.0		7.8	-1.5
	BMPR1A			2.7	2.9	-1.7	2.5	-3.1
	BMPR2			-1.2	2.4	-2.0	2.4	-1.6
	ENG				4.7	-1.7	4.9	-1.9
	GDF11					-1.7		-1.6
	GDF15	2.2			2.2	1.4	4.1	
	GDF7	7.6		2.5	2.6		15.2	
	INHBA	2.4			25.6	2.4	84.0	2.2
	TGFB1				1.9	-1.6	2.3	-1.8
	TGFB1			-1.7	1.7		2.0	1.5
	TGFB2	1.4	1.5		-1.7	1.8	-1.9	1.9
	TGFB3	3.2	1.4	3.7	-2.8	-1.7		-4.4
SMAD2/3 Target Genes	CTGF		-1.4		6.6		5.3	
	CYR61	-2.3	-2.0	-1.3	3.0	1.9	2.7	1.2
	PDGFB	-1.8	-1.3	-2.0	2.2	1.4	1.6	2.1
	SERPINE1		-1.5		5.2	4.9	12.3	3.1
	SMAD7	3.3			38.3	-2.2	103.1	-1.4
	SNAI2	-2.0	2.6		7.1	-1.9		
	THBS1		-1.3		2.9		3.4	-1.3
SMAD1/5 Target Genes	GJA4	1.9	1.4	2.4		-5.1		-8.7
	HES1			-1.7	-6.3	2.4	-6.2	3.5
	HEY2	3.1		1.9	13.8	-2.5	40.6	-4.6
	ID1				46.1	-2.9	32.7	-2.5
	ID3	-1.2	1.5	1.3	4.1	-1.9	2.2	-1.7
	JAG1			1.9	9.1	-1.5	11.1	-2.6
	SMAD6	1.4	1.2		71.1	-2.5	79.0	-2.3
	TMEM100	2.8		5.8	92.6	-3.9	228.3	-19.9
	UNC5B		1.3	1.3	1.4	-2.3	1.2	-2.3
WNT Pathway	AXIN2	1.7	2.4		-5.6	-2.6	-7.9	1.9
	BAMBI	-2.0	3.2	1.8	17.2	-2.7	2.7	-1.5
	DKK1	2.5		4.8	18.0	-14.3	55.2	-85.2
	DKK2		5.2	7.9	315.0	-10.8	255.8	-16.3
	FZD1		1.3			-2.7		-2.5
	FZD2	4.4	5.8	5.8	4.0	-3.3	3.1	-3.3
	LRP5	4.4	2.1	4.5	-2.0	-4.5		-9.7
	LRP6	1.4			1.5	-1.8	2.1	-2.1
	PORCN		2.0	1.6	3.0	-4.0	1.7	-3.1
	PRICKLE1	2.2	-1.4	2.4	2.1	-2.5	6.3	-8.5
	PRICKLE2		-1.4	1.8	149.5	-3.6	469.8	-8.8
	SOX17	-1.4		-1.4	2.4	-1.4	1.5	
	VANGL2	2.4	4.8	18.4	2.6	-2.1		-8.1
	WNT3		1.5	1.8	3.4	-2.4	2.2	-2.9

■ UP HHT1^{WT}
■ UP HHT1^{c.1678C>T}
■ UP
 ■ DOWN

Figure S11. Dysregulated TGFβ and WNT pathways in ECs from HHT1 patient-derived isogenic hiPSCs. (a) Heatmap showing hierarchical clustering of selected DEGs associated with TGFβ signaling pathway from RNA-seq. **(b)** Heatmap showing hierarchical clustering of established TGFβ downstream targets among identified DEGs from RNA-seq. **(c)** Heatmap showing hierarchical clustering of selected of selected DEGs associated with WNT signaling pathway from RNA-seq. **(d)** Table summarizing FC in gene expression from RNA-seq (identified DEGs, [FDR<0.05]): FC of gene expression between HHT1^{WT} ECs vs HHT1^{c.1678C>T} ECs cultured in complete medium (FC_{FULL}), upon treatment with BMP9 (FC_{BMP9}), or upon treatment with BMP9 and TNFα (FC_{TNF}); FC of gene expression in HHT1^{WT} ECs upon BMP9 treatment vs complete growth medium (FC_{WT BMP}) or HHT1^{WT} ECs upon BMP9 and TNFα vs BMP9 treatment (FC_{WT TNF});

FC of gene expression in HHT1^{c.1678C>T} ECs upon BMP9 treatment vs complete growth medium (FC_{MUT BMP}) or HHT1^{c.1678C>T} ECs upon BMP9 and TNFα vs BMP9 treatment (FC_{MUT TNF}).

Sequence of primes used for qPCR			
Gene	Forward sequence	Reverse sequence	Product size
<i>hARP</i>	CACCATTGAAATCCTGAGTGATGT	TGACCAGCCCAAAGGAGAAG	116
<i>ENG</i>	CCCGCACCGATCCAGACCACTCCT	TGTCACCCCTGTCCTCTGCCTCAC	117
<i>ALK1</i>	CTGGTTCGCGGAGACTGAGAT	TGCGGGAGGTCATGTCTGA	89
<i>ALK5</i>	ACGGCGTTACAGTGTCTCTG	GCACATACAAACGGCCTATCT	167
<i>CD31</i>	GCATCGTGGTCAACATAACAGAA	GATGGAGCAGGACAGGTTTCAG	101
<i>VEGFR2</i>	CCATCTCAATGTGGTCAACCTTCT	TCCTCAGGTAAGTGGACAGGTTTC	107
<i>VEC</i>	GGCATCATCAAGCCCATGAA	TCATGTATCGGAGGTCGATGGT	100
<i>ID1</i>	CTGCTCTACGACATGAACGG	GAAGGTCCTGATGTAGTCGAT	124
<i>SERPINE1</i>	CACAAATCAGACGGCAGCACT	CATCGGGCGTGGTGAAGTC	85
<i>HES1</i>	GGTACTTCCCCAGCACACTT	TGAAGAAAGATAGCTCGCGG	138
<i>HEY1</i>	AGTTGCGCGTTATCTGAGC	TGTTGAGATGCGAAACCAG	80
<i>HEY2</i>	TCATGAAGTCCATGGCAAGA	TTGTGCCAACTGCTTTTGAA	147
Sequence of primers used for Sanger sequencing			
Gene	Forward sequence	Reverse sequence	Product size
ENG (exon 11, c.1678C>T)	CCAGAGTCAGGAGGGAGACA	GCGTCCAGGATAGATTGCCT	974
ENG (exon 5, c.689+2T>C)	CTGGAAGCCAGCCAGGACATG	GGTGGGGCTTTATAAGGGACCG	238
ENG (exon 8, c.1084_1085del)	GATCACACAGTGACCAGCCG	AACTAAGGCTTGCAGAGGGAC	313

Supplemental Table 1. List of primers

Antibody	Fluorochrome	Source	Dilution	Catalog #
VE-Cadherin	A488	eBiosciences	1:50	53-1449-42
CD31	APC	eBiosciences	1:100	17-0319-42
CD34	PerCP-Cy5.5	BD Pharmingen	1:20	347222
ENG	VioBlue	Miltenyi Biotec	1:20	130-099-666
KDR	PE	R&D systems	1:20	FAB357P
VCAM-1	PE	R&D systems	1:20	FAB5649P
E-Selectin	FITC	R&D systems	1:20	BBA21
ICAM-1	FITC	R&D systems	1:20	BBA20
CD34	APC	Miltenyi Biotec	1:20	130-113-176
ENG	PE-Vio-770	Miltenyi Biotec	1:20	130-099-889
CD14	FITC	BD	1:200	345784
ENG	PE	Life Technologies	1:200	MHCD10504

Supplemental Table 2. List of FACS antibodies

Antibody	Species	Source	Dilution	Catalog #
SSEA-4	Mouse	Biologend	1:30	330402
Nanog	Mouse	Santa Cruz	1:150	sc-293121
OCT3/4	Mouse	Santa Cruz	1:100	sc-5279
AFP	Rabbit	Quartett	1:25	2011200530
CD31	Mouse	Dako	1:200	M0823
β III-tubulin	Mouse	Covance	1:4000	MMS-435P
TRA-1-81	Mouse	Biologend	1:125	330702
SMA	Mouse	Sigma	1:200	A2547
VE-Cadherin	Rabbit	CellSignaling	1:200	2158S
vWF	Rabbit	Dako	1:200	A0082
SOX17	Goat	R&D systems	1:200	AF1924
SM22	Rabbit	Abcam	1:200	AB14106
Alexa Fluor 488	Mouse IgG	Invitrogen	1:500	A11001
Alexa Fluor 568	Mouse IgM	Invitrogen	1:200	A21043
Alexa Fluor 488	Mouse IgG3	Invitrogen	1:250	A21151
Alexa Fluor 568	Mouse IgG1	Invitrogen	1:250	A21124
Alexa Fluor 647	Mouse IgG2b	Invitrogen	1:250	A21242
Alexa Fluor 568	Mouse IgG	Invitrogen	1:500	A11031
Alexa Fluor 488	Rabbit IgG	Invitrogen	1:500	A21206

Supplemental Table 3. List of antibodies for IF

METHODS

HHT1 patient-derived hiPSC lines

hiPSC lines were derived from control individuals or HHT1 patients carrying different *ENG* mutations (Fig. S1B). Depending on the availability of patient and unaffected donor samples, fibroblast from (surplus surgical) skin biopsies and erythroblast or blood outgrowth endothelial cells (BOECs) were used for reprogramming. Somatic cells were isolated and reprogrammed with a self-inactivating polycistronic lentivirus encoding the four Yamanaka factors and d-Tomato as a reporter (kindly provided by C. Baum) as described previously (Dambrot et al., 2013). Reprogramming with episomal vectors without was done as described (Okita et al., 2011), except that a newer generation of vectors without *TP53* shRNA were used. hiPSCs were routinely cultured on Matrigel (BD) in mTeSR1 or on Vitronectin XF in TeSR-E8 (all from Stem Cell Technologies) according to the manufacturer's protocol. Standard characterization of hiPSCs was performed as described previously (Bouma et al., 2017; Dambrot et al., 2013; Freund et al., 2010). Karyotype analysis of undifferentiated cells was performed using combined binary ratio labelling-fluorescence in situ hybridization (COBRA-FISH) (Szuhai and Tanke, 2006), and pluripotency of the hiPSC clones was confirmed by PluriTest, immunofluorescent staining for OCT3/4, SSEA-4, NANOG and TRA-1-81 and spontaneous differentiation

towards three germ lineages (Bouma et al., 2017; Dambrot et al., 2013).

Sanger sequencing

ENG mutations were confirmed by Sanger sequencing. DNA of hiPSCs was extracted using the Gentra Puregene Cell Kit (QIAGEN) according to the manufacturer's protocol. PCR was performed to amplify *ENG* exon/intron 5, exon 8 or exon 11. The PCR products were purified using the QIAquick PCR Purification Kit and were sent for Sanger sequencing (BaseClear).

Differentiation of hiPSC-ECs

hiPSC differentiation towards endothelial cells and CD31 magnetic bead isolation were performed as described previously (Halaidych et al., 2018; Orlova et al., 2014a; 2014b). Briefly, hiPSCs were passaged in normal culture conditions one day before inducing differentiation. Mesoderm differentiation was induced by changing the media to B(P)EL with human recombinant BMP4 (30 ng/ml, Miltenyi), Activin (25 ng/ml, Miltenyi), VEGF (50 ng/ml, R&D) and CHIR99021 (1.5 μ M, Tocris) as described previously or with a high concentration CHIR99021 (8 μ M). At day 3, 6 and 9 of differentiation the cells were refreshed with B(P)EL with VEGF (50 ng/ml) and SB43152 (10 μ M, Tocris). ECs were purified with CD31 coupled magnetic beads at day 10 (Life Technologies) and the culture was further scaled up on 0,1% gelatin coated tissue culture flasks in human endothelial serum free media (EC-SFM) (Life Technologies) with additional VEGF (30 ng/ml), bFGF (20 ng/ml, R&D) and 1% platelet poor serum (PPS)(Hyclutec). Functional assays were performed on cells between passages 2-3.

Culture of HBVPs

Primary human brain vascular pericytes (HBVPs) were purchased from ScienceCell. HBVPs were cultured in Pericyte Medium (ScienceCell, cat. n. 1201) supplemented with Pericyte Growth Supplement (ScienceCell, cat.n. 1152) and 2% fetal bovine serum.

Generation of perfused vascular networks in microfluidic chips

Vascular networks were generated as described previously (Chen et al., 2017) with some adjustments that were developed during optimization of the protocol with hiPSC-ECs and HBVPs, and microfluidic chips with one gel channel and two media channels (AIM biotech). Cells were resuspended in EGM-2 supplemented with thrombin (4 U/ml) at 10×10^6 cells/ml for hiPSC-ECs and 0.5×10^6 cells/ml for HBVPs. The cell suspension was next mixed with an equal volume of fibrinogen solution (10 mg/ml) and injected into the gel channel of the microfluidic chip, that was left for 15 min at room temperature (RT) to allow fibrin gel to form. EGM-2 medium supplemented with VEGF (50 ng/ml) was added to each of the flanking media channels. Interstitial flow through the gel was achieved by adding a larger volume of media to one of the media inlets generating a pressure gradient. The

microfluidic chips were refreshed every 24 hours with EGM-2 medium supplemented with VEGF (50 ng/ml) and γ -secretase inhibitor DAPT (10 μ M) (from day 1 onwards). Small molecule inhibitors/activators were added from day 1 till day 3. For immunofluorescent staining, 3D cultures were fixed with 4% PFA for 30 min at RT, permeabilized with 0.5% TX-100 for 15 min at RT and blocked with 2% bovine serum albumin (BSA) in PBS for 2 hours at RT. Primary antibodies (see supplemental table) were added in 1% BSA-PBS and incubated at +4°C overnight (ON). Secondary antibodies were incubated for 2 hours at RT.

EdU assay for EC proliferation in 3D microfluidic chips

Proliferation was measured using an EdU Click-iT kit Alexa-488 (Thermofisher #C10337) according to manufacturers' protocol. Briefly, on day 6 of culture, were refreshed with EGM-2 medium (VEGF 50 ng/ml and DAPT 10 μ M) additionally supplemented with EdU (1:1000) for 8 hours. Cells were fixed with 4% PFA for 30 minutes, permeabilised with 0.5% TX-100 for 15 minutes at RT. Freshly prepared Click-iT reaction cocktail was added for 30 minutes at RT. Microfluidic chips were washed three times with 3% BSA-PBS, followed by co-staining with primary and secondary antibodies.

Imaging and quantification of perfused vessels in microfluidic chips

Microfluidic chips were imaged with the EVOS FL AUTO2 Imaging system (ThermoFischer Scientific) with the 10X Objective with autofocus either on the cells in phase-contrast mode (for time series experiments) or on CD31, and auto tilling multiple focus planes to cover the entire gel channel for an overview of pictures prior to imaging with the confocal. EdU, SOX17⁺ nuclei, CD31 and SM22 high magnification images were acquired with the WLL1 confocal microscope (Leica), using the 40x DRY objective with 0.75 Zoom factor and auto tilling option. For vascular network quantification 8-bit greyscale CD31⁺ images were processed with ImageJ software using the same parameters for all the images with custom-made macros. Briefly, an adaptive brightness enhancement based on the image histogram was applied first. A median filter was then added to reduce the heterogeneities in the pixel values and to improve the following segmentation process. Finally, the resulting segmented images were median filtered to remove small unfilled areas that may appear inside the vascular network, as well as the noise outside of the vessels. From these processed images, the vascular density was calculated as the ratio of black (corresponding to the vessels) against white (corresponding to the background) pixels in the segmented image. The Skeletonize ImageJ tool, based on work from Lee et al. (Lee et al., 1994), was used as a basis to calculate the total vessel length of the vascular network (Niemisto et al., 2005). The total number of branching points was calculated from the freely available ImageJ plugin "Skeleton Intersections" (http://jvsmicroscope.uta.fi/?q=skeleton_intersections). Finally, the mean vessel diameter of the vascular network in the images was obtained using the also freely available ImageJ plugin "(Hotaling et al., 2015)". The number of EdU and SOX17 positive

nuclei were quantified with a custom-made pipeline in (Carpenter et al., 2006). SM22 positive pericyte quantification was obtained using ImageJ plugin NeuronJ (Meijering et al., 2004).

Whole blood FACS analysis

Whole blood was collected into sodium citrate blue top tubes (Vacutainer, BD) and processed immediately or stored at room temperature with the gentle agitation and processed the next day. Whole blood staining protocol was performed as described before (Altman Lab, Emory) with a slight modification. Whole blood (100 μ l) was blocked with the human FC-block (5 μ l, Miltenyi) for 5 min at room temperature. Antibodies were added directly to the whole blood samples for additional 10 minutes. A combination of the following antibodies was used: CD14-FITC (1:200, BD), ENG-PE (1:200, Life Technologies). Red blood cells were lysed with fluorescence-activated cell sorting (FACS) lysing solution (2 ml, BD) for 10 min at RT. Samples were washed once with the FACS buffer, and fixed with 1%PFA. Samples were analysed on LSRII (BD) with the following instrument setup: Blue/488 FITC, A488: 505LP-530/30, PerCP-Cy5.5: 630LP-670/14; Yellow/561 PE: 570LP-582/15, APC: 635LP-660/20.

FACS analysis of hiPSC-ECs

FACS analysis was performed as described previously (Halaidych et al., 2018; Orlova et al., 2014a; 2014b). Day 10 differentiating cultures or purified hiPSC-ECs were dissociated with TrypLE Select (Life Technologies). Combinations of the following antibodies were used in flow cytometry experiments: VE-Cadherin-A488 (1:50, eBiosciences), CD31-APC (1:100, eBiosciences), CD34-PerCP-Cy5.5 (1:20, BD Pharmingen), CD34-APC (1:20, Miltenyi Biotec), KDR-PE (1:20, R&D Systems), ENG-VioBlue or PE-Vio-770 (1:20, Miltenyi Biotec), VCAM-1-PE (1:20, R&D Systems), E-Selectin-FITC (1:20, BBA21; R&D Systems), ICAM-1-FITC (1:20, BBA20; R&D Systems). Samples were analysed either on LSRII (BD) with the following instrument setup: Blue/488 FITC, A488: 505LP-530/30, PerCP-Cy5.5: 630LP-670/14; Yellow/561 PE: 570LP-582/15, APC: 635LP-660/20; or on MACSQuant VYB (Miltenyi) with the following instrument setup: Blue/488 FITC, A488: 525/50; Yellow/561 PE: 586/15, APC: 661/20, APC-Cy7: 750LP.

Gene expression analysis of HHT1-iPSC-ECs

hiPSC-ECs in complete EC-SFM (FULL) or ECs that were serum-starved in EC-SFM medium for 6 hours and stimulated with 1 ng/ml BMP9 (R&D) and 1 ng/ml TGF β 3 (a generous gift of Kenneth K. Iwata, OSI Pharmaceuticals) for another 4 h were collected in RA1 Lysis Buffer (Macherey-Nagel). Total RNA was isolated using the NucleoSpin[®] RNA kit (Macherey-Nagel) and used in reverse transcriptase PCR to generate cDNA, which was used in real-time PCR (SYBR green based detection system) according to the standard procedure. Relative gene

expression was determined according to the standard delta Ct calculation, with the acidic ribosomal protein (hARP) being used as a housekeeping gene. Primer sequences are listed in Table S1.

RNA sequencing and analysis

hiPSC-ECs were either cultured in complete EC growth culture medium (EC-SFM supplemented with VEGF 30 ng/ml, bFGF 20 ng/ml and 1% PPS), or in EC-SFM supplemented with 1% PPS and BMP9 (10ng/ml) for 24 hours followed for additional 12 hours stimulation with either BMP9 (10ng/ml) or BMP9 and TNF α (10ng/ml). RNA for RNA-seq was extracted using the NucleoSpin[®] RNA kit (Macherey-Nagel). Whole transcriptome data were generated at BGI (Shenzhen, China) using the Illumina Hiseq4000 (100bp reads). Raw data was processed using the LUMC BIOPET Gentrap pipeline (<https://github.com/biopet/biopet>), which comprises FASTQ preprocessing, alignment and read quantification. Sickle (v1.2) was used to trim low-quality read ends (<https://github.com/najoshi/sickle>). Cutadapt (v1.1) was used for adapter clipping (Martin, 2011), reads were aligned to the human reference genome GRCh38 using GSNAP (gmap-2014-12-23) (Wu and Nacu, 2010; Wu and Watanabe, 2005) and gene read quantification with htseq-count (v0.6.1p1) against the Ensembl v87 annotation. Gene length and GC content bias were normalized using the R package *cqn* (v1.24.0) (Hansen et al., 2012). Median chromosome X and Y expression were used to verify the sex of included samples. Genes were excluded if the number of reads was below 5 reads in $\geq 90\%$ of the samples. The final dataset comprised gene expression levels of 36 samples and 22,227 genes. Differentially expressed genes were identified using generalized linear models as implemented in edgeR (Robinson et al., 2010). P-values were adjusted using the Benjamini-Hochberg procedure and $P_{FDR} \leq 0.05$ was considered significant. Analyses were performed using R (version 3.4.4). Figures were produced with the R package ggplot2 (v2.2.1). Hierarchical clustering analyses were performed using normalized RPKM matrix using all DEGs to further enrich for cell type-specific signature DEGs. Normalized RPKM values were \log_2 transformed and standardized across each gene using z-scores and hierarchical clustering was performed with Euclidean distance and average linkage functions using Morpheus software (Broad Institute). Gene ontology (GO) enrichment analysis was carried out using Enrichr (Chen et al., 2013; Kuleshov et al., 2016) computational tool. P-values < 0.1 after Benjamini-Hochberg correction for multiple hypothesis testing were used.

Immunofluorescent staining of hiPSC-ECs

Immunofluorescent staining was performed as described previously (Halaidych et al., 2018; Orlova et al., 2014a; 2014b). Briefly, ECs were seeded on FN-coated 96-well black imaging plates (Corning) at the seeding density $\sim 10,000$ cells/well in complete EC growth culture medium (EC-SFM supplemented with VEGF 30 ng/ml, bFGF 20 ng/ml and 1% PPS).

48h post-seeding ECs were fixed with 4% paraformaldehyde (PFA, Sigma), permeabilized with the 0.1%TX-100 and stained with anti-VE-Cadherin (1:200, CellSignaling), anti-CD31 (1:200, Dako), anti-vWF (1:200, Dako), anti-ZO1 (ThermoFisher) or VEC (CellSignaling). High magnification images were acquired with the WLL1 confocal microscope (Leica), using 40x DRY objective.

Endothelial cell proliferation (MTS assay)

hiPSC-ECs were seeded into on FN-coated 96-well plates at the seeding density 2,000 cells/well in EC-SFM for 12 h and subsequently refreshed with EC-SFM containing various stimuli. After 4 days the MTS assay (CellTiter, Promega) was used to determine the relative number of ECs.

Assessment of hiPSC-ECs functionality in an in vitro vasculogenesis assay

The co-culture experiments with hiPSC-ECs or primary ECs and stromal cells were performed essentially as previously described (Halaidych et al., 2018; Orlova et al., 2014a; 2014b). The co-cultures were stopped at day 10 and post-fixed and stained with anti-CD31 (DAKO) and anti-SOX17 (R&D), and anti-SM22 (Abcam) antibodies. The co-cultures were imaged with the EVOS FL AUTO2 Imaging system (ThermoFischer Scientific) with the 10X Objective for quantifications with autofocus on CD31, and auto stitching 4X4 focus planes or 20X Objective for CD31 and SOX17 images. The co-cultures were quantified using publicly available software AngioTool (Zudaire et al., 2011).

Stimulation with pro-inflammatory cytokines

ECs were stimulated in complete EC growth medium with pro-inflammatory cytokines (TNF α 10ng/ml) in complete EC growth medium (Halaidych et al., 2018) or in EC-SFM supplemented with 1%PPS and BMP9 (10ng/ml). FACs analysis of the expression of E-selectin, ICAM-1 and VCAM-1 was performed at 12 hours post-stimulation.

Endothelial barrier function analysis

Endothelial barrier function was measured using impedance-based cell monitoring with an electric cell-substrate impedance sensing system (ECIS Z θ , Applied Biophysics), as previously described (Halaidych et al., 2018). hiPSC-ECs were seeded on FN-coated ECIS arrays each containing 8 wells with 10 gold electrodes per well (8W10E PET, Applied Biophysics). The cell seeding density was estimated ~50,000cells/cm². For barrier function and migration studies the cells were seeded for at least 24h in complete EC growth medium followed by 6h serum starvation step in EC-SFM. For the assessment of cell migration after serum starvation, the medium was changed to EC-SFM or EC-SFM supplemented with 1% PPS, BMP9 (2ng/ml), TGF β 3 (1ng/ml) or TNF α (10ng/ml), and electric wound (10 sec pulse of 5V at 60 kHz) was applied to the cells 1h after medium change. Recovery of the barrier was

monitored in real time over 6-12h. Multiple frequency/time (MFT) mode was used for the real-time assessment of the barrier and monolayer confluence.

Cytokine protein array

hiPSC-ECs were cultured in EC-SFM supplemented with 1% PPS and BMP9 (10ng/ml) for 24 hours followed by 12 hours stimulation with either BMP9 (10ng/ml) or BMP9 and TNF α (10ng/ml), after which supernatants were collected and used in the Proteome Profiler Human XL Cytokine Array Kit (ARY022B; R&D) according to the manufacturer's protocol.

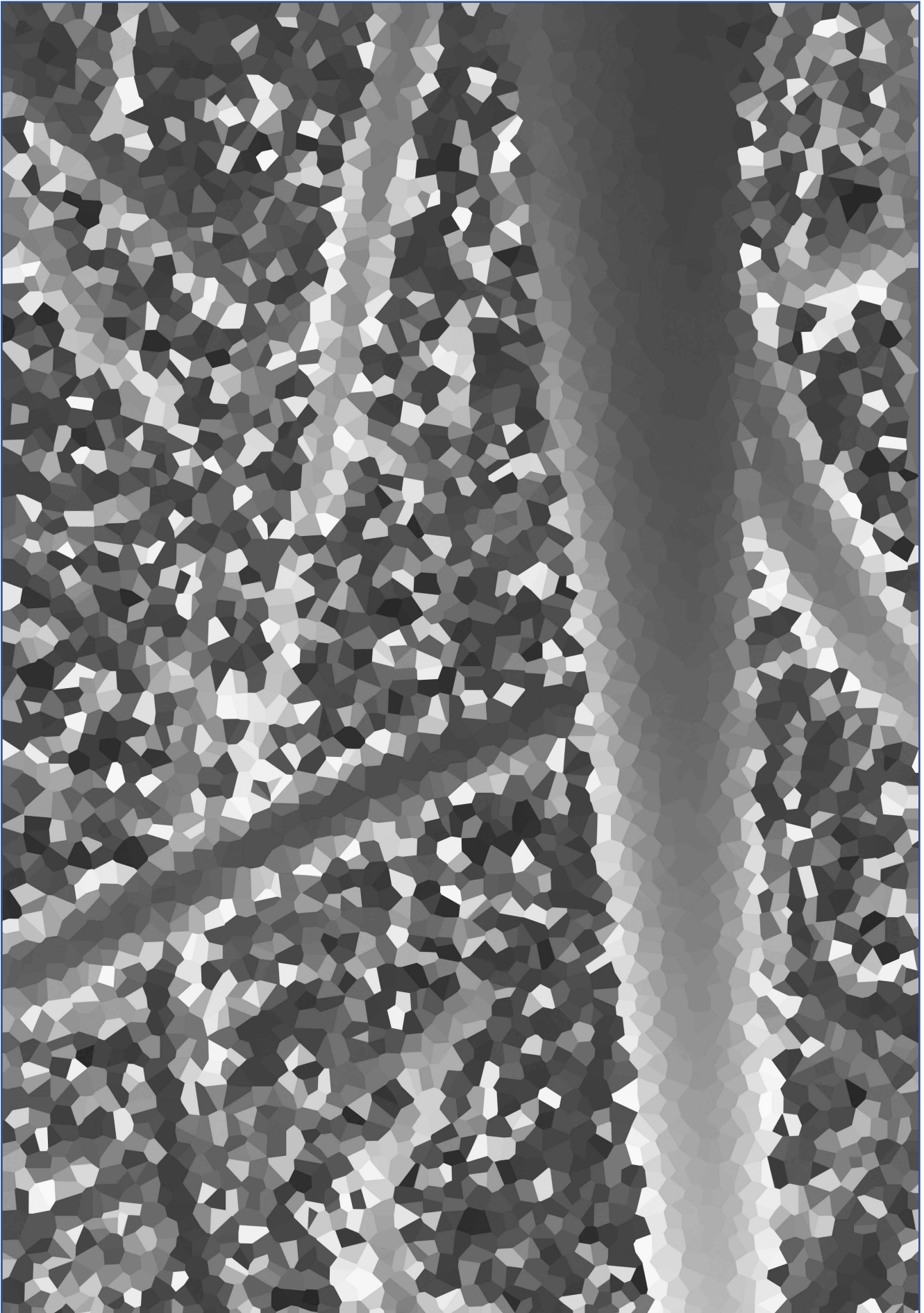
Statistics

One-way ANOVA, non-parametric Student's t-test for unpaired measurements were applied as appropriate to test for differences in means between the groups. Detailed statistics are indicated in each figure legend. Data are expressed and plotted as the Mean \pm SD. Statistical significance was indicated in each figure legend. Statistical analysis was performed with GraphPad Prism 7.0b.

Supplemental references

- Bouma, M.J., van Iterson, M., Janssen, B., Mummery, C.L., Salvatori, D.C., and Freund, C. (2017). Differentiation-Defective Human Induced Pluripotent Stem Cells Reveal Strengths and Limitations of the Teratoma Assay and In Vitro Pluripotency Assays. *Stem Cell Rep* 8, 1340–1353.
- Carpenter, A., Jones, T., Lamprecht, M., Clarke, C., Kang, I., Friman, O., Guertin, D., Chang, J., Lindquist, R., Moffat, J., et al. (2006). CellProfiler: image analysis software for identifying and quantifying cell phenotypes. *Genome Biol* 7, R100.
- Chen, E., Tan, C., Kou, Y., Duan, Q., Wang, Z., Meirelles, G., Clark, N., and Ma'ayan, A. (2013). Enrichr: interactive and collaborative HTML5 gene list enrichment analysis tool. *Bmc Bioinformatics* 14, 128.
- Chen, M.B., Whisler, J.A., Fröse, J., Yu, C., Shin, Y., and Kamm, R.D. (2017). On-chip human microvasculature assay for visualization and quantification of tumor cell extravasation dynamics. *Nat Protoc* 12, 865–880.
- Dambrot, C., van de Pas, S., van Zijl, L., Brändl, B., Wang, J., Schali, M., Hoebe, R., Atsma, D., Mikkers, H., Mummery, C., et al. (2013). Polycistronic lentivirus induced pluripotent stem cells from skin biopsies after long term storage, blood outgrowth endothelial cells and cells from milk teeth. *Differ Res Biological Divers* 85, 101–109.
- Freund, C., Davis, R., Gkatzis, K., Oostwaard, W.D., and Mummery, C. (2010). The first reported generation of human induced pluripotent stem cells (iPS cells) and iPS cell-derived cardiomyocytes in the Netherlands. *Neth Hear J Mon J Neth Soc Cardiol Neth Hear Found* 18, 51–54.
- Halaidych, O., Freund, C., van den Hil, F., Salvatori, D., Riminucci, M., Mummery, C., and Orlova,

- V. (2018). Inflammatory Responses and Barrier Function of Endothelial Cells Derived from Human Induced Pluripotent Stem Cells. *Stem Cell Rep* 10, 1642–1656.
- Hansen, K., Irizarry, R., and Wu, Z. (2012). Removing technical variability in RNA-seq data using conditional quantile normalization. *Biostatistics* 13, 204–216.
- Hotaling, N.A., Bharti, K., Kriel, H., and Simon, C.G. (2015). DiameterJ: A validated open source nanofiber diameter measurement tool. *Biomaterials* 61, 327–338.
- Kuleshov, M.V., Jones, M.R., Rouillard, A.D., Fernandez, N.F., Duan, Q., Wang, Z., Koplev, S., Jenkins, S.L., Jagodnik, K.M., Lachmann, A., et al. (2016). Enrichr: a comprehensive gene set enrichment analysis web server 2016 update. *Nucleic Acids Res* 44, W90–7.
- Lee, T., Kashyap, R., and Chu, C. (1994). Building Skeleton Models via 3-D Medial Surface Axis Thinning Algorithms. *Cvgip Graph Model Image Process* 56, 462–478.
- Martin, M. (2011). Cutadapt removes adapter sequences from high-throughput sequencing reads. *Embnet J* 17, 10.
- Meijering, E., Jacob, M., Sarria, -C JF, Steiner, P., Hirling, H., and Unser, M. (2004). Design and validation of a tool for neurite tracing and analysis in fluorescence microscopy images. *Cytometry* 58A, 167–176.
- Niemisto, A., Dunmire, V., Yli-Harja, O., Zhang, W., and Shmulevich, I. (2005). Robust quantification of in vitro angiogenesis through image analysis. *Ieee T Med Imaging* 24, 549–553.
- Okita, K., Matsumura, Y., Sato, Y., Okada, A., Morizane, A., Okamoto, S., Hong, H., Nakagawa, M., Tanabe, K., Tezuka, K., et al. (2011). A more efficient method to generate integration-free human iPS cells. *Nat Methods* 8, 409–412.
- Orlova, V., Drabsch, Y., Freund, C., Petrus-Reurer, S., van den Hil, F., Muenthaisong, S., Dijke, P., and Mummery, C. (2014a). Functionality of endothelial cells and pericytes from human pluripotent stem cells demonstrated in cultured vascular plexus and zebrafish xenografts. *Arteriosclerosis Thrombosis Vasc Biology* 34, 177–186.
- Orlova, V., van den Hil, F., Petrus-Reurer, S., Drabsch, Y., Dijke, T.P., and Mummery, C. (2014b). Generation, expansion and functional analysis of endothelial cells and pericytes derived from human pluripotent stem cells. *Nat Protoc* 9, 1514–1531.
- Robinson, McCarthy, D., and Smyth, G. (2010). edgeR: a Bioconductor package for differential expression analysis of digital gene expression data. *Bioinformatics* 26, 139–140.
- Szuhai, K., and Tanke, H.J. (2006). COBRA: combined binary ratio labeling of nucleic-acid probes for multi-color fluorescence in situ hybridization karyotyping. *Nat Protoc* 1, 264–275.
- Wu, T., and Nacu, S. (2010). Fast and SNP-tolerant detection of complex variants and splicing in short reads. *Bioinformatics* 26, 873–881.
- Wu, T., and Watanabe, C. (2005). GMAP: a genomic mapping and alignment program for mRNA and EST sequences. *Bioinformatics* 21, 1859–1875.
- Zudaire, E., Gambardella, L., Kurcz, C., and Vermeren, S. (2011). A computational tool for quantitative analysis of vascular networks. *Plos One* 6, e27385.



Chapter 6

Pseudomyogenic hemangioendothelioma recapitulated in endothelial cells from human induced pluripotent stem cells engineered to express the *SERPINE1-FOSB* translocation

David G.P. van IJendoorn¹, Daniela C.F. Salvatori^{2,6#}, Xu Cao^{3#}, Francijna van den Hil³, Inge H. Briaire-de Bruijn¹, Danielle de Jong⁴, Hailiang Mei⁵, Christine L. Mummery³, Karoly Szuhai⁴, Judith V.M.G. Bovee^{1*}, Valeria V. Orlova^{3*}

¹Department of Pathology, Leiden University Medical Center, Leiden, The Netherlands

²Central Laboratory Animal Facility, Leiden University Medical Center, Leiden, The Netherlands; ⁶Department of Pathobiology, Anatomy and Physiology Division, Faculty of Veterinary Medicine, Utrecht University, Utrecht, The Netherlands.

³Department of Anatomy and Embryology, Leiden University Medical Center, Leiden, The Netherlands

⁴Department of Cell and Chemical Biology, Leiden University Medical Center, Leiden, The Netherlands

⁵Sequencing analysis support core, Leiden University Medical Center, Leiden, The Netherlands

#Contributed equally

*Contributed equally, Correspondence: v.orlova@lumc.nl and J.V.M.G.Bovee@lumc.nl

Data submitted in part to Cell Reports Medicine;
Extended data in **Chapter 6 Appendix**: Follow up bioinformatics analysis of hiPSC-endothelial cells expressing the SERPINE1-FOSB translocation

ABSTRACT

Chromosomal translocations are prevalent among soft tissue tumors including those of the vasculature. Pseudomyogenic hemangioendothelioma (PHE) is one such tumor. It has features of endothelial cells (ECs) and a tumor-specific t(7;19)(q22;q13) *SERPINE1-FOSB* translocation, but has been difficult to study since to date no cell lines have been derived from the tumor. To address this, we engineered the PHE chromosomal translocation into human induced pluripotent stem cells (hiPSCs) using CRISPR/Cas9 and differentiated these into ECs (hiPSC-ECs). Comparison of parental and modified (PHE) lines with the t(7;19)(q22;q13) *SERPINE1-FOSB* translocation showed (i) elevated expression of *FOSB* specifically in hiPSC-ECs *in vitro* and *in vivo* (ii) increased proliferation and tube formation but decreased endothelial barrier function (iii) invasive growth and abnormal vessel formation in mouse after transplantation of the mutated cells (iv) transcriptome alterations specific for hiPSC-ECs that reflect the PHE phenotype and elucidate pathways regulated by the fusion that can be targeted for treatment (PI3K-Akt and MAPK signaling). hiPSC-ECs carrying the *SERPINE1-FOSB* translocation thus recapitulated functional features of PHE and demonstrated that this approach can yield models of translocation-driven tumors for identification of therapeutic targets and deeper understanding of underlying tumorigenic mechanisms.

INTRODUCTION

Chromosomal translocations and their corresponding gene fusions are common in neoplasia and are important in the initiation of tumorigenesis (Mitelman et al., 2007). These gene fusions are especially prevalent in soft tissue tumors, of which ~15-20% carry a recurrent chromosomal translocation with no, or few, additional genomic alterations (Mertens et al., 2016). Moreover, translocations are usually specific for each subtype. The identification of specific fusion genes has significantly increased the understanding of the pathogenesis of these (often-rare) tumor types and are used as an auxiliary diagnostic tool.

Pseudomyogenic hemangioendothelioma (PHE) is a rare soft tissue tumor characterized by a specific recurrent balanced translocation, t(7;19)(q22;q13), which fuses *SERPINE1* to *FOSB* (Trombetta et al., 2011; Walther et al., 2014). The translocation leads to the loss of the first exon of *FOSB* containing the start codon, resulting in a novel start codon in exon 2 of *FOSB*. The translocation therefore causes loss of 48 amino acids at the start of the *FOSB* protein which then falls consequently under control of the *SERPINE1* promoter (Walther et al., 2014). PHE is locally aggressive, rarely metastasizing and often affecting young adults, especially men between 20-50 years of age. The disease most often presents as multiple discontinuous lesions in different tissue planes (Hornick and Fletcher, 2011). Approximately 60% of the

patients show relapse after surgical removal or develop additional nodules which can necessitate limb amputation. The tumors display loose spindle-shaped cells with abundant eosinophilic cytoplasm, that invade in the surrounding soft tissues, expressing vascular (CD31, ERG) and epithelial (keratin) markers. Moreover, the translocation results in overexpression of FOSB protein in patient tumor samples (Hung et al., 2017). Although PHE does not form functional blood vessels, vascular markers are expressed suggesting that PHE arises from endothelial cells (ECs) or their precursors. The tumor is therefore classified among the group of vascular tumors (Billings et al., 2003; Hornick and Fletcher, 2011; Ide et al., 2015).

Further understanding of the underlying molecular mechanisms is required to rationally design systemic therapy for patients with inoperable disease. However, like many other soft tissue tumors with translocations, PHE is rare and no cell lines have yet been derived from the tumor, confounding understanding of tumorigenesis and the identification of potential therapeutic targets. A possible approach to model translocation driven tumors is to engineer the complete chromosomal translocation in human pluripotent stem cells and examine the effects on appropriately differentiated derivatives (Sánchez-Rivera and Jacks, 2015). Engineered nucleases were recently shown to be useful in generating chromosomal translocations in human cells. Clustered regularly interspaced short palindromic repeats (CRISPR) and Cas9 nucleases have been used to introduce chromosomal translocations in human umbilical cord-derived mesenchymal stromal cells (hMSCs), umbilical cord blood-derived CD34+ cells, and more recently human induced pluripotent stem cells (hiPSCs) (Schneidawind et al., 2018; Torres et al., 2014; Torres-Ruiz et al., 2017; Vanoli et al., 2017). hiPSCs in particular are increasingly used as human disease models, as they can be propagated indefinitely *in vitro* and differentiated into most cell types of the body (Takahashi et al., 2007), including ECs (Halaidych et al., 2018a; Orlova et al., 2014a; 2014b). They are thus a renewable source of cells to study human physiology and disease. We hypothesized that hiPSC-derived ECs (hiPSC-ECs) could be valuable for modeling rare tumors such as those of the vasculature and demonstrated in the study described here that this is indeed the case for PHE.

We introduced the t(7;19)(q22;q13) *SERPINE1-FOSB* translocation into hiPSCs and thus generated control and modified isogenic hiPSC pairs. We carried out functional analysis of hiPSC-ECs and whole genome and transcriptome sequencing of isogenic pairs of hiPSC and hiPSC-EC with and without translocation. We showed that hiPSC-ECs with the *SERPINE1-FOSB* fusion were distinct from their isogenic controls and exhibited phenotypic and transcriptomic characteristics very similar to PHE. More importantly, in mice mutant hiPSC-ECs became invasive and formed abnormal vessels. Our hiPSC model thus mimics PHE, but in more general terms, the approach can serve as a blueprint for using CRISPR/Cas9 in hiPSCs to explore the role of fusion genes in the

development of specific rare cancer subtypes for which cell lines are lacking, providing deeper understanding of tumorigenesis resulting from gene fusions.

RESULTS

Introduction of t(7;19)(q22;q13) *SERPINE1-FOSB* translocation in hiPSCs

We used CRISPR/Cas9-facilitated gene targeting to introduce the t(7;19)(q22;q13) translocation in hiPSCs. We generated a fusion between intron 1 of *SERPINE1* and intron 1 of *FOSB*, which leads to the same novel start codon as found in PHE tumors from patients (figure 1a). Two double stranded DNA breaks were introduced in the genome guided by two gRNAs targeting *SERPINE1* intron 1 and *FOSB* intron 1. A repair template was provided for homologous directed recombination (HDR) containing two 1000 bp homology arms for *SERPINE1* and *FOSB*, separated by an excisable neomycin resistance cassette flanked by Flp-recombinase sequences (FRT) (figure 1a). A wild-type hiPSC line generated from an anonymous "healthy" donor using non-integrating Sendai virus (SeV) was used for targeting (Halaidych et al., 2018a). hiPSCs were simultaneously transfected with vectors containing Cas9, gRNAs and HDR template (schematic overview of the targeting strategy in hiPSCs is shown in supplementary figure 1a). Neomycin selection allowed enrichment of hiPSCs with integration of the targeting template. The neomycin cassette was next removed by transient transfection of Flp-recombinase. Three color fluorescence in situ hybridization (FISH) revealed that translocations occurred relatively frequently, with 20 of 100 screened cells harboring a split of the *FOSB* bracketing probes (chromosome 19) and a colocalization of the distal *FOSB* probe to the *SERPINE1* (chromosome 7) (supplementary figure 1b). hiPSC clones derived from single cells were screened by PCR and the presence of the *SERPINE1-FOSB* gene fusion was confirmed in 2 out of 73 (2.7% of targeted cells, clones D3 and G6) (figure 1b). Sanger sequencing of PCR products confirmed the correct translocation (figure 1a and supplementary figure 2a). This shows that although translocations between chromosomes 7 and 19 were relatively common events (20% of targeted cells showed translocation detected by FISH), most of these translocations likely occur via non-homologous end joining (NHEJ) and possibly contain large deletions/insertions. They were therefore not detected during PCR screening, resulting in only 2 correctly targeted clones (2.7% targeting efficiency). The targeted allele of hiPSC clone D3 was found to have an FRT remaining between *SERPINE1* and *FOSB* as expected (figure 1a), while this insert was absent in the targeted allele of hiPSC clone G6 due to the translocation occurring via NHEJ (supplementary figure 2a). The non-targeted wild-type alleles of *SERPINE1* and *FOSB* were also Sanger sequenced. In clone D3 a single nucleotide insertion was found in both the non-targeted wild-type *SERPINE1* intron 1 and the non-targeted wild-type *FOSB* intron 1 (supplementary figure 2b, c). In clone G6, a 9 base-pair deletion was found in the non-targeted wild-type *FOSB* intron 1 (supplementary figure 2b). In addition, clone G6

contained an insertion of ~1220 bp of the repair template in the non-targeted wild-type SERPINE1 intron 1, which was evident on the DNA gel and Sanger sequencing (figure 1b and supplementary figure 2c). Analysis of the corresponding cDNA showed presence of fused SERPINE1 5' UTR and FOSB exon 2 in both clones D3 and G6 (supplementary figure 2d) identical to that found in PHE patients, and the presence of correctly spliced wild-type SERPINE1 (supplementary figure 2e). Neither clone D3 or G6 had karyotypic abnormalities, other than the balanced t(7;19)(q22;q13) translocation, as seen using COmbined Binary RAtio Labeling Fluorescence in Situ Hybridization (COBRA-FISH) (figure 1c).

To verify that the targeting with CRISPR/Cas9 did not result in deleterious off-target effects, whole-genome sequencing was performed. No additional copy number variations, insertions or deletions, structural variants or single nucleotide variants (SNVs) were found in the coding genome of the targeted hiPSC clones D3 and G6 (hiPSCSERPINE1^{-FOSB}) compared to the parental control hiPSCs (hiPSC^{WT}) (figure 1d). Furthermore, the *in silico* predicted off target sites for the guide-RNAs used showed no additional alterations (synonymous or non-synonymous) compared with the untargeted parental control hiPSCs (figure 1d).

To verify pluripotency of the targeted and parental control hiPSC lines, teratoma assay was performed in mice. Targeted and parental control hiPSCs retained the ability to form tissues derived from all three germ layers (endoderm, mesoderm and ectoderm), showing that CRISPR-Cas9 targeting has not affected pluripotency (figure 1e).

Differentiation and characterization of ECs from hiPSC^{WT} and hiPSC^{SERPINE1-FOSB} lines

hiPSCs with and without *SERPINE1-FOSB* fusion were differentiated into ECs using a protocol previously described (Halaidych et al., 2018a; Orlova et al., 2014b; 2014a) (figure 2a). hiPSC-ECs were purified on day 10 of differentiation by CD31⁺ cell selection, expanded and cryopreserved for further characterization. hiPSC-ECs^{WT} and hiPSC-ECs^{SERPINE1-FOSB} differentiated from two targeted clones (D3 and G6) exhibited typical EC morphology (figure 2b and data not shown) and showed cell surface expression of known EC markers, such as vascular endothelial (VE)-cadherin (VEC), CD31, CD34, VEGFR2, VEGFR3 and CD105, as expected and in accordance with our previous findings (Orlova et al., 2014a) (figure 2c,d and supplementary figure 3a,b). Interestingly, hiPSC-ECs derived from both the D3 and G6 targeted clones displayed increased expression of CD105 (figure 2d and supplementary figure 3b), which is known to be upregulated in tumor endothelial cells (Miller et al., 1999) as well as in vascular tumors (Verbeke et al., 2013). Moreover, expression of FOSB mRNA showed a 4.9 log2 fold increase in hiPSC-ECs from clone D3 and a 5.9 log2 fold increase in hiPSC-ECs from clone G6 compared to the isogenic hiPSC-ECs derived from parental non-targeted hiPSC line (figure 2e and supplementary figure 3c). The increase in *FOSB* expression at the mRNA

Figure 1. Generation and characterization of hiPSCs with a *SERPINE1-FOSB* fusion. (a) Schematic overview of the targeting strategy for generation of a *SERPINE1-FOSB* gene fusion. Filled boxes are exons, lines introns. FOSB start codons are labeled in the figure, in black text represents the original start codon while the new start codon after the fusion is shown in red. Two double stranded breaks were introduced in the genome guided by two gRNAs in *SERPINE1* intron 1 and *FOSB* intron 1. A repair template used for homologous recombination (HR template) with neomycin resistance cassette flanked by Flp-recombinase sequences (FRT), as well targeted genomic locus prior (After HR) and after FLP-mediated neomycin removal (after FLPO). Bottom panel shows Sanger sequencing of PCR products from the clone with translocation validating HDR recombination of *SERPINE1* and *FOSB* with remaining FRT sequence left from the repair template (D3 clone). (b) Representative results of PCR screen on single cell-derived hiPSC clones using primers (F2, R2 and SF, SR; F2, SR and FF and FR) shown in panel above the PCR screen results. Two targeted clones (D3 and G6) were identified out of 73 screened clones. PCR shows clone G6 has a large insert in the *SERPINE1* wild-type allele. (c) COBRA-FISH on colony metaphase cells of WT, D3 and G6 hiPSC clones shows a balanced translocation t(7;19)(q22;q13); furthermore no additional chromosomal abnormalities were evident in any of the screened cells. (d) Whole genome sequencing was performed and the results are summarized in a Circos plot. The first layer shows all genes that are potential off-target sites for the gRNA for *FOSB* (red) and *SERPINE1* (blue). No mutations were found in the off-target sites and the surrounding 100 bases. The second and third layers show Copy Number Analysis (CNA) for clones D3 and G6 respectively compared to the isogenic control. No Copy Number Variations (CNVs) are detected. The green connection line shows the detected *SERPINE1-FOSB* fusion, as detected in both clones D3 and G6. Chromosomes 7 and 19, involved in the translocation, are highlighted in red. (e) Teratoma formation in mice. Top panel shows teratomas formed from the hiPSC^{WT}, the bottom panel from the hiPSC^{*SERPINE1-FOSB* (D3)}; two sections of each are shown. Cellular derivatives of the three germ lineages are indicated: mesoderm (MES), ectoderm (ECT) and endoderm (END). Scale bar indicates 200 μ m.

Functionality of ECs from hiPSC^{WT} and hiPSC^{*SERPINE1-FOSB*} lines

To investigate the effect of the *SERPINE1-FOSB* fusion on hiPSC-ECs functionality, we next performed assessment of proliferation and Matrigel tube formation assay. *SERPINE1-FOSB* fusion caused increased EC proliferation. The effect measured after 24 hours was most prominent in basal EC growth medium supplemented with 1% platelet-poor serum (PPS) (1.9-fold increase), followed by basal EC growth medium supplemented with both 1% PPS and VEGF (1.58 vs 2.27-fold) (figure 2g). No significant differences in EC proliferation were observed using complete EC growth medium (full) that in addition to VEGF also contained bFGF, indicating that FOSB overexpression

caused by the *SERPINE1-FOSB* fusion may result in a VEGF-independent growth advantage for ECs. Matrigel tube formation assays showed significant increase in number of junctions (147 vs 218, $p<0.001$) and meshes (53 vs 85, $p<0.005$) in hiPSC-ECs *SERPINE1-FOSB* compared to isogenic control hiPSCs-ECs^{WT} after 48 hours (figure 2h).

Barrier function of ECs from hiPSC^{WT} and hiPSC^{SERPINE1-FOSB} lines

Barrier function of hiPSC-ECs with and without the *SERPINE1-FOSB* fusion was next examined by real-time impedance spectroscopy with an integrated assay of electric wound healing, as demonstrated previously (Halaidych et al., 2018a). The *SERPINE1-FOSB* fusion resulted in a significant decrease in barrier function of hiPSC-ECs (figure 3a, b and supplementary figure 4a,b). Barrier function depends on the integrity of cell junction complexes that form tight- and adherence junctions. Therefore, we also investigated junctional integrity in hiPSC-ECs with *SERPINE1-FOSB* fusion using the tight junctional marker *zonula occludens* (ZO)-1, the adherence junctional marker VEC and counterstained for F-actin and CD31 (figure 3c, d). Presence of less organized, “zig-zag” patterns of ZO1 and VEC was evident for hiPSC-ECs^{*SERPINE1-FOSB*} compared to the hiPSC-ECs^{WT} (figure 3c, d), which is in line with reduced barrier function of hiPSC-ECs with *SERPINE1-FOSB* fusion.

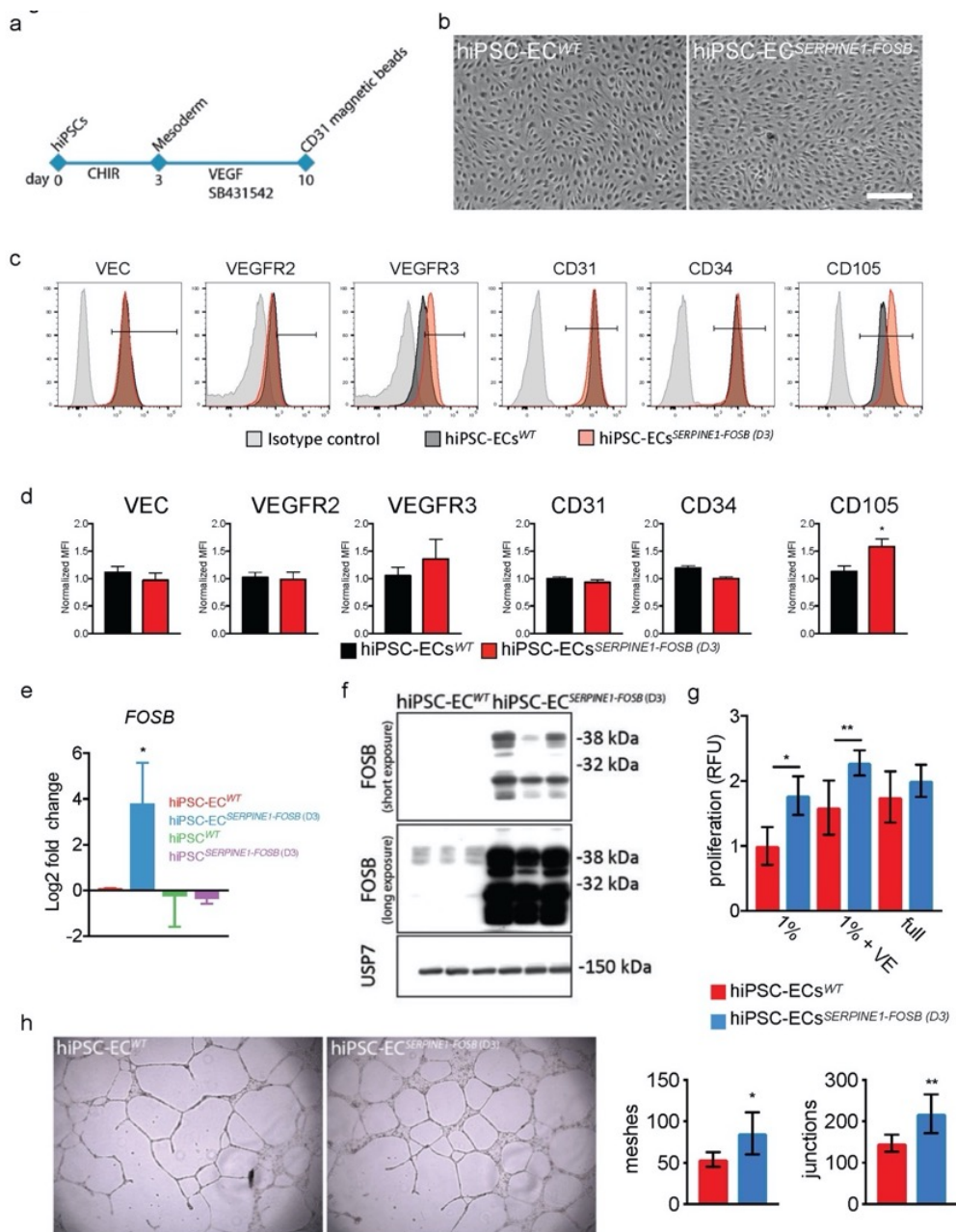


Figure 2. Differentiation and characterization of hiPSC-ECs with *SERPINE1-FOSB* fusion. (a) Schematic overview of the differentiation protocol and purification of ECs from hiPSCs. (b) Bright field images showing typical EC morphology of hiPSC-ECs. Scale bar represents 500 μ m. (c) FACS analysis of EC markers expression on isolated ECs at passage 3 (P3) from hiPSC-ECs^{WT} (black filled histogram) and hiPSC-ECs^{SERPINE1-FOSB} (D3) (red filled histogram), and relevant isotype control (gray filled histogram). (d) Quantification of normalized relative surface expression levels (MFI) of VEC, VEGFR2, VEGFR3, CD31, CD34 and CD105. Error bars are SD, * $p < 0.005$. (e) Real-time qPCR analysis of FOSB expression in hiPSCs^{WT}, hiPSCs^{SERPINE1-FOSB} (D3), hiPSC-ECs^{WT} and hiPSC-ECs^{SERPINE1-FOSB} (D3). (f) Western blot analysis of FOSB and USP7. (g) Proliferation analysis. (h) Tube formation assay.

FOSB (D3). Expression is determined relative to hiPSC-ECs^{WT}, shown as log2 fold change. Error bars are SD, * p<0.05. (f) Western blot of *FOSB* expression in hiPSC-ECs^{WT} and hiPSC-ECs^{SERPINE1-FOSB} (D3). Short and long exposure of the gel is shown. USP7 was used as a housekeeping control. (g) Analysis of hiPSC-ECs^{WT} and hiPSC-ECs^{SERPINE1-FOSB} (D3) proliferation rates when cultured in basal endothelial cell growth medium supplemented with 1%PPS (1%), 1%PPS supplemented with 50 ng/ml VEGF (1% VE) or complete EC growth medium (full) for 24 hours. Proliferation was determined by using a Presto Blue assay. Error bars are shown as SD, * p<0.0001, ** p<0.0005. (h) Representative images of Matrigel tube formation assay using hiPSC-ECs^{WT} and hiPSC-ECs^{SERPINE1-FOSB} (D3) at the 48h time point. Right panel shows quantification of the number of junctions and meshes. Error bars are SD, * p<0.005, ** p<0.001. All experiments were performed in triplicate using three independent batches of hiPSC-ECs.

Functionality of hiPSC-ECs from hiPSC^{WT} and hiPSC^{SERPINE1-FOSB} lines *in vivo* in mice

In order to test the functionality and the ability to form functional perfused blood vessels, hiPSC-ECs with and without *SERPINE-FOSB* translocation were injected in mice in a Matrigel Plug Assay that allows assessment of vasculogenesis, as described previously (Halaidych et al., 2018). Matrigel plugs were excised and analyzed 4- and 16-weeks post-transplantation. Both hiPSC-ECs^{WT} and hiPSC-ECs^{SERPINE1-FOSB} (D3) formed stable vessels *in vivo* composed of human ECs evident at the 4-weeks (figure 4a) and 16-weeks post-transplantation (figure 4c). Quantification of the vessel density showed comparable areas covered by human vessels, demonstrating that both hiPSC-ECs^{WT} and hiPSC-ECs^{SERPINE1-FOSB} (D3) had similar abilities to form vessels *in vivo* (figure 4b, d). The vessels were perfused (as indicated by the presence of red blood cells) (figure 4a, c). Moreover, *FOSB* positive ECs were evident in the Matrigel plugs with hiPSC-ECs^{SERPINE1-FOSB} (D3), but not the Matrigel plugs with hiPSC-ECs^{WT} (figure 4e). Furthermore, *FOSB* positive hiPSC-ECs^{SERPINE1-FOSB} (D3) also invaded the surrounding mouse soft tissues (the striated muscle) at 16-weeks post-transplantation in two of the three mice whereas this was not observed in any of the mice with hiPSC-ECs^{WT} transplants (figure f, g and h).

The hiPSC-ECs^{SERPINE1-FOSB} (D3) vessels at 16 weeks were disorganized and disarrayed and often contained thrombi (conglomeration of fibrin and platelets, containing red blood cells) (figure 4h, i). Thrombi were quantified using phosphotungstic acid-haematoxylin (PTAH) staining (thrombus positive vessels 20.67 vs 81.33 counted in 5.7 mm², n=3, p=0.1) (figure 5j).

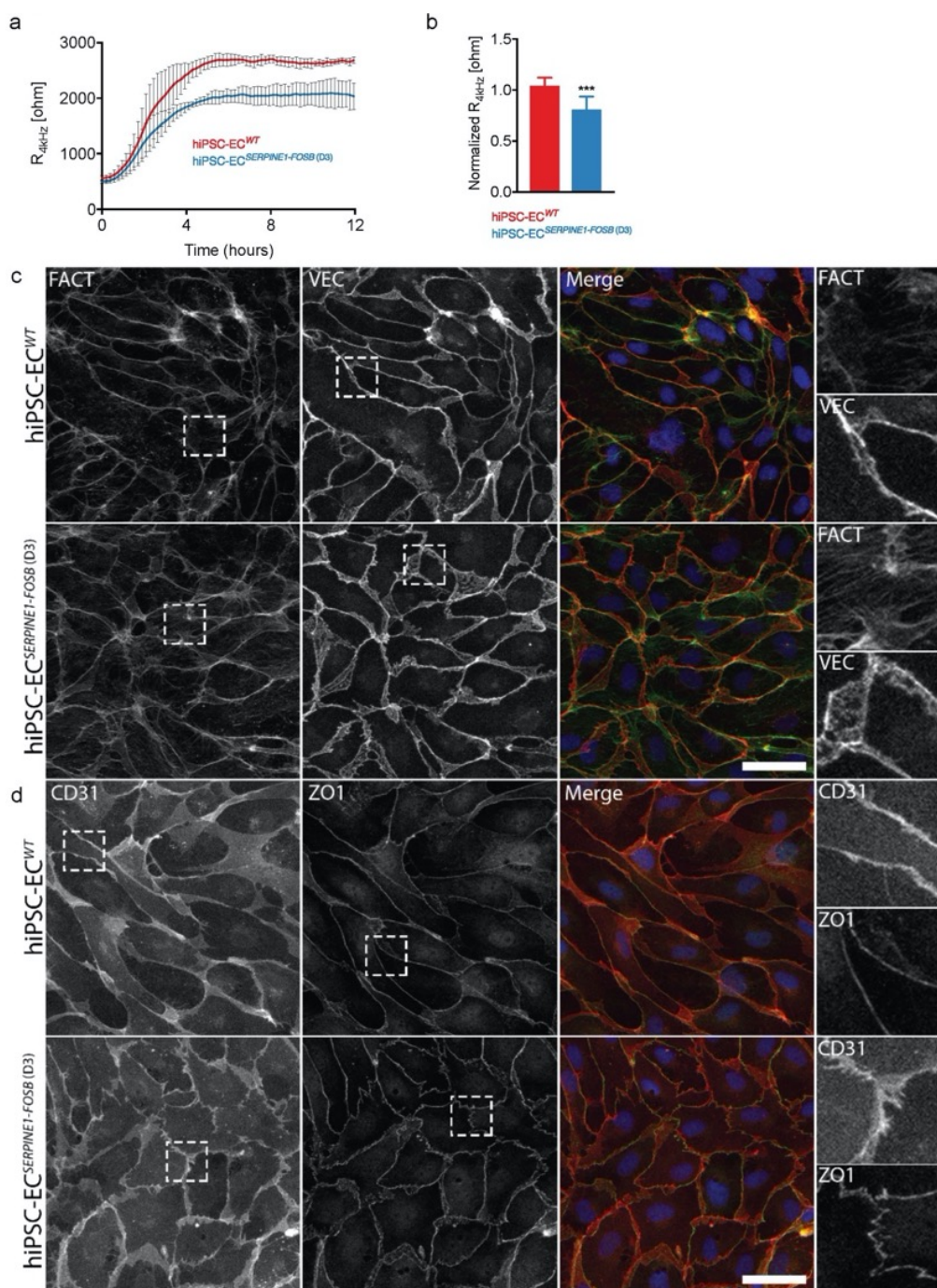


Figure 3. Assessment of barrier function of hiPSC-ECs with *SERPINE1-FOSB* fusion.

(a) Representative absolute resistance of the EC monolayer in complete EC growth medium. Errors bars are shown as \pm SD. **(b)** Normalized resistance [4 kHz] of the EC monolayer in complete EC growth medium. Error bars are shown as \pm SD of six independent biological experiments. *** p<0.001. **(c, d)** Representative immunofluorescent images of FACT, VEC **(c)** and CD31, ZO1 **(d)** to

analyze the cell adherence and tight junctions. Merged images show FACT in green, VEC in red and DAPI in blue **(c)** and CD31 in red, ZO1 in green and DAPI in blue **(d)**. The right panels show further enlarged areas selected from the shown images (dashed squares). Scale bar represents 50 μm . Experiments were performed in triplicate using three independent batches of hiPSC-ECs.

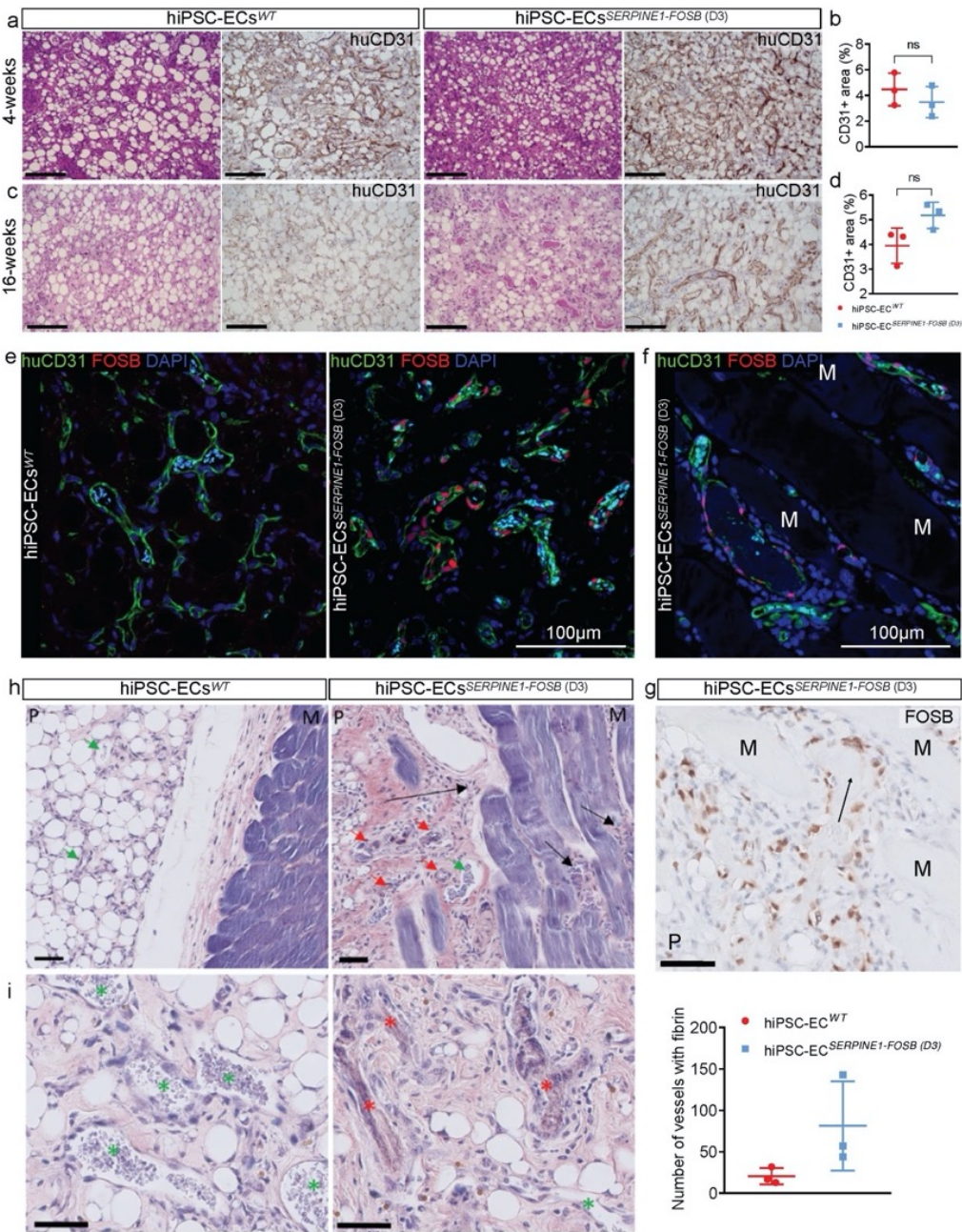


Figure 4. *In vivo* vasculogenesis assay for hiPSC-ECs^{WT} and hiPSC-ECs^{SERPINE1-FOSB (D3)}. **(a, c)** H&E and human CD31 staining of FFPE tissue from the Matrigel plug harvested after 4- (shown in

panel (a)) and 16- (shown in panel (c)) weeks. Both hiPSC^{WT} and hiPSC^{SERPINE-FOSB (D3)} show vessel formation. Scale bar indicates 100 μ m. (b, d) Vessel density was estimated by quantification of the human CD31⁺ area at 4- and 16-weeks. The 4- and 16-week timepoints showed no significant difference in human CD31⁺ area. (e, f) Double immunofluorescent staining with FOSB and human CD31 antibodies counterstained with DAPI on cryosections from Matrigel plug containing hiPSC-ECs^{WT} and hiPSC-ECs^{SERPINE-FOSB (D3)}. FOSB is shown in red, CD31 in green and DAPI is blue. The left panel shows the hiPSC-ECs^{WT} experiment, the right panel the hiPSC-ECs^{SERPINE-FOSB (D3)} experiment. Cyan colored objects are representing erythrocytes fluorescing in multiple detection channels. Panels (f, g) show invasion of FOSB positive hiPSC-ECs^{SERPINE1-FOSB (D3)} into the striated muscle at 16-weeks post-transplantation. (g) FOSB IHC on FFPE tissue from Matrigel plug with hiPSC^{SERPINE1-FOSB (D30)} ECs. Scale bar 50 μ m. Surrounding mouse muscle (indicated by M) and the matrigel plug (indicated by P). (h, i) PTAH stained sections from the in vivo vasculogenesis assay. hiPSC-ECs^{WT} (left panel) and hiPSC-ECs^{SERPINE1-FOSB (D3)} (right panel) are shown. Both images show the surrounding mouse muscle (indicated by M) and the Matrigel plug (indicated by a P). Vessels with and without thrombi are indicated by red and green arrows, respectively (h) and red and green stars (i). The black arrows indicate areas with infiltration in the mouse muscle. The scale bar indicates 50 μ m. (j) Quantification of vessels containing PTAH positive thrombi in hiPSC-ECs^{WT} and hiPSC-ECs^{SERPINE-FOSB (D3)}, in an area of 5.7 mm², n=3 and p=0.1.

Transcriptome analysis of ECs from hiPSC^{WT} and hiPSC^{SERPINE1-FOSB} lines

The transcriptomes of hiPSC-ECs with and without SERPINE1-FOSB fusion were compared. 630 and 592 differentially expressed genes (DEGs)(PFDR \leq 0.05) were upregulated and downregulated respectively in hiPSC-ECs^{SERPINE1-FOSB} compared to hiPSC-ECs^{WT} (figure 5a). Both FOSB and SERPINE1 were significantly upregulated in hiPSC-ECs^{SERPINE1-FOSB} compared to hiPSC-ECs^{WT}. Enrichment analysis using the KEGGs (Kyoto Encyclopedia of Genes and Genomes) pathway database revealed several signaling pathways significantly enriched in DEGs upregulated in hiPSC-ECs^{SERPINE1-FOSB}. These included focal adhesion, ECM-receptor interaction, Pathways in cancer, PI3K-Akt, MAPK, TGF-beta and HIF-1 signaling pathways, and Glycolysis/Gluconeogenesis (figure 5b and supplementary figure 5). Upregulation of glycolytic genes in hiPSC-ECs^{SERPINE1-FOSB} (supplementary figure 5h) indicates possible changes in the metabolic state of ECs, as previously demonstrated for tumor ECs (Cantelmo et al., 2016). No signaling pathways were significantly enriched in DEGs upregulated in hiPSC-EC^{WT}. Gene Ontology (GO) enrichment analysis revealed alterations in the following biological processes in hiPSC-ECs^{SERPINE1-FOSB}: extracellular matrix organization, angiogenesis, cell-matrix adhesion, inflammatory response, cell junction organization, regulation of TGF-beta receptor signaling pathway and others (figure 5c). By contrast, response to interferon-gamma

was the only biological process significantly enriched in DEGs upregulated in hiPSC-EC^{WT} (figure 5c). To demonstrate the relationship between the genes and identified GOs, a gene network map was next constructed using DEGs upregulated in hiPSC-ECs^{SERPINE1-FOSB} (total of 182 genes) (figure 5d). Gene interaction analysis was next performed using Ingenuity pathway analysis (IPA). Gene interaction networks related to cancer, cellular movement and growth, and TGF- β signaling pathway were used to demonstrate interaction between the identified dysregulated genes and FOSB in hiPSC-ECs^{SERPINE1-FOSB} (figure 5e). FOSB regulates SERPINE1 directly, which is in line with our previous finding that truncated FOSB was able to regulate its own transcription (van IJendoorn et al., 2018), as well as via SMAD3. Both exhibit a self-regulatory mechanism, which could further activate many genes in the network of cellular growth and proliferation and cancer processes directly or indirectly through activation of the TGF- β signaling pathway (figure 5e).

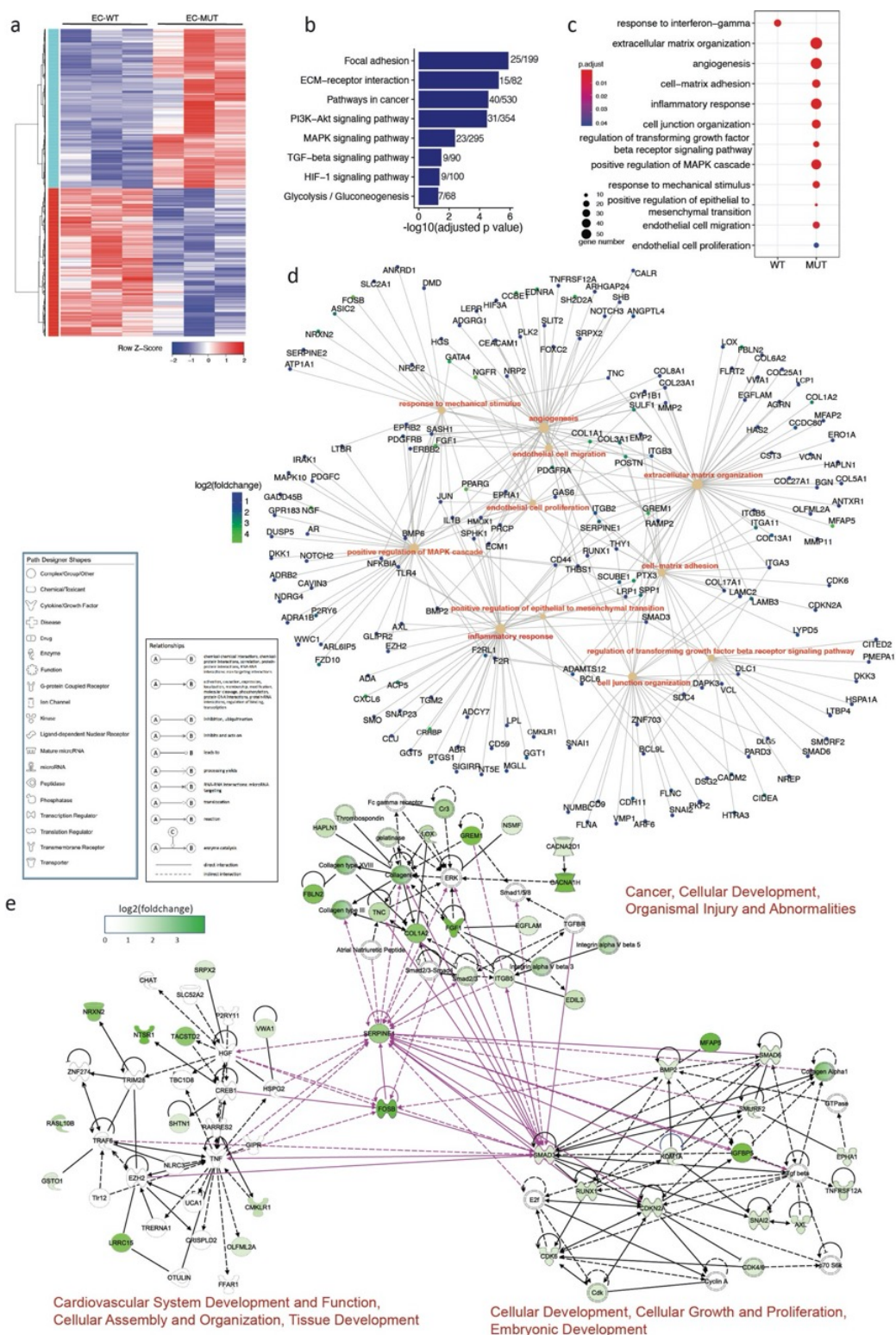


Figure 5. Transcriptome analysis of hiPSC-ECs with and without SERPINE1-FOSB translocation.

(a) Hierarchical clustering analysis (HCA) of differentially expressed genes (DEGs) between hiPSC-ECs^{WT} (WT) and hiPSC-ECs^{SERPINE1-FOSB} (D3) (MUT) samples (three independent differentiations and isolation for each clone). 630 and 592 significantly upregulated and downregulated genes in MUT were identified compared to WT ECs (PFDR≤0.05). (b) Representative KEGG pathways enriched in upregulated DEGs in MUT ECs (-log₁₀(adjusted p value)) and number of enriched genes within total genes of each pathway are shown. (c) Representative Gene ontologies (GOs) that enriched in downregulated (WT) and upregulated (MUT) DEGs. Size and color indicate gene number and adjusted p value of each GO. (d) Cnetplot of genes associated with enriched GOs (c), color indicates the log₂(fold change) of gene expression in MUT compared to WT. (e) Gene interaction network constructed using all genes shown in (c) with Ingenuity pathway analysis (IPA). SERPINE1, FOSB were added manually. Interactions among FOSB and TGF-β signaling pathway and two networks were generated using IPA. Color indicates the log₂(fold change) of gene expression in MUT compared to WT.

DISCUSSION

There is an urgent need for *in vitro* models to study rare translocation-driven tumors, both to identify the functional consequences of the translocation, and to identify potential therapeutic targets. We used CRISPR/Cas9 to induce a tumor-associated translocation in hiPSCs, specifically the *SERPINE1-FOSB* translocation to model the rare vascular tumor PHE. Two hiPSC clones among 73 clones screened contained the translocation. In one of the clones (D3), the translocation was introduced via HDR using the donor DNA template, while in the second clone (G6) the translocation occurred via NHEJ. As the breakpoints were in intronic regions of the two involved genes, in both clones the transcribed and spliced RNA resulted in the typical *SERPINE1-FOSB* chimeric RNA. Other groups have also shown that CRISPR/Cas9 can be used to introduce chromosomal translocations in other cells, notably hMSCs via both NHEJ, but also via HDR using donor DNA templates and additional exposure to low doses of DNA-PKC inhibitor (NU7441) to block NHEJ (Vanoli et al., 2017).

Whole genome sequencing of both parental and targeted hiPSC lines showed no deleterious structural variations, copy number variations or mutations at the predicted off-target sites for the gRNAs. Any phenotypic changes observed were thus most likely associated with the *SERPINE1-FOSB* translocation.

We recently showed that overexpression of truncated *FOSB* in human umbilical vein ECs (HUVECs) recapitulated some features of PHE pathology (van Ijzendoorn et al., 2017). However, the drawback of overexpression is that they lack the regulatory elements for cell type-specific expression at levels found in tumor cells. Here we addressed the shortcomings of our previous model by introducing the truncated protein under the endogenous *SERPINE1* regulatory elements via *SERPINE1-FOSB* fusion using

CRISPR/Cas9-induced translocation in hiPSCs, thereby recreating the fusion with endogenous regulatory elements of SERPINE1. We found that the *SERPINE1-FOSB* fusion results in upregulation of FOSB expression specifically in ECs, and not in undifferentiated hiPSCs, in line with known high SERPINE1 expression in vascular cells and its function as a direct transcriptional target of the activator protein 1 (AP-1) family of proteins that includes FOSB (Milde-Langosch, 2005; Walther et al., 2014). Thus, we here show that self-regulation of its own promoter, and thereby of the expression of the fusion product that is considered the driver alteration in PHE, only occurs in endothelial cells and not in undifferentiated hiPSCs. These results indicate lineage restricted expression of the fusion and confirm that PHE should be considered a vascular tumor.

Vasculogenesis assays *in vivo* in mice in which hiPSC-ECs^{*SERPINE1-FOSB* (D3)} or hiPSC-ECs^{WT} were co-injected with bone marrow stromal cells (BMSCs) supported our *in vitro* findings and showed most strikingly the infiltrative growth pattern reminiscent of human PHE (Hornick and Fletcher, 2011). Vessels from hiPSC-ECs^{*SERPINE1-FOSB* (D3)} were haphazardly arranged compared to hiPSC-ECs^{WT} and contained higher numbers of fibrin thrombi, in two of three hiPSC-ECs^{*SERPINE1-FOSB* (D3)}. These results are in line with the *in vitro* barrier function analysis and suggest that the endothelium is aberrant inducing thrombi formation. However, some aspects of PHE were not recapitulated *in vivo*. The tumor cells typically do not form vessels in PHE but instead are spindle-shaped and co-express endothelial markers (CD31 and ERG) and keratin AE1/AE3, features that are absent in our *in vivo* model. It might be that the 16 weeks time frame is not enough to develop these features *in vivo*. Invasion of hiPSC-ECs^{*SERPINE1-FOSB* (D3)} into surrounding mouse soft tissue was observed at 16-weeks, but not at the 4-week time-point, which may suggest that the development of the phenotype takes time.

Transcriptome analysis of hiPSC-ECs with the fusion revealed differentially expressed genes associated with several pathways that are known to be related to cancer, such as TGF-beta signaling, adhesion, metabolism, inflammatory response, angiogenesis and endothelial cell migration. These are all linked to the phenotypes we observed *in vitro* and *in vivo* in our model, and recapitulate some aspects of PHE. Moreover, these pathways that we here identify to be regulated by the *SERPINE1-FOSB* fusion provide rationale to develop targeted treatment strategies for inoperable multifocal PHE patients. In line with our previous report of a patient with a complete clinical remission following the multi-tyrosine kinase inhibitor telatinib, we confirm upregulated MAPK signaling and overexpression of PDGFRA and -B induced by the fusion in the current model. Moreover, we identify PI3K-Akt signaling which can be targeted using mTOR inhibitors. Indeed, anecdotal responses to mTOR inhibition in patients with PHE have been reported (Gabor et al., 2018; Joseph et al., 2015; Ozeki et al., 2017).

In summary, we showed that hiPSCs and hiPSC-ECs can be used to model fusion-

driven tumors using CRISPR/Cas9 and a donor DNA template to introduce the translocation. The differentiated hiPSC-ECs carrying the pathognomonic translocation gave insights into the tumorigenesis of PHE, and elucidated the pathways regulated by the fusion product, that may provide rationale to develop targeted treatment strategies for inoperable multifocal PHE. Overall, this approach facilitated the elucidation of the role of specific fusion genes in the development of specific rare cancer subtypes for which cell lines are presently lacking.

METHODS

hiPSC lines and culture

The SeV reprogrammed hiPSC line LUMC0054iCTRL was used (additional information available in public databases: <http://hpscreg.eu/cell-line/LUMCi001-A> and <http://hpscreg.eu/cell-line/LUMCi001-A-1>) (Halaidych et al., 2018a). hiPSCs were cultured on recombinant vitronectin (VN)-coated plates in TeSR-E8 all from STEMCELL Technologies (SCT), according to the manufacturer's instructions. For targeting experiments, hiPSCs were adapted to single cell passaging on mouse embryonic fibroblasts (MEFs) in Dulbecco's modified Eagle's medium/Ham's F-12 medium (DMEM/F12) supplemented with 20% knockout serum replacement (Invitrogen), 1 mM L-glutamine, 0.1 mM nonessential amino acids, 0.1 mM 2-mercaptoethanol, and 8 ng/ml recombinant human basic fibroblast growth factor (bFGF; Milteny). Single cell adapted hiPSC were passaged using 1X TrypLE Select with additional supplementation with 1X RevitaCell (Invitrogen).

Construction of dual-guide Cas9-encoding plasmids and repair template

A dual sgRNA and Cas9-expressing plasmid was generated by introducing a second gRNA scaffold in the SpCas9-2A-Puro V2.0 (Addgene, Feng Zang) plasmid using Gibson ligation as described (Vidigal and Ventura, 2015). The final plasmid contains *FOSB* sgRNA TCCACTACACCGTGACGCAG and *SERPINE1* sgRNA TGAACACTAGGGCAAGGTGC. The repair template was generated by blunt ligation of *FOSB* and *SERPINE1* homology arms (around 1kb each) into a P15 backbone containing a Neomycin resistance cassette surrounded by two flippase recognition target (FRT) sequences (kindly provided by Dr. Konstantinos Anastassiadis, Technical University Dresden). The CAGGs-Flpo-IRES-puro vector which expresses codon-optimized Flp recombinase was used for transient transfection to recombine FRT sites (Kranz et al., 2010) (kind gift of Dr Konstantinos Anastassiadis). The U6 vector used for the Gibson ligation was a kind gift from Dr Andrea Ventura (Addgene plasmid # 69312).

Transfection

hiPSCs were transfected at 60-70% confluence the day after seeding in a 60 mm dish.

Transfection was carried out using Lipofectamine® 2000 (Invitrogen). First, 20 µl Lipofectamine® 2000 was diluted in 300 µl Opti-MEM® Medium and incubated at RT for 5 min. In parallel, 8 µg of both the repair template and double guide RNA/Cas9 was diluted in 300 µl Opti-MEM® Medium. Diluted plasmid DNA was added to diluted Lipofectamine® 2000 in a 1:1 ratio and incubated another 5 min at RT before the DNA-lipid complex was added to the cells in a drop-wise manner. Cells were allowed to grow in the incubator for ~18 hours before the medium was changed. Antibiotic selection with 50 µg/ml G-418 was performed 24 hours post transfection and was continued for 7 days to select for targeted cells. Once recovered, cells were passaged into 6-well plates and transfected the next day with 4 µg Flp recombinase expression vector to excise the neomycin cassette (using Lipofectamine® 2000, according to the manufacturer's protocol). At 24h post transfection the medium was supplemented with 0.5 µg/ml Puromycin for 48h to enrich for transfected cells. At 80% confluence, the cells were passaged for clonal expansion on 96-well plates using limited dilution.

Fluorescence In Situ Hybridization

Three-color Fluorescence In Situ Hybridization (FISH) was performed using BAC clones (BACPAC Resource Center). Proximal to *SERPINE1* BAC clone RP11-395B7 was selected. Proximal and distal to *FOSB* respectively BAC clone RP11-84C16 and RP11-902P17 were selected. BAC DNA was extracted using the High Pure plasmid isolation kit (Roche). The RP11-395B7, RP11-84C16 and RP11-902P17 were respectively labeled with Cy5-dUTP, Fluorescein-12-dCTP and Cy3-dUTP using a nick translation labeling reaction. FISH was performed as previously described by our group (van Ijzendoorn et al., 2015). Representative images were taken using an epifluorescence microscope (Leica).

Identification of targeted hiPSC clones by PCR

PCR screening was performed to determine the presence of both the 5' homology arm of *SERPINE1* (primers SF and FR), the 3' homology arm of *FOSB* (primer F2 and R2), the wild-type *SERPINE1* (primer SF and SR) and wild-type *FOSB* (primer FF and FR) in clonal lines (Supplementary table 1). Colonies were picked in maximum 2 µl hESC-food and added to 20 µl QuickExtract Solution (Epicentre) in 0.5 mL tubes. The tubes were vortexed for 15s and DNA was extracted by heating the samples to 65 °C for 15 minutes, 68 °C for 15 minutes and 98 °C for 10 minutes in a thermocycler. 2-Step PCR was performed with Terra PCR Direct Polymerase (TaKaRa) according to the manufacturer's protocol. Sanger sequencing was performed (BaseClear) to confirm the *SERPINE1-FOSB* fusion and to screen the *SERPINE1* and *FOSB* wild-type allele for on-target mutations due to NHEJ.

COBRA-FISH

COmbined Binary RAtio Fluorescence in Situ Hybridization (COBRA-FISH) was performed on metaphase cells as previously described in detail (Szuhai and Tanke, 2006).

Differentiation and characterization of hiPSCs to ECs

hiPSCs were differentiated to hiPSC-ECs and characterized as previously described (Halaidych et al., 2018a; Orlova et al., 2014b; 2014a).

Real-Time qPCR

RNA isolation was performed with the Direct-zol RNA isolation kit (Zymo-research) according to the manufacturer's protocol. cDNA was synthesized using M-MLV with oligo dT primers (Promega) according to the manufacturer's protocol. Real-Time qPCR was performed with Sybr Green (Bio-Rad) on a CFX384 thermocycler (Bio-Rad). All real time PCR experiments were performed in triplicate. Primers are listed in supplementary table 2.

Western blotting

Western blotting was performed as previously described (van Ijzendoorn et al., 2017) using FOSB monoclonal rabbit antibody (#2251; Cell Signaling) and USP7 monoclonal rabbit antibody (A300-033A; Bethyl).

Assessment of hiPSC-EC proliferation

To quantify proliferation, cells were cultured in a 96-well plate for 24 hours. Presto Blue (ThermoFisher) was subsequently added to the medium and cells were incubated at 37 °C for 30 minutes before determining the Relative Fluorescence Units (RFU) using a plate reader (Perkin Elmer).

Matrigel tube formation assay

Tube formation assays were performed in 96-well plates coated with 50 µl Matrigel (Corning). hiPSC-ECs were seeded at a density of 15,000 cells per well in 150 µl EC-SFM supplemented with 1% BSA and 50 ng/µl VEGF. Tube formation was analyzed with ImageJ (NHI, v1.51s). Tube formation was imaged with the EVOS Cell Imaging System (ThermoFisher). To quantify tube formation a custom plugin in ImageJ (NIH, v1.51s) was used. Analysis scripts are available on GitHub (github.com/davidvi) for analysis of tube formation.

Endothelial barrier function and analysis

Endothelial barrier function was determined as previously described (Halaidych et al., 2018a). Briefly, hiPSC-ECs were plated on FN-coated ECIS arrays (8W10E PET, Applied Biophysics) at a density of 50,000 cells/cm². Wounding of the cells grown on the

electrodes was performed by applying a 10 sec pulse of 5V at 60 kHz. Barrier function was estimated by applying a current to the electrodes at 4 kHz and measuring the R [ohm]. Barrier function was measured for over 8 hours. Quantification was performed over a period of 5 hours, when the barrier had stabilized.

Immunofluorescence and immunohistochemistry

Immunofluorescence was performed as previously described (Halaidych et al., 2018a; Orlova et al., 2014a). Briefly, hiPSC-ECs were fixed with 4% PFA and permeabilized with 0.1% Triton-X100. The following primary antibodies were used: anti-ZO1 (61-7300; ThermoFisher), VEC (53-1449-42; CellSignaling), CD31 (M082301; Dako) and cells were counterstained with A488 conjugated Phalloidin (ThermoFisher). Incubation with primary antibodies was overnight at +4 °C and secondary antibodies for 30 minutes at room temperature. Immunohistochemistry with human-specific CD31 (huCD31) and FOSB was performed as previously described (Halaidych et al., 2018b). Images were acquired using EVOS FL AUTO2 Imaging System (ThermoFisher) or with the WLL1 confocal microscope (Leica), using 40x DRY objective and 0.75 Zoom factor. Used Antibodies are listed (supplementary table 3).

Vasculogenesis *in vivo* in mice

All animal experiments were performed in accordance with legal regulations with approved protocols by the Central Commissie voor Dierproeven (CCD, Central Commission for Animal Experiments). Mice were maintained at the animal facility of Leiden University Medical Center (LUMC). Teratoma and Matrigel plug assays (figure 5a) were performed in eight-week-old male NSG mice (NOD.Cg-Prkdcscid Il2rgtm1Wjl/SzJ, Charles River).

Teratoma assay

The teratoma assay was performed on the parental hiPSC^{WT} and hiPSC^{SERPINE-FOSB (D3)} as reported before (Salvatori et al., 2018). On the same day, three animals per cell-line were injected using the same batch of cells for each mouse.

In vivo mouse Matrigel plug assay

The Matrigel plug assay was performed as described previously (Halaidych et al., 2018a; Sacchetti et al., 2016). Plugs were removed after 4 and 16 weeks. For each time points three mice were injected with hiPSC^{WT} and three mice with hiPSC^{SERPINE-FOSB (D3)} (figure 5a). Each mouse was subcutaneously injected in the right and left flank with a mixture of hiPSC-ECs, human bone marrow-derived stromal cells (BMSCs) (PromoCell) and Matrigel (Corning). Vessel density was estimated by quantifying the human CD31⁺ area in serial sections as described previously (Halaidych et al., 2018a).

Phosphotungstic acid-haematoxylin staining and analysis

PTAH staining was performed on 4 µm FFPE sections. Paraffin was removed with xylene and sections were rehydrated in an ethanol gradient. Sections were incubated for 15 minutes in 0.25% potassium permanganate then 5 minutes in 5% oxalic acid. Last, the sections were incubated for 24 hours in PTAH solution. To analyze thrombus formation in vessels all vessels with fibrin were counted in an area of 5.7 mm².

Whole genome and transcriptome sequencing and analysis

DNA was isolated for whole genome sequencing using the Wizard Genomic DNA Purification Kit (Promega) and sequenced on the BGISEQ-500 platform (BGI). Reads were aligned to the GRCh38/hg19 reference genome using the Burrow-Wheeler Aligner (v0.7.12) and further processed according to the GATK (Broad institute) best practice pipeline. Copy Number Analysis (CNA) was performed using VarScan (v2.2.4) and analyzed using DNACopy R package (v3.6). Off-target sites for the used gRNAs were determined using an online tool (crispr.cos.uni-heidelberg.de). Data was visualized with the circlize R package (v0.4.3).

RNA for transcriptome sequencing was isolated using Direct-zol RNA miniprep kit (Zymo Research). After library preparation, sequencing was performed on the BGISEQ-500 platform (BGI). Raw data was processed using the LUMC BIOPET Gentrap pipeline (<https://github.com/biopet/biopet>), which comprises FASTQ preprocessing, alignment and read quantification. Sickel (v1.2) was used to trim low-quality read ends¹⁵. Cutadapt (v1.1) was used for adapter clipping¹⁶, reads were aligned to the human reference genome GRCh38 using GSNAP (gmap-2014-12-23) (Wu and Nacu, 2010; Wu and Watanabe, 2005) and gene read quantification with htseq-count (v0.6.1p1) against the Ensembl v94. Gene length and GC content bias were normalized using the R package cqn (v1.28.1) (Hansen et al., 2012). Genes were excluded if the number of reads was below 5 reads in ≥90% of the samples. The final dataset comprised gene expression levels of 6 samples and 16,510 genes. Differentially expressed genes were identified using generalized linear models as implemented in (Robinson et al., 2009). P-values were adjusted using the Benjamini-Hochberg procedure and PFDR ≤ 0.05 was considered significant. Normalized RPKM values were log₂ transformed and standardized across each gene using z-scores and heatmap was produced with the R package ggplot2 (v2.2.1). KEGG pathway enrichment analysis was carried out using Enrichr (Chen et al., 2013; Kuleshov et al., 2016) computational tool and q < 0.05 was used as the cutoff for significant pathways. Gene ontology (GO) enrichment analysis and cnetplot of selected GOs were done with R package clusterProfiler (v3.10.1) (Yu et al., 2012), q < 0.05 was used as the cutoff for significant GOs. Interaction networks of input genes were predicted using Interaction network analysis function of Ingenuity Pathway

Analysis (IPA) software. Then, interactions between specific genes and selected networks were generated using the Build function of IPA.

Statistical Analysis

Statistics and graphs for real-time PCR, proliferation, tube formation and barrier function were generated with GraphPad Prism (GraphPad Software). One-way ANOVA with Tukey's multiple comparison for the analysis of three or more groups or Mann-Whitney test for analysis of two groups were used. The data are reported as mean \pm SD.

Data availability

Whole-genome and transcriptome sequencing data was deposited to the Sequence Read Archive under accession PRJNA448372.

Acknowledgements

We would like to thank Dr Konstantinos Anastasiadis for providing P15 backbone with a Neomycin resistance cassette surrounded by two FRT sequences and CAGGs-Flpo-IRES-puro vector, Dr Andrea Ventura for providing the U6 vector (Addgene plasmid # 69312), Dr Milena Bellin for her valuable comments on the manuscript, AE Versnel for her help in designing the figures.

JVMGB is supported by the Netherlands Organization for Scientific Research (ZON-MW VICI 016.VICI.170.055 to J.V.M.G.B.). FvdH, CLM and VVO were supported by the European Research Council (ERCAdG 323182 STEMCARDIOVASC to C.L.M.); the European Community's Seventh Framework Programme (FP7/2007-2013 under 602423); the European Union's Horizon 2020 Framework Programme (668724).

Author contributions

DGPvI conceived the study, performed experiments, collected and interpreted data and wrote the manuscript. DCFS designed and performed the animal experiments, collected and interpreted data and wrote the manuscript. XC performed analysis of RNA sequencing data. FvdH and IdB-B performed experiments. DJ performed COBRA-FISH and three-color FISH. HM performed alignment of RNA sequencing data. KS & CLM contributed to editing of the manuscript and interpreted data. VO and JB conceived the study, interpreted data and wrote the manuscript.

REFERENCES

Billings, S.D., Folpe, A.L., Weiss, S.W., 2003. Epithelioid sarcoma-like hemangioendothelioma. The American Journal of Surgical Pathology 27, 48–57. doi:10.1097/00000478-200301000-00006

- Cantelmo, A.R., Conradi, L.-C., Brajic, A., Goveia, J., Kalucka, J., Pircher, A., Chaturvedi, P., Hol, J., Thienpont, B., Teuwen, L.-A., Schoors, S., Boeckx, B., Vriens, J., Kuchnio, A., Veys, K., Cruys, B., Finotto, L., Treppe, L., Stav-Noraas, T.E., Bifari, F., Stapor, P., Decimo, I., Kampen, K., De Bock, K., Haraldsen, G., Schoonjans, L., Rabelink, T., Eelen, G., Ghesquière, B., Rehman, J., Lambrechts, D., Malik, A.B., Dewerchin, M., Carmeliet, P., 2016. Inhibition of the Glycolytic Activator PFKFB3 in Endothelium Induces Tumor Vessel Normalization, Impairs Metastasis, and Improves Chemotherapy. *Cancer Cell* 30, 968–985. doi:10.1016/j.ccell.2016.10.006
- Chen, E.Y., Tan, C.M., Kou, Y., Duan, Q., Wang, Z., Meirelles, G., Clark, N.R., Ma'ayan, A., 2013. Enrichr: interactive and collaborative HTML5 gene list enrichment analysis tool. *BMC Bioinformatics* 14, 128. doi:10.1186/1471-2105-14-128
- Gabor, K.M., Sapi, Z., Tiszlavicz, L.G., Fige, A., Bereczki, C., Bartyik, K., 2018. Sirolimus therapy in the treatment of pseudomyogenic hemangioendothelioma. *Pediatr Blood Cancer* 65, e26781. doi:10.1002/pbc.26781
- Halaidych, O.V., Freund, C., van den Hil, F., Salvatori, D.C.F., Riminucci, M., Mummery, C.L., Orlova, V.V., 2018a. Inflammatory Responses and Barrier Function of Endothelial Cells Derived from Human Induced Pluripotent Stem Cells. *STEMCR* 10, 1642–1656. doi:10.1016/j.stemcr.2018.03.012
- Halaidych, O.V., Freund, C., van den Hil, F., Salvatori, D.C.F., Riminucci, M., Mummery, C.L., Orlova, V.V., 2018b. Inflammatory Responses and Barrier Function of Endothelial Cells Derived from Human Induced Pluripotent Stem Cells. *STEMCR* 10, 1642–1656. doi:10.1016/j.stemcr.2018.03.012
- Hansen, K.D., Irizarry, R.A., Wu, Z., 2012. Removing technical variability in RNA-seq data using conditional quantile normalization. *Biostatistics* 13, 204–216. doi:10.1093/biostatistics/kxr054
- Hornick, J.L., Fletcher, C.D.M., 2011. Pseudomyogenic hemangioendothelioma: a distinctive, often multicentric tumor with indolent behavior. *The American Journal of Surgical Pathology* 35, 190–201. doi:10.1097/PAS.0b013e3181ff0901
- Hung, Y.P., Fletcher, C.D.M., Hornick, J.L., 2017. FOSB is a Useful Diagnostic Marker for Pseudomyogenic Hemangioendothelioma. *The American Journal of Surgical Pathology* 41, 596–606. doi:10.1097/PAS.0000000000000795
- Ide, Y.-H., Tsukamoto, Y., Ito, T., Watanabe, T., Nakagawa, N., Haneda, T., Nagai, M., Yamanishi, K., Hirota, S., 2015. Penile pseudomyogenic hemangioendothelioma/epithelioid sarcoma-like hemangioendothelioma with a novel pattern of SERPINE1-FOSB fusion detected by RT-PCR – Report of a case. *Pathology -- Research and Practice* 211, 415–420. doi:10.1016/j.prp.2015.02.003
- Joseph, J., Wang, W.-L., Patnana, M., Ramesh, N., Benjamin, R., Patel, S., Ravi, V., 2015. Cytotoxic and targeted therapy for treatment of pseudomyogenic hemangioendothelioma. *Clinical Sarcoma Research* 5, 22–6. doi:10.1186/s13569-015-0037-8
- Kranz, A., Fu, J., Duerschke, K., Weidlich, S., Naumann, R., Stewart, A.F., Anastassiadis, K., 2010.

- An improved Flp deleter mouse in C57Bl/6 based on Flpo recombinase. *genesis* 48, 512–520. doi:10.1002/dvg.20641
- Kuleshov, M.V., Jones, M.R., Rouillard, A.D., Fernandez, N.F., Duan, Q., Wang, Z., Koplev, S., Jenkins, S.L., Jagodnik, K.M., Lachmann, A., McDermott, M.G., Monteiro, C.D., Gundersen, G.W., Ma'ayan, A., 2016. Enrichr: a comprehensive gene set enrichment analysis web server 2016 update. *Nucleic Acids Research* 44, W90–W97. doi:10.1093/nar/gkw377
- Mertens, F., Antonescu, C.R., Mitelman, F., 2016. Gene fusions in soft tissue tumors: Recurrent and overlapping pathogenetic themes. *Genes Chromosomes Cancer* 55, 291–310. doi:10.1002/gcc.22335
- Milde-Langosch, K., 2005. The Fos family of transcription factors and their role in tumourigenesis. *European Journal of Cancer* 41, 2449–2461. doi:10.1016/j.ejca.2005.08.008
- Miller, D.W., Graulich, W., Karges, B., Stahl, S., Ernst, M., Ramaswamy, A., Sedlacek, H.H., Müller, R., Adamkiewicz, J., 1999. Elevated expression of endoglin, a component of the TGF-beta-receptor complex, correlates with proliferation of tumor endothelial cells. *Int. J. Cancer* 81, 568–572. doi:10.1002/(sici)1097-0215(19990517)81:4<568::aid-ijc11>3.0.co;2-x
- Mitelman, F., Johansson, B., Mertens, F., 2007. The impact of translocations and gene fusions on cancer causation. *Nat Rev Cancer* 7, 233–245. doi:10.1038/nrc2091
- Orlova, V.V., Drabsch, Y., Freund, C., Petrus-Reurer, S., van den Hil, F.E., Muenthaisong, S., Dijke, P.T., Mummery, C.L., 2014a. Functionality of endothelial cells and pericytes from human pluripotent stem cells demonstrated in cultured vascular plexus and zebrafish xenografts. *Arteriosclerosis, Thrombosis, and Vascular Biology* 34, 177–186. doi:10.1161/ATVBAHA.113.302598
- Orlova, V.V., van den Hil, F.E., Petrus-Reurer, S., Drabsch, Y., Dijke, ten, P., Mummery, C.L., 2014b. Generation, expansion and functional analysis of endothelial cells and pericytes derived from human pluripotent stem cells. *Nature Protocols* 9, 1514–1531. doi:10.1038/nprot.2014.102
- Ozeki, M., Nozawa, A., Kanda, K., Hori, T., Nagano, A., Shimada, A., Miyazaki, T., Fukao, T., 2017. Everolimus for Treatment of Pseudomyogenic Hemangioendothelioma. *J. Pediatr. Hematol. Oncol.* 39, e328–e331. doi:10.1097/MPH.0000000000000778
- Robinson, M.D., McCarthy, D.J., Smyth, G.K., 2009. edgeR: a Bioconductor package for differential expression analysis of digital gene expression data. *Bioinformatics* 26, 139–140. doi:10.1093/bioinformatics/btp616
- Sacchetti, B., Funari, A., Remoli, C., Giannicola, G., Kogler, G., Liedtke, S., Cossu, G., Serafini, M., Sampaolesi, M., Tagliafico, E., Tenedini, E., Saggio, I., Robey, P.G., Riminucci, M., Bianco, P., 2016. No Identical “Mesenchymal Stem Cells” at Different Times and Sites: Human Committed Progenitors of Distinct Origin and Differentiation Potential Are Incorporated as Adventitial Cells in Microvessels. *STEMCR* 6, 897–913. doi:10.1016/j.stemcr.2016.05.011
- Salvatori, D.C.F., Dorssers, L.C.J., Gillis, A.J.M., Perretta, G., van Agthoven, T., Gomes Fernandes, M., Stoop, H., Prins, J.-B., Oosterhuis, J.W., Mummery, C., Looijenga, L.H.J., 2018. The

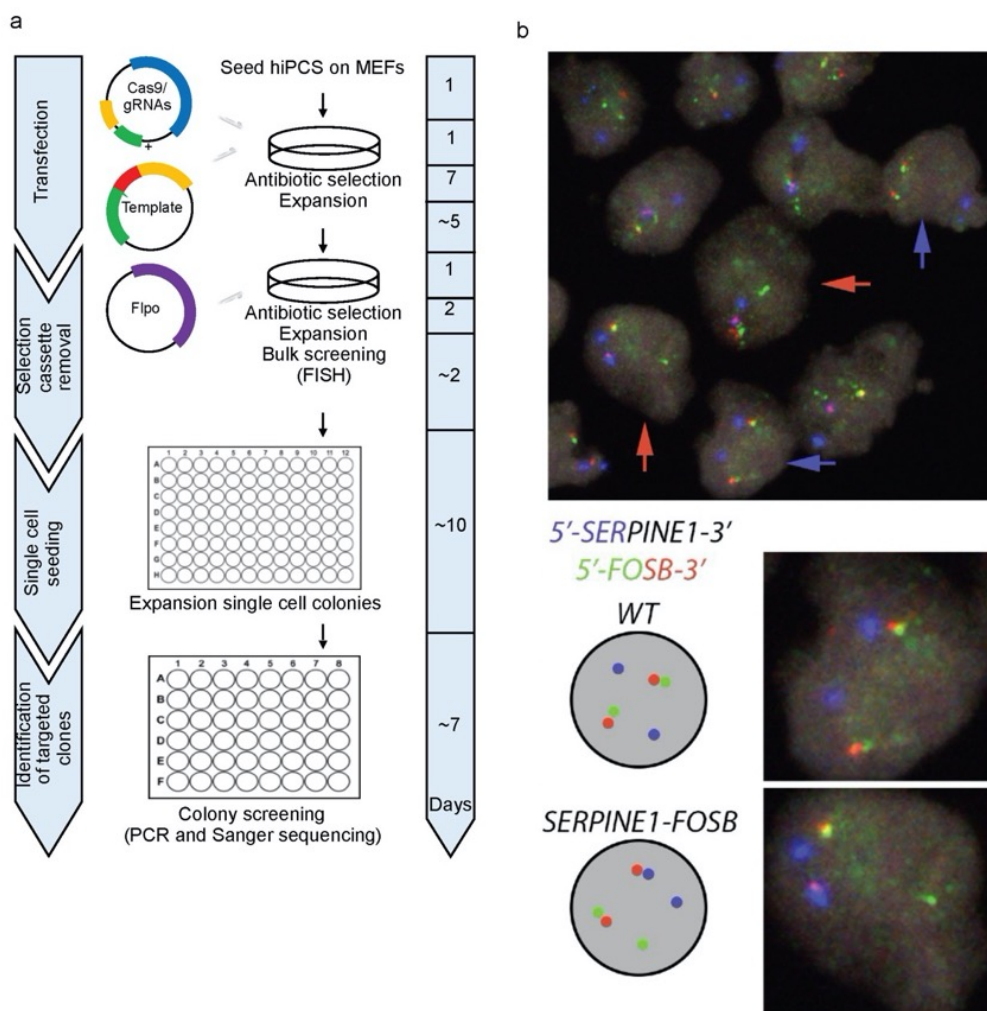
- MicroRNA-371 Family as Plasma Biomarkers for Monitoring Undifferentiated and Potentially Malignant Human Pluripotent Stem Cells in Teratoma Assays. *STEMCR* 11, 1493–1505. doi:10.1016/j.stemcr.2018.11.002
- Sánchez-Rivera, F.J., Jacks, T., 2015. Applications of the CRISPR–Cas9 system in cancer biology. *Nat Rev Cancer* 15, 387–393. doi:10.1038/nrc3950
- Schneidawind, C., Jeong, J., Schneidawind, D., Kim, I.-S., Duque-Afonso, J., Wong, S.H.K., Iwasaki, M., Breese, E.H., Zehnder, J.L., Porteus, M., Cleary, M.L., 2018. MLL leukemia induction by t(9;11) chromosomal translocation in human hematopoietic stem cells using genome editing. *Blood Adv* 2, 832–845. doi:10.1182/bloodadvances.2017013748
- Szuhai, K., Tanke, H.J., 2006. COBRA: combined binary ratio labeling of nucleic-acid probes for multi-color fluorescence in situ hybridization karyotyping. *Nature Protocols* 1, 264–275. doi:10.1038/nprot.2006.41
- Takahashi, K., Tanabe, K., Ohnuki, M., Narita, M., Ichisaka, T., Tomoda, K., Yamanaka, S., 2007. Induction of pluripotent stem cells from adult human fibroblasts by defined factors. *Cell* 131, 861–872. doi:10.1016/j.cell.2007.11.019
- Torres, R., Martin, M.C., Garcia, A., Cigudosa, J.C., Ramirez, J.C., Rodriguez-Perales, S., 2014. Engineering human tumour-associated chromosomal translocations with the RNA-guided CRISPR-Cas9 system. *Nature Communications* 5, 3964. doi:10.1038/ncomms4964
- Torres-Ruiz, R., Martinez-Lage, M., Martin, M.C., Garcia, A., Bueno, C., Castaño, J., Ramirez, J.C., Menendez, P., Cigudosa, J.C., Rodriguez-Perales, S., 2017. Efficient Recreation of t(11;22) EWSR1-FLI1+ in Human Stem Cells Using CRISPR/Cas9. *STEMCR* 8, 1408–1420. doi:10.1016/j.stemcr.2017.04.014
- Trombetta, D., Magnusson, L., Steyern, von, F.V., Hornick, J.L., Fletcher, C.D.M., Mertens, F., 2011. Translocation t(7;19)(q22;q13)–a recurrent chromosome aberration in pseudomyogenic hemangioendothelioma? *Cancer Genet* 204, 211–215. doi:10.1016/j.cancergen.2011.01.002
- van Ijzendoorn, D.G.P., de Jong, D., Romagosa, C., Picci, P., Benassi, M.S., Gambarotti, M., Daugaard, S., van de Sande, M., Suzhai, K., Bovée, J.V.M.G., 2015. Fusion events lead to truncation of FOS in epithelioid hemangioma of bone. *Genes Chromosomes Cancer* 54, 565–574. doi:10.1002/gcc.22269
- van Ijzendoorn, D.G.P., Forghany, Z., Liebelt, F., Vertegaal, A.C., Jochemsen, A.G., Bovée, J.V.M.G., Suzhai, K., Baker, D.A., 2017. Functional Analyses of a Human Vascular Tumor FOS Variant Identify a Novel Degradation Mechanism and a link to Tumorigenesis. *Journal of Biological Chemistry jbc*.C117.815845–21. doi:10.1074/jbc.C117.815845
- van Ijzendoorn, D.G.P., Sleijfer, S., Gelderblom, H., Eskens, F.A.L.M., van Leenders, G.J., Suzhai, K., Bovée, J.V.M.G., 2018. Telatinib is an effective targeted therapy for pseudomyogenic hemangioendothelioma. *Clinical Cancer Research clincanres*.3512.2017–22. doi:10.1158/1078-0432.CCR-17-3512
- Vanoli, F., Tomishima, M., Feng, W., Lamribet, K., Babin, L., Brunet, E., Jasin, M., 2017. CRISPR-

- Cas9-guided oncogenic chromosomal translocations with conditional fusion protein expression in human mesenchymal cells. *Proceedings of the National Academy of Sciences* 114, 3696–3701. doi:10.1073/pnas.1700622114
- Verbeke, S.L.J., Bertoni, F., Bacchini, P., Oosting, J., Sciot, R., Krenács, T., Bovée, J.V.M.G., 2013. Active TGF- β signaling and decreased expression of PTEN separates angiosarcoma of bone from its soft tissue counterpart. *Mod. Pathol.* 26, 1211–1221. doi:10.1038/modpathol.2013.56
- Vidigal, J.A., Ventura, A., 2015. Rapid and efficient one-step generation of paired gRNA CRISPR-Cas9 libraries. *Nature Communications* 6, 8083–7. doi:10.1038/ncomms9083
- Walther, C., Tayebwa, J., Lilljebjörn, H., Magnusson, L., Nilsson, J., Steyern, von, F.V., Øra, I., Domanski, H.A., Fioretos, T., Nord, K.H., Fletcher, C.D., Mertens, F., 2014. A novel SERPINE1-FOSB fusion gene results in transcriptional up-regulation of FOSB in pseudomyogenic haemangioendothelioma. *J. Pathol.* 232, 534–540. doi:10.1002/path.4322
- Wu, T.D., Nacu, S., 2010. Fast and SNP-tolerant detection of complex variants and splicing in short reads. *Bioinformatics* 26, 873–881. doi:10.1093/bioinformatics/btq057
- Wu, T.D., Watanabe, C.K., 2005. GMAP: a genomic mapping and alignment program for mRNA and EST sequences. *Bioinformatics* 21, 1859–1875. doi:10.1093/bioinformatics/bti310
- Yu, G., Wang, L.-G., Han, Y., He, Q.-Y., 2012. clusterProfiler: an R package for comparing biological themes among gene clusters. *OMICS* 16, 284–287. doi:10.1089/omi.2011.0118

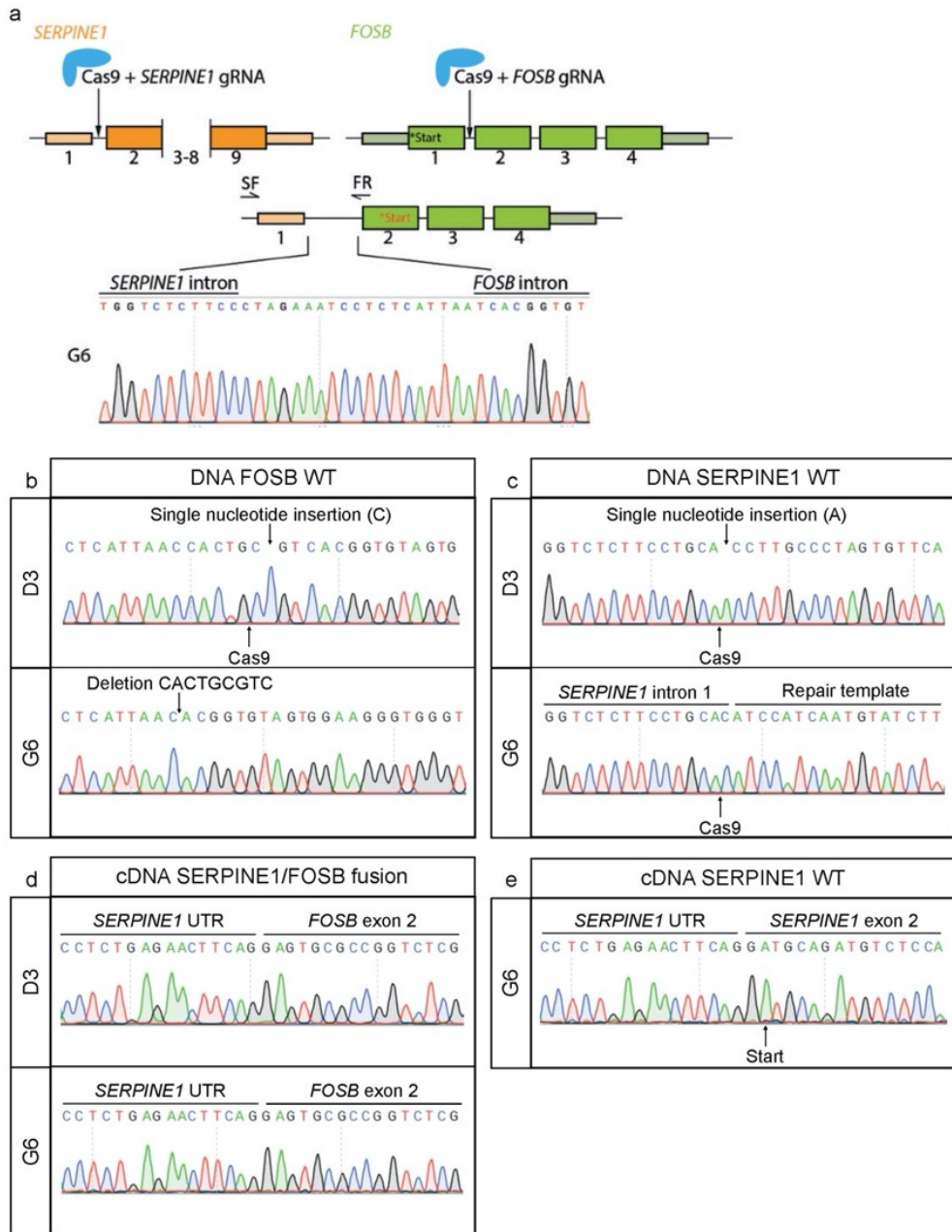
SUPPLEMENTARY INFORMATION

Supplementary Figures S1-S5

Supplementary Tables 1-3

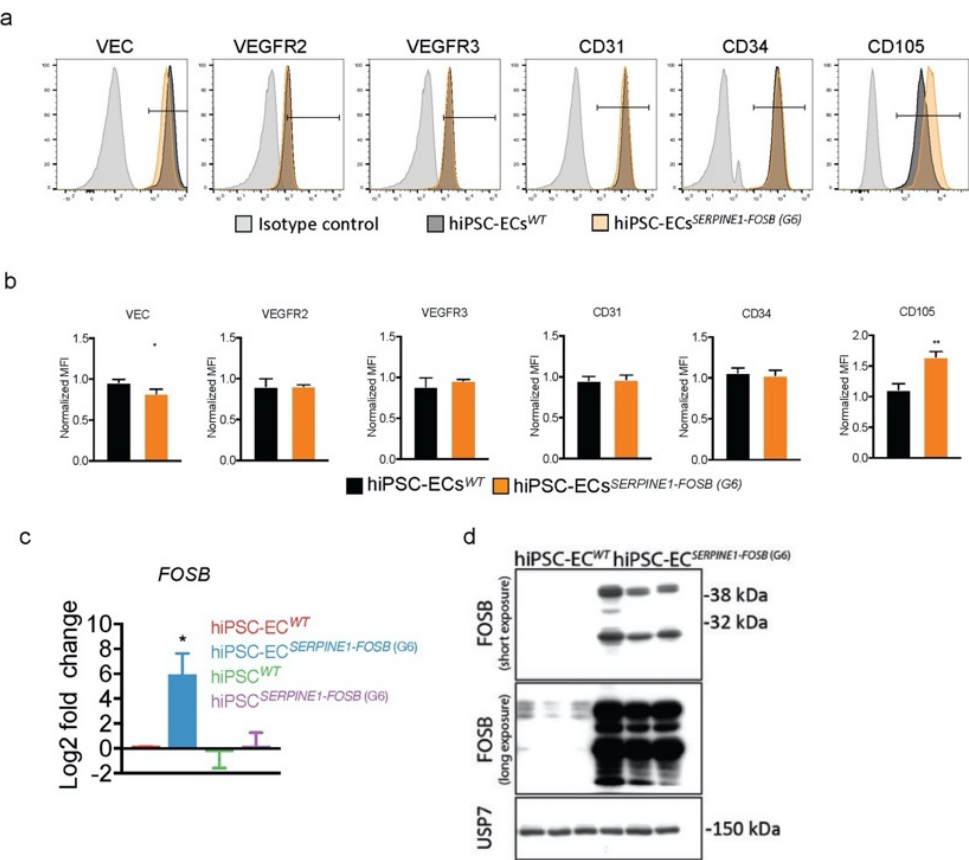


Supplementary figure S1. Generation and characterization of hiPSCs with a *SERPINE-FOSB* fusion. (a) Schematic overview of the targeting and screening experimental workflow. (b) Three color FISH (Blue at 5' side of *SERPINE1*; green at 5' side of *FOSB* and red at 3' side of *FOSB*) for the detection of *SERPINE1-FOSB* fusion on hiPSC "bulk" culture prior to single-cell deposition. Red arrows indicate cells with the fusion, and blue arrows show wild-type cells. The right image shows a schematic and representative overview of targeted and wild-type cells, as detected with three color FISH.

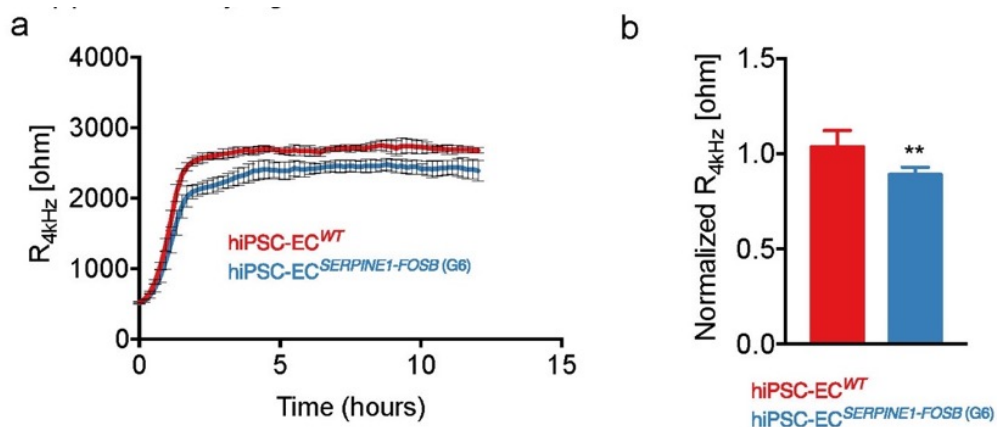


Supplementary figure S2. Sanger sequencing of hiPSCs with a *SERPINE-FOSB* fusion. (a) Upper panel: schematic overview of NHEJ-mediated repair resulting in generation of clone G6. Bottom panel: Sanger sequencing of PCR products from G6 clone validating NHEJ recombination of *SERPINE1* and *FOSB* with a random piece of DNA inserted in the intron between the fusion. (b,c) Sanger sequencing of the non-targeted wild-type *FOSB* intron 1 and wild-type *SERPINE1* intron 1 in hiPSC clones D3 and G6. (d) Sanger sequencing of cDNA from clones D3 and G6 showing normal splicing of fusion *SERPINE1-FOSB* mRNA using forward primer on the *SERPINE1* UTR and a reverse primer on *FOSB* exon 3. (e) Sanger sequencing of the non-targeted wild-type

SERPINE1 cDNA with primers on the SERPINE1 UTR and exon 2 showing that the insertion of the selection cassette fragment had no effect on splicing of SERPINE1 mRNA in colony G6.

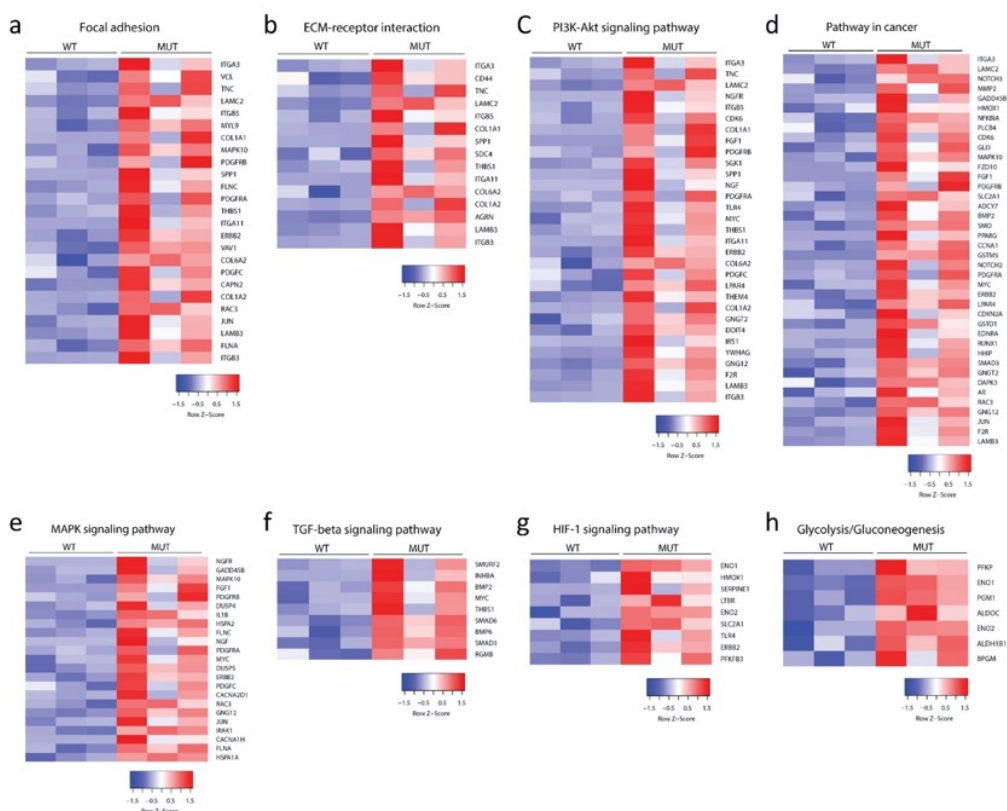


Supplementary figure S3. Characterization of hiPSC-ECs with *SERPINE1-FOSB* fusion. (a) FACS analysis of EC markers expression on isolated hiPSC-ECs^{WT} (black filled histogram) and hiPSC-ECs^{SERPINE1-FOSB (G6)} (orange filled histogram) at passage 2 (P2) and relevant isotype control (gray filled histogram). (b) Quantification of relative surface expression levels (MFI) of VEC, VEGFR2, VEGFR3, CD31, CD34 and CD105. Experiments were performed in triplicate with three independent batches of hiPSC-ECs. Error bars are SD. (c) Real-time qPCR analysis of *FOSB* expression in hiPSCs^{WT}, hiPSCs^{SERPINE1-FOSB (G6)}, hiPSC-ECs^{WT} and hiPSC-ECs^{SERPINE1-FOSB (G6)}. Experiments were performed with three independent batches of hiPSC-ECs. Expression is determined relative to hiPSC-ECs^{WT}, shown as log2 fold change. Error bars are SD. * p<0.005. (d) Western blot analysis of *FOSB* expression in hiPSC-ECs^{WT} and hiPSC-ECs^{SERPINE1-FOSB (G6)}. USP7 was used as a housekeeping control.



Supplementary figure S4. Assessment of barrier function of hiPSC-ECs with *SERPINE1-FOSB* fusion.

(a) Representative absolute resistance of the hiPSC-EC monolayer in complete EC growth medium. Errors bars are shown as \pm SD. **(b)** Normalized resistance [4 kHz] of the hiPSC-EC monolayer in complete EC growth medium. Error bars are shown as \pm SD of six independent biological experiments. *** $p < 0.001$. Experiments were performed in triplicate using three independent batches of hiPSC-ECs.



Supplementary figure S5. KEGG pathways identified in hiPSC-ECs^{SERPINE1-FOSB (D3)} upregulated DEGs.

(a-h) Heatmaps of genes from eight representative KEGG pathways enriched in hiPSC-ECs^{SERPINE1-FOSB(D3)} upregulated DEGs.

Supplementary table 1: PCR primers used to screen targeted clones.

Name	Sequence
SERPINE1 (SF)	ACACAGGCAGAGGGCAGAAAGGTCAA
SERPINE1 (SR)	CCTGCGCCACCTGCTGAAACAC
FOSB (FF)	GCCTTCAGAGCAGTTCCAGGAGTCCATTTA
FOSB (FR)	ACCGACACACACACACCCAACACACATAA
F2	TGGGCTGCAAAGGCAGAGAGTGGTAAT
R2	AAGCGATCCTCCCACTAAAGCCTCCATAGT

Supplementary table 2: qPCR primers.

Name	Sequence
HPRT_f	TGACACTGGCAAAACAATGCA
HPRT_r	GGTCCTTTTCACCAGCAAGCT
FOSB_f	AGCAGCAGCTAAATGCAGGA
FOSB_r	CCAAGTATCTGTCTCCGCC

Supplementary table 3: Antibodies and their dilutions.

Antibody	Cat#	Manufacturer	Clone	Dilutions
VE-cadherin-A488	53-1449-42	eBiosciences	16B1	1:100
KDR-PE	FAB357P	R&D systems	89106	1:50
VEGFR3-PE	FAB3492P	R&D systems	54733	1:50
CD31-APC	17-0319-42	eBiosciences	WM59	1:200
CD34- PerCP-Cy5.5	347222	BD Pharmingen	8G12	1:100
CD105-VioBlue	130-099-666	Miltenyi Biotec	43A4E1	1:50
Phalloidin-A488	A12379	ThermoFisher	N/A	1:20

VE-Cadherin	2158S	Cell Signaling	Polyclonal	1:200
ZO-1	61-7300	ThermoFisher	Polyclonal	1:200?
CD31	M0823	Dako	JC70A	1:200 IF 1:30 IHC
FOSB	2251S	Cell Signaling	5G4	1:200 IF 1:30000 WB
USP7	A300-033A	Bethyl Laboratories	Polyclonal	1:10000

Appendix Chapter 6:

Follow up bioinformatics analysis of hiPSC-endothelial cells expressing the *SERPINE1-FOSB* translocation

Xu Cao¹, Judith V.M.G. Bovée², Christine L. Mummery¹, Valeria V. Orlova^{1,*}

¹Department of Anatomy and Embryology, Leiden University Medical Center, Leiden, The Netherlands

²Department of Pathology, Leiden University Medical Center, Leiden, The Netherlands

*Correspondence: v.orlova@lumc.nl

Abstract

Establishing an *in vitro* model of Pseudomyogenic hemangioendothelioma (PHE) using human induced pluripotent stem cells (hiPSCs) would provide a powerful tool for the study of pathology and rationale for treatment strategies. In **Chapter 6**, we generated a PHE hiPSC line by introducing the chromosomal translocation into wild type (WT) hiPSCs using CRISPR/Cas9 and established a disease model of PHE with hiPSC-endothelial cells (hiPSC-ECs). RNA sequencing (RNAseq) analysis of hiPSC-ECs described in **Chapter 6** gave an initial in-depth view on the disease mechanism at the gene expression and signaling pathway levels. In this chapter (appendix chapter 6), I describe and extended RNAseq analysis for this disease model. This bioinformatic analysis provided extra information on the dysregulated transcriptional networks in mutated ECs that are relevant for the disease pathologies in PHE. Most importantly, candidate drug targets are predicted here based on Ingenuity pathway analysis (IPA). These offer new potential treatment opportunities for PHE.

Introduction

In Chapter 6, we established an *in vitro* model of Pseudomyogenic hemangioendothelioma (PHE) using human induced pluripotent stem cell-derived ECs (hiPSC-ECs) carrying the *SERPINE1-FOSB* translocation. hiPSC-ECs^{*SERPINE1-FOSB*} showed several disease phenotypes *in vitro* and in mice after transplantation, which resembling certain aspects of the PHE phenotype observed in patients (Hornick and Fletcher, 2011). Whole transcriptome sequencing and bioinformatic analysis performed in **Chapter 6** for the hiPSC model provided a powerful approach to revealing dysregulated transcription networks as a result of the translocation and indications of underlying disease

mechanisms of PHE. The transcriptome of ECs derived from wild type (WT) and mutated hiPSCs were compared and dysregulated genes in hiPSC-ECs^{SERPINE1-FOSB} were identified. Gene Ontology (GO) and KEGG pathway enrichment analysis were performed to identify signaling pathways and cellular activities linked to these differentially expressed genes (DEGs). Ingenuity pathway analysis (IPA) was next performed to investigate the gene regulation networks between DEGs and thus reveal new pathways underlying disease pathologies. These RNAseq analyses provided the rationale for new therapeutic strategies that could be used for PHE. However, only the most critical RNAseq analysis results were included in **Chapter 6** due to the restriction of the length of the article.

Here, we present additional RNAseq analysis carried out in this hiPSC model of PHE. Although beyond the scope of the manuscript in chapter 6, the data are valuable and informative in terms of the understanding the pathology and development of treatment strategies for PHE. WT and mutated hiPSC-ECs together with hiPSCs were included in the bioinformatic analysis. Additional gene-gene interaction- and regulatory networks of DEGs between WT and mutated hiPSC-ECs were identified; Two candidate drugs that target on dysregulated genes of hiPSC-ECs^{SERPINE1-FOSB} were predicted using a powerful bioinformatic tool IPA. This extra bioinformatic analysis not only complemented the RNAseq analysis in **Chapter 6**, but also give new insights into the disease mechanism and drug development for PHE.

Results

Transcriptome analysis of hiPSCs and hiPSC-ECs with and without *SERPINE1-FOSB* translocation.

To obtain an overview of cell identities and transcriptome profiles, principle component analysis was performed for WT hiPSCs, hiPSC-EC^{WT} and hiPSC-ECs^{SERPINE1-FOSB}, with three replicates in each group (Figure 1a). Samples from the same group clustered together. hiPSC samples clustered separately from EC samples by PC1, while hiPSC-EC^{WT} and hiPSC-EC^{SERPINE1-FOSB} are separated principally by PC2 (Figure 1a). hiPSC-ECs^{SERPINE1-FOSB} samples showed the highest variation within the group compared to other groups. 1222 DEGs identified between hiPSC-EC^{WT} and hiPSC-EC^{SERPINE1-FOSB} (see **Chapter 6**) were divided into 4 clusters based on their expression pattern in different groups (Figure 1b). Cluster 1 genes are highest in hiPSCs and lowest in hiPSC-EC^{WT}. Cluster 2 genes are highest in hiPSCs but also present in hiPSC-EC^{SERPINE1-FOSB}. Cluster 3 and 4 genes are mainly expressed by ECs. Cluster 3 was higher in hiPSC-EC^{WT}, while cluster 4 was higher in hiPSC-EC^{SERPINE1-FOSB}.

To characterize genes in each cluster, GO enrichment analysis was performed with the cluster Profiler R package (Figure 1c). Mucosal immune response was enriched in cluster 1. A large number of GOs including extracellular matrix organization, cell growth, regeneration, asymmetric cell division were identified in cluster 2. Cluster 3 genes were

mainly related to immune responses. Meanwhile, genes in cluster 4 were associated with processes like angiogenesis, cell migration, endothelial cell proliferation, response to transforming growth factor beta, regulation of ERK1 and ERK2 cascade.

Gene-gene interaction analysis for dysregulated genes in hiPSC-EC^{SERPINE1-FOSB}

To investigate the interaction between *SERPINE1-FOSB* translocation and dysregulated genes/signaling pathways, IPA was applied for DEGs between hiPSC-EC^{WT} and hiPSC-EC^{SERPINE1-FOSB}. First, upstream and downstream genes which have direct connections with *FOSB* and *SERPINE1* were identified. Interactions among these identified genes were thus revealed. All of these genes and interactions were mapped based on their cellular positions as shown in Figure 2a. *FOSB* regulates *SERPINE1* expression directly. Both *FOSB* and *SERPINE1* show self-regulatory effects. *FOSB* is regulated by several extracellular growth factors, like TGFβ3, IGF1, HGF, GDNF, FGF2. Many upstream regulators of *FOSB* and *SERPINE1* were expressed at higher levels in hiPSC-EC^{SERPINE1-FOSB} than hiPSC-EC^{WT} (Figure 2a, labeled in green).

Next, regulatory effects among upregulated genes of hiPSC-EC^{SERPINE1-FOSB} were identified using IPA software, which allowed us to identify upstream regulators as well as downstream cellular function and activities (similar to GO enrichment) linked to these genes. ADA and LOX were found to promote the expression of most upregulated genes in hiPSC-EC^{SERPINE1-FOSB} (Figure 2b). These upregulated genes are involved in many cellular processes, including angiogenesis, vascularization, invasion of tumor cells, cell proliferation of tumor cells, mitogenesis et al. (Figure 2b).

Potential drugs predicted by IPA that target on dysregulated genes in hiPSC-EC^{SERPINE1-FOSB}

Using the Drug prediction function incorporated in IPA software, two candidate drugs were identified which could inhibit the expression of upregulated genes in hiPSC-EC^{SERPINE1-FOSB}. Both LY294002 and PD98059 were identified as inhibitors of a large number of dysregulated genes caused by the *SERPINE1-FOSB* translocation. LY294002 can inhibit *FOSB* expression but promote *SERPINE1* expression, while PD98059 inhibits expression of both *FOSB* and *SERPINE1*.

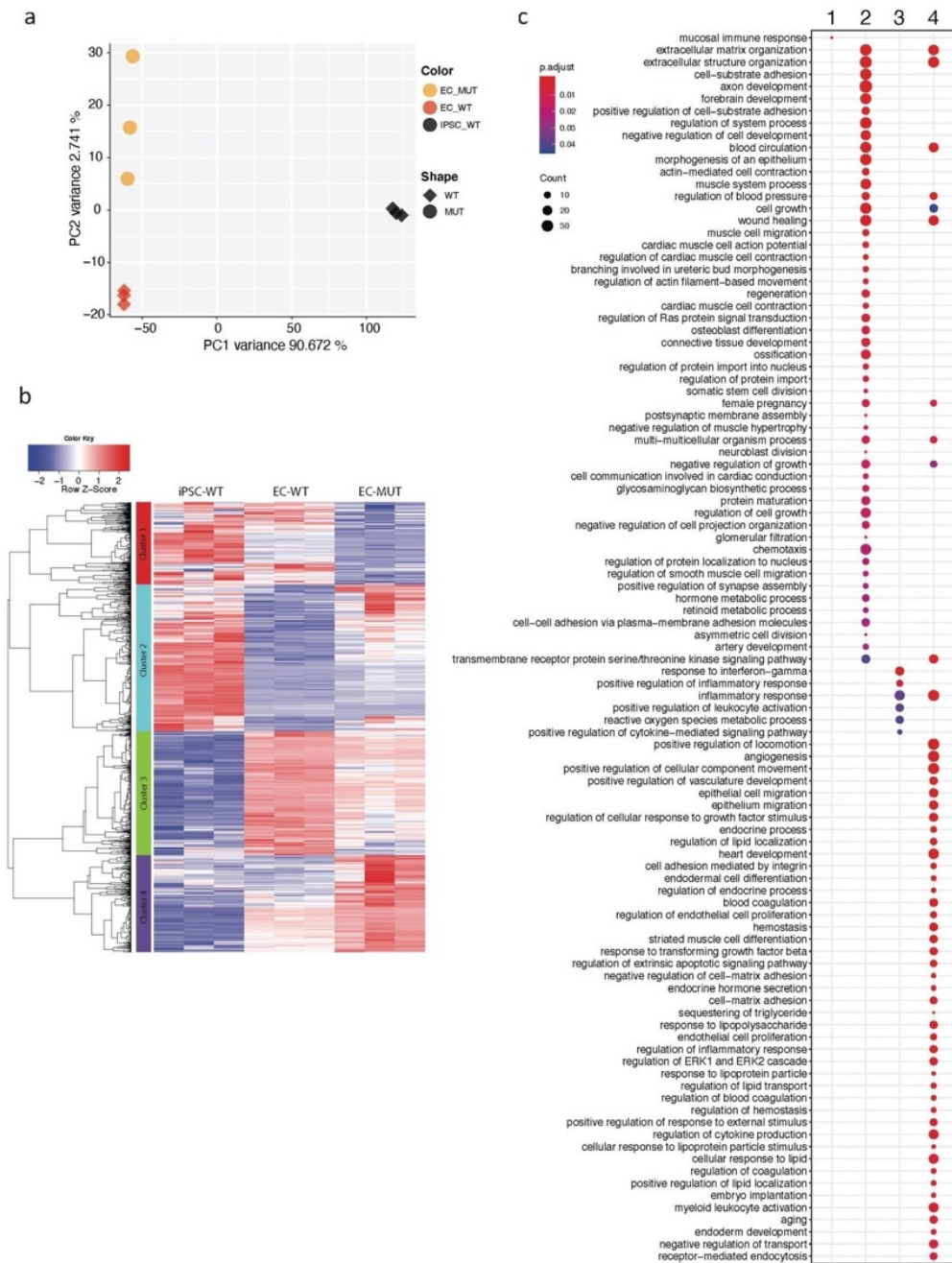
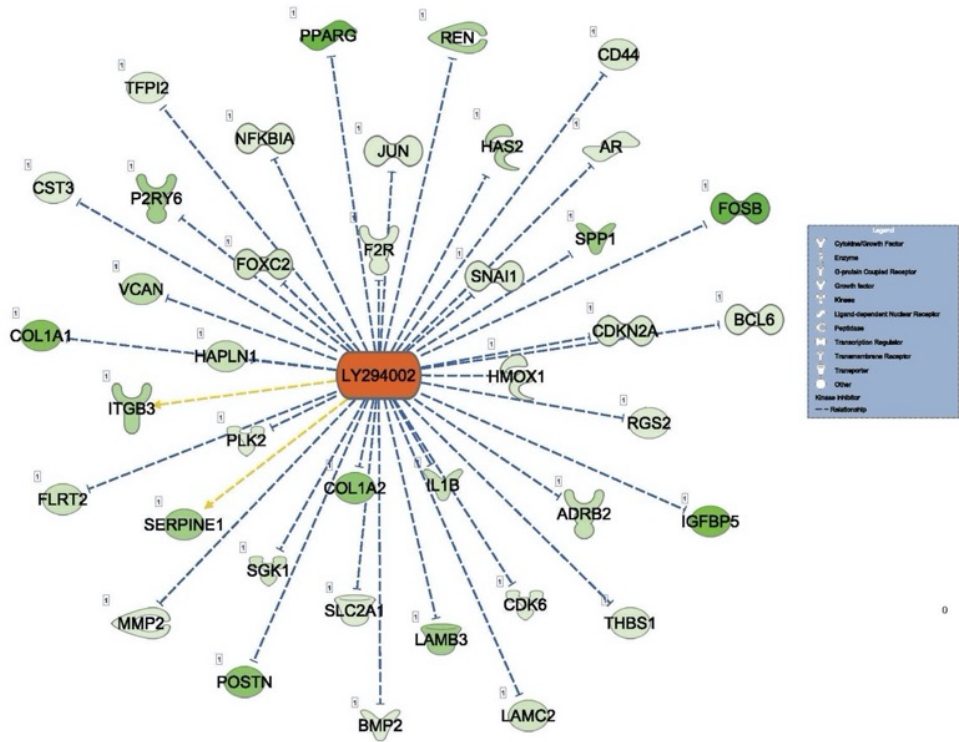


Figure 1. Transcriptome analysis of hiPSCs and hiPSC-ECs with and without *SERPINE1-FOSB* translocation. (a) Principle component analysis (PCA) of hiPSCs and hiPSC-ECs with (EC_MUT) and without (EC_WT) *SERPINE1-FOSB* translocation. (b) Hierarchical clustering analysis for 1222 differentially expressed genes (DEGs) between EC_MUT and EC_WT. All genes were divided into 4 clusters by setting Cutree to 4. (c) Gene Ontology (GO) enrichment for each cluster of genes using clusterProfiler R package.

a



b

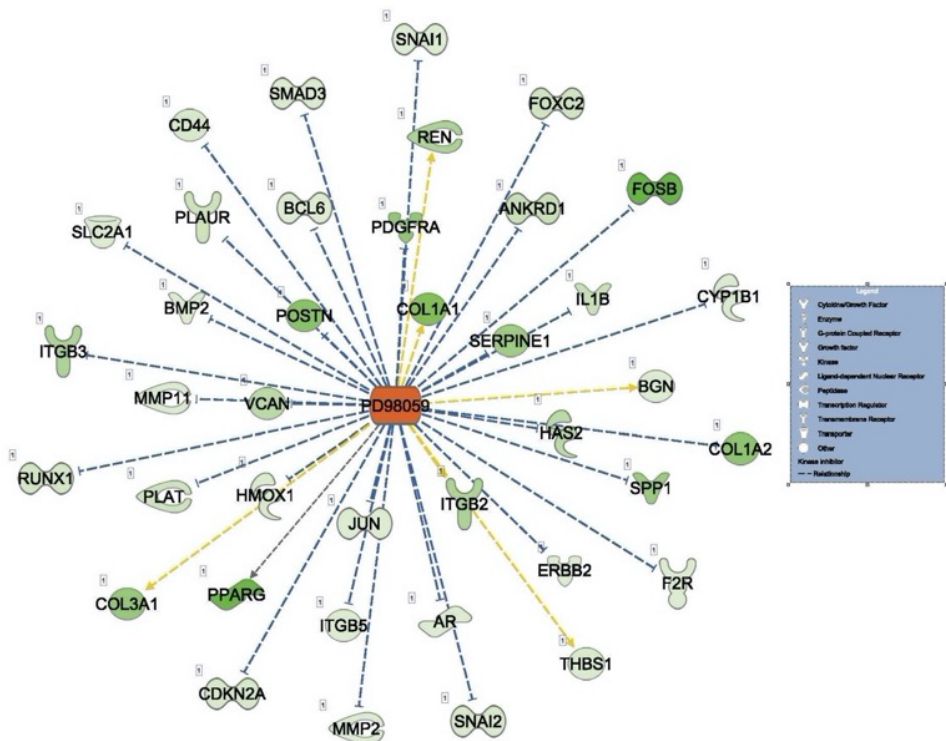


Figure 3. Two drugs called LY294002 (a) and PD98059 (b) predicted by IPA which could inhibit

dysregulated genes that higher in MUT ECs compared to WT ECs.

Discussion

In this chapter appendix, we included extra bioinformatic analysis for the transcriptome profiles of hiPSCs and hiPSC-ECs with and without *SERPINE1-FOSB* translocation, which reveal important new information but could not be included in **Chapter 6** for space reasons. We found that hiPSC-ECs carrying the *SERPINE1-FOSB* translocation preserved a clear EC identity that was distinct from undifferentiated hiPSCs. Around half of DEGs between hiPSC-EC^{WT} and hiPSC-EC^{*SERPINE1-FOSB*} were hiPSCs specific genes. Interestingly, a large number of hiPSCs specific genes (cluster 2) were upregulated only in hiPSC-EC^{*SERPINE1-FOSB*} but not in hiPSC-EC^{WT}. These genes are involved in cell proliferation and migration, which correlated with the PHE tumor phenotypes in patients and the hiPSC model established in **Chapter 6**. Genes related to EC proliferation, response to transforming growth factor beta and regulation of inflammatory response were upregulated in hiPSC-EC^{*SERPINE1-FOSB*}, which also correlated with the abnormal phenotypes observed with hiPSC-EC^{*SERPINE1-FOSB*} *in vitro*, like aberrant cell barrier function and formation of haphazardly arranged vessels after transplantation in mice. Gene-gene interaction networks and regulatory effects identified by IPA revealed the disease mechanism in a transcriptional level. A clear overview of the complex interactions among dysregulated genes caused by *SERPINE1-FOSB* translocation, as well as cellular functions and activities that were affected by these dysregulated genes were obtained in this part of the study. Notably, angiogenesis, vascularization and tumor-related process were activated/promoted by these dysregulated genes in hiPSC-EC^{*SERPINE1-FOSB*}. This explained pathologies of PHE tumor development at the transcriptional level: the driver *SERPINE1-FOSB* mutation caused downstream dysregulated genes in hiPSC-EC^{*SERPINE1-FOSB*} which further lead to aberrant cellular function and activities in ECs. Compared to the interaction map included in the main Chapter (**chapter 6**), the interaction map drawn in this appendix provided new information about the gene-gene interactions and thus new insights into the disease mechanisms of PHE. Most importantly, two candidate drugs which could target on a large number of dysregulated genes in hiPSC-EC^{*SERPINE1-FOSB*} were also identified in this appendix. Especially, drug PD98059 was predicted as able to have an inhibitory effect on both *SERPINE1* and *FOSB* expression. We conclude it could be a potential drug for PHE, which should be further tested both *in vitro* and *in vivo* in the future.

In summary, these extra bioinformatic analyses of PHE hiPSC model provided extra key insights about disease mechanisms of PHE and identified two candidate drugs for the treatment of the disease. The analysis here was not only complementary to the

analysis in the main chapter, but also presented important new information about the disease.

METHODS

*Methods of this chapter appendix only cover the methods that are specific to this appendix which were not included in the main chapter (**Chapter 6**).*

Principle component analysis (PCA) and HCA

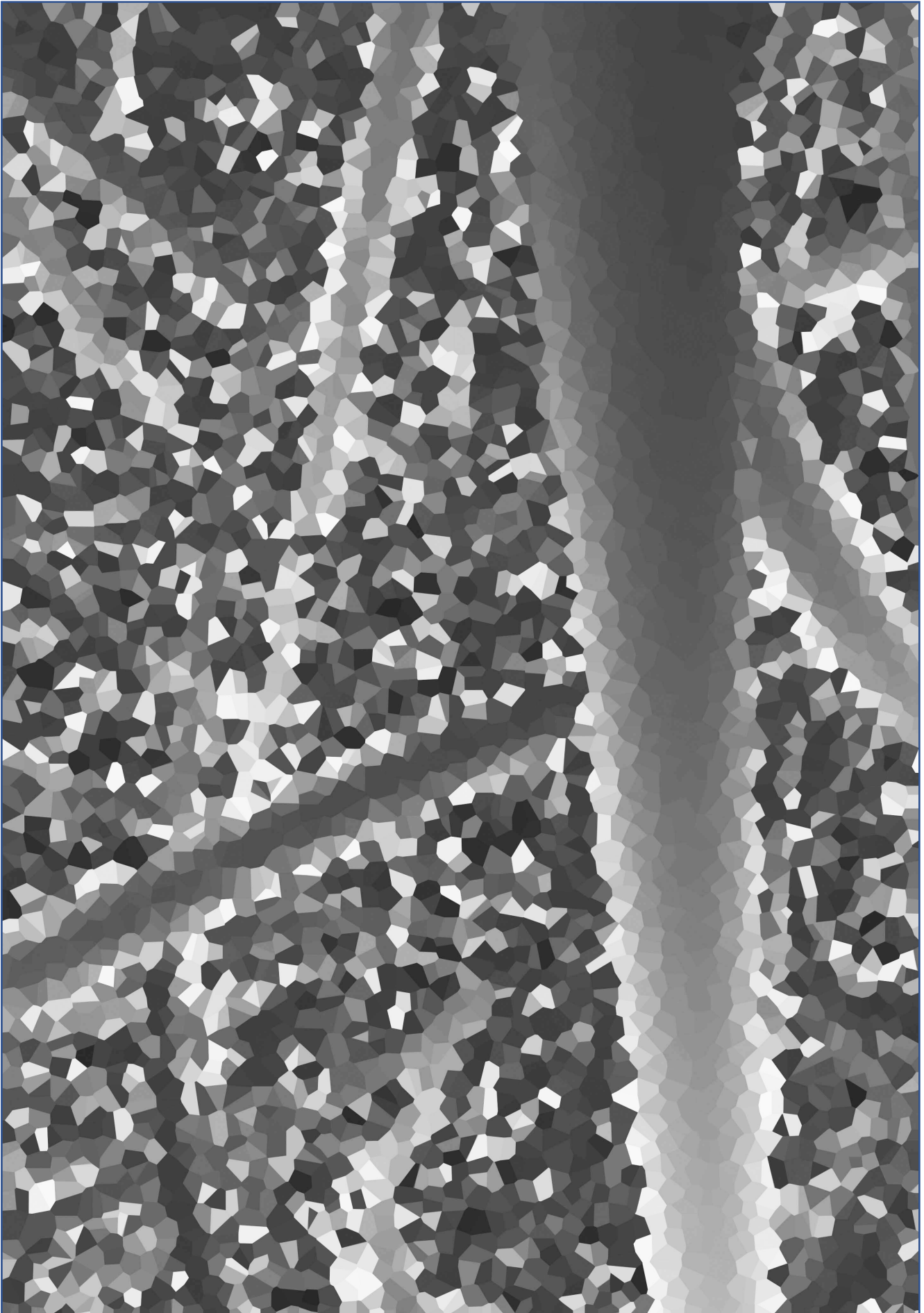
PCA plot was generated with the built-in R functions `prcomp` using transposed normalized RPKM matrix.

Ingenuity pathway analysis (IPA)

Interaction networks among input genes were generated using Interaction network analysis function of IPA software. Map of genes in specific cellular positions was generated with build-in **layout** option of IPA software. Upstream regulators and downstream functions/activities of input genes were identified with build-in **Regulatory effects** function of IPA. Candidate drugs that target on a list of input genes were identified using a build-in **Drug prediction** function of IPA.

REFERENCES

Hornick, J.L., and Fletcher, C.D. (2011). Pseudomyogenic Hemangioendothelioma. *Am J Surg Pathology* 35, 190–201. WT.



Chapter 7

Discussion and Future Perspectives

GENERAL DISCUSSION

In depth analysis of endothelial cells (ECs) and myeloid cells differentiated from human induced pluripotent stem cells (hiPSCs) were shown in this thesis to be very similar to tissue derived equivalents *in vivo*. They thus provided an essential tool to study their biology and various vascular and inflammatory diseases that are caused by their dysfunction. In this thesis, we first established an efficient protocol to derive fully functional monocytes and different subtypes of macrophages from hiPSCs in order to provide an inflammatory component for modelling of vascular diseases *in vitro*. Next, we characterized the developmental path of hiPSC-derived ECs (hiPSC-ECs) using an *ETV2*^{mCherry} reporter hiPSC line which we had generated earlier using Crispr-Cas9 gene targeting. These hiPSC-derived cells were then used to model two vascular diseases Hereditary Hemorrhagic Telangiectasia type 1 (HHT1) and Pseudomyogenic hemangioendothelioma (PHE) *in vitro*.

A 3D vasculature model in an Organ-on-Chip microfluidic format was established using hiPSC-derived cells. The cells as necessary in combination with the Organ on Chip model were then used to study two disease pathologies: HHT1, which is characterized by weak vessel walls in patients and a strong tendency to hemorrhage, and a vascular tumor, PHE, caused by translocation in the *SERPNE1-FOSB* genes and characterized by malignant behaviour of vascular cells for which the tumor cell of origin was unknown. Work in this thesis generated an *in vitro* model for HHT1 as well as for the vascular tumor PHE; these models provided valuable tools to investigate underlying pathologies of human vascular diseases and contributed to moving this area of research forward.

hiPSC-derived monocytes and macrophages

Human peripheral blood mononuclear cells (PBMCs) are widely used as a source of human monocytes for biomedical research. However, their availabilities are strictly limited by human tissue donation regulations and cell batches vary from different donors which restricts for their application in disease modeling *in vitro*. IPSDMs as described in this thesis represent an unlimited source of patient specific tissue resident macrophages-like cells which could be incorporated into *in vitro* disease models and organoid cultures. Previous differentiation protocols of IPSDMs mainly used a continuous harvesting strategy which lasts for several weeks with a high accumulated yield IPSDMs (Happle et al., 2018; Lachmann et al., 2015; van Wilgenburg et al., 2013). In **Chapter 2** and **3**, we developed a robust protocol for the induction of primitive erythro-myeloid progenitors (EMP)-like cells from hiPSCs, which could be further differentiated into hiPSC-derived monocytes (hiPSC-mono) and IPSDM subtypes. The differentiation process goes through several stages: lateral plate mesoderm, VEC+CD73-hemogenic endothelium, CD43+ hematopoietic progenitors (HPs), CD14+ monocytes and polarized macrophages. More than 90% purity of hiPSC-mono could be obtained

after magnetic purification in 15 days. As an advantage of the protocol, these hiPSC-mono can be either applied immediately or cryopreserved for later applications. Their post-thaw recovery rate could reach up to 50%. hiPSC-mono were still fully functional after cryopreservation proved by their high adhesion to ECs in a microfluidic flow assay previously established in our group (Halaidych et al., 2018a, 2018b). hiPSC-mono were more adhesive compared to blood monocytes (PB-mono), which correlated to their higher expression of VLA-4. This indicated a more activated state of hiPSC-mono than PB-mono, either due to their distinct development origin or different microenvironments they exposed to (*in vivo* vs *in vitro*). Thawed hiPSC-mono could be polarized to inflammatory (M1) and anti-inflammatory (M2) subtypes, manifested by their distinct gene expression and cytokines secretion profiles. IPSDMs were also characterized in various functional assays we established, where PBDMs were included for comparison. IPSDMs were fully functional regarding their high uptake of acetylated low-density lipoprotein (AcLDL), bacteria, apoptotic cells. Endocytic and efferocytotic activities were higher in IPSDMs than PBDMs, which was another indication of their primitive development origin as tissue resident macrophages (A-Gonzalez et al., 2017; Roberts et al., 2017).

The potential of macrophages in tumor immunotherapy has drawn considerable great attention and been intensively studied due to their high tumor phagocytosis activity (Chao et al., 2012; Gul and van Egmond, 2015; Weiskopf and Weissman, 2015). PBDMs were previously used to study the anti-tumor activities of blocking antibodies for the CD47-CD172a pathway. In **Chapter 2**, we described for the first time high tumor phagocytotic activity of IPSDMs in the presence of CD47 blocking antibody, which was comparable to PBDMs. This indicates potential also of IPSDMs in the development of new cancer immunotherapies and their application in candidate drugs screening *in vitro*.

The differentiation protocol and all functional assays described in **Chapter 2** were tested with three different hiPSC lines. Immune cells derived from different hiPSC lines and batches showed similar gene expression profiles and functional activities, indicating high reproducibility across lines. Compared to continuous harvesting methods, our single time harvesting protocol is shorter and more robust which is critical for the application of hiPSC-derivatives in disease modeling. The ability to be cryopreserved with preservation of function greatly facilitates downstream applications of hiPSC-mono, e.g. in disease modeling. However, this protocol is not suitable for transformation to bioreactors for mass production. Another disadvantage is that the purification step required for hiPSC-mono can be labor intensive and expensive. Besides, the extracellular matrix used for coating in this protocol including Matrigel and fetal calf serum (FCS) are animal derived and not defined, which could limit their application in terms of reproducibility in biomedical research.

Both **Chapter 2** and **3** focus on the myeloid cells derived from hiPSCs. **Chapter 2**

included detailed characterization for each stage along the differentiation. For instance, we measured the differentiation efficiency and quality of mesoderm cells, hemogenic endothelium, HPs, monocytes and IPSDMs across lines and batches. HPs on day 9 were shown to be multipotential and give rise not only to monocytes, but also erythrocytes and granulocytes. Their lymphocyte differentiation potential was not examined in our study, although a previous study using a comparable differentiation method for HPs showed that T lymphoid could also be generated from these HPs (Uenishi et al., 2014). In **Chapter 2**, we also performed phenotypic and functional characterization of hiPSC-mono and IPSDMs, where blood-mono and PBDMs were included as controls for comparison. **Chapter 3** described mainly the detailed experiment set up and protocols for the differentiation and functional assays related to **Chapter 2**. This detailed protocol could support and enhance the reproducibility of studies using hiPSC-derived myeloid cells in the field in general.

In summary, **Chapter 2** and **3** described a robust protocol to derive hiPSC-mono which could be cryopreserved and further differentiated into IPSDMs. Pro-inflammatory M1-IPSDMs and anti-inflammatory M2-IPSDMs could be further polarized. IPSDMs were phenotypically and functionally similar to PBDMs in many aspects. However, differences were also observed between IPSDMs and PBDMs, like their endocytosis and efferocytosis activities, suggesting a primitive development origin and tissue resident macrophage-like identities of these IPSDMs. This part of work in **Chapter 2** and **3** allows us to obtain adequate fully functional patient specific monocytes and macrophages from hiPSCs, which could be added into HHT1 disease models in future works.

hiPSC-ECs

ECs are a constitutive and integral part of the cardiovascular system and their dysfunction contributes to various of cardiovascular diseases. They are also play a key role in inflammation, which are responsible for the recruitment of leukocytes into the tissue. ECs show high degree of heterogeneity *in vivo*, and can be broadly classified into arterial, venous and lymphatic based on their location and functions. ECs from different organs also show organ specific characteristics. hiPSCs provided an unlimited source of patient-specific ECs which can be potentially used for disease modeling to reveal underlying disease pathology and for drug screening. Previously our group developed an efficient monolayer differentiation protocol of CD31+ ECs from hiPSCs. These ECs were functional as evidenced by the formation of primary vascular plexus *in vitro* and their incorporation into zebrafishes' vasculature after transplantation (Orlova et al., 2014b, 2014a).

Cardiovascular cells and related diseases are one of the major research interests of our lab. Cardiomyocytes and ECs are two major cell types in the heart. They interact through both physical signals and secretion of paracrine, autocrine, endocrine factors,

which contributes to maintenance of cardiac homeostasis and responses to hypertrophic stimuli (Tirziu et al., 2010). It had been shown previously that ECs and cardiomyocytes have the same development origin, arising from *Mesp1*⁺ progenitors in primitive streak, which later migrate to the cardiac field of lateral plate mesoderm (cardiac mesoderm). However, it is still not clear how and when ECs and cardiomyocytes segregate from their common multipotent precursors. Previously our group developed a co-differentiation system of ECs and cardiomyocytes from hiPSCs (Giacomelli et al., 2017). ECs derived from this protocol expressed high levels of cardiac genes *MEOX2*, *GATA4*, *GATA6* and *ISL1*, indicating a cardiac endothelial identity (Giacomelli et al., 2017). In **Chapter 4** of this thesis, we took advantage of this protocol to study the development path and transcriptional control of cardiac mesoderm derived endothelial cells and myocardial cells from hiPSCs. In this chapter, single cell RNA sequencing (scRNAseq) was performed for the co-differentiation system on day 6 when both early multipotent progenitors and committed cell lineages were present. The whole population could be divided into three clusters: *MESP1*⁺ cardiac mesoderm (CM), *CDH5*⁺ endothelial progenitors (EPs) and *MYL4*⁺ cardiac progenitors (CPs). Unbiased pseudotime analysis showed a common development origin of EPs and CPs from CM, which correlated with previous findings *in vivo* that both ECs and cardiomyocytes in the heart developed from *MESP1*⁺ progenitors. Interestingly, we observed *ETV2* expression in both CP and EP populations. *ETV2* was previously identified as a master regulator of development for the hemangiogenic lineages (Ferdous et al., 2009; Lee et al., 2008; Val et al., 2008). Its overexpression could directly reprogram human fibroblasts into EC-like cells (Morita et al., 2015). To characterize the expression and role of *ETV2* during EC and cardiomyocyte development, an *ETV2*^{mCherry} reporter hiPSC line was generated using CRISPR/Cas9 system. As expected, the EPs expressed the highest level of *ETV2*, although it was also expressed in a subpopulation of the CPs. We were interested in the expression and function of *ETV2* during cardiomyocytes development as no related studies had been reported to date. To understand the identity of these *ETV2*⁺ cells in CPs, we isolated both *ETV2*⁺ EC (double positive, DP) and *ETV2*⁺ non-EC (single positive, SP) populations on different days of differentiation and carried out bulk RNAseq analysis. DPs upregulated large number of EC-specific and NOTCH signaling pathway-related genes from day 4 to day 8, indicating a gradual maturation process of ECs. Interestingly, SPs acquired a cardiomyocyte identity during differentiation evidenced by increased expression of cardiomyocyte function-related genes. Thus, SP cells appeared to represent progenitors of cardiomyocytes. Most importantly, SP isolated on day 7 could be directly differentiated into contracting cardiomyocytes with more than 50% efficiency, while only a minor population (~5%) of ECs could be derived from these cells, providing direct evidence of the commitment of myocardial fate in SPs. Another question we were trying to answer in this chapter was whether *ETV2* also plays a role

during early cardiomyocyte differentiation. ETV2+ from CPs readily acquired a cardiac identity. ETV2+ cells from EPs showed a short burst of ETV2 expression, while ETV2+ CPs expressed a steady and lower level of ETV2. A much higher percentage of ETV2+ cells were also observed in EPs than CPs. *ETV2* was also expressed in EPs for a longer period of time compared to CPs. Our results suggested that segregation of cardiac endothelial and myocardial lineages may be determined by an ETV2 expression level threshold, as well as the duration of ETV2 expression.

In summary, our work in **Chapter 4** described a time-course of RNAseq in bulk and single cell populations during the co-differentiation of EC and cardiomyocyte from hiPSCs. Transcriptional dynamics during the specification and maturation of cardiac and ECs during differentiation were characterized based on scRNAseq and bulk RNAseq results, which correlated well with each other. Moreover, we report for the first time that cardiomyocytes could also be derived from ETV2+ precursors which were previously thought to be only progenitors for hemangiogenic lineages. Our study helped to reveal more fully the *in vivo* differentiation process of cardiac mesoderm derived ECs and cardiomyocytes from multipotent CPCs in human development. Overall, this chapter helped provide more insight into the developmental biology of ECs and cardiomyocytes, which may be essential for applications in the *in vitro* modeling of cardiovascular diseases.

One limitation of our work in **Chapter 4** is that although the cardiac mesoderm derived ECs showed a heart specific signature, we did not observe more fully matured and specialized intramyocardial ECs or endocardial cells among the hiPSC-derived ECs. Recently, a scRNAseq study had been carried out on human embryonic heart which revealed two distinct EC populations, representing intramyocardial and endocardial EC identities respectively (Asp et al., 2019). We therefore hypothesized that environmental cues may play an essential role in the acquisition of tissue-specific (intramyocardial or endocardial) identities of hiPSC-derived ECs. Although work in **Chapter 4** revealed the developmental process of ECs and cardiomyocytes, and roles of ETV2 in this process, we nevertheless believe that a combination of this chapter with more work related to the characterization of tissue specific identities of hiPSC-derived ECs would further expand the novelty and importance of this work. In recent work not shown here, we generated ECs from both paraxial mesoderm and cardiac mesoderm precursors and made cardiac microtissues from both types of ECs using a protocol we previously published (Giacomelli et al., 2017). ECs before and after multicellular microtissue culture, as well as ECs from different mesodermal environments were compared based on their transcriptome profile. Our preliminary results indicate that both developmental origin (cardiac vs paraxial mesoderm) and cardiac specific environment (microtissue) guide and promote the further maturation and acquisition of heart tissue-specific (intramyocardial or endocardial) identities of hiPSC-derived ECs. For this part of the

work (not included in this thesis), we have completed most experiments and the data analysis is ongoing through collaborations. This will be combined and published later together with data in **Chapter 4**.

Modeling of HHT1 using hiPSC-derivatives

HHT1 is an autosomal dominant genetic disease caused by the defect of TGF β signaling pathway due to the mutation of endoglin. Although EC is the major cell type being affected and contribute to disease phenotypes of HHT1, myeloid cells including monocytes and macrophages have been shown to be closely related to the pathologies of this disease. Both HHT1 patients and *ENG* knockout mice tend to develop more severe inflammation than healthy controls (Girod et al., 2007; Jerkic et al., 2010; Rossi et al., 2013). Functions of myeloid cells that carry *ENG* mutation were also impaired (van Laake et al., 2006; Ojeda-Fernandez et al., 2016; Post et al., 2010). Besides, it had been found that inflammation was an important trigger for the development of HHT1. Thus, we concluded that both ECs and myeloid cells need to be included in order to establish an *in vitro* model of HHT1. Although mouse models have been widely used to study HHT1, both complete knockout and conditional knockout mice fail to fully recapitulate HHT1 phenotypes in patients (Bourdeau et al., 1999, 2000; Torsney et al., 2003; Tual-Chalot et al., 2015). In comparison, hiPSC models had several advantages including patient specific genetic background, unlimited cell source, less time consuming and easier for genome editing but their use in modelling the disease in humans has not yet been described. In **Chapter 5**, we aimed to establish an *in vitro* model of HHT1 using patient specific hiPSC-derived endothelial and myeloid cells. Multiple hiPSC lines were generated from HHT1 patients that carried different *ENG* mutations. Unexpectedly, one patient was identified as mosaic with the *ENG* mutation being present only in some but not all tissues. Therefore, we could generate a pair of isogenic hiPSC lines with and without the *ENG* mutation from different somatic tissues of this patient. ECs were successfully derived from all of these hiPSC lines. ECs from disease lines showed clear reduction of *ENG* and unaffected expression of other EC specific makers. These mutated hiPSC-ECs responded to BMP9 and transforming growth factor- β (TGF β) stimulation normally, behaving exactly as (isogenic) wild type ECs. In addition, cell barrier function, migration rate and ability to form 2D sprouts were also not affected in the mutated ECs. To better recapitulate the *in vivo* condition, however, we then established a 3D vascular model by coculturing of ECs and pericytes in a microfluidic chip. Using this model, we found that the ability of HHT1 ECs to form a perfusable microvascular network was severely compromised, which was partially attributable to their lower cell proliferation in 3D culture. Inflammatory responses of HHT1 ECs were enhanced when they were challenged by TNF α in the presence of BMP9, while in the same condition, their barrier function was impaired compared to WT ECs. These disease

phenotypes were only observed in the presence of the endoglin ligand BMP9. These results suggest that impairment of BMP9-ENG signaling could exacerbate inflammation, which correlated with the observation of more serious infections in HHT1 patients and mouse models (Girod et al., 2007; Jerkic et al., 2010).

To reveal the disease mechanism HHT1 using the hiPSC model, RNAseq analysis was performed for HHT1 hiPSC-ECs cultured in different conditions. *ENG*^{+/-} hiPSC-ECs upregulated more inflammatory genes compared to WT ECs upon TNF α stimulation. Both WT and mutated hiPSC-ECs could respond to BMP9 stimulation, although SMAD2/3 was higher and SMAD1/5, WNT pathway genes were lower in *ENG*^{+/-} hiPSC-ECs compared to WT. Interestingly, TNF α stimulation further increased these differences between HHT1 and WT hiPSC-ECs upon BMP9 treatment. Previous studies showed that WNT signaling could interplay with TGF β /BMP pathway (Attisano and Wrana, 2013; Fuentealba et al., 2007) and was dysregulated in HHT1 patients (Tørring et al., 2015), which agreed with our RNAseq results. Notably, we found activation of WNT pathway by CHIR99021 could rescue the impaired vasculature formation of HHT1 hiPSC-ECs.

In summary, work in **Chapter 5** developed an *in vitro* HHT1 3D model using patient-derived isogenic hiPSC lines. *ENG*^{+/-} hiPSC-ECs performed similarly to WT ECs in many aspects when cultured in 2D conditions without extra challenges of inflammation and BMP9. However, impaired vasculature formation by HHT1-ECs was observed in a 3D culture system. Barrier functions and TGF β /BMP and WNT pathways were also dysregulated in mutated ECs upon inflammation and BMP9 activation. The HHT1 hiPSC model established in this chapter can be used for the study not only of hiPSC-EC biology, but also of the role of WNT signaling pathways and inflammation in HHT1 pathology. This work provides new insights into the disease mechanism underlying HHT1 which could lay the foundation for drug discovery and other pre-clinical applications in the future. HHT1 hiPSC-derived myeloid cells will be characterized in more detail in the future and incorporated into the disease model developed in this chapter. This is further discussed in **Future perspectives**. This Chapter will eventually be divided into two parts and published separately. Both manuscripts are in preparation. One of the manuscripts is a report of the mosaic HHT1 patient and the derivation of isogenic HHT1 hiPSC lines from this patient. Characterizations of hiPSC-derived myeloid and endothelial cells derived from these isogenic lines will also be included in this manuscript in the context of discussing when he became mosaic in development. Another manuscript is focusing on modeling HHT1 using hiPSC-derived 3D microvasculature model and underlying disease mechanisms revealed using this model. Experimental work is almost completed and both manuscripts are in preparation for submission in the coming months after finishing of this thesis.

Modeling of PHE using hiPSC-derivatives

In **Chapter 6 and Appendix Chapter 6**, hiPSC-ECs were used for modeling of another disease called Pseudomyogenic hemangioendothelioma (PHE) which is a chromosomal translocation-driven tumor with vascular features. *SERPINE1-FOSB* translocation was successfully introduced into a control hiPSC line using CRISPR/Cas9 system. No off-target effects were observed by whole genome sequencing. ECs were successfully differentiated from the targeted hiPSC line, and showed upregulated *FOSB* expression, reflecting the notion that PHE may be a vascular specific tumor. An infiltrative pattern of hiPSC-ECs^{*SERPINE1-FOSB*} was observed after injection into mice, resembling certain aspects the PHE phenotype observed in patients (Hornick and Fletcher, 2011). Vessels formed by hiPSC-ECs^{*SERPINE1-FOSB*} in mice were less organized, more invasive and showed higher fibrin thrombi than hiPSC-ECs^{WT}. In addition, lower cell barrier function was also observed with mutated ECs. This correlated with aberrant thrombi formation (conglomeration of fibrin and platelets, containing red blood cells) in the mice transplanted with hiPSC-ECs^{*SERPINE1-FOSB*}. My focus in the study was the transcriptomic analysis of hiPSC-ECs with and without *SERPINE1-FOSB* translocation. Although it is already known that the *FOSB* overexpression caused by the translocation is the major drive of the tumorigenesis, the overview of all dysregulated signaling pathways and their correlation with disease phenotypes are still missing. Thorough comparison of the transcriptome profiles of WT and mutated hiPSC-ECs could give valuable insight about the pathology of PHE. With the whole transcriptome data obtained from control and mutated hiPSC-ECs, I first examined Differentially Expressed Genes (DEGs) using an available bioinformatic tool (edgeR), which allowed us to identify dysregulated genes affected by *SERPINE1-FOSB* translocation in ECs. Next, in order to understand functions of these dysregulated genes and signaling pathways they involved, Gene ontology (GO) and KEGG pathway enrichment analyses were performed for these DEGs identified. This showed genes related to TGF-beta signaling, adhesion, metabolism, inflammatory response, angiogenesis and endothelial cell migration were upregulated in hiPSC-ECs^{*SERPINE1-FOSB*}. In addition, I generated comprehensive gene-gene interaction networks for genes abnormally expressed in hiPSC-ECs^{*SERPINE1-FOSB*} using Ingenuity Pathway Analysis (IPA), which revealed the causal relationship between *FOSB* overexpression and its target genes related to cancer, cellular movement and growth, and the TGF- β signaling pathway. My work also indicated direct regulation of *SERPINE1* by *FOSB*, as well as self-regulatory effects of both genes, which further activated cellular growth and proliferation and cancer processes directly or indirectly through the activation of the TGF- β signaling pathway. My work in Appendix Chapter 6 mainly complemented the transcriptomic analysis of Chapter 6. These extra bioinformatic analyses provided more insights into the disease mechanisms of PHE and predicted two candidate drugs which can be potentially used for the treatment of this disease. Overall, my work related to the transcriptomic analysis in this project provided explanations at the molecular level

for many aberrant features of hiPSC-ECs^{SERPINE1-FOSB} observed *in vitro* and *in vivo* and provided rationale for the development of targeted treatment strategies for inoperable multifocal PHE patients. In summary, the work in **Chapter 6 and Appendix Chapter 6** established an hiPSC model for the study of chromosomal translocation-induced vascular disease PHE, which gave an insight into the tumorigenesis of PHE and helped to elucidate underlying pathologies of specific rare cancer subtypes caused by specific gene fusion. Work in **Chapter 6** has been deposited in BioRxiv and also been submitted for peer review.

Future perspectives

Modeling genetic diseases using hiPSC derivatives provides new avenues for the study of disease pathologies and screening of candidate drugs. Nowadays hiPSC lines can be routinely generated in many research labs all over the world and protocols for the induction of different functional cell types are reported continuously. Focus now though, is not just obtaining generic exemplars of different cell types but on the tissue specific variants. ECs from different organs show high heterogeneity in terms of their morphology, structure, barrier function, angiogenic potential, angiocrine/endocrine profile and metabolic rates. The complexity of EC phenotypes came from both intrinsic EC properties and programming by their surrounding environment (Reiterer and Branco, 2019). RNAseq and scRNAseq of ECs from different tissues/organs could provide in-depth profiles of tissue specific characteristics of ECs in different organs, thus help in establishing better differentiation protocols or culture conditions in the future. Recently, RNAseq analysis of brain, lung and heart endothelial cells showed specific identities of the endothelium in each organ (<http://www.rehmanlab.org/ribo>) (Jambusaria et al., 2020). To faithfully recapitulate disease phenotypes in tissue- or organs *in vivo*, more complex cell culture systems may be required for some diseases (eg. HHT1), where the phenotype might not be autonomous to one target cell type. Organoids mimicking different tissues or organs have already been established from hiPSCs, and include neural, gastrointestinal, liver, kidney, lung and cardiac organoids (Rowe and Daley, 2019). Most recently, a 3D human blood vessel organoid was also generated from hiPSCs through self-organizing of hiPSC-derived ECs and pericytes, which formed stable, perfusable vascular trees after transplantation into mice (Wimmer et al., 2019a, 2019b). Some of these organoids have been applied for the investigation of new therapeutic approaches for different diseases. A challenge for the application hiPSC disease models is the immature phenotype of hiPSC-derivatives compared to their primary counterparts *in vivo*. For example, hiPSC-ECs showed aberrant responses to the pro-inflammatory molecule TNF- α , as E-selectin or VCAM-1 were only upregulated in primary ECs but not in hiPSC-ECs under the same conditions *in vitro* (Rosa et al., 2019). More effort is required for the optimization of differentiation protocols or culture

conditions to obtain mature phenotypes of hiPSC-derivatives. Introduction of flow and shear stress into the ECs culture environment is a possible solution, given the essential role of mechanotransduction on vascular development (Hahn and Schwartz, 2009). Another challenge is the reproducibility of protocols across different hiPSC lines and heterogeneity in the emerging derivatives. On the one hand, genetic heterogeneities could affect the efficiency of the differentiation protocol and quality of cells produced; On the other hand, background-related variations could be confounders of the disease-relevant phenotypic changes caused by the genetic mutation of interest. Gene correction of patient-derived hiPSC lines using advanced genome editing technologies provides a powerful control which can be applied for distinguishing pathologically relevant phenotypes from other gene background-related variations-caused phenotypes. In the groundwork for modelling HHT1 in this thesis, we mainly focused on an isogenic pair of hiPSC lines that were generated from different tissues of a mosaic HHT1 patient who carried the c.1678C>T mutation. Other HHT1 hiPSC lines mentioned in this study, including c.1084_1085del and c.689+2T>C, mutated hiPSC lines, are still need to be corrected by CRISPR/Cas9 gene editing in order to obtain their isogenic healthy controls.

Blood vessels are essential for nutrients and oxygen supply and play an important instructive role during organ development. Therefore, including an EC component and functional vasculature would be an important next step for the generation of complex and functional organoids from hiPSCs (Passier et al., 2016). Aside from ECs, mural cells (pericytes and vascular smooth muscle cells (vSMCs)) are also critical for the generation of functional vasculature *in vitro*. Dysregulated interactions between EC and mural cells was found to underlie many pathological conditions including HHT1. For instance, it had been shown that defective TGF β /BMP signaling pathway in the HHT1 mouse model resulted in impaired vSMC development and mural cells recruitment and coverage, which lead to the fragile blood vessels and hemorrhage (Lebrin et al., 2010). In **Chapter 5**, we generated 3D vasculature for HHT1 through self-organization of hiPSC-ECs and primary human vSMCs. These self-organized vascular networks formed lumens that could be perfused with medium. In the future, this vasculature model could be further characterized in several aspects. First, the integrity and barrier function of the lumenized vasculature could be tested by connecting a microfluidic pump to the 3D microfluidic chip to introduce a steady fluid flow in the vasculature. Leakage assays could be applied to check vessel integrity and barrier function. Another interesting experiment to do would be testing the recruitment of leukocytes by these hiPSC-derived vasculatures in inflammatory conditions, which is an important aspect of blood vessels behavior *in vivo*. Specifically, monocytes could be perfused through the hiPSC-derived vasculature by connecting a microfluidic pump. Before flow through of monocytes, hiPSC-ECs in the chip should be challenged by inflammatory stimulus like TNF- α in order

to upregulate their expression of adhesion molecules. Monocytes (labeled with fluorescent dye) should be captured by ECs in the chip and their transmigration through the EC lumen could be monitored by time-lapse with a high-speed fluorescent microscope. In addition, hiPSC-mono derived using the protocol described in **Chapter 2 and 3**, could also be a source of leukocytes in this flow assay; it would be interesting to investigate their adhesion and transmigration behavior in the 3D hiPSC vasculature.

Inflammation is also closely related to the onset of many diseases such as ischemic heart disease, stroke, cancer, diabetes mellitus, chronic kidney disease, auto-immune and neurodegenerative diseases (Furman et al., 2019). We and others found that inflammatory cells, especially myeloid cells were closely related to the development of HHT1 (van Laake et al., 2006; Ojeda-Fernandez et al., 2016; Rossi et al., 2015). In these cases, it would be beneficial to include immune cells in hiPSC disease models, in order to recapitulate the inflammation component and investigate the effect of immune cells on disease phenotypes. Monocytes and macrophages play an essential role in inflammation. In **Chapter 2 and 3**, we established a robust protocol to derive monocytes and macrophages from hiPSCs and performed detailed functional characterization of these cells. This showed that the IPSDMs we derived were more similar to primitive rather than definitive macrophages. Regarding to the differentiation protocol, it would be possible to optimize it further in some respects. First, the differentiation procedure as such is relatively expensive due to the large volumes of reagents needed, most importantly the growth factor component. The requirement for and optimal concentration of growth factors could be further examined and some reagents at least replace by small molecules. For instance, Thrombopoietin (TPO) was used to induce the hematopoietic differentiation from hemogenic endothelium at a high concentration. However, it has not been tested whether it is necessary for the myeloid lineage specification. Although optimization could be time consuming and labor intensive, it may reduce the cost and time required for differentiation in the long term. Second, the differentiation efficiency of monocytes from HPCs was ~50% in our protocol, which could potentially be improved in order to avoid the purification step and intrinsic loss of cells from the protocol required for monocytes. Third, hiPSC-monocytes on differentiation day 15 already started to show an activated phenotype, as they were more adhesive and larger than blood-monocytes. Therefore, it would worth further optimizing monocyte induction and culture conditions to obtain a less activated phenotype. Last but not least, although IPSDMs were close to primitive macrophages based on their functional activities, direct evidence for their developmental trajectory is still needed. For example, the requirement of MYB expression during the differentiation process of IPSDMs should be examined, as MYB was previously found to be specifically required during definitive (third wave) differentiation (Lieu and Reddy, 2009; Schulz et al., 2012) but not primitive (first and second wave) hematopoiesis

(Mucenski et al., 1991; Schulz et al., 2012).

As a next step of the work in this thesis, monocytes and macrophages derived from HHT1 hiPSCs could be added to the existing disease model to better recapitulate the disease phenotypes. On the one hand, myeloid cells derived from isogenic HHT1 hiPSC lines with and without *ENG* mutation could be compared in 2D culture condition to study the effect of *ENG* mutation on their characteristics and functions, like their inflammatory responses and adhesion to ECs. On the other hand, due to the close association between tissue resident macrophages and angiogenesis (**section 1.2.3** of this thesis), it would be interesting to include IPSDMs as an extra component of the 3D vasculature model established in **Chapter 5**. Hopefully, more severe and perhaps new aspects of disease phenotypes will be observed during inflammation in the presence of immune cells in the system. Bulk and single cell RNAseq could be used for the identification of dysregulated signaling pathways, multicellular interactions and other underlie disease mechanisms of HHT1. Except for HHT1, hiPSC-derived myeloid cells could also potentially be used for other disease modeling or generation of complex organoids *in vitro*. For instance, macrophages could be incorporated into the 3D cardiac microtissues which was previously established in our lab, to better mimic and study the cardiac inflammatory responses and related cardiac diseases using this system.

Regarding to the PHE study in **Chapter 6 and Appendix Chapter 6**, through my RNAseq analysis of ECs derived from disease hiPSCs line that carry the translocation mutation, multiple dysregulated pathways were revealed, such as altered TGF-beta signaling, adhesion, metabolism, inflammatory response, angiogenesis and endothelial cells migration. These pathways are known to be related to cancer and correlated to disease phenotypes observed in other cellular models we established. Our RNAseq analysis contributed to explaining the disease pathology of PHE at the molecular level and provided the rationale for the development of targeted treatment strategies for this vascular tumor. Notably, from our RNAseq analysis, MAPK signaling and PDGFRA and -B were found to be upregulated by the *SERPINE1-FOSB* translocation in mutated ECs. A previous study had shown that the multi-tyrosine kinase inhibitor telatinib could be a highly specific treatment for patients with multifocal unresectable PHE (van IJzendoorn et al., 2018). Thus, it would be an interesting experiment to test the effect of this drug on our PHE-hiPSC cellular models to see whether it has a positive effect on the disease phenotypes we observed *in vitro* and *in vivo*. Additionally, PI3K-Akt signaling pathway was also identified among these upregulated pathways by the chromosomal fusion in mutated ECs. This observation from our RNAseq analysis provides more rationale for the application of mTOR inhibitors as a specific treatment strategy of PHE which would be worth further investigated in the future.

In summary, this thesis explored the application of hiPSC-derived myeloid and endothelial cells in disease modeling and provided valuable insights of HHT1 and PHE

pathologies through the establishment of a hiPSC-derived vascular models. This work provided key cell sources and laid a firm foundation for the related future studies within and outside our research group.

REFERENCES

- A-Gonzalez, N., Quintana, J.A., García-Silva, S., Mazariegos, M., de la Aleja, A., Nicolás-Ávila, J.A., Walter, W., Adrover, J.M., Crainiciuc, G., Kuchroo, V.K., et al. (2017). Phagocytosis imprints heterogeneity in tissue-resident macrophages. *J Exp Medicine* **214**, 1281–1296.
- Asp, M., Giacomello, S., Larsson, L., Wu, C., Fürth, D., Qian, X., Wårdell, E., Custodio, J., Reimegård, J., Salmén, F., Österholm, C., Ståhl, P., Sundström, E., Åkesson, E., Bergmann, O., Bienko, M., Månsson-Broberg, A., Nilsson, M., Sylvén, C., Lundeberg, J. (2019). A Spatiotemporal Organ-Wide Gene Expression and Cell Atlas of the Developing Human Heart. *Cell* **179**(7), 1647–1660.e19.
- Attisano, L., and Wrana, J.L. (2013). Signal integration in TGF- β , WNT, and Hippo pathways. *F1000prime Reports* **5**, 17.
- Bourdeau, A., Dumont, D., and Letarte, M. (1999). A murine model of hereditary hemorrhagic telangiectasia. *J Clin Invest* **104**, 1343–1351.
- Bourdeau, A., Faughnan, M., and Letarte, M. (2000). Endoglin-deficient mice, a unique model to study hereditary hemorrhagic telangiectasia. *Trends Cardiovas Med* **10**, 279–285.
- Buchrieser, J., James, W., and Moore, M. (2017). Human Induced Pluripotent Stem Cell-Derived Macrophages Share Ontogeny with MYB-Independent Tissue-Resident Macrophages. *Stem Cell Rep* **8**, 334–345.
- Chao, M.P., Weissman, I.L., and Majeti, R. (2012). The CD47–SIRP α pathway in cancer immune evasion and potential therapeutic implications. *Curr Opin Immunol* **24**, 225–232.
- Dou, D.R., Calvanese, V., Sierra, M.I., Nguyen, A.T., Minasian, A., Saarikoski, P., Sasidharan, R., Ramirez, C.M., Zack, J.A., Crooks, G.M., et al. (2016). Medial HOXA genes demarcate haematopoietic stem cell fate during human development. *Nat Cell Biol* **18**, 595–606.
- Ferdous, A., Caprioli, A., Iacovino, M., Martin, C.M., Morris, J., Richardson, J.A., Latif, S., Hammer, R.E., Harvey, R.P., Olson, E.N., et al. (2009). Nkx2–5 transactivates the Ets-related protein 71gene and specifies an endothelial/endocardial fate in the developing embryo. *Proc National Acad Sci* **106**, 814–819.
- Fuentealba, L., Eivers, E., Ikeda, A., Hurtado, C., Kuroda, H., Pera, E., and Robertis, D.E. (2007). Integrating patterning signals: Wnt/GSK3 regulates the duration of the BMP/Smad1 signal. *Cell* **131**, 980–993.
- Furman, D., Campisi, J., Verdin, E., Carrera-Bastos, P., Targ, S., Franceschi, C., Ferrucci, L., Gilroy, D., Fasano, A., Miller, G., et al. (2019). Chronic inflammation in the etiology of disease across the life span. *Nat Med* **25**, 1822–1832.
- Giacomelli, E., Bellin, M., Sala, L., van Meer, B.J., Tertoolen, L.G., Orlova, V.V., and Mummery, C.L.

- (2017). Three-dimensional cardiac microtissues composed of cardiomyocytes and endothelial cells co-differentiated from human pluripotent stem cells. *Development* **144**, 1008–1017.
- Ginhoux, F., and Jung, S. (2014). Monocytes and macrophages: developmental pathways and tissue homeostasis. *Nat Rev Immunol* **14**, 392–404.
- Girod, S., Giraud, S., Decullier, E., Lesca, G., Cottin, V., Faure, F., Merrot, O., Saurin, J., Cordier, J., and Plauchu, H. (2007). Hemorrhagic Hereditary Telangiectasia (Rendu-Osler Disease) and Infectious Diseases: An Underestimated Association. *Clin Infect Dis* **44**, 841–845.
- Gul, N., and van Egmond, M. (2015). Antibody-Dependent Phagocytosis of Tumor Cells by Macrophages: A Potent Effector Mechanism of Monoclonal Antibody Therapy of Cancer. *Cancer Res* **75**, 5008–5013.
- Hahn, C., and Schwartz, M. (2009). Mechanotransduction in vascular physiology and atherogenesis. *Nat Rev Mol Cell Bio* **10**, 53–62.
- Halaidych, O., Freund, C., van den Hil, F., Salvatori, D., Riminucci, M., Mummery, C., and Orlova, V. (2018a). Inflammatory Responses and Barrier Function of Endothelial Cells Derived from Human Induced Pluripotent Stem Cells. *Stem Cell Rep* **10**, 1642–1656.
- Halaidych, O., van den Hil, F., Mummery, C., and Orlova, V. (2018b). Microfluidic Assay for the Assessment of Leukocyte Adhesion to Human Induced Pluripotent Stem Cell-derived Endothelial Cells (hiPSC-ECs). *J Vis Exp*.
- Happle, C., Lachmann, N., Ackermann, M., Mirenska, A., Göhring, G., Thomay, K., Mucci, A., Hetzel, M., Glomb, T., Suzuki, T., et al. (2018). Pulmonary Transplantation of Human Induced Pluripotent Stem Cell-derived Macrophages Ameliorates Pulmonary Alveolar Proteinosis. *Am J Resp Crit Care* **198**, 350–360.
- Hornick, J.L., and Fletcher, C.D. (2011). Pseudomyogenic Hemangioendothelioma. *Am J Surg Pathology* **35**, 190–201.
- van Ijendoorn, D.G., Sleijfer, S., Gelderblom, H., Eskens, F.A., van Leenders, G.J., Suzhai, K., and Bovée, J.V. (2018). Telatinib Is an Effective Targeted Therapy for Pseudomyogenic Hemangioendothelioma. *Clin Cancer Res* **24**, 2678–2687.
- Ivanovs, A., Rybtsov, S., Ng, E., Stanley, E., Elefanty, A., and Medvinsky, A. (2017). Human haematopoietic stem cell development: from the embryo to the dish. *Development* **144**, 2323–2337.
- Jambusaria, A., Hong, Z., Zhang, L., vastava, S., Jana, A., Toth, P.T., Dai, Y., Malik, A.B., and Rehman, J. (2020). Endothelial heterogeneity across distinct vascular beds during homeostasis and inflammation. *Elife* **9**, e51413.
- Jerkic, M., Peter, M., Ardelean, D., Fine, M., Konerding, M., and Letarte, M. (2010). Dextran sulfate sodium leads to chronic colitis and pathological angiogenesis in Endoglin heterozygous mice. *Inflamm Bowel Dis* **16**, 1859–1870.
- van Laake, L.W., van den Driesche, S., Post, S., Feijen, A., Jansen, M.A., Driessens, M.H., Mager, J.J., Snijder, R.J., Westermann, C.J., Doevendans, P.A., et al. (2006). Endoglin Has a Crucial

- Role in Blood Cell–Mediated Vascular Repair. *Circulation* **114**, 2288–2297.
- Lachmann, N., Ackermann, M., Frenzel, E., Liebhaber, S., Brenig, S., Happle, C., Hoffmann, D., Klimenkova, O., Lüttge, D., Buchegger, T., et al. (2015). Large-Scale Hematopoietic Differentiation of Human Induced Pluripotent Stem Cells Provides Granulocytes or Macrophages for Cell Replacement Therapies. *Stem Cell Rep* **4**, 282–296.
- Lebrin, F., n, S., Raymond, K., Martin, S., van den Brink, S., Freitas, C., Bréant, C., Mathivet, T., Larrivée, B., Thomas, J.-L., et al. (2010). Thalidomide stimulates vessel maturation and reduces epistaxis in individuals with hereditary hemorrhagic telangiectasia. *Nat Med* **16**, 420–428.
- Lee, D., Park, C., Lee, H., Lugus, J.J., Kim, S., Arentson, E., Chung, Y., Gomez, G., Kyba, M., Lin, S., et al. (2008). ER71 Acts Downstream of BMP, Notch, and Wnt Signaling in Blood and Vessel Progenitor Specification. *Cell Stem Cell* **2**, 497–507.
- Lieu, Y.K., and Reddy, P.E. (2009). Conditional c-myb knockout in adult hematopoietic stem cells leads to loss of self-renewal due to impaired proliferation and accelerated differentiation. *Proc National Acad Sci* **106**, 21689–21694.
- Morita, R., Suzuki, M., Kasahara, H., Shimizu, N., Shichita, T., Sekiya, T., Kimura, A., Sasaki, K., Yasukawa, H., and Yoshimura, A. (2015). ETS transcription factor ETV2 directly converts human fibroblasts into functional endothelial cells. *Proc National Acad Sci* **112**, 160–165.
- Mucenski, M., McLain, K., Kier, A., Swerdlow, S., Schreiner, C., Miller, T., Pietryga, D., Scott, W., and Potter, S. (1991). A functional c-myb gene is required for normal murine fetal hepatic hematopoiesis. *Cell* **65**, 677–689.
- Ojeda-Fernandez, L., Recio-Poveda, L., Aristorena, M., Lastres, P., Blanco, F., Sanz-Rodriguez, F., Gallardo-Vara, E., de las Casas-Engel, M., Corbi, A., Arthur, H., et al. (2016). Mice Lacking Endoglin in Macrophages Show an Impaired Immune Response. *Plos Genet* **12**.
- Orlova, V., van den Hil, F., Petrus-Reurer, S., Drabsch, Y., Dijke, T.P., and Mummery, C. (2014a). Generation, expansion and functional analysis of endothelial cells and pericytes derived from human pluripotent stem cells. *Nat Protoc* **9**, 1514–1531.
- Orlova, V., Drabsch, Y., Freund, C., Petrus-Reurer, S., van den Hil, F., Muenthaisong, S., Dijke, P., and Mummery, C. (2014b). Functionality of endothelial cells and pericytes from human pluripotent stem cells demonstrated in cultured vascular plexus and zebrafish xenografts. *Arteriosclerosis Thrombosis Vasc Biology* **34**, 177–186.
- Passier, R., Orlova, V., and Mummery, C. (2016). Complex Tissue and Disease Modeling using hiPSCs. *Cell Stem Cell* **18**, 309–321.
- Post, S., Smits, A., van den Broek, A., Sluijter, J., Hoefer, I., Janssen, B., Snijder, R., Mager, J., Pasterkamp, G., Mummery, C., et al. (2010). Impaired recruitment of HHT-1 mononuclear cells to the ischaemic heart is due to an altered CXCR4/CD26 balance. *Cardiovasc Res* **85**, 494–502.
- ram, G., Tan, J., Islam, I., Rufaihah, A., and Cao, T. (2015). Efficient differentiation of human embryonic stem cells to arterial and venous endothelial cells under feeder- and serum-free

- conditions. *Stem Cell Res Ther* 6, 43.
- Reiterer, M., and Branco, C.M. (2019). Endothelial cells and organ function: applications and implications of understanding unique and reciprocal remodelling. *Febs J*.
- Roberts, A., Lee, B., Deguine, J., John, S., Shlomchik, M., and Barton, G. (2017). Tissue-Resident Macrophages Are Locally Programmed for Silent Clearance of Apoptotic Cells. *Immunity* 47, 913-927 e6.
- Rosa, S., Praça, C., Pitrez, P., Gouveia, J.P., Aranguren, X., Ricotti, L., and Ferreira, S.L. (2019). Functional characterization of iPSC-derived arterial- and venous-like endothelial cells. *Sci Rep-Uk* 9, 3826.
- Rossi, E., Sanz-Rodríguez, F., Eleno, N., Düwell, A., Blanco, F.J., Langa, C., Botella, L.M., Cabañas, C., Lopez-Novoa, J.M., and Bernabeu, C. (2013). Endothelial endoglin is involved in inflammation: role in leukocyte adhesion and transmigration. *Blood* 121, 403–415.
- Rossi, E., Lopez-Novoa, J.M., and Bernabeu, C. (2015). Endoglin involvement in integrin-mediated cell adhesion as a putative pathogenic mechanism in hereditary hemorrhagic telangiectasia type 1 (HHT1). *Frontiers Genetics* 5, 97.
- Rowe, G.R., and Daley, G.Q. (2019). Induced pluripotent stem cells in disease modelling and drug discovery. *Nat Rev Genet* 20, 377–388.
- Schulz, C., Perdiguero, E., Chorro, L., Szabo-Rogers, H., Cagnard, N., Kierdorf, K., Prinz, M., Wu, B., Jacobsen, S.W., Pollard, J.W., et al. (2012). A lineage of myeloid cells independent of Myb and hematopoietic stem cells. *Science* 336, 86–90.
- Takata, K., Kozaki, T., Lee, C., Thion, and Otsuka, M. (2017). Induced-Pluripotent-Stem-Cell-Derived Primitive Macrophages Provide a Platform for Modeling Tissue-Resident Macrophage Differentiation and Function. *Immunity*.
- Tirziu, D., Giordano, F.J., and Simons, M. (2010). Cell Communications in the Heart. *Circulation* 122, 928–937.
- Tørring, P.M., Larsen, M., Kjeldsen, A.D., Ousager, L., Tan, Q., and Brusgaard, K. (2015). Global gene expression profiling of telangiectasial tissue from patients with hereditary hemorrhagic telangiectasia. *Microvasc Res* 99, 118–126.
- Torsney, E., Charlton, R., Diamond, A.G., Burn, J., Soames, J.V., and Arthur, H.M. (2003). Mouse Model for Hereditary Hemorrhagic Telangiectasia Has a Generalized Vascular Abnormality. *Circulation* 107, 1653–1657.
- Tual-Chalot, S., Oh, P.S., and Arthur, H.M. (2015). Mouse models of hereditary hemorrhagic telangiectasia: recent advances and future challenges. *Frontiers Genetics* 6, 919.
- Uenishi, G., Theisen, D., Lee, J.-H., Kumar, A., Raymond, M., Vodyanik, M., Swanson, S., Stewart, R., Thomson, J., and Slukvin, I. (2014). Tenascin C Promotes Hematoendothelial Development and T Lymphoid Commitment from Human Pluripotent Stem Cells in Chemically Defined Conditions. *Stem Cell Rep* 3, 1073–1084.
- Val, S., Chi, N.C., Meadows, S.M., Minovitsky, S., Anderson, J.P., Harris, I.S., Ehlers, M.L., Agarwal, P., Visel, A., Xu, S.-M., et al. (2008). Combinatorial Regulation of Endothelial Gene

- Expression by Ets and Forkhead Transcription Factors. *Cell* 135, 1053–1064.
- Vanhee, S., Mulder, K., Caeneghem, Y., Verstichel, G., Roy, N., Menten, B., Velghe, I., Philippé, J., Bleser, D., Lambrecht, B.N., et al. (2015). In vitro human embryonic stem cell hematopoiesis mimics MYB-independent yolk sac hematopoiesis. *Haematologica* 100, 157–166.
- Weiskopf, K., and Weissman, I. (2015). Macrophages are critical effectors of antibody therapies for cancer. *Mabs* 7, 303–310.
- van Wilgenburg, B., Browne, C., Vowles, J., and Cowley, S.A. (2013). Efficient, Long Term Production of Monocyte-Derived Macrophages from Human Pluripotent Stem Cells under Partly-Defined and Fully-Defined Conditions. *Plos One* 8, e71098.
- Wimmer, R.A., Leopoldi, A., Aichinger, M., Kerjaschki, D., and Penninger, J.M. (2019a). Generation of blood vessel organoids from human pluripotent stem cells. *Nat Protoc* 14, 3082–3100.
- Wimmer, R.A., Leopoldi, A., Aichinger, M., Wick, N., Hantusch, B., Novatchkova, M., Taubenschmid, J., Hämmerle, M., Esk, C., Bagley, J.A., et al. (2019b). Human blood vessel organoids as a model of diabetic vasculopathy. *Nature* 565, 505–510.

APPENDIX

Summary

Samenvatting

Curriculum Vitae

List of publications

Acknowledgments

SUMMARY

Endothelial cells (ECs) and myeloid cells derived from human induced pluripotent stem cells (hiPSCs) provided a novel and powerful tool for the study of various vascular and inflammatory diseases which are caused or correlated to dysfunctions of these cell types. This thesis mainly focuses on the derivation and characterization of ECs and myeloid cells from hiPSCs, and their application in modeling two vascular diseases Hereditary Hemorrhagic Telangiectasia type 1 (HHT1) and Pseudomyogenic hemangioendothelioma (PHE).

Chapter 1 provides general introduction of hiPSC-derived ECs and macrophages. This chapter summarized the current developed differentiation method for these cell types and their phenotype and functional activities compared to their primary counterparts *in vivo*. As we are mainly interested in two vascular diseases HHT1 and PHE, this chapter also describes known underlying disease mechanism of these diseases, with an emphasize ECs and myeloid cells.

In **chapter 2 and 3**, an efficient protocol was developed to derive monocytes and macrophages from hiPSCs and performed detailed functional characterization and comparison with peripheral blood (PB)-derived monocytes and macrophages. We showed that hiPSC-derived monocytes were functional after cryopreservation and could be used to model the inflammation response *in vitro* in a microfluidic chip. Both pro-inflammatory and anti-inflammatory M1 and M2 subtypes of macrophages could be polarized from hiPSC-monocytes, which were similar to PB-derived macrophages in terms of their gene expression profiles and functional activities. Interestingly, we observed a higher endocytosis and efferocytosis activities with hiPSC-derived macrophages than blood-derived macrophages, although both showed similar bacterial and tumour cell phagocytosis capacities. In summary, hiPSC-monocytes and macrophages could be generated robustly from independent hiPSC-lines, which were fully functional and comparable with PB-derived myeloid cells.

In **chapter 4**, the development process of EC and cardiomyocytes from hiPSCs in a co-differentiation system was investigated utilizing an ETV2^{mCherry} reporter line and bulk and single cell RNA sequencing (RNAseq) approaches. This chapter showed that EC and cardiomyocytes had a common development origin from cardiac mesoderm precursors in this co-differentiation system. A critical role of transient expression of ETV2 was revealed during endothelial fate specification. Besides, this chapter indicated that functional cardiomyocytes could also differentiate from ETV2+ progenitors.

In **chapter 5**, a 3D vasculature model was established in a microfluidic chip using ECs derived from isogenic HHT1 hiPSC lines, which were generated from a mosaic HHT1 patient. Disease related phenotypes were observed using this 3D vascular model with mutant hiPSC-ECs, including increased inflammatory responses and defected vascular

organization. TGF β , BMP and WNT signaling pathways were revealed being dysregulated in mutant ECs based on their whole transcriptomic profile. Work of this chapter further revealed the underlying disease mechanism of HHT1 which is crucial for developing potential therapeutic strategies in the future.

In **chapter 6 and appendix**, a PHE tumor specific hiPSC line was established by introducing a chromosomal translocation into WT hiPSCs using CRISPR/Cas9. Then ECs were differentiated from the disease line in order to model PHE *in vitro*. Mutated hiPSC-ECs showed a number of disease related phenotypes *in vitro* and *in vivo* after transplantation into mice, which correlated to disease symptoms observed in PHE patients. RNAseq of WT and mutated hiPSC-ECs revealed transcriptome alterations causing hiPSC-EC dysfunction, which reflected the PHE phenotypes. Signaling pathways dysregulated in PHE hiPSC-ECs were also identified, which can be potentially be targeted for the treatment of PHE in the future.

Finally, **chapter 7** is a general discussion about the research conducted in this thesis, which summarized both the importance of our findings and limitations of the work. This chapter also includes future perspectives of the research in each chapter of this thesis, which are either already under investigation in our lab or could be potentially conducted in the future.

SAMENVATTING

Endotheelcellen (ECs) en myeloïde cellen, afgeleid van humane geïnduceerde pluripotente stamcellen (hiPSCs), vormen een nieuw en krachtig hulpmiddel voor de studie van verschillende vaat- en ontstekingsziekten die worden veroorzaakt door, of gecorreleerd aan, het disfunctioneren van deze celtypen. Dit proefschrift richt zich voornamelijk op de differentiatie en karakterisering van hiPSC-afgeleide ECs en myeloïde cellen en hun toepassing bij het modelleren van twee vaatziekten, namelijk Hereditaire Hemorragische Teleangiëctasie (HHT1) en Pseudomyogeen hemangioendotheloom (PHE).

Hoofdstuk 1 geeft een algemene introductie over hiPSC-afgeleide ECs en macrofagen. In dit hoofdstuk wordt de huidige ontwikkelde differentiatiemethode voor deze celtypen samengevat en wordt het fenotype en de functionele activiteit van deze cellen vergeleken met hun primaire tegenhangers *in vivo*. Aangezien we voornamelijk geïnteresseerd zijn in de vaatziekten HHT1 en PHE, beschrijft dit hoofdstuk ook het onderliggende mechanisme van deze ziekten, met de nadruk op ECs en myeloïde cellen.

Hoofdstuk 2 en 3 beschrijven de ontwikkeling van een efficiënt protocol voor de differentiatie van monocyt en macrofagen van hiPSCs en geven een gedetailleerde functionele karakterisering en vergelijking met perifeer bloed (PB) -afgeleide monocyt en macrofagen. We tonen aan dat hiPSC-afgeleide monocyt na cryopreservatie functioneel zijn en kunnen worden gebruikt om de ontstekingsreactie *in vitro* te modelleren in een microfluidische chip. Zowel pro-inflammatoire als ontstekingsremmende M1- en M2-subtypen van macrofagen konden worden gepolariseerd van hiPSC-monocyt, deze waren vergelijkbaar met PB-afgeleide macrofagen wat betreft hun genexpressieprofiel en functionele activiteit. Interessant is dat we een hogere endocytose- en efferocytoseactiviteit waarnamen in hiPSC-afgeleide macrofagen dan in bloed-afgeleide macrofagen, terwijl beide vergelijkbare bacteriële en tumorcel fagocytosecapaciteiten vertoonden. Samengevat, hiPSC-monocyt en macrofagen konden robuust worden gegenereerd uit onafhankelijke hiPSC-lijnen, deze cellen waren volledig functioneel en vergelijkbaar met PB-afgeleide myeloïde cellen.

In **hoofdstuk 4** wordt het ontwikkelingsproces van ECs en cardiomyocyten van hiPSCs in een co-differentiatiesysteem onderzocht met behulp van een ETV2^{mCherry} reporterlijn en bulk- en single cell RNA sequencing (RNAseq). Dit hoofdstuk toont aan dat ECs en cardiomyocyten in dit co-differentiatie systeem een gemeenschappelijke ontwikkelingsoorsprong hebben, ze zijn beide ontstaan uit cardiogene mesoderm voorlopers. De cruciale rol van kortstondige expressie van ETV2 werd onthuld tijdens de specificatie van het endotheel. Bovendien bewijst dit hoofdstuk dat functionele cardiomyocyten ook kunnen worden ontwikkeld vanuit ETV2+ voorlopers.

Hoofdstuk 5 toont een vasculair 3D model in een microfluidische chip gevormd met

behulp van ECs, afgeleid van isogene HHT1 hiPSC-lijnen, die werden gegenereerd uit een HHT1-patiënt met mozaïcisme. Ziektegerelateerde fenotypen werden waargenomen met behulp van dit vasculaire 3D-model met mutante hiPSC-ECs, waaronder een stijging in ontstekingsreacties en defecte vasculaire organisatie. TGF β -, BMP- en WNT-signaleringsroutes bleken ontregeld te zijn in mutante ECs op basis van hun gehele transcriptomische profiel. Het onderzoek in dit hoofdstuk onthulde verder het onderliggende ziektemechanisme van HHT1 dat cruciaal is voor het ontwikkelen van potentiële therapeutische strategieën in de toekomst.

Hoofdstuk 6 en de **appendix** beschrijven de ontwikkeling van een PHE-tumorspecifieke hiPSC-lijn. Deze lijn werd gegenereerd door een chromosomale translocatie in WT hiPSCs te introduceren met CRISPR/Cas9. Vervolgens werden ECs gedifferentieerd van deze lijn om PHE *in vitro* te kunnen modelleren. De gemuteerde hiPSC-ECs vertoonden een aantal ziektegerelateerde fenotypen *in vitro* en *in vivo* na transplantatie in muizen, die correleren met symptomen die zijn waargenomen bij PHE-patiënten. RNAseq op wildtype (WT) en gemuteerde hiPSC-ECs onthulde transcriptoomveranderingen die hiPSC-EC-disfuncties veroorzaken en die de PHE-fenotypen weerspiegelen. Signaleringsroutes die in PHE hiPSC-ECs ontregeld zijn werden ook geïdentificeerd, deze kunnen mogelijk doelwit zijn voor de behandeling van PHE in de toekomst.

Tot slot, **hoofdstuk 7** verstrekt een algemene discussie over het onderzoek in dit proefschrift, waarin zowel het belang van de bevindingen als de beperkingen van dit werk zijn samengevat. Dit hoofdstuk bespreekt ook de toekomstperspectieven van het onderzoek dat in de voorgaande hoofdstukken is beschreven. De genoemde mogelijkheden worden al in ons laboratorium onderzocht of zouden mogelijk in de toekomst kunnen worden uitgevoerd.

CURRICULUM VITAE

Xu Cao was born on 7th July, 1990 in Linyi, Shandong Province, China. Xu obtained his Bachelor degree in Biotechnology at Shandong University in 2012. During his bachelor study, he performed an internship in the group of Prof. Dong Li at Qilu Hospital of Shandong University, where he conducted his bachelor thesis entitled “Optimization of culture condition for hematopoietic stem cell isolated from rat bone marrow”. From 2012 to 2015, Xu did his Master studies at the Institute of Zoology, Chinese Academy of Science in Beijing, China, supervised by Prof. Baoyang Hu. During his master study, he worked on establishing a knock-in reporter human embryonic stem cell (hESC) line for two specific genes of dopaminergic neuron (DA) progenitor cells using CRISPR/Cas9, as well as studying the influence of the stiffness of extracellular matrix (ECM) and the density of ECM protein on neuronal differentiation from hESCs. After obtaining his master degree, he moved to Netherlands to pursue a doctorate degree in Leiden University Medical Center, under the supervision of Prof. Dr. C.L Mummery and Dr. V.V. Orlova. He was mainly work on the modeling of vascular diseases using human induced pluripotent stem cells (hiPSCs). The results of the research are shown in this thesis. After obtaining his PhD, he plans to carry out a postdoc in the US.

LIST OF PUBLICATIONS

Differentiation and Functional Comparison of Monocytes and Macrophages from hiPSCs with Peripheral Blood Derivatives

Xu Cao, Gopala Krishna Yakala, Francijna E. van den Hil, Amy Cochrane, Christine L. Mummery and Valeria V. Orlova

Published in **Stem Cell Reports**, Vol. 12, pages 1282–1297, June 11, 2019 Doi: 10.1016/j.stemcr.2019.05.003

An efficient Protocol for Derivation and Functional Characterization of Monocytes and Macrophages from hiPSCs

Xu Cao, Francijna E. van den Hil, Christine L. Mummery and Valeria V. Orlova

Published in **Current Protocols in Stem Cell Biology**, 2020 e108, Volume 52 Doi: 10.1002/cpsc.108

Transcriptional Dynamics During the Segregation of Endothelial and Myocardial Lineages from Cardiac Mesoderm

Xu Cao, Maria Mircea, Gopala Krishna Yakala, Francijna E. van den Hil, Hailiang Mei, Konstantinos Anastassiadis, Christine L. Mummery, Stefan Semrau and Valeria V. Orlova

Manuscript in preparation

Vascular Defects Associated with Hereditary Haemorrhagic Telangiectasia Revealed in Patient-derived Isogenic iPSCs in 3D Microfluidic Chips

Valeria V. Orlova, Xu Cao, Amy Cochrane, Roderick C. Sliker, Christian Freund, Francijna van den Hil, David Lemmonier, Gonzalo Sánchez-Duffhues, Hailiang Mei, Cornelius J.J. Westermann, Repke J. Snijder, Frans Disch, Johannes Kristian Ploos van Amstel, Peter ten Dijke, Franck Lebrin, Hans-Jurgen Mager, Christine L. Mummery

Manuscript in preparation

Pseudomyogenic Hemangioendothelioma Recapitulated in Endothelial Cells from Human Induced Pluripotent Stem Cells Engineered to Express the SERPINE1-FOSB Translocation

David G.P. van IJendoorn, Daniela C.F. Salvatori[#], Xu Cao[#], Francijna van den Hil, Inge H. Briaire-de Bruijn, Danielle de Jong, Hailiang Mei, Christine L. Mummery, Karoly Szuhai, Judith V.M.G. Bovée, Valeria V. Orlova

Under review in **Cell Reports Medicine**, [#]joint second author

Cardiac- but not dermal fibroblasts induce structural and functional maturation of hiPSC-derived cardiomyocytes in 3D microtissues via CX43 gap-junctions

Elisa Giacomelli[#], Viviana Meraviglia[#], Giulia Campostrini[#], Amy Cochrane, Xu Cao, Ruben W.J van Helden, Ana Krotenberg Garcia, Maria Mircea, Sarantos Kostidis, Richard P. Davis, Berend J van Meer, Carolina R Jost, Abraham J Koster, Hailiang Mei, David G. Míguez, Aat A Mulder, Mario Ledesma-Terrón, Giulio Pompilio, Luca Sala, Daniela C.F. Salvatori, Roderick C. Sliker, Elena Sommariva, Antoine A. F. de Vries, Martin Giera, Stefan Semrau, Leon GJ Tertoolen, Valeria V Orlova* & Milena Bellin* & Christine L Mummery*

Published in **Cell Stem Cell**, 2020, 1934-5909, Doi: 10.1016/j.stem.2020.05.004

Phosphatidic Acid Improves Reprogramming to Pluripotency by Reducing Apoptosis

Yuan Jiang, Mingxia Du, Menghua Wu, Yanbing Zhu, Xing Zhao, Xu Cao, Xin Li, Peipei Long, Wei Li, Baoyang Hu

Published in **Stem Cells and Development**, 25(2016), 43-54. Doi: 10.1089/scd.2015.0159

ACKNOWLEDGMENTS

The PhD marathon is coming to an end and I would like to express my sincere appreciation to all people that helped and accompanied me in the past 5 years and made this wonderful and tough journey possible.

I would like to start by thanking to my supervisor Valeria Orlova. Thank you for taking me as your PhD student at the beginning: for training and pushing me to become an independent researcher while always having you to back me up; for sharing that passion and motivation for science; for all your help with my publications and thesis and for your valuable advice not only on my research career but also on my life in general as a friend.

I want to express my great gratitude to my promoter Christine Mummery. For offering this great working opportunity which is a turning point of my life. For your guidance, support and advice along the journey of my PhD. For your great help with this thesis. I am lucky and honored for being mentored by you.

A great thanks to all technicians of Anatomy and Embryology Department, for your assistance with my PhD work. Specially to Lisa van den Hil, for training me at the start of my PhD, answering my questions, conducting experiments (numerous qPCR) and contribution to the manuscripts.

To my dear friends Karina and Oleh, for sharing both good and bad moments with me inside and outside the lab, which for sure made my PhD journey less stressful. To Yang, Lettine and Jun, for those joyful moments during our lunches.

To Gopi Karishna Yakala, for all your help with my research project and contribution to the manuscript, also for sharing research experience, giving advice and company for lunches. To Amy Cochrane for advice and helping with the manuscript. To Maria Mircea and Stefan Semrau, for the great help and contribution with our collaborative projects.

Great thanks to my paranymphs Karina and Lisa, for the great work you have done

and lots of help in this graduation process.

To Richard, Christian and Milena and Daniela, for your great suggestions and help with my research, for sharing knowledge and experience during our numerous group meetings in the past 5 years.

To all ANA fellow PhD students and postdocs, for being helpful and nice, good company and creating great memories along this journey. I am really happy to work with you all.

To Atie, for all your help with the administration work. To Daniel and Paul, for the IT support which is really helpful.

To my wife Merissa, thanks for appearing in my life, for your love and patience to be my side at the toughest times during this journey. Thanks for your words and smiles that keeping me optimistic and energetic about work and life.

最后，我想感谢远在中国的我的家人们对我生活和工作的鼓励和支持！感谢父母对我一直以来对我竭尽所能的培养和我所取得的成绩的肯定，以及对我常年不能陪伴左右的包容和理解。